4-PI COMPTON IMAGING USING A SINGLE 3-D POSITION SENSITIVE CdZnTe DETECTOR

by

Carolyn E. Lehner

A dissertation submitted in partial fulfillment
of the requirements for the degree of
Doctor of Philosophy
(Nuclear Engineering and Radiological Sciences)
in The University of Michigan
2004

Doctoral Committee:

Assistant Professor Zhong He, Chair
Associate Professor James P. Holloway
Professor Emeritus Glenn F. Knoll
Professor Emeritus W. Leslie Rogers

For my family

ACKNOWLEDGMENTS

First and foremost I would like to thank Prof. Zhong He for the guidance and support he has given me throughout my graduate career. This work would not have been possible without his help. I am thankful for the opportunity to work with Prof. Glenn Knoll, who provided hours of fun conversation (and weeks of additional work). I would also like to thank Dr. James Holloway and Dr. Leslie Rogers for serving on my dissertation committee and providing many helpful comments about this thesis.

There would have been no experimental results to report without the intense efforts of Feng Zhang, who has performed miracles with the 3-D CZT system used here. I cannot thank him enough for all his help to make my experiments run well. Many thanks are due to Dan Xu, who always found my mistakes and never failed to question the processes I chose. I am also thankful for the support of my other group members: Prof. James Baciak, Benjamin Sturm, and Scott Kiff. We had completely separate projects, but our conversations were invaluable. I would like to thank James Berry for his technical support and electrical engineering expertise. I am grateful to Dr. Yanfeng Du, Dr. Scott Wilderman, and Prof. Jeffrey Fessler, who provided much needed assistance with the maximum likelihood reconstruction techniques. I also thank Dr. Jose Perez for a very useful GEANT tutorial.

I would also like to thank the Department of Nuclear Engineering and Radiological Sciences, and the students, staff, and faculty that made the last 4 ½ years fun. I am thankful to the Department of Energy, which supported my graduate education through the Nuclear Engineering and Health Physics Fellowship Program for four years.

There have been other people over the years that have had a profound influence on my growth as a scientist. Dr. Kai Vetter has been a mentor to me since we worked together at Lawrence Berkeley National Laboratory. I value his input and encouragement. I have appreciated and enjoyed many discussions with Dr. Richard Kroeger and Dr. Eric Wulf about their own Compton imagers. And this list would be incomplete without Jay Friberg, who taught the toughest high school science class I ever took. I thank him for the challenge.

I am so thankful for the love and encouragement of my family, which kept me mostly sane all of these years. My dad, Dale Lehner, and I always discussed politics and history, and from him I learned how to think independently. My mom, Tricia Lehner, was always on my side, and she taught me how to take good care of people. When we were children, my sister, Cathy Beck, used to teach me from her own math book "because I was going to have to learn it sometime," and I still hope to learn the secret to her abundant energy. My younger sister, Andrea Lehner, has simply amazed me with her capacity for giving and acceptance, and I hope even a small fraction of it rubs off to me. My best friend, Shana Helton, has always been my one-woman cheering section, and I am eternally grateful for her friendship. And, finally, I am so thankful for the love and support of my future husband, Dr. Allen Seifert, who read this thesis from cover to cover (some of it twice) and still had to bear the brunt of my dissertation stress. Although he is last in this list, he will always be first in my heart.

TABLE OF CONTENTS

CHAPTER

LIST OF FIGURES

Figure

LIST OF TABLES

Table

CHAPTER 1

INTRODUCTION

1.1 Principles of Compton Imaging

Compton imaging is the use of Compton scatter kinematics to reconstruct an image of a gamma-ray source distribution. In Compton scatter a gamma ray interacts with an atomic electron, providing enough energy to overcome the binding energy and eject it from the atom. The gamma ray, which transfers energy to the electron in the form of kinetic energy, is scattered at an angle with respect to its initial direction. The gamma ray may then scatter again or undergo other types of interactions in the material. Of particular interest in Compton imaging is photoelectric absorption in which the total gamma-ray energy is transferred to an atom, which then ejects an electron. After any interaction the energy carried by the electron is then deposited in the surrounding material through electron scattering which generates electron-ion pairs in gases or electron-hole pairs in semiconductor detectors. For initial gamma-ray energy E_0, deposited energy E_1, and scattered gamma-ray energy E', the Compton scatter angle, θ, can be calculated via Equation 1.1,

$$\cos\theta = 1 - \frac{m_e c^2 E_1}{E_0 E'}, \tag{1.1}$$

where $m_e c^2$ is the rest mass energy of an electron (511 keV). Equation 1.1 is commonly called the "Compton scatter formula" and is derived under the assumptions that the electron is unbound and at rest.

The traditional Compton imager consists of two detectors that register the positions and energies of gamma-ray interactions. Pixellated detectors[1-3], orthogonal strip detectors[4, 5], or arrays of conventional planar detectors[6] can be used as position-sensitive spectrometers. When a gamma ray scatters in the first ("front plane") detector and then is absorbed in the second ("back plane") detector, the locations and energies of each interaction are measured. By using the Compton scatter formula the scatter angle can be determined from the deposited and initial gamma-ray energies. As illustrated in Figure 1.1, a line connecting the positions of the interactions (labeled *1* and *2*) determines the axis of a cone of possible source locations. The vertex and half-angle of the cone are given by the first interaction position and the Compton scatter angle, θ, respectively. The source location can only be determined to within a cone due to the azimuthal ambiguity in the Compton scatter formula. Each sequence of events in the two detectors results in a cone, and over many events the cones typically are summed in the source plane (which must be known or estimated) to generate an image of the source distribution. Various backprojection and iterative image reconstruction methods can then be used to improve the quality of the image[7-9].

Two performance measurements are often quoted for Compton imagers: efficiency and angular resolution. The intrinsic camera efficiency is the fraction of gamma rays incident on the front-plane detector that result in imaged sequences (i.e. sequences that deposit full energy and result in Compton cones at least partially within the field-of-view). The intrinsic efficiency is a measure of the sensitivity of the device. Angular resolution—usually taken as the full-width at half-maximum (FWHM) of a central slice through the 3-D point source response function of the system—is used to characterize the quality of the images. Large angular resolutions correspond to poor images while small resolutions correspond to good images.

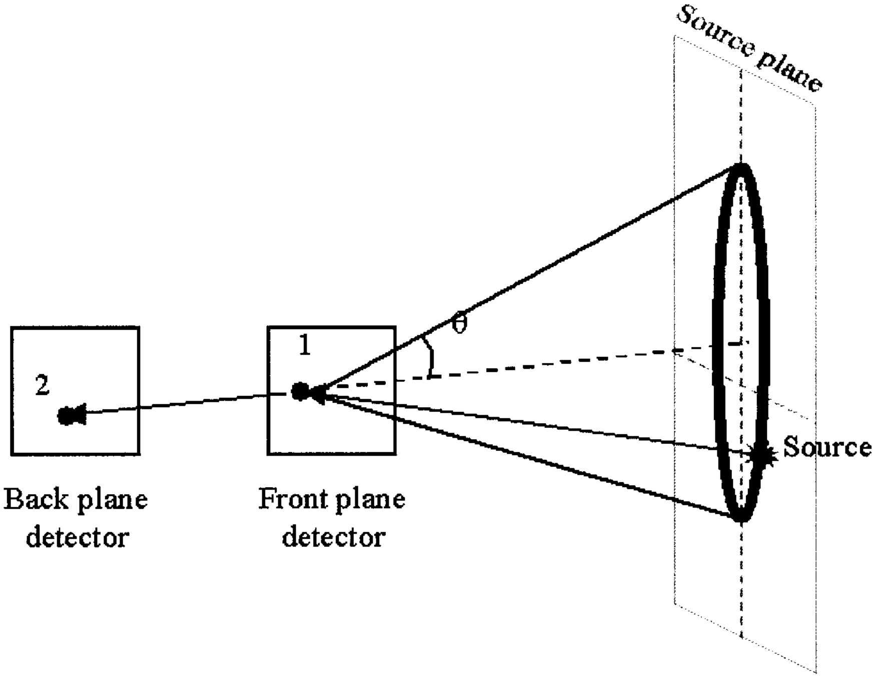

Figure 1.1. Illustration of Compton imaging. A line between the first and second interaction locations determines the axis of a cone whose half-angle is given by the Compton scatter formula. The cone is projected onto the source plane. Summing cones from many events gives an estimate (image) of the source distribution.

1.2 History of Compton Imaging

Research with Compton imagers—also called "electronically collimated gamma cameras" or "Compton telescopes"—has been active for thirty years. The first Compton scatter device was proposed in 1973 by Schonfelder, Hirner, and Schneider from the Max-Planck Institute in order to study the nature of the astronomical sources of MeV gamma rays[10]. The Compton telescope used a 3375-cm^3 plastic scintillator cube separated by 1.2 m from a 3 × 3 array of 8000-cm^3 plastic scintillator cubes to register gamma-ray events with limited angular incidence (30°). The telescope did not produce images, but it had directional sensitivity such that observable differences could be expected for point sources, galactic background, and the diffuse electromagnetic spectrum. The authors reported an energy resolution of 20% half-width at half-maximum (HWHM) at 2.75 MeV and absolute detection efficiency of 0.5%.

In 1974 Herzo *et al.* at the University of California-Riverside reported the design for a combined neutron and gamma ray double-scatter telescope[11]. As before, the purpose of the telescope was obtaining directional sensitivity and not gamma-ray imaging. The device consisted of two groups of liquid scintillation tanks separated by 1 m. The total volumes of the front plane and back plane detectors were 0.125 m^3 and 0.2 m^3, respectively. Time-of-flight measurements discriminated between gamma rays and neutrons. As with the Max-Planck Institute design, the double-scatter telescope did not require full gamma-ray absorption in the second detector array, but instead a correction factor was used to estimate the initial gamma-ray energy based on the observed deposited energies and interaction positions. Simulations demonstrated an expected energy resolution of 25% HWHM at 2.2 MeV and 20% HWHM at 4.4 MeV. Angular resolution was estimated near 8° HWHM with a maximum field of view of about π steradians. The maximum calculated efficiency of 3% occurred at 3 MeV.

The first Compton imaging device was proposed by Todd *et al.* from the University of Southampton in 1974 as an alternative to a mechanically collimated imaging system[12]. They were the first to recognize that by using the kinematics of Compton scatter, one can localize the source direction of a gamma ray within a cone surface, given the position and energy deposited in each of two interactions. In a 1977 publication[13], they showed through simulations that a Compton imager composed of planes of Si strip detectors could localize the direction of a point source and could even reconstruct an image of an object phantom.

The first working prototype imager was reported in 1983 by Singh and Doria from the University of Southern California[14]. Three-dimensional tomographic and 2-D planar images were reconstructed using a cylindrical 6 mm diameter × 6 mm thick high-purity germanium (HPGe) front-plane detector separated by 5 cm from an uncollimated

NaI(Tl) scintillation detector in the back plane. The initial gamma-ray energy was known and used to discard partial energy deposition events. A 9° full-width at half-maximum (FWHM) angular resolution can be inferred based on data published in the manuscript. In 1988, Brechner and Singh used simulations to compare the above Compton imaging ("electronically collimated") system with mechanically collimated systems[15]. They reported a simulated factor of 20 gain in sensitivity compared with a cone-beam collimated gamma camera (which has better sensitivity than a traditional parallel-hole collimated camera).

The early successes of Compton imaging systems led to the development of COMPTEL, a Compton telescope selected to fly on NASA's Gamma Ray Observatory (later referred to as the Arthur Holly Compton Gamma Ray Observatory, or simply the CGRO)[16]. Schonfelder, who helped develop the first Compton telescope, led the international team of scientists that designed COMPTEL. The front-plane detector was an array of seven liquid scintillator cells (28 cm in diameter and 8.5 cm thick) coupled to photomultiplier tubes (PMTs). The back plane detector consisted of 14 NaI(Tl) scintillators (28 cm in diameter and 7.5 cm thick) also coupled to PMTs. The observed energy resolution was 12% FWHM at 511 keV and 6% FWHM at 2.75 MeV. Due to the large separation distance between detectors (over 2 m), the angular resolution of the system was at or below 4.7° FWHM for gamma-ray energies between 1 and 10 MeV.

At the time of its flight COMPTEL was the most sensitive astronomical gamma-ray detector in the 1-30 MeV range. The efficiency and angular resolution of the system were, however, abysmal by medical imaging standards. Thus, different schemes were investigated to maximize the efficiency of such systems while improving the imaging resolution. In 1988, Kamae and Hanada devised an imager consisting of a stack of 6 mm × 6 mm × 500 μm Si strip detectors surrounded by a 2-cm thick cylindrical CsI(Tl) scintillator, increasing the solid angle subtended by the back plane detector, and thus increasing the efficiency of the device[17]. They calculated a total intrinsic efficiency near 20% for a simulated beam source with energy less than 500 keV and estimated an expected angular resolution between 3-5.5° FWHM when the initial gamma-ray energy is known. In the same year, Soloman and Ott determined that germanium and silicon were ideal material candidates for the front-plane detector, based on efficiency, absorption, and position resolution characteristics[18]. Only high atomic number scintillators were considered for the back plane detector in their study. It should be noted that by the late 1980s pixellated anode structures had not yet been used with semiconductor detectors; thus semiconductors with poor charge carrier transport properties were not considered viable for these devices.

As semiconductor detectors improved throughout the 1980s and 1990s, more researchers looked to Si, Ge, and CdZnTe detectors as possibilities for Compton imaging. In 1990, Dogan, Wehe, and Knoll from the University of Michigan proposed a multiple scatter Compton camera using stacks of Si detectors surrounded by a CsI(Tl) scintillator [19]. This was the first demonstration of using multiply scattered gamma rays for Compton imaging. At 511 keV, the estimated efficiency was about 7% and the angular resolution was estimated between 3 – 7° depending on electronic noise level[20].

In 1993 Martin *et al.* proposed a ring Compton camera that used a 4×4 array of 5mm × 5mm × 6mm Ge detectors as the front plane detector followed by a ring of cylindrical NaI(Tl) back plane detectors 19.1 mm in diameter and 50.8 mm in length[6]. The Ge detector could be moved along the axis of the NaI(Tl) ring to vary the observed Compton scatter angles. The camera had an angular resolution of about 9° FWHM and an intrinsic efficiency of 1.5×10^{-4} at a scatter angle of 45°. It was later determined by Gormley *et al.* that the device performed better than a mechanically collimated pinhole camera for energies above 400 keV[21].

LeBlanc *et al.* also from the University of Michigan, introduced the C-SPRINT camera in 1998[22]. It consisted of a 22×22 array of 1.2 mm × 1.2 mm × 1.0 mm Si pad detectors in the front plane followed by a ring of a variable number of 1.27 cm thick planar NaI(Tl) detectors. The camera showed an angular resolution performance between 4° and 40° FWHM depending on reconstruction method and the number of back plane detectors used.

A system similar to those reported by Kamae and Hanada and by Dogan, Wehe, and Knoll, was developed by the University of California at Riverside in 1995[4]. The Tracking and Imaging Gamma-Ray Experiment (TIGRE) used seven 3.2 cm × 3.2 cm × 300 μm Si strip detectors sandwiched for thickness and 36 CsI(Tl) scintillators with dimensions 1 cm × 1 cm × 1.7 cm. The device was designed for astronomical imaging in the range of 0.3 to 100 MeV. The group proposed to track the recoil electron through the Si detector. Knowing the Compton scatter angle and the recoil electron direction eliminates the azimuthal uncertainty in the backprojected image, resulting not in a cone but in a ray. Using "up" versus "down" electron momentum determination, they measured a 10° FWHM angular resolution at 900 keV. At 511 keV, the measured resolution was approximately 11° FWHM.

One year later, Phlips *et al.* from the Naval Research Laboratory reported the performance of a Compton telescope using planar 5 cm × 5 cm Ge detectors as both the front and back plane detectors[5]. The second detector was rotated 90° relative to the first, such that the detector planes were orthogonal. With an intrinsic efficiency of approximately 3%, the design was capable of 1° FWHM angular resolution.

In 1997, Bolozdynya *et al.* reported the performance of a gaseous xenon Compton imager[23]. The detector was composed of a cylindrical pressure chamber with a low electric field drift region and a high-field electroluminescent region. Position-sensitive photomultiplier tubes measured two dimensional interaction positions, and the third coordinate was determined from the time delay between the signals generated by the original scintillation and the electroluminescence. An imaging resolution of 13.6° FWHM at 140 keV can be inferred from the presented data.

In 1998, Aprile *et al.* proposed the first liquid xenon Compton imager, composed of a 20 cm × 20 cm × 7 cm (active volume) time-projection chamber (TPC) enclosed in a cylindrical pressure chamber[24]. Another proposed design contained two large area (2500 cm^2) time-projection chambers in a single pressure vessel[25]. Orthogonal wires in the TPCs were used to measure interaction position in two dimensions, and the third dimension was determined from the electron collection time. With a 1σ energy resolution of 2.5% at 1 MeV and 1σ position resolution of 1 mm, the expected 1σ angular resolution varied from 0.4° to 2.4° over the 120° field-of-view.

Du *et al.* from the University of Michigan developed a Compton imager prototype composed of two 1-cm^3 CdZnTe detectors with three-dimensional position sensitivity in 2001[26]. This system was the prototype for the current work. The detectors were separated by 5 cm, and the field-of-view was limited to scatter angles between 20° and 80°. Only gamma rays that scattered in the first detector and were absorbed in the second detector were used for imaging. The measured intrinsic efficiency at 662 keV was only 1.5×10^{-4}, due to the small back plane detector size compared with the distance between detectors. The imager had a measured angular resolution of about 5° FWHM at that energy[27].

In the same year, Schmid *et al.* proposed using large segmented coaxial germanium detectors for Compton imaging[2]. This design combined excellent energy resolution of HPGe detectors with the increased efficiency of using a single detector to do Compton imaging. Pulse shape analysis was proposed to determine interaction locations within each segment, resulting in calculated position resolution of about 1 mm in each direction. Measurements and simulations performed on the Gamma-Ray Energy Tracking Array (GRETA)[28] detectors demonstrated that a large preamplifier noise was inhibiting the imaging performance at 186 and 244 keV. The source location could not be identified in experiments, but could be found in simulations with reduced noise levels. This work was the first attempt at 4π Compton imaging.

In 2002 the Naval Research Laboratory published experimental data from a Compton imager composed of a single HPGe double-sided strip detector[29]. They used two-event sequences in a 5 cm × 5 cm × 1.1 cm detector. Measurements demonstrated the ability to resolve two point sources at 662 and 511 keV separated by 20 cm at 41 cm from the detector. The reported angular resolution was 7°. This was the first successful attempt at Compton imaging using a single detector, although only planar images were reconstructed. In the following year they successfully demonstrated using two detectors with the three-Compton technique, where gamma rays are not required to deposit full energy in the detectors as long as three interactions occur[30].

In 2003, Lebrun *et al.* proposed a Compton cube for imaging galactic and extragalactic phenomena[31]. Planar CdTe or CdZnTe detectors (4 mm × 4 mm) are arranged in six arrays of 32 × 32 detectors each. The arrays are arranged as sides of a cube, with supporting electronics on the outside of the cube. The overall cube dimension is about 15 cm. The authors propose to do all-sky imaging with this system, and cite a field-of-view six times larger than that of COMPTEL. They estimate between 4 – 2.5° FWHM angular resolution for gamma-ray energies from 100 keV to 1 MeV, although it is unclear if they have considered Doppler broadening in this estimate. The uniqueness of the design is the use of any detector array as the front plane or back plane. In this way, the field-of-view is much larger than other geometries. However, it is unclear how the authors plan to properly sequence the observed events, or if they have considered the possibilities for full 4π field-of-view imaging capability.

Also in 2003, Orito *et al.* from Kyoto University proposed using a TPC filled with gaseous xenon as the scatter detector and surrounding scintillators for detecting the gamma-ray absorption[32]. The TPC has pixel electrodes only 400 μm in size, and thus it is possible to track the recoil electron from Compton scatter processes, similar to the UC Riverside design. They estimate between 1% and 0.1% intrinsic efficiency between 100 keV and 2 MeV and an angular resolution on the order of 15°, although the performance has not been measured.

In early 2004, Zhang, Rogers, and Clinthorne from the University of Michigan proposed a Compton imager for scintimammography[33]. The camera is a dual-head imager consisting of two planes of 1-mm thick Si arrays 10 cm × 10 cm placed directly above and below the breast followed by two 40 cm × 40 cm × 2 cm thick NaI(Tl) detectors. Using a realistic simulated anthropomorphic phantom, they estimate an absolute efficiency of several percent and a spatial resolution of several millimeters for gamma-ray energies up to 511 keV, depending on the depth of the tumor in the breast. They demonstrate better confidence in detecting 5 mm tumors using Compton imaging compared with traditional scintimammography.

Other efforts have examined the use of Compton cameras for tomography[34, 35] or combined them with coded apertures to achieve better angular resolution[36]. Compton imagers have been proposed for everything from prostate imaging[37] to nuclear materials inspection[2] to environmental monitoring[38]. To assess the practicality of using Compton imaging for any application, it is important to understand the advantages and disadvantages of traditional Compton imaging in comparison with other imaging modalities.

1.3 Comparison with Collimated Imaging Systems

Compton imagers were designed to compete with traditional collimated gamma-ray imaging devices. In Anger cameras scintillation detectors coupled to position-sensitive photomultiplier tubes were used with heavy collimators made of materials with large atomic numbers[39]. Very good images can be obtained from Anger cameras with pinhole collimators, although parallel hole, diverging, and converging collimators can also be used. In coded aperture systems, the collimator holes are typically parallel and are

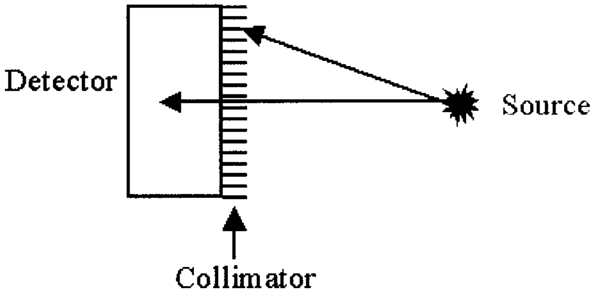

Figure 1.2. Illustration of an Anger camera. Most gamma rays emitted from the source will not penetrate the collimator walls. Only gamma rays emitted parallel to the collimator axis will arrive at the detector.

arranged in a redundant pattern[40]. The resulting shadow image is deconvolved with the coded aperture function to yield an image of the source distribution. In both collimated systems, the collimators absorb gamma rays obliquely incident on the detector face, as shown in Figure 1.2. Despite low imaging efficiencies, these cameras can produce good images for x-rays and low-energy gamma rays. However, high-energy gamma rays (greater than a few hundred keV) can penetrate collimator walls, reducing the effectiveness of the collimation and blurring the image. To mechanically collimate high-energy gamma rays thicker materials are needed, thus reducing imaging efficiency and increasing detector size and weight. In astrophysics applications, the activation by cosmic rays in the shielding materials can decrease the signal-to-noise ratio for measurements with balloon-borne and orbiting instruments.

Compton imagers have several advantages over collimated imaging systems. The absence of a collimator results in greater incident gamma-ray flux, which can lead to higher sensitivities. Also, without a collimator the imager has less mass, which is important for patient safety in nuclear medicine applications and for weight reduction of orbiting cameras used in astrophysics. In Anger cameras collimator geometry determines both the efficiency and imaging resolution, which are coupled and inversely related. Improvement in one results in degradation of the other. In Compton imagers resolution depends on the energy and position resolutions in the detectors, whereas efficiency depends on the sizes, materials, and geometry of the detectors. Due to the decoupling of these properties, it is possible to improve both image resolution and efficiency simultaneously. In addition, Compton imagers are more suited to high-energy imaging because they rely on Compton scatter processes, which dominate in most materials for gamma-ray energies from a few hundred keV to several MeV. Collimated imaging, on the other hand, requires photoelectric absorption in a single interaction—a process whose probability decreases quickly as gamma-ray energy increases.

Despite practical advantages, Compton imagers on the whole have not experimentally demonstrated improved performance over collimator systems, except in the area of high-energy astrophysics. The efficiency of the two-detector system can be orders of magnitude lower than other imagers due to the limited solid angle subtended by the back plane detector. Compton cameras can be made much more efficient by increasing the detector areas, but increasing thickness adds the complication of increased multiple scatters in the first detector. The resolution of Compton imaging systems has been shown to match the resolution of parallel hole Anger cameras used in nuclear medicine, usually at the expense of efficiency[22]. The 1° angular resolution quoted above from Phlips *et al.* may seem impressive, but it is still large compared with the 0.5° angle subtended by our moon as viewed from earth. Astronomers would prefer devices with arcminute or even arcsecond resolutions.

Compton imagers also typically require some accessory electronics and shielding materials not necessary for collimated imaging systems. Determining the event sequence is usually done by shielding the back plane detector from any radiation directly from the source, forcing the first interaction to occur in the front plane detector, or by separating the detectors sufficiently so that time-of-flight measurements can be performed. In either case, the two detectors must register interactions within a very short delay time, requiring coincidence circuitry to gate on these sequences. In addition, image reconstruction for

Compton imagers is more difficult than for Anger cameras, where position locations in the detector directly correspond to positions in the image. Typically, direct reconstruction methods for Compton imaging such as backprojection filtering require little computation time but generate poorer images than iterative reconstruction methods in which computation time can be on the order of minutes or hours on a personal computer.

Throughout the years, Compton imagers have been widely researched but not widely implemented in astrophysics, nuclear medicine, nonproliferation, or high-energy physics (the notable exception being the COMPTEL device). With the development of position-sensitive semiconductors, there has been much effort recently to reexamine the Compton imaging concept. These devices show promise for many applications, although there is still much work to be done.

1.4 Objectives of this Work

In this work 4π Compton imaging is successfully demonstrated with a single three-dimensional position-sensitive CdZnTe detector. This is the first of its kind. The use of a single detector results in an increased efficiency by three orders of magnitude over the prototype geometry[41] simply due to the probability of capturing the scattered gamma ray. The three-dimensional position sensitivity in the detector allows for the determination of all interaction locations and deposited energies. By reconstructing tracks with three or more events (in the manner of Wulf *et al.* [30]) in addition to full-energy two-event sequences, further efficiency increases can be obtained. Using CdZnTe as the detector material has several advantages. The high atomic numbers—48, 30, and 52—result in high gamma-ray capture efficiency compared with Si and Ge. In addition, CdZnTe is a room-temperature semiconductor and does not require sophisticated annealing procedures or cooling electronics which add power consumption and weight to the design. The field-of-view is not limited by the scatter angles between the two detectors, and no shielding is required because there is no back plane detector. Hence, this Compton imager can reconstruct the full 4π sky view without moving the detector—something no Anger camera can do. With low weight, no collimator or shielding materials, and room-temperature operation, the CdZnTe Compton imager can operate as a hand held 4π gamma-ray camera.

With the absence of time-of-flight capabilities or shielding of the back plane detector, the sequence order must be determined by other means. In this work a probabilistic approach that depends on the number of observed interactions is examined for determining the correct sequence. Also, iterative image reconstruction techniques, which have been shown to be superior to backprojection filtering for Compton imaging[1, 14, 26], are explored. Maximum likelihood methods are examined in particular, and a weighting method is introduced to improve the imaging resolution of the camera. The performance of the 4π imager is demonstrated using medium- and high-energy gamma-ray sources (300 keV to 2.6 MeV), and the factors which negatively affect the imaging performance are discussed.

This work is organized according to the process of generating Compton images. First, the energy deposited and the locations of interactions must be determined. Then, it is necessary to determine the proper sequence of events in the detector. Images can be reconstructed using various models and reconstruction algorithms. Finally, imaging capabilities can lead to improvements in the energy spectrum observed for a given source. Thus the 4π Compton imager becomes a true spectroscopic imager. In this work, Chapter 2 discusses 3-D position sensitivity and how energies and positions are calculated from measured signals. Chapter 3 describes the experimental hardware used in this Compton imager. In Chapter 4 a probabilistic algorithm for determining event sequences is examined. Chapter 5 describes image reconstruction using backprojection in addition to an enhanced maximum likelihood reconstruction algorithm that emphasizes the contribution of gamma-ray tracks with better angular uncertainty. Chapter 6 discusses factors that can degrade the performance of the imager. Measured performance of the 4π imager and its response to multiple sources and high energy gamma rays are shown in Chapter 7. Finally, concluding remarks about the system and areas for further research are discussed in Chapter 8.

1.5 References

[1] J. W. LeBlanc, N.H. Clinthorne, C-H. Hua, E. Nygard, W.L. Rogers, D.K. Wehe, P. Weilhammer, S.J. Wilderman, "Experimental Results from the C-SPRINT prototype Compton camera," *IEEE Transactions on Nuclear Science*, vol. 46, pp. 201-204, 1999.

[2] G. J. Schmid, D.A. Beckedahl, J.E. Kammeraad, J.J. Blair, K. Vetter, A Kuhn, "Gamma-ray Compton camera imaging with a segmented HPGe," *Nuclear Instruments and Methods in Physics Research*, vol. A459, pp. 565-576, 2001.

[3] Z. He, W. Li, G.F. Knoll, D.K. Wehe, J. Berry, C.M. Stahle, "3-D position sensitive CdZnTe gamma-ray spectrometers," *Nuclear Instruments and Methods in Physics Research*, vol. A422, pp. 173-178, 1999.

[4] T. J. O'Neill, D. Bhattacharya, S. Blair, G. Case, O.T. Tumer, R.S. White, A.D. Zych, "The TIGRE desktop prototype results for 511 and 900 keV gamma rays," *IEEE Transactions on Nuclear Science*, vol. 42, pp. 933-939, 1995.

[5] B. F. Phlips, S.E. Inderhees, R.A. Kroeger, W.N. Johnson, R.L. Kinzer, J.D. Kurfess, B.L. Graham, N. Gehrels, "Performance of a Compton telescope using position-sensitive germanium detectors," *IEEE Transactions on Nuclear Science*, vol. 43, pp. 1472-1475, 1996.

[6] J. B. Martin, G.F. Knoll, D.K. Wehe, N. Dogan, V. Jordanov, N. Petrick, "A ring Compton scatter camera for imaging medium energy gamma rays," *IEEE Transactions on Nuclear Science*, vol. 40, pp. 972-978, 1993.

[7] L. Parra, H.H. Barrett, "List-mode likelihood: EM algorithm and image quality estimation demonstrated on 2-D PET," *IEEE Transactions on Nuclear Science*, vol. 17, pp. 228-235, 1998.

[8] S. J. Wilderman, N.H. Clinthorne, J.A. Fessler, W.L. Rogers, "List-mode likelihood reconstruction of Compton scatter camera images in nuclear medicine," *IEEE Nuclear Science Symposium Conference Record*, pp. 1716-1720, 1999.

[9] L. C. Parra, "Reconstruction of cone-beam projections from Compton scattered data," *IEEE Transactions on Nuclear Science*, vol. 47, pp. 1543-1550, 2000.

[10] V. Schonfelder, A. Hirner, K. Schneider, "A telescope for soft gamma ray astronomy," *Nuclear Instruments and Methods*, vol. 107, pp. 385-394, 1973.

[11] D. Herzo, R. Koga, W.A. Millard, S. Moon, J. Ryan, R. Wilson, A.D. Zych, R.S. White, "A large double scatter telescope for gamma rays and neutrons," *Nuclear Instruments and Methods*, vol. 123, pp. 583-597, 1975.

[12] R. W. Todd, J.M. Nightingale, D.B. Everett, "A proposed gamma camera," *Nature*, vol. 251, pp. 132-134, 1974.

[13] D. B. Everett, J.S. Fleming, R.W. Todd, J.M. Nightingale, "Gamma-radiation imaging system based on the Compton effect," *Proceedings of the IEE*, vol. 124, pp. 995-1000, 1977.

[14] M. Singh, D. Doria, "An electronically collimated gamma camera for single photon emission computed tomography. Part II: Image reconstruction and preliminary experimental measurements," *Medical Physics*, vol. 10, pp. 428-435, 1983.

[15] R. R. Brechner, M. Singh, "Comparison of an electronically collimated system and a mechanical cone-beam system for imaging single photons," *IEEE Transactions on Nuclear Science*, vol. 33, pp. 649-653, 1988.

[16] V. Schonfelder, R. Diehl, G.G. Lichti, H. Steinle, B.N. Swanenburg, A.J.M. Deerenberg, H. Aarts, J. Lockwood, W. Webber, J. Macri, J. Ryan, G. Simpson, B.G. Taylor, K. Bennett, M. Snelling, "The imaging Compton telescope on the Gamma Ray Observatory," *IEEE Transactions on Nuclear Science*, vol. NS-31, pp. 766-770, 1984.

[17] T. Kamae, N. Hanada, "Prototype design of multiple Compton gamma-ray camera," *IEEE Transactions on Nuclear Science*, vol. 35, pp. 352-355, 1988.

[18] C. J. Solomon, R.J. Ott, "Gamma-ray imaging with silicon detectors: A Compton camera for radionuclide imaging in medicine," *Nuclear Instruments and Methods*, vol. A273, pp. 787-792, 1988.

[19] N. Dogan, D.K. Wehe, and G.F. Knoll, "Multiple Compton scattering gamma ray imaging system," *Nuclear Instruments and Methods in Physics Research*, vol. A299, pp. 501-506, 1990.

[20] N. Dogan, and D.K. Wehe, "Optimization and angular resolution calculations for a multiple Compton scatter camera," *IEEE Nuclear Science Symposium Conference Record*, pp. 269-273, 1994.

[21] J. E. Gormley, W.L. Rogers, N.H. Clinthorne, D.K. Wehe, G.F. Knoll, "Experimental comparison of mechanical and electronic gamma-ray collimation," *Nuclear Instruments and Methods in Physics Research*, vol. A397, pp. 440-447, 1977.

[22] J. W. LeBlanc, N.H. Clinthorne, C-H. Hua, E. Nygard, W.L. Rogers, D.K. Wehe, P. Weilhammer, S.J. Wilderman, "C-SPRINT: A prototype Compton camera system for low energy gamma ray imaging," *IEEE Transactions on Nuclear Science*, vol. 45, pp. 943-949, 1998.

[23] A. I. Bolozdynya, V.V. Egorov, A.V. Koutchenkov, G.A. Safronov, G.N. Smirnov, S.A. Medved, V.L. Morgunov, "High-pressure xenon electronically collimated camera for low-energy gamma-ray imaging," *IEEE Transactions on Nuclear Science*, vol. 44, pp. 2408-2414, 1997.

[24] E. Aprile, V. Egorov, K.-L. Giboni, T. Kozu, F. Xu, T. Doke, J. Kikuchi, T. Kashiwagi, G.J. Fishman, R. Rehage, D. Trice, "The electronics readout and data acquisition system for a liquid xenon time projection chamber as a balloon-borne Compton telescope," *Nuclear Instruments and Methods in Physics Research*, vol. A412, pp. 425-436, 1998.

[25] E. Aprile, V. Egorov, K.-L. Giboni, S.M. Kahn, T. Kozu, U. Oberlack, S. Centro, S. Ventura, T. Doke, J. Kikuchi, E.L. Chupp, P.P. Dunphy, D.H. Hartmann, M.D. Leising, H. Bloeman, "XENA -- A liquid xenon Compton telescope for gamma-ray astrophysics in the MeV regime," *SPIE Proceedings*, vol. 3446, pp. 88-99, 1998.

[26] Y. Du, Z. He, G.F. Knoll, D.K. Wehe, W. Li, "Evaluation of a Compton scattering camera using 3-D position sensitive CdZnTe detectors," *Nuclear Instruments and Methods in Physics Research*, vol. A457, pp. 203-211, 2001.

[27] Y. Du, "Development of a prototype Compton scattering Camera using 3-D position-sensitive CZT detectors," in *Nuclear Engineering and Radiological Sciences*. Ann Arbor, MI: University of Michigan, 2001, pp. 137.

[28] M. A. Deleplanque, I.Y. Lee, K. Vetter, G.J. Schmid, F.S. Stephens, R.M. Clark, R.M. Diamond, P. Fallon. A.O. Macchiavelli, "GRETA: utilizing new concepts in gamma-ray detection," *Nuclear Instruments and Methods in Physics Research*, vol. A430, pp. 292-310, 1999.

[29] E. A. Wulf, J. Ampe, W.N. Johnson. R.A. Kroeger, J.D. Kurfess, B.F. Phlips, "Depth measurements in a germanium strip detector," *IEEE Transactions on Nuclear Science*, vol. 49, pp. 1876-1880, 2002.

[30] E. A. Wulf, B.F. Phlips, W.N. Johnson, R.A. Kroeger, J.D. Kurfess, E.I. Novikova, "Germanium strip detector Compton telescope using three-dimensional readout," *IEEE Transactions on Nuclear Science*, vol. 40, pp. 1182-1189, 2003.

[31] F. Lebrun, A. Bazzano, V. Borrel, M. Casse, A. Bykov, A. Coc, F. Daigne, P. Goldoni, J. Grigorczuck, M. Hernanz, P. Laurent, P. Mandrou, R. Marcinkowski, R. Mochkovitch, L. Natalucci, E. Parizot, J. Paul, P.-O. Petrucci, V. Tatischeff, P. Ubertini, "The Compton cube," *Nuclear Instruments and Methods in Physics Research*, vol. A504, pp. 38-43, 2003.

[32] R. Orito, H. Kubo, K. Miuchi, T. Nagayoshi, A. Takada, T. Tanimori, M. Ueno, "A novel design of the MeV gamma-ray imaging detector with Micro-TPC," *Nuclear Instruments and Methods in Physics Research*, vol. A513, pp. 408-412, 2003.

[33] L. Zhang, W.L. Rogers, and N.H. Clinthorne, "Potential of a Compton camera for high performance scintimammography," *Physics in Medicine and Biology*, vol. 49, pp. 617-638, 2004.

[34] B. L. Evans, J.B. Martin, L.W. Burggraf, M.C. Roggemann, T.N. Hangartner, "Demonstration of energy-coded Compton scatter tomography with fan beams for one-sided inspection," *Nuclear Instruments and Methods in Physics Research*, vol. A480, pp. 797-806, 2002.

[35] T. O. Tumer, S. Yin, S. Kravis, "A high sensitivity, electronically collimated gamma camera," *IEEE Transactions on Nuclear Science*, vol. 44, pp. 899-904, 1997.

[36] L. E. Smith, C. Chen, Z. He, D.K. Wehe, "Hybrid collimation for industrial gamma ray imaging: Combining spatially coded and Compton aperture data," *IEEE Nuclear Science Symposium Conference Record*, 1999.

[37] L. Zhang, S.J. Wilderman, N.H. Clinthorne, W.L. Rogers, "An anthropomorphic phantom integrated EGS4 Monte Carlo code and its application in Compton probe," *IEEE Nuclear Science Symposium Conference Record*, vol. 3, pp. 119-122, 2000.

[38] L. J. Meng, and D.K. Wehe, "Feasibility study of using hybrid collimation for nuclear environmental imaging," *IEEE Transactions on Nuclear Science*, vol. 50, pp. 1103-1110, 2003.

[39] H. O. Anger, "Scintillation camera," *Review of Scientific Instruments*, vol. 29, pp. 27, 1958.

[40] G. K. Skinner, "Imaging with coded-aperture masks," *Nuclear Instruments and Methods in Physics Research*, vol. 221, pp. 33-40, 1984.

[41] Y. Du, "Development of a prototype Compton scattering camera using 3-D position sensitive CZT detectors," in *Nuclear Engineering and Radiological Sciences*. Ann Arbor: University of Michigan, 2001, pp. 137.

CHAPTER 2

3-D POSITION SENSING IN PIXELLATED DETECTORS

2.1 Introduction

The first step in Compton imaging is the measurement of the positions and deposited energies for every gamma-ray interaction in the device. For early designs that used a front and back plane detector, the problem was reduced to finding the location of a single event in each detector and determining the energy deposited there. There are several detector options for such a system.

Position-sensitive photomultipliers optically coupled to scintillating detectors provide a good means to measure both the energy and 2-D position of an interaction. The depth of interaction in the scintillators is normally not determined, but the thickness of the crystal provides a maximum range of coordinates. The front and back plane detectors are necessarily far apart in order to achieve good imaging resolution. In terms of energy resolution scintillators are poor spectrometers by today's standards, and typically yield energy resolutions between 4% and 9% full-width at half-maximum (FWHM) for 662 keV gamma rays.

Another option is to use position-sensitive gas detectors. Two sets of wires inside the gas chamber will pickup signals from the electrons (liberated by the energy deposited in the gamma-ray interaction) moving through an electric field. The relative magnitudes of the signals on the wires indicate the position of the interaction in two dimensions. The third coordinate can be inferred from the drift time of the moving charges. The spectroscopic performance of gas detectors varies but is limited to several percent at best.

Semiconductors became popular due to their excellent energy resolutions, which can range from one-tenth of a percent to several percent for 662 keV gamma rays. Germanium detectors (typically 0.2% at 662 keV) are still the "gold standard" in gamma-ray spectroscopy. Along with the computer industry, the gamma-ray detection field grew rapidly as semiconductor processing improved. The greatest benefit has been the ability to deposit electrodes on a semiconductor using a mask pattern. In this way, so-called "single carrier" spectrometers like coplanar grid and pixellated detectors were developed. Coplanar grid and pixellated detectors rely on the movement of electrons only. The Shockley-Ramo theorem, which describes the currents induced on a conductor by moving charges, is used to predict signal shapes and determine the depth coordinate of the interaction.

Starting with this theorem, this chapter describes the process of determining the interaction positions and energies in a pixellated semiconductor detector. The processes for single-pixel events (in which only one pixel collects electrons) and multiple-pixel sequences are described separately. Charge sharing between pixels, weighting potential cross talk, and other difficulties of 3-D sensing are discussed.

2.2 The Shockley-Ramo Theorem

When a gamma-ray interaction occurs in a semiconductor detector electron-hole pairs are created. An electric field in the detector accelerates the holes toward the cathode and the electrons towards the anode. The movement of these charges generates a signal on each of the electrodes. In the late 1930s Shockley[1] and Ramo[2] independently published papers detailing the calculation of currents on a conductor due to moving charges. The Shockley-Ramo Theorem[3] provides a method for calculating the induced currents, and hence induced charge signals, on the electrodes. This theorem is the basis for all single-carrier detector devices.

The Shockley-Ramo Theorem states that to calculate the induced charge on an electrode the "weighting potential" is first determined by solving Poisson's equation throughout the detector volume under the conditions that the space charge is removed and the electrode under inspection is given a unit potential and all other conductors are grounded. Poisson's equation is given by Equation 2.1, where φ is the weighting potential and ∇^2 is the Laplacian operator. The total induced charge, Q, is then directly proportional to difference in weighting potentials between the initial and final positions of the moving charge as in Equation 2.2, where e is the unit charge of an electron and n is the number of charge pairs generated in the detector. The leading sign is determined by the sign of the charge carrier (positive for holes and negative for electrons).

$$\nabla^2 \varphi = 0 \tag{2.1}$$

$$Q = \pm ne\Delta\varphi \tag{2.2}$$

To illustrate the use of the Shockley-Ramo Theorem, induced charge is calculated for an infinite planar semiconductor detector with no fixed space charge as shown in Figure 2.1. Electron-hole pairs are generated by gamma-ray interactions, and the electric field (established by setting the anode to a higher potential than the cathode) forces the electrons to drift toward the anode and the holes to drift toward the cathode. Solving Equation 2.1 under the appropriate conditions yields the weighting potential for the anode given in Figure 2.2. The weighting potential function for the anode increases linearly from zero at the cathode surface to unit potential at the anode.

For an interaction that occurs halfway between the cathode and anode, the initial weighting potential is 0.5. The electrons then travel to the anode, where the weighting potential is 1, resulting in a potential difference of 0.5. The holes travel to the cathode, where the weighting potential is 0, resulting in a potential difference of -0.5. The total induced charge on the anode is then the sum of the electron and hole contributions—in this case the total charge created in the detector: $Q = ne(-0.5 + (-0.5)) = -ne.$

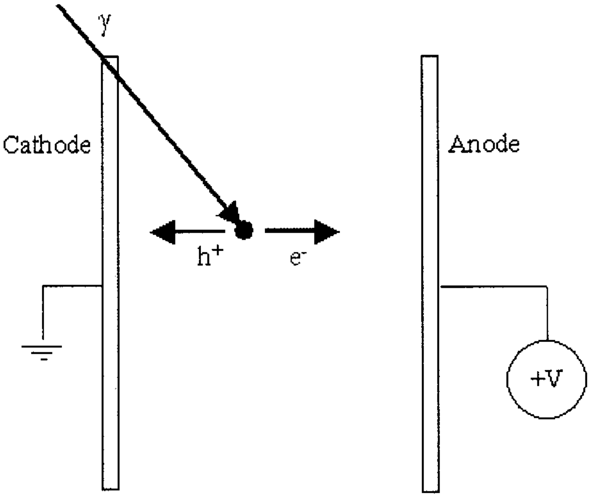

Figure 2.1. Illustration of a planar semiconductor detector. The cathode is grounded and the anode is set to positive voltage. Electrons and holes drift along the electric field lines toward their respective electrodes.

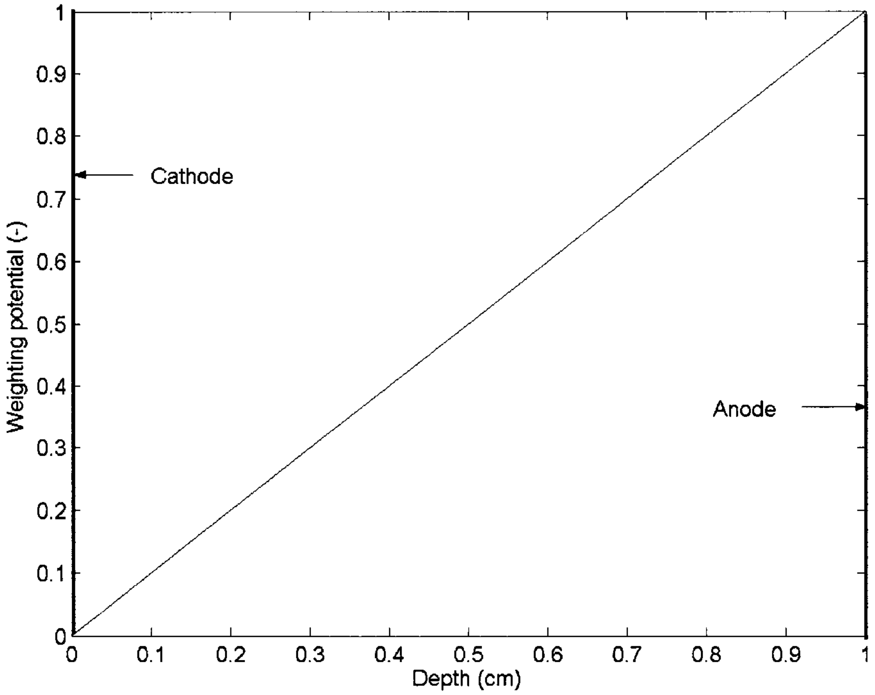

Figure 2.2. Weighting potential calculated for the anode in the geometry of Figure 2.1.

In semiconductors like Ge the electrons and holes have similar mobilities such that the transit times of charge carriers across the detector are not widely different. In CdZnTe, however, the mobility of electrons (~1000 $cm^2/V/s$) is significantly higher than that of holes (~80 $cm^2/V/s$). During electron collection times in CdZnTe, the holes move only slightly toward the cathode. For an electric field of 2000 V/cm the holes travel only 1.6 mm in 1 μs. Assuming the holes do not move at all and that electrons are not trapped in transit to the anode, Equations 2.1 and 2.2 predict an induced charge on the anode that is linearly dependent on the depth of the interaction in the detector. In the above case where the interaction occurs in the middle of the detector, the induced charge on the anode would be $0.5ne$. For an interaction at a depth of 0.25, the induced charge would be $0.75ne$. When electron trapping is taken into consideration, the induced charge becomes a non-linear function of interaction depth. Thus, in semiconductors with widely different electron and hole transport properties the energy resolution observed in a planar detector will be poor because the same amount charge created at different interaction locations will lead to different induced charges on the anode.

To alleviate this problem, CdZnTe detectors in the past were made only a few millimeters thick and were operated using high electric fields. In that case the holes travel further due to the high electric field and are collected due to the small detector thickness. It is also possible to increase the shaping time to tens of microseconds in order to collect all the holes. However, the efficiency suffers due to the small detector thickness. To use thicker detectors it is necessary to employ single-polarity charge sensing.

2.3 Single-Polarity Charge Sensing

One way to mitigate the depth dependence of induced charge for semiconductors with poor hole transport, such as CdZnTe, is to use an array of pixels as the anode, as in Figure 2.3. The weighting potential of the anode pixel electrode is then low for most

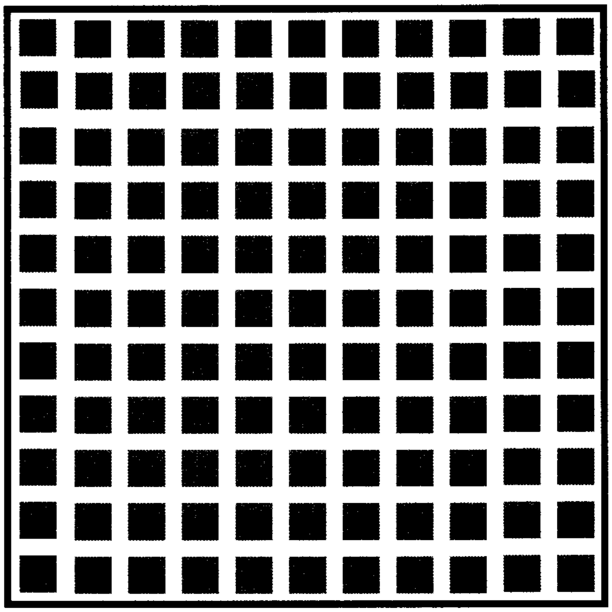

Figure 2.3. Illustration of 11 × 11 pixellated anode array.

depths in the detector and sharply rises to 1 near the pixel electrode, as shown in Figure 2.4. This is known as the "small pixel effect[4]." When holes travel only a small distance through the bulk, the weighting potential difference due to holes is small compared with the weighting potential difference associated with the motion of electrons. Only for events very close to anode will the contribution of holes to the signal be significant. For the rest of the detector the electrons dominate the induced charge signal, and this is referred to as "single-polarity charge sensing."

There is a serious problem with an anode structure as shown in Figure 2.3. Each anode is biased to the same potential. Therefore, some electric field lines will intersect the nonmetal surface of the detector between pixels before terminating on one of the anode pixels, and electrons will be directed toward the gap, as illustrated in Figure 2.5. When electrons created underneath the gap between pixels do not reach the anode the result is a reduced induced charge and an observed energy that underestimates the true deposited energy. To alleviate this problem, a steering grid electrode is introduced into the anode array, as shown in Figure 2.6. The grid is negatively (or less positively) biased

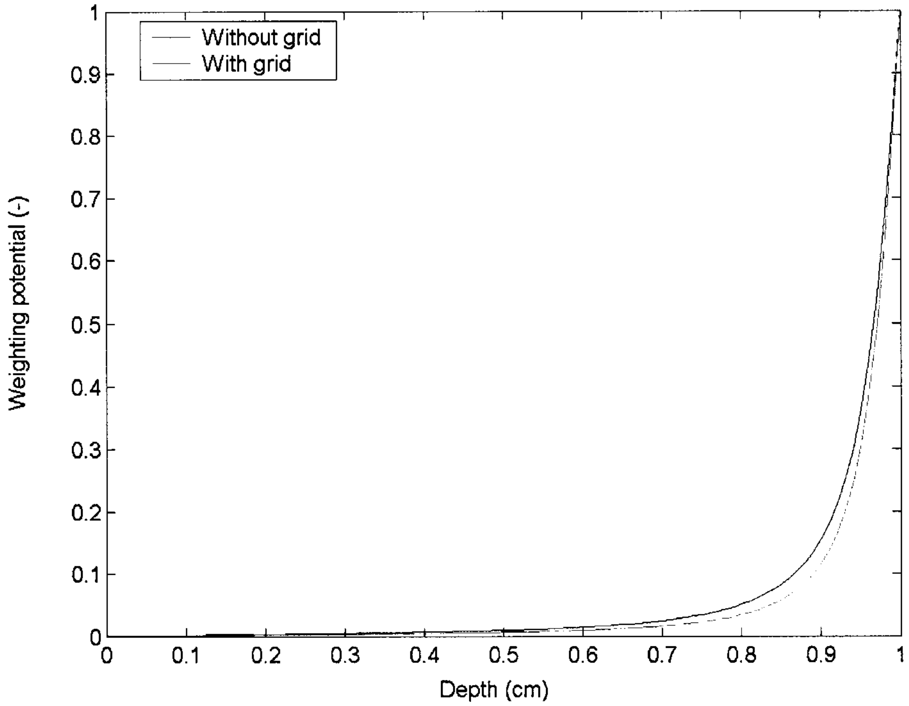

Figure 2.4. Weighting potential at the center of an anode pixel with and without a steering grid electrode present.

compared with the anodes. The electric field between pixels will then drive electrons in the gap to be collected by the anodes. The weighting potential for the anode configuration with a steering grid present (generated using Maxwell3D) is also shown in Figure 2.4. The weighting potential with a steering grid present is lower throughout the bulk than the weighting potential from the simple pixel array. This is an added benefit of the grid design because lower weighting potential in the bulk leads to less variability in the induced charge as a function of depth.

One drawback of using the steering grid electrode is the manufacturing of the anode structure. A continuous mask pattern can be constructed to make simple pixels on a surface. The electrode materials can be deposited on the entire surface over the mask, which is then removed leaving only pixels. However, when a steering grid is present, a single mask is insufficient and special photolithography procedures are required.

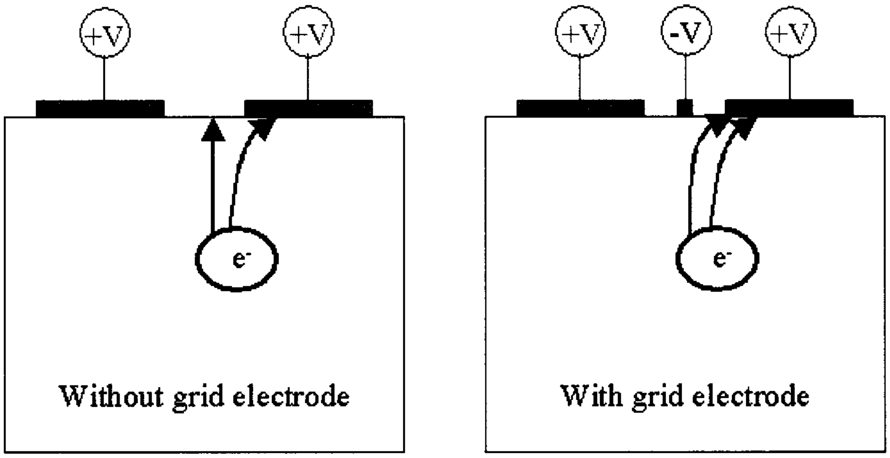

Figure 2.5. Illustration of the function of the steering grid electrode. Electrons in the gap are steered toward the anode pixels by the electric field established between the grid and the pixels.

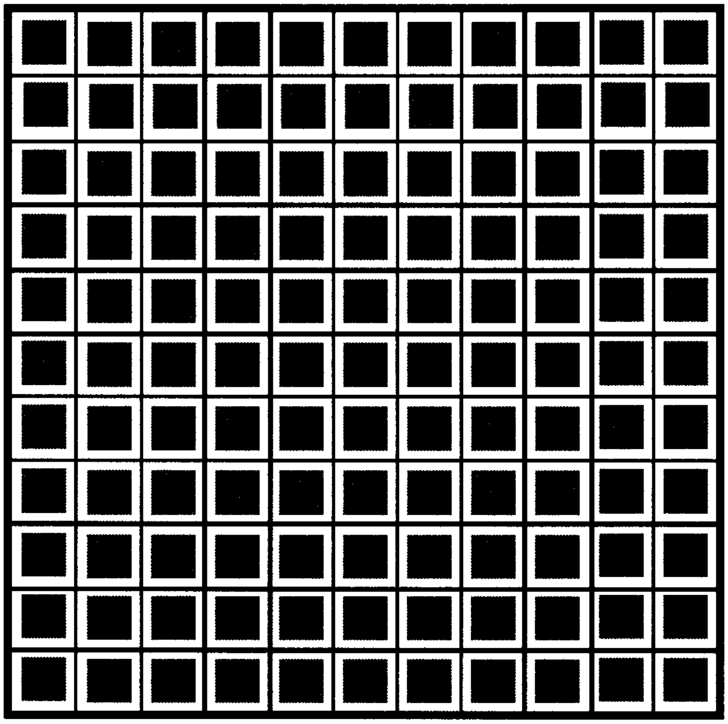

Figure 2.6. Illustration of 11 × 11 pixel anode array with steering grid electrode.

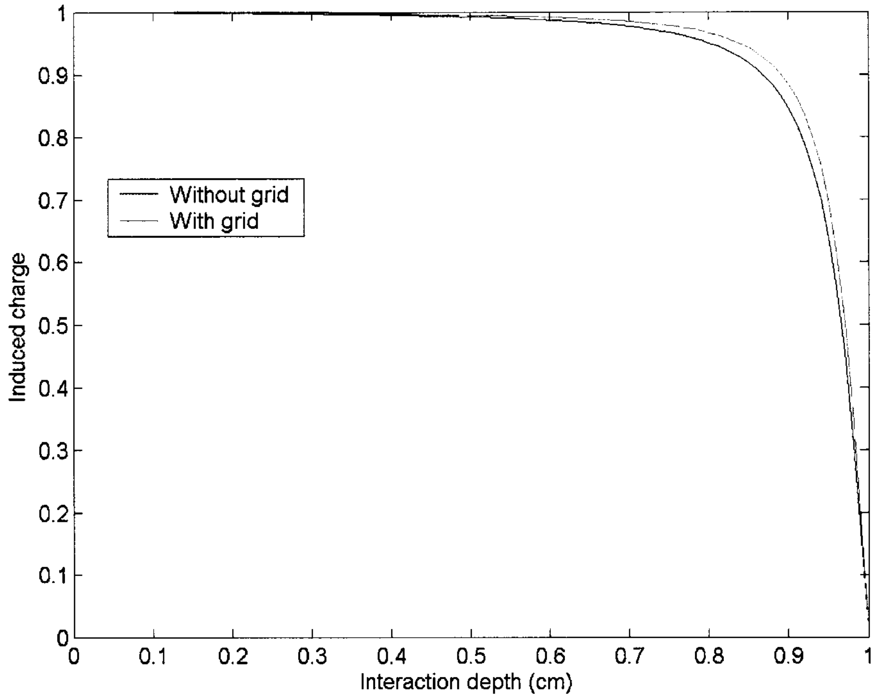

Figure 2.7. Induced charge (as a fraction of the total energy deposited) for the weighting potentials shown in Figure 2.4.

The induced charge due to electrons is calculated using Equation 2.2 and is given in Figure 2.7 as a function of depth in the detector along a path through the center of an anode for an array of 11 × 11 pixels on a 15 mm × 15 mm × 10 mm detector. The variation in induced charge is almost 15% in the bulk of the detector (greater than 1 mm from the anode surface) without the steering grid, but only 10% with the grid present. This variability is due to the slow rise of the weighting potential throughout the bulk of the detector.

It is clear there is still some residual dependence of the induced charge on the depth of interaction after pixellating the anodes with or without the steering grid present. To overcome this, He *et al.* proposed in 1996 to use the cathode and anode signals together to directly determine depth of interaction for coplanar grid detectors[5]. This same method was later applied to pixellated detectors[6]. The authors recognized that (in the absence of electron trapping) the cathode signal amplitude is proportional to the depth of interaction, and the anode signal amplitude is nearly independent of depth. Thus, the ratio of the cathode to anode signals should yield the depth of interaction. By separating the gamma-ray spectra into different depths, the variation in the induced charge (and hence observed energy) can be directly measured. Corrections are then applied to align each depth spectrum. This correction can account for any weighting potential effects, electron trapping, and also nonuniform defects in the material[7], and can be applied to an anode structure with or without a steering grid electrode. However, without a steering grid some electrons may not reach the collecting anode (as shown in Figure 2.5 previously), and this effective charge loss cannot be corrected.

This method only works correctly when only one interaction occurs in the detector. When more than one event occurs, the cathode signal is the sum of the contributions from each event, while each anode signal is the sum of the contribution of the event that occurred underneath it and the weighting potential cross talk from the other events in the detector (see Section 2.4). The cathode-to-anode ratio no longer determines the interaction depths, but rather the energy-weighted centroid depth of the interactions. Another method must be used to determine interaction depths for multiple events.

One popular way is to use signal timing, as illustrated in Figure 2.8. The cathode signal begins to rise linearly as soon as the electron cloud starts to drift toward the anodes. The signal is passed through a shaping amplifier with a very short shaping time, and then a threshold trigger can determine the start time of the drift. The anode signal rises very slowly until the electron cloud underneath it arrives close to the anode, where it sharply rises. The anode triggers just before the electrons are collected. In this way, the difference in time between the two triggers determines how long the electron cloud drifted and, hence, the depth of interaction in the detector. (The illustration is a simplification of the timing determination because each signal has a separate threshold level in the detector.) This method works for any number of interactions in the detector.

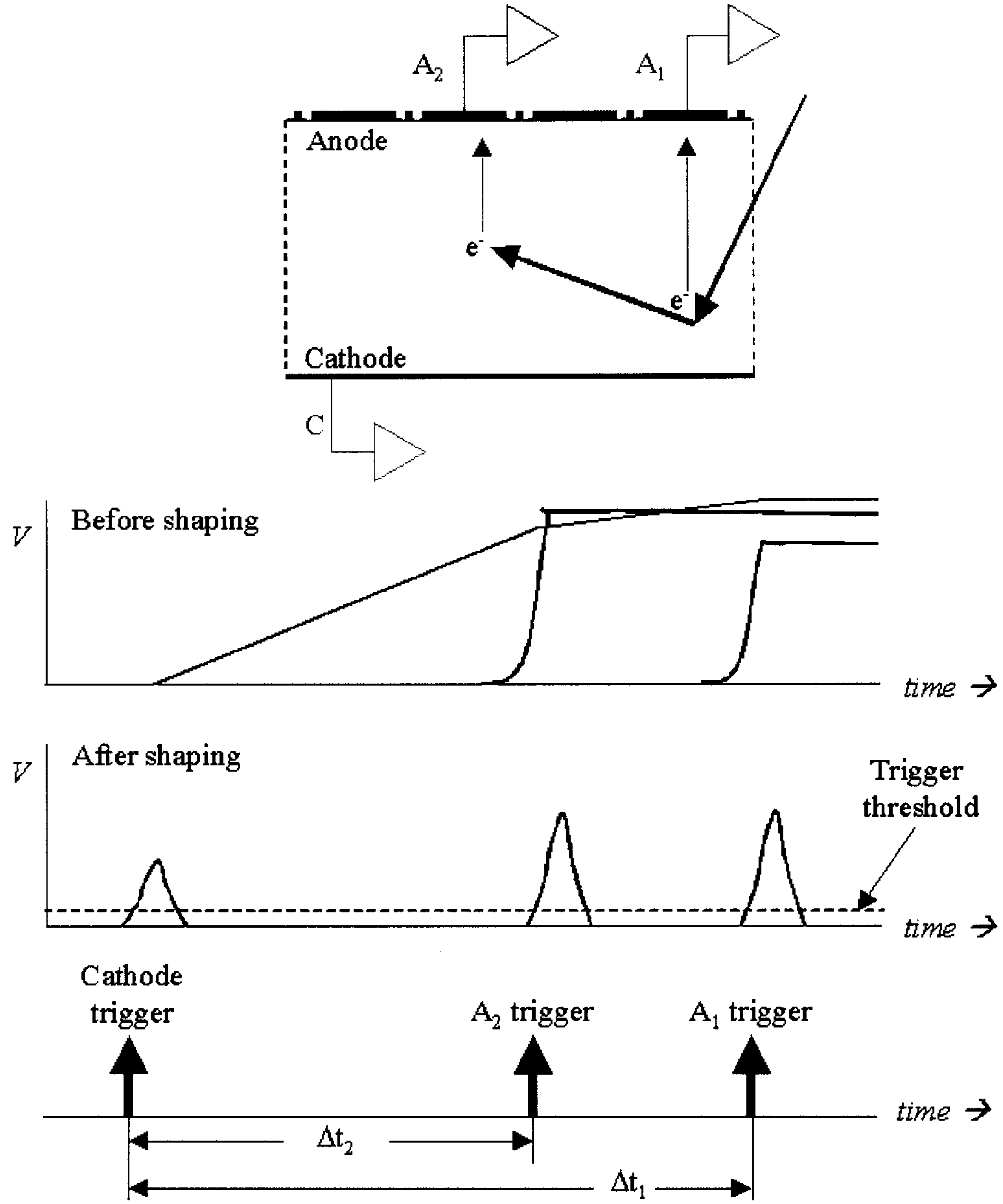

Figure 2.8. Illustration of depth determination of multiple events. The cathode triggers first, followed by each of the anode triggers as the electron clouds near the pixels. The time between the cathode and anode triggers determines the interaction depth.

The limiting factors for using the cathode-to-anode ratio to determine the depth of single events are the energy resolution on both the cathode and anode and the electronic noise on the cathode signal[5]. However, for multiple events, the timing resolution of the system is critical to achieving good performance. Because single events cannot be used in Compton imaging, only the timing method is used to determine depth in this work.

2.4 Weighting Potential Cross Talk

As an electron travels toward the anode structure, it induces a charge not only on the pixel that eventually collects it, but also on the other anode pixels. This is referred to as "weighting potential cross talk." In detector materials with similar electron and hole mobilities, the induced signals on these non-collecting pixels are transient and integrate to zero net charge. The hole contribution exactly cancels the electron contribution. However, for CdZnTe and other detector materials with poor hole transport, there is a net induced charge on the neighboring pixels. The weighting potential for the non-collecting pixel is always non-negative throughout the detector for any initial electron position, and the weighting potential at the electron collection location is always zero. According to Equation 2.2 the difference in the weighting potentials of the final and initial electron positions gives the magnitude of the induced charge on the non-collecting pixel. Thus, the induced charge signal on a non-collecting pixel is always negative or zero.

The magnitude of the cross talk signal as a function of depth of interaction for several interaction positions is given in Figure 2.9 for the anode geometries with and without a steering electrode. This magnitude is measured as a fraction of the total deposited charge. Thus, if an interaction occurs in the center of one pixel 1 mm from the anode depositing 1000 keV, then the neighboring pixel will observe a cross talk signal of 35 keV if a steering grid is used. Without the grid, the cross talk would be nearly 60 keV. The presence of the steering grid electrode reduces the effect of cross talk.

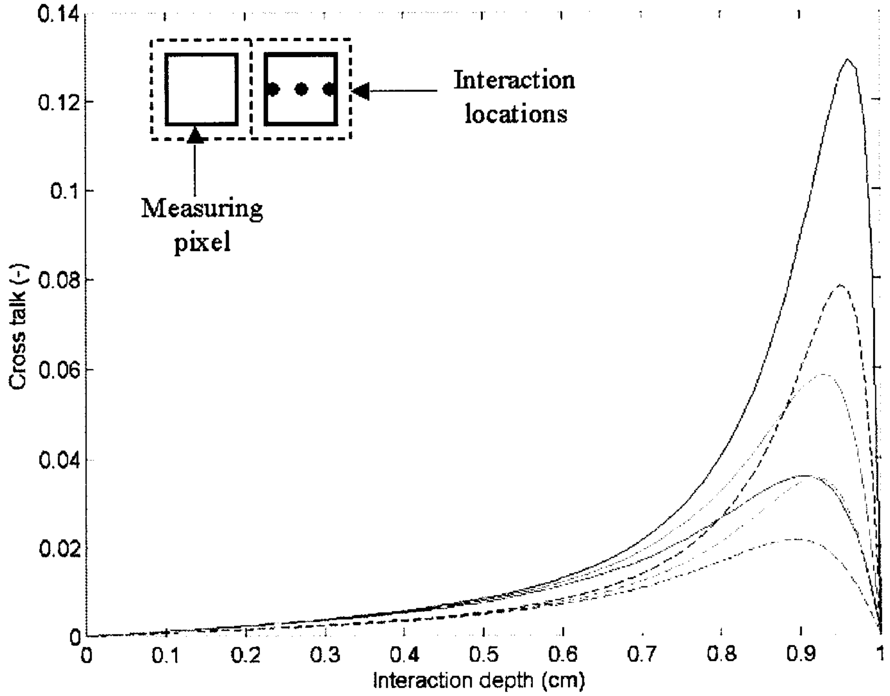

Figure 2.9. Magnitude of the fractional cross talk signal measured on one anode pixel due to interactions occurring under a neighboring pixel, shown for three distances from the measuring (non-collecting) pixel. Solid curves are without a steering grid, and dashed curves are for the geometry with a grid.

The magnitude of the cross talk can yield information about the location of the interaction within the collecting pixel. If the non-collecting pixel signal is relatively large, then the event occurred close to that pixel (indicated by the blue point in Figure 2.9). A small cross talk signal would result from an interaction further from the non-collecting pixel (corresponding to the green point in Fig 2.9). With a sufficiently low anode threshold, the cross talk signals on the eight non-collecting pixels surrounding the collecting pixel could be used to obtain subpixel position resolution. However, the anode thresholds in the detector used in this work are too high to use the cross talk information. Measuring the induced signals on non-collecting pixels would be difficult even with low anode thresholds because the cross talk signals are of opposite polarity to the collecting pixel signal. Thus, bipolar triggers and amplitude measurements would have to be implemented. This is not possible with the current electronics design.

The effect of weighting potential cross talk becomes problematic for multiple-pixel sequences. If two events occur under neighboring pixels, then each pixel acts as both a collecting and a non-collecting pixel. The observed signal amplitude on each pixel is the sum of the induced charge from the event under that pixel (a positive signal) plus the cross talk contribution from the event under the neighboring pixel (a negative signal). The amplitudes measured from both pixels are reduced, and the observed energies are less than the actual deposited energies. It is possible to correct these signals for events that occur in the bulk of the detector. For deposited energies E_1 and E_2 the observed energies A_1 and A_2 are given by Equations 2.3 and 2.4, where f_1 and f_2 are the fractional cross talk contributions from E_1 and E_2.

$$A_1 = E_1 - f_2 E_2 \tag{2.3}$$

$$A_2 = E_2 - f_1 E_1 \tag{2.4}$$

For interactions at depths of 0.6 cm and below, as shown in Figure 2.9, the cross talk fractions f_1 and f_2 depend only on the depth of the interaction and not on its lateral position. At depths near the anode surface the cross talk becomes a stronger function of the lateral position under the anode and an average value must be used to correct the observed energy. For events very close the anode the holes can contribute significantly to the cross talk signal as well, and the cross talk contribution may increase or decrease, depending on the interaction position. In the bulk of the detector the true energies can be obtained by solving Equations 2.3 and 2.4 for E_1 and E_2, as in Equations 2.5 and 2.6.

$$E_1 = \frac{A_1 + f_2 A_2}{1 - f_1 f_2} \tag{2.5}$$

$$E_2 = \frac{A_2 + f_1 A_1}{1 - f_1 f_2} \tag{2.6}$$

Using an average value for the cross talk fractions for events within 4 mm of the anode can overestimate or underestimate the weighting potential cross talk. Because this represents a significant fraction of the detector volume, an experimental correction of the weighting potential is used[8]. This method does not take into account the dependence of the cross talk on the energy deposited under the other pixel in the sequence, but the energy resolution of the current system is not good enough for this approximation to significantly detract from the weighting potential correction. The experimental method can also account for the small movement of holes, which is beneficial for events near the anode. The simple execution of the experimental cross talk correction makes it an attractive alternative to the inaccurate analytical method outlined above.

The weighting potential cross talk correction method also works for correcting the energies observed in charge sharing events. In this case one event creates an electron cloud near the pixel boundary. The cloud separates due to the electric field and is collected by more than one anode pixel. Charge sharing makes one event appear as two or more. Weighting potential cross talk will reduce the observed signals on each pixel, as if two separate interactions occurred. Applying the above correction will improve the summed energy spectrum. Of course, if charge sharing occurs, the sequence cannot be used for Compton imaging unless the energies are summed and an average lateral position is calculated from the determined energies. In this work no such corrections are made, and when charge sharing is observed the sequence is discarded.

Three-dimensional position-sensing is performed in this work using a 2.25-cm^3 pixellated CdZnTe spectrometer with a steering grid electrode. Interaction positions in two dimensions are determined by which anode pixels collected charge. Due to the high anode threshold there is no attempt to obtain subpixel resolution. The third interaction position is determined by the timing of events in the detector. Energy information is obtained by separating the spectrum from each pixel into separate depths, creating virtually 2420 voxels in the detector. A gain correction is applied to each depth spectrum using the method described by Li *et al.*[9] to align the energies. This measured correction value can account for weighting potential, electron trapping, and material nonuniformities. In multiple-pixel sequences, an experimental weighting potential cross talk correction is also applied. The detector hardware and characterization of the system are described next in Chapter 3.

2.5 References

[1] W. Schockley, "Currents to conductors induced by a moving point charge," *Journal of Applied Physics*, vol. 9, pp. 635-636, 1938.

[2] S. Ramo, "Currents induced by electron motion," *Proceedings of the IRE*, pp. 584-585, 1939.

[3] Z. He, "Review of the Shockley-Ramo theorem and its application in semiconductor gamma-ray detectors," *Nuclear Instruments and Methods in Physics Research*, vol. A463, pp. 250-267, 2001.

[4] H. H. Barrett, J.D. Eskin, H.B. Barber, "Charge transport in arrays of semiconductor gamma-ray detectors," *Physics Review Letters*, vol. 75, pp. 156, 1995.

[5] Z. He, G.F. Knoll, D.K. Wehe, R. Rojeski, C.H. Mastrangelo, M. Hammig, C. Barrett, A. Uritani, "1-D position sensitive single carrier semiconductor detectors," *Nuclear Instruments and Methods in Physics Research*, vol. A380, pp. 228-231, 1996.

[6] Z. He, W. Li, G.F. Knoll, D.K. Wehe, J. Berry, C.M. Stahle, "3-D position sensitive CdZnTe gamma-ray spectrometers," *Nuclear Instruments and Methods in Physics Research*, vol. A422, pp. 173-178, 1999.

[7] Z. He, W. Li, G.F. Knoll, D.K. Wehe, C.M. Stahle, "Measurement of material uniformity using 3-D position sensitive CdZnTe gamma-ray spectrometers," *Nuclear Instruments and Methods in Physics Research*, vol. A441, pp. 459-467, 2000.

[8] F. Zhang, and D. Xu. *personal communication*, 2004.

[9] W. Li, Z. He, G.F. Knoll, D.K. Wehe, C.M. Stahle, "Spatial variation of energy resolution in 3-D position sensitive CZT gamma-ray spectrometers," *IEEE Transactions on Nuclear Science*, vol. 46, pp. 187-192, 1999.

CHAPTER 3

DETECTOR HARDWARE AND SYSTEM DESCRIPTION

3.1 Introduction

To obtain energy and 3-D position information for each gamma-ray interaction, the concepts of single-polarity charge sensing discussed in Chapter 2 were implemented in two detector systems in this work. One system was designed for low- and medium-energy gamma-rays (less than 1 MeV); the other could measure gamma-ray energies up to a few MeV. Both systems used CdZnTe detectors of the same size and design, although the corresponding electronics used with each detector were different. A description of the detectors is given in this chapter along with a discussion of the procedures used to calibrate the systems to yield correct energy and position information for each interaction in the detector. The measured performance of each detector system is also discussed.

3.2 Detector Description

The CdZnTe detectors used in this work were built by eV Products, Inc., in Saxonburg, PA. They each consist of a single crystal 15 mm × 15 mm × 10 mm in size, grown using the high-pressure Bridgman method[1]. On one square side of the crystal, a planar gold cathode is deposited. The cathode covers the entire 15 mm × 15 mm surface. On the opposite side of the detector the anode structure—also made from gold—is deposited using photolithography techniques. The anode structure consists of an 11 × 11 array of pixels contained within a grid structure, as illustrated in Figure 3.1.

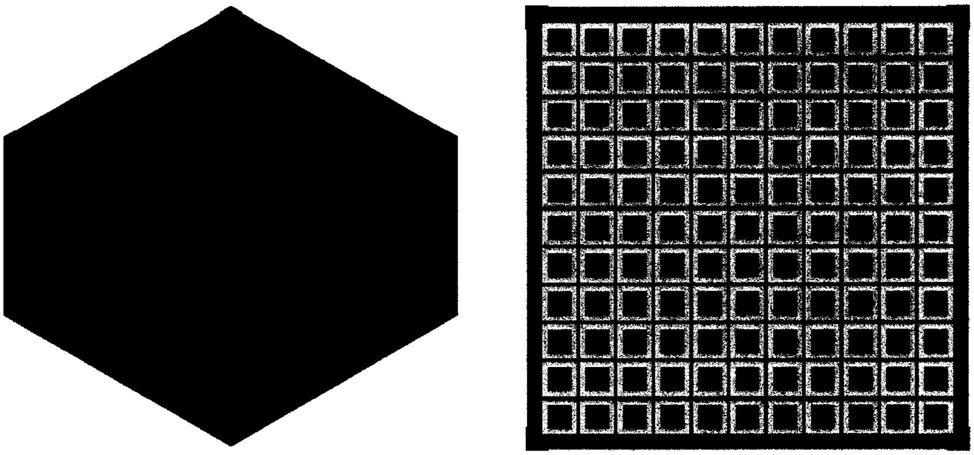

Figure 3.1. Illustration of the anode structure. There are 121 anode pixels surrounded by a steering grid electrode.

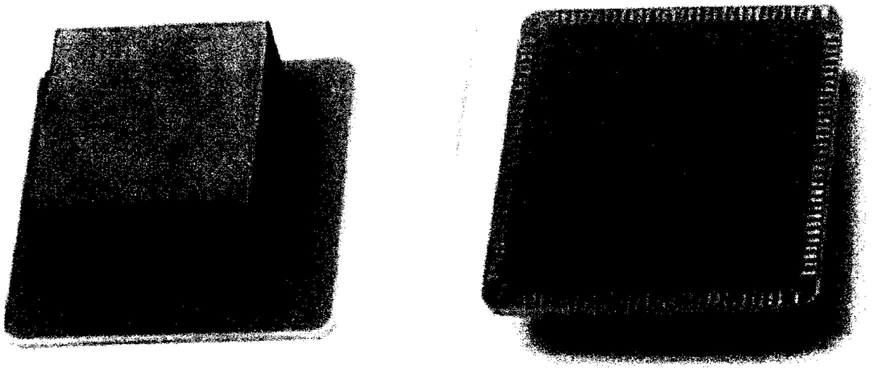

Figure 3.2. Photographs of a CdZnTe detector mounted to a ceramic substrate. The planar cathode is visible in the left image, and the gold finger contacts are shown in the image to the right.

The total pixel pitch is 1.3 mm with a pixel size of 0.8 mm, a gap between the pixel and grid of 0.2 mm, and a grid width of 0.1 mm. The array is surrounded by a guard ring 0.5 mm thick which is connected to the grid.

Each anode pixel is glued via conductive epoxy to a ceramic substrate, as shown in Figure 3.2. The epoxy forms a contact between each anode pixel and its corresponding conductive pad on the substrate. The substrate acts as a plate-thru-via, and embedded wires carry the anode signals to gold fingers at the edge of the opposite surface of the ceramic. These gold fingers are then wirebonded to a hybrid board, shown in Figure 3.3. A polyvinyl chloride (PVC) mount is attached around both sides of the hybrid board to protect the detector and wirebonds from mechanical shock, as shown in Figure 3.4.

The hybrid board and controller card were designed and built by Integrated Detector & Electronics AS (IDE AS) in Norway. The hybrid board performs all energy and timing determination for the 121 anode pixels plus the cathode. There are four pairs of VAS/TAT application specific integrated circuits (ASICs) located on the hybrid card. Each pair can measure the voltage (VAS) and timing (TAT) of 31 anode channels and 1 cathode channel. This results in four possible cathode channels, which is beneficial given the fragility of these special channels, but only one cathode channel is actually connected to the cathode at any time. There are 124 possible anode channels, but only 121 are used; thus, three ASIC channels are not used.

When a gamma-ray interaction occurs underneath a pixel, the electrons are collected by the pixel, generating a signal. This signal is simultaneously sent to the VAS

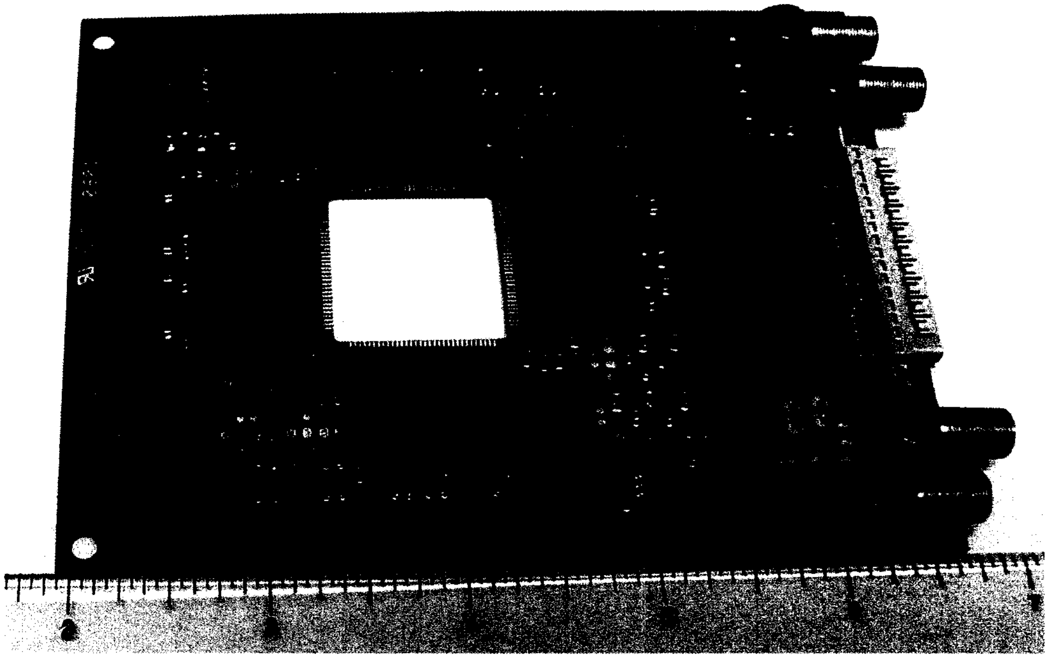

Figure 3.3. Photograph of the VAS2/TAT2 hybrid card. The ceramic plate to which the detector is glued is wirebonded to the gold fingers seen in the center of the board.

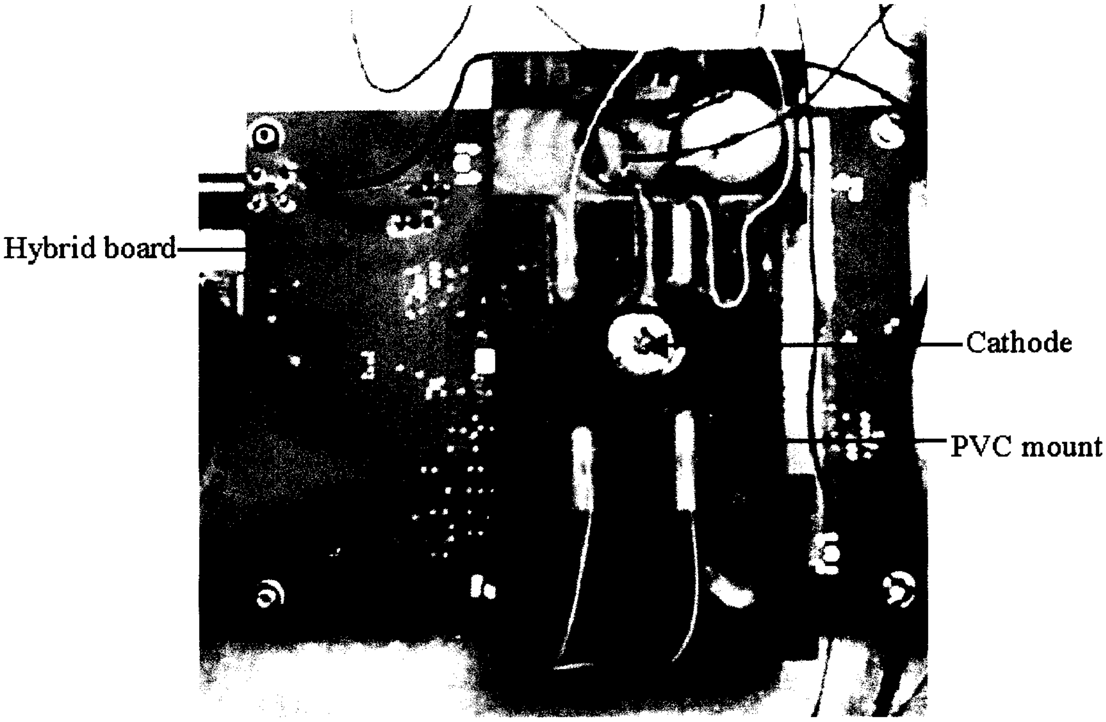

Figure 3.4. Photograph of the PVC mount attached to the detector and hybrid board. The cathode surface is visible through a hole in the mounting structure.

and TAT chips. The VAS contains a slow (1 μs) shaper for measuring signal amplitudes, while the TAT has a fast (75 ns) shaper for measuring signal timing. If the signal from the fast shaper exceeds a given threshold, a trigger is generated for that anode, and the maximum VAS signal amplitude is detected and held until it is read out by the controller card. In this way, each anode pixel is self-triggering. This is an improvement over the original VA/TA design in which the triggers were generated from the steering grid electrode. The energies and positions of multiple events in the detector could not be correctly identified using the previous design which had sample-hold rather than peak-hold circuitry, meaning that the time between the trigger and the sampling of the signal amplitude was constant rather than variable[2].

There are two versions of the hybrid board used in this work. The VAS2/TAT2 system is used for measurements of low- and medium-energy gamma rays. The dynamic range of the VAS2/TAT2 system is approximately 1 MeV. The VAS3/TAT3, an updated version of the VAS2/TAT2 system, has a much higher dynamic range (1.6 MeV) and is used for the high-energy measurements. It is not used in the lower energy measurements due to its poor energy resolution performance (see Section 3.4).

The signals held on the hybrid board are then read out using the MCR3 controller card, which communicates with the data acquisition software on a personal computer. The controller card reads out the 128 ASIC channels sequentially (including the channels not connected to anodes or the cathode), resulting in a 500 μs dead time after the initial cathode trigger. If any additional gamma-ray events occur within this time, they will not be measured. The maximum trigger rate in the detector cannot exceed 2000 triggers per second. Using a sparse readout in which only anodes that trigger are read out would improve the dead time to only tens of μs and increase the allowable trigger rate, but that is not done in this work.

The controller card sends digital signals to the computer, and software then controls the data acquisition parameters. The TA mask can be set to prevent the disconnected cathode channels and any noisy anode pixels from triggering the system. The mask essentially turns these TAT channels off. Anode thresholds are also set with the software. (The cathode threshold is set via hardware on the MCR3 controller card.) The observed pulse height and timing information is collected for all 128 ASIC channels for each triggered event in the detector.

3.3 Detector Calibration

To obtain accurate energy and interaction depth information from events recorded in the detector, it is necessary to first calibrate the system. To demonstrate the calibration process, data from the VAS2/TAT2 system will be used. The cathode and steering grid electrode were biased to –2000V and –80V, respectively, and the anode pixels were grounded. The cathode threshold was set at about 5 mV, while the anode threshold was set to 13 mV, or about 60-90 keV. The calibration is performed in two steps: corrections for single-pixel events, and then corrections for multiple-pixel sequences. The calibration process involves making corrections for channel-to-channel gain variations, the non-linearity of the ASICs, electron trapping and weighting potential as a function of depth, weighting potential cross talk, and other contributing factors. After calibration, the correct energy and interaction depth for each event in the detector can be determined. The calibration procedures for single- and multiple-pixel sequences are discussed in this section.

3.3.1 Single-pixel events

A ^{137}Cs source was placed on top of the detector, and data were acquired for many hours. Single-pixel events are identified by a TAT trigger on only one pixel. The energy spectrum obtained by summing the anode signal pulse heights observed in single-pixel events before calibration is shown in Figure 3.5. The variations in gain between ASICs create the double-peak feature in the spectrum. Channel-to-channel gain variations on a single ASIC also cause shifting of the photopeaks for each pixel spectrum, which sum to produce the broad peaks observed in Figure 3.5.

As discussed in Chapter 2, the depth for single-pixel events can be determined by measuring the ratio of the amplitude of the cathode signal to the amplitude of anode signal (C/A ratio). Small C/A ratios correspond to events that occur near the anode, and large C/A ratios correspond to events that occur near the cathode. The distribution of C/A ratios can be separated into bins, and each bin corresponds to a specific depth in the detector. The energy spectrum for each individual pixel can then be separated into different depths.

Figure 3.6 shows the resulting depth-separated energy spectra for a typical pixel in the detector (#94). Near the cathode side there is a reduction in the low-energy count

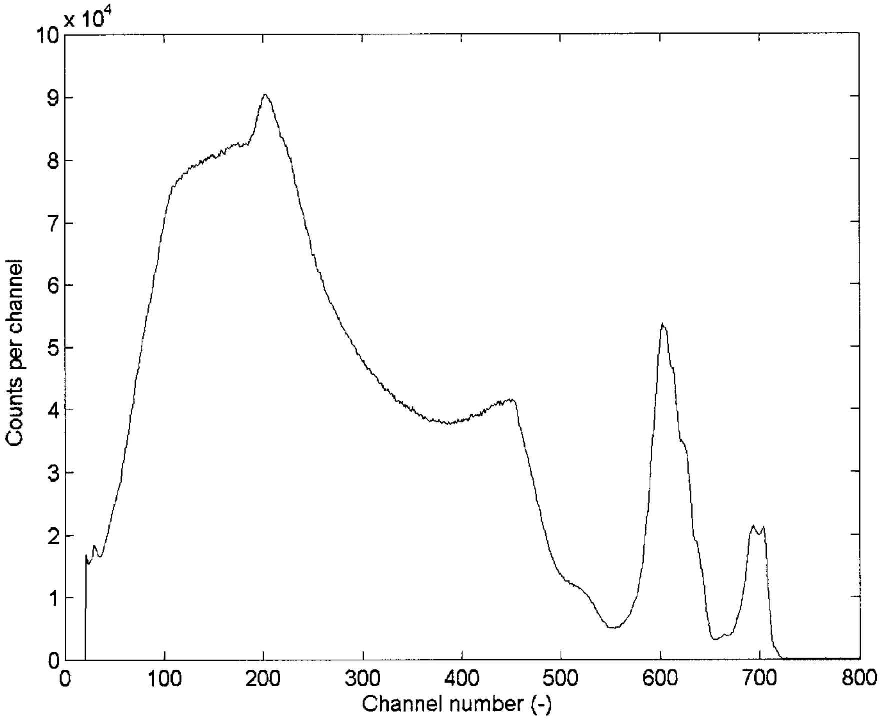

Figure 3.5. Single-pixel energy spectrum of ^{137}Cs source summed for all 116 working pixels before calibration.

rate. This is not surprising considering that the detector was irradiated from the cathode side. When a gamma ray scatters at a small angle (depositing a small energy), it is likely that after the scatter it will interact again. Therefore, this gamma ray cannot contribute to the energy spectrum of single-pixel sequences. If the gamma ray interacts in the middle or toward the anode side of the detector, there is a higher probability that it will escape the detector after a Compton scatter; these single-pixel events are included in the spectra shown in Figure 3.6.

The position of the photopeak shifts as a function of depth in the detector due to electron trapping. The drift of the photopeak position is given in Figure 3.7 for pixel #94. The variation in peak position is 3.2%. After separating the timing spectrum into depths, the photopeaks are aligned by rebinning the energy spectrum with an appropriate

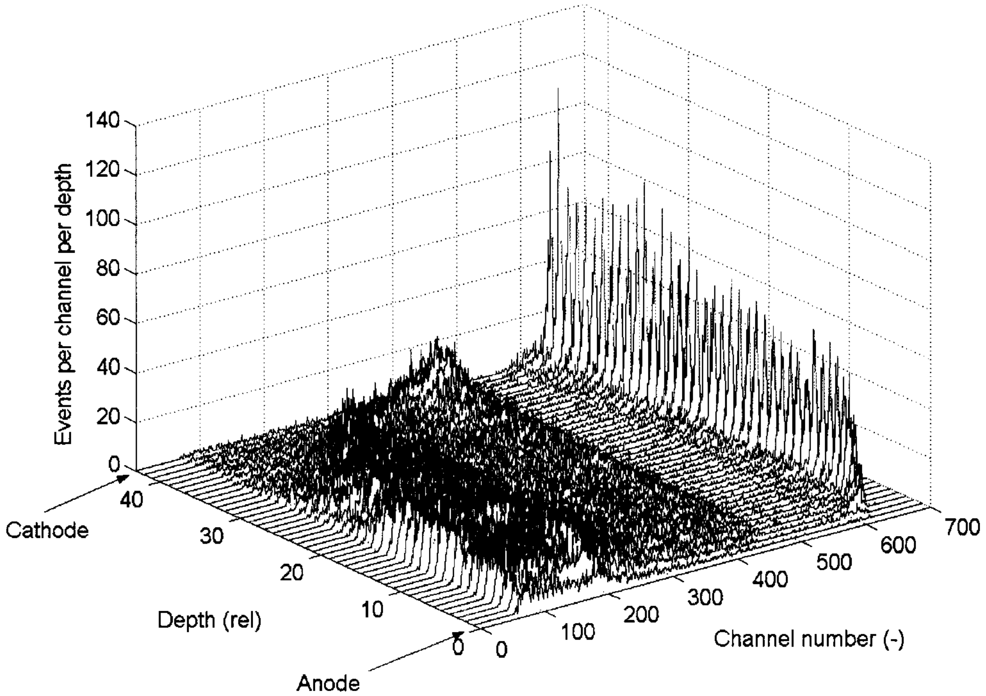

Figure 3.6. Energy spectrum for single-pixel sequences before calibration from ^{137}Cs for pixel #94 as a function of interaction depth. The peak position shifts to lower energies near the cathode.

correction factor using the method described by Li[3]. Thus, for each depth (given by the C/A ratio) under each anode pixel there is a measured correction.

After the correction factors at 662 keV are determined, the next step is to calibrate the system at other energies. This entails acquiring data from gamma-ray sources with energies from 122 keV to 662 keV; specifically, ^{57}Co, ^{133}Ba, ^{22}Na, and ^{137}Cs sources are used. The photopeak position as a function of energy is then measured, and a correction for the non-linearity of the ASICs is performed for each anode pixel. The relationship between gamma-ray energy and observed channel number (pulse height) is shown in Figure 3.8 for pixel #94. A quadratic function is fit to the calibration curve and is also shown in the figure. The observed pulse heights can then be converted to the appropriate energies using the calibration equation for each pixel.

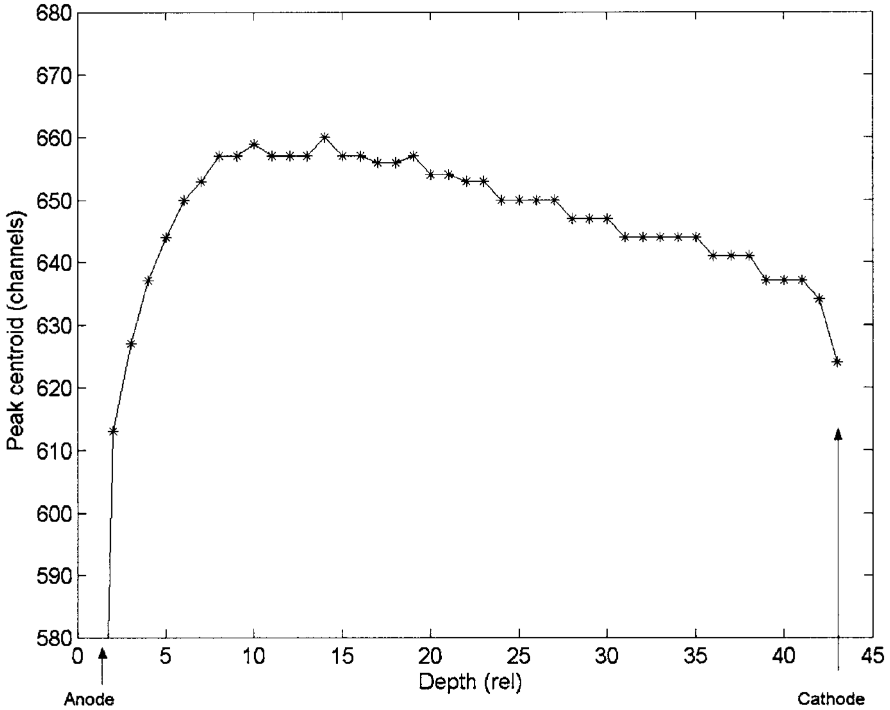

Figure 3.7. Drift of the peak centroid position for pixel #94. The drift near the anode is due to the large slope of the weighting potential. Near the cathode electron trapping creates a decrease in peak position.

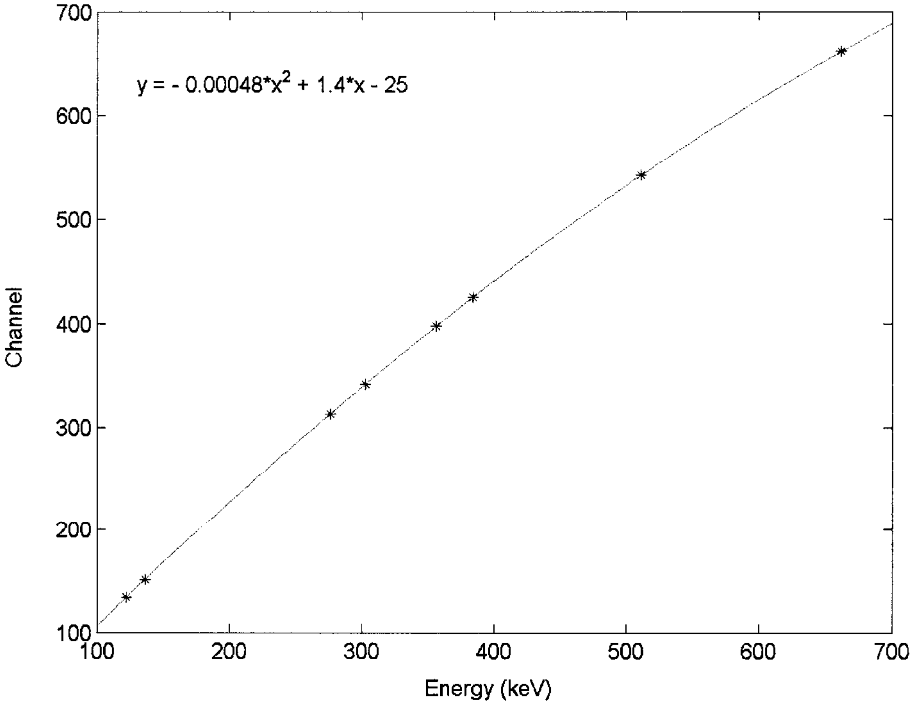

Figure 3.8. Energy calibration curve for pixel #94. The ASIC response is fit with a quadratic function.

To some extent the initial depth calibration is energy dependent. Due to the non-linearity of the anode channels, the C/A ratio will also have a non-linear dependence on energy. To account for this effect, the depth and energy calibrations are performed in an iterative manner. The depth calibration is used to estimate the non-linearity, which is then fed back into the depth calibration. The process is repeated until the photopeak energies predicted from correcting the measured data using the current estimates for depth and channel number match the known gamma-ray energies. Typically 5-6 iterations are required.

The data from the uncalibrated spectrum in Figure 3.5 are shown in Figure 3.9 after the energy and interaction depth calibrations. Only a single peak is observed, as expected. The energy resolution at 662 keV is 1.18% full-width at half-maximum (FWHM) for single-pixel events.

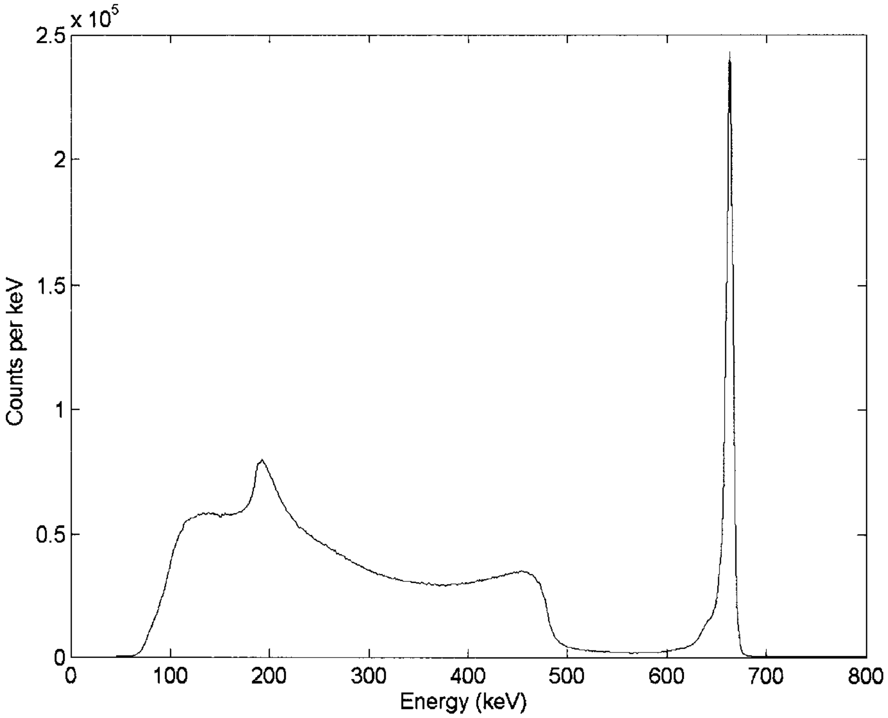

Figure 3.9. Energy spectrum using all single-pixel events of ^{137}Cs source after calibration using the data shown in Figure 3.5.

3.3.2 Multiple-pixel sequences

As discussed in Chapter 2, the C/A ratio cannot provide information about the individual depths when multiple interactions occur in the detector. Only the centroid depth of the interactions can be determined. Therefore, it is necessary to use the timing information available from the TAT ASICs to determine the depth for each event. When a single gamma ray interacts more than once in the detector, all events appear to occur simultaneously. As the separate electron clouds drift toward their respective anodes, the cathode signal immediately begins to rise due to the motion of all charges. The signals on each individual anode begin to rise when their respective electron clouds reach close to the pixel. In this way the cathode signal timing is the same for all events, but each anode pixel triggers just before its electron cloud is collected.

Shown in Figure 3.10 is the timing spectrum for pixel #94. The timing spectrum shows the distribution of time observed between the cathode trigger and anode trigger for many events. Events that occur close the anode appear on the right side of the spectrum, and those that occur on the cathode side appear at the lower times. (Events near the anode show small timing differences, but these correlate to high numbers in the timing spectrum shown here.) As with the C/A ratio, the distribution of time between the cathode and anode signals can be separated into bins, each of which corresponds to a depth in the detector.

With the depth determined by the timing of events, the correction factors generated in the single-pixel calibration can be used on each of the multiple events to account for electron trapping, weighting potential, and other effects. Multiple-pixel sequences also require a weighting potential cross talk correction, as discussed in Chapter 2. The two- and three-pixel energy spectra for ^{137}Cs after calibration are shown in Figure 3.11.

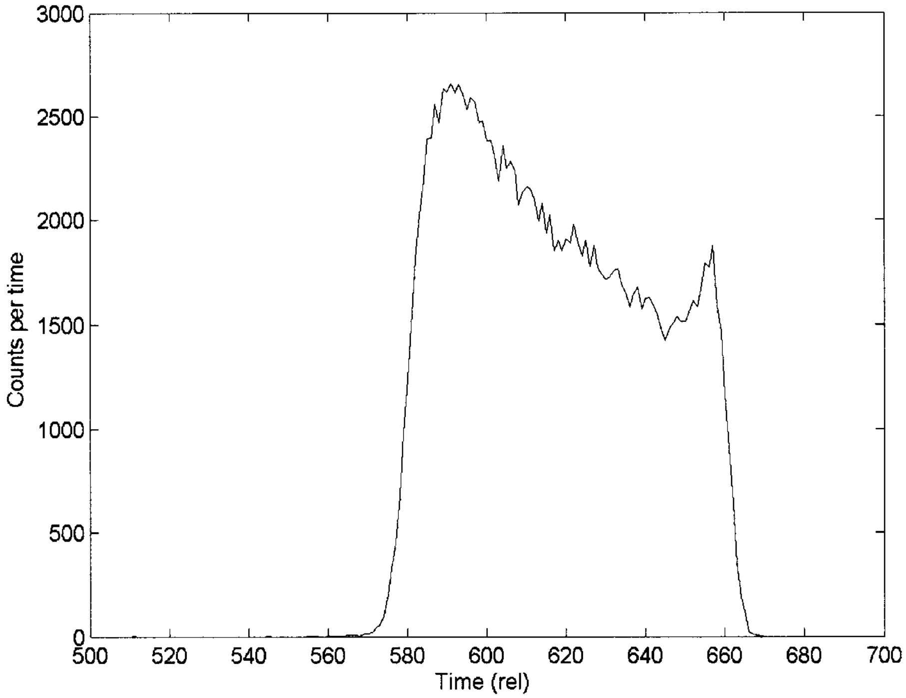

Figure 3.10. Timing spectrum of ^{137}Cs source from pixel #94.

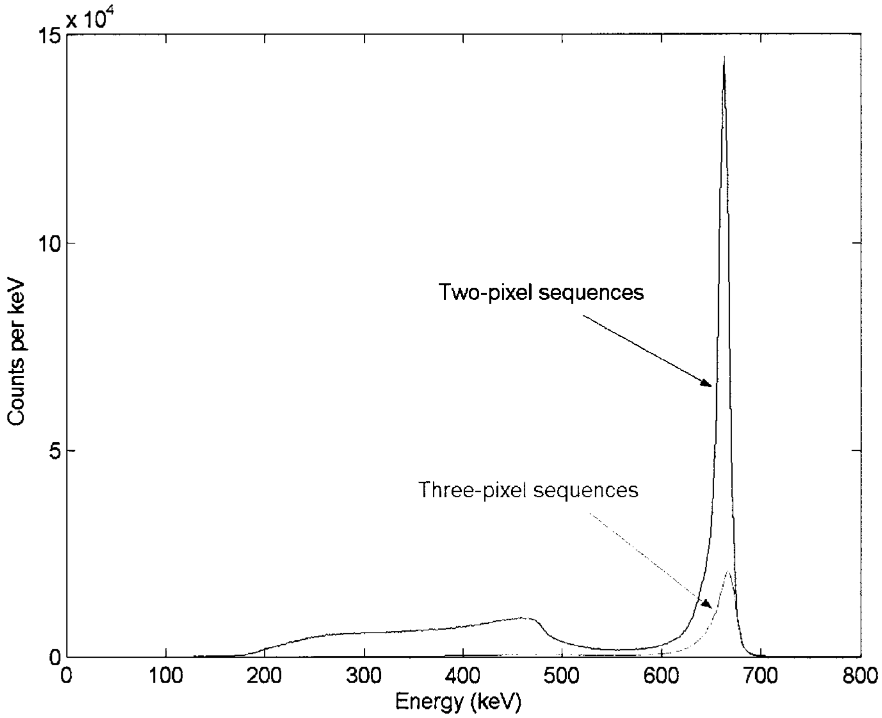

Figure 3.11. Two- and three-pixel energy spectra of ^{137}Cs after calibration summed from all 116 working pixels in the detector.

Once calibration is performed, the correction parameters are fed back into the data acquisition program so that the true energies and interaction positions can be determined in real time. The acquisition software can save both the raw data (pulse height and timing information for every channel from every event in the detector) and the calibrated data. The number of events, the energies deposited, and the interaction positions are written to a file for every sequence of gamma-ray interactions in the detector. This file is later used offline to reconstruct Compton images.

3.4 VAS2/TAT2 System Performance

In this work the VAS2/TAT2 system is used for measuring gamma rays with energies lower than 1 MeV. This section describes the performance of the system at several gamma-ray energies. An examination of energy and timing spectra for individual pixels is performed to compare good and poor pixels in the detector.

Data were acquired for several sources placed individually on top of the detector. Calibrated energy spectra were generated separately for single-pixel, two-pixel, and three-pixel sequences. The one-, two-, and three-pixel sequence energy resolutions measured using the whole detector volume are shown in Figure 3.12 as a function of gamma-ray energy. At 662 keV the resolution is only 1.18% full-width at half-maximum (FWHM) for single-pixel events. For two-pixel sequences the resolution worsens to 1.91%, and for three-pixel sequences a resolution of 3.63% is observed.

The total energy spectrum for multiple sources is shown in Figure 3.13. All recorded sequences are included. It is evident that some pixels have a threshold lower than 80 keV; part of the 81 keV peak from ^{133}Ba is observed in the energy spectrum. (If all pixels had a low threshold, the 81 keV peak would dominate over the other barium gamma-ray lines due to its higher probability of absorption.) The peak centroids in Figure 3.13 are within 1 keV of the true energies, demonstrating a good correction for the ASIC

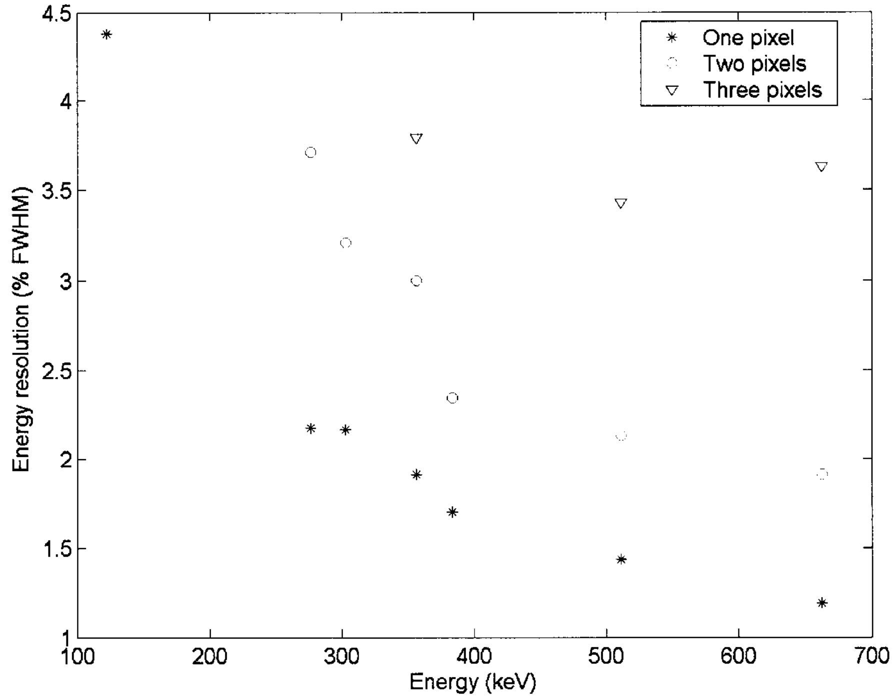

Figure 3.12. Energy resolution (in % FWHM) measured at selected gamma-ray energies in one-, two-, and three-pixel sequences. At least 200 keV or 300 keV is required for a two- or three-pixel sequence, respectively, due to the anode threshold.

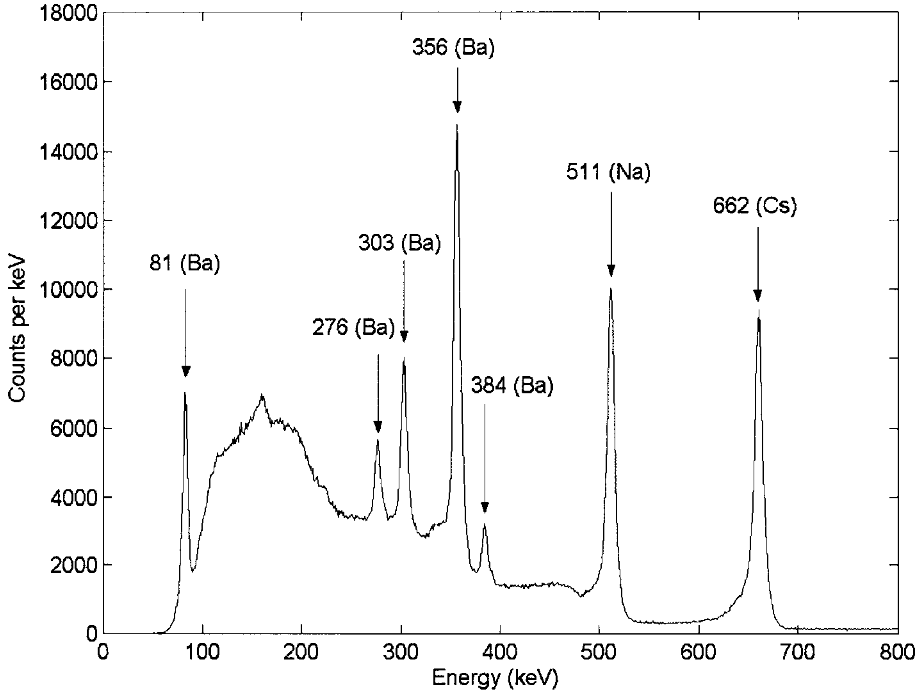

Figure 3.13. Total energy spectrum summed for all working pixels for ^{133}Ba, ^{22}Na, and ^{137}Cs sources. Gamma-ray energies in keV are provided for reference.

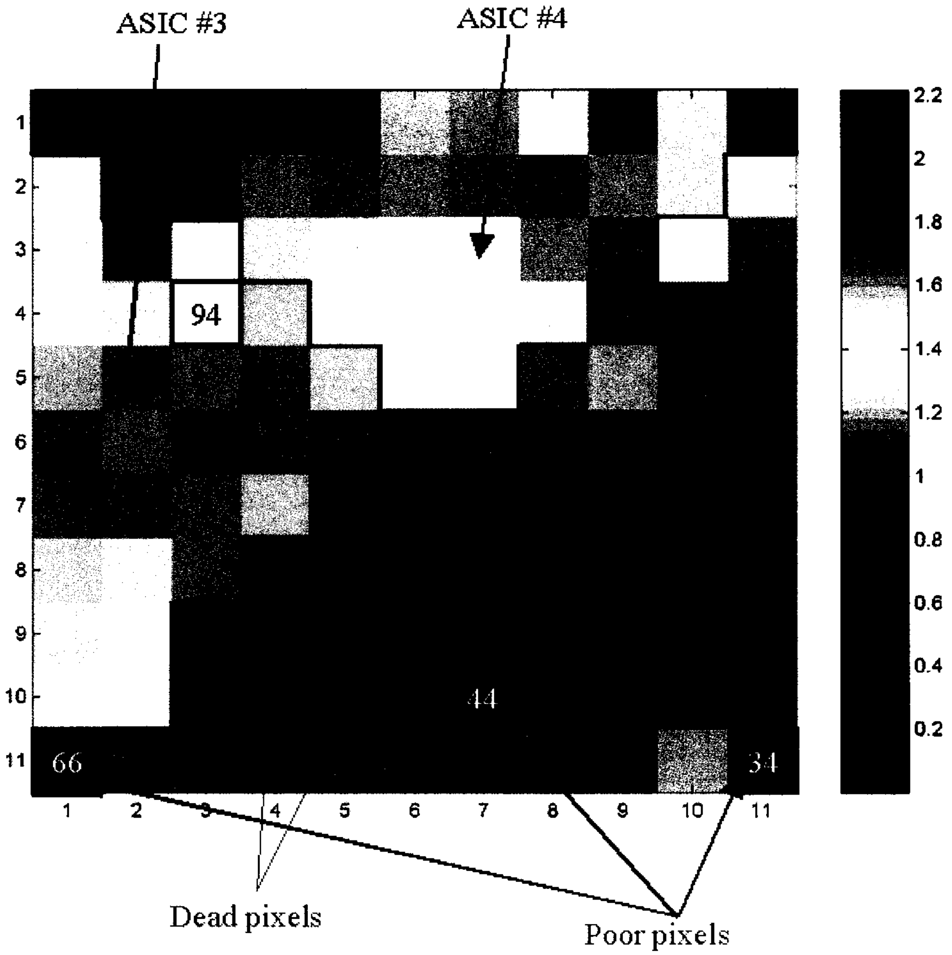

Figure 3.14. Energy resolution for each pixel in percent FWHM for single-pixel sequences in VAS2/TAT2 system. Also shown are the locations of pixels discussed throughout the text.

non-linearity, except at 81 keV where the lower part of the peak is cut off due to the anode thresholds. Despite this effect at 81 keV the difference is only 3 keV.

The energy resolution at 662 keV for single-pixel events is represented in Figure 3.14 for each individual pixel. Nearly half the pixels have an energy resolution near 1%. The upper quadrant of the detector outlined in black shows poorer energy resolution than other channels. These are all connected to ASIC #4. The pixels on ASIC #3 (the left quadrant in Figure 3.14) also show a poorer energy resolution than the rest of the detector. The most likely cause for the poor resolution is lower gain in the ASIC or electronic cross talk on the hybrid board or MCR3 repeater card. The poor energy resolution behavior may also be in part due to material defects in the crystal. This same detector connected to a different hybrid board (with different ASICs) also demonstrated a poor energy resolution on the pixels connected to ASICs #3 and #4, especially the top three rows. From the distribution of energy resolutions it is not surprising that the two-pixel energy resolution is 1.91% compared with only 1.18% for single pixels.

There are two pixels without signals ("dead pixels") due to either ASIC channel failure or wirebonding problems and three poor pixels, which may be caused by material defects or problems with the anode contacts. The energy spectra after gain correction (before depth and non-linearity corrections) from two of the poor pixels are shown in Figure 3.15. Also shown is the typical spectrum observed from pixel #94.

Pixel #34 is the poor pixel in the lower right corner of Figure 3.14, and #44 is the poor pixel in the horizontal center of the detector. In the pixel #34 energy spectrum, there is extreme tailing on the low-energy side of the photopeak and a buildup of the Compton continuum. In the spectrum for pixel #44, the photopeak is spread between two energies. The timing spectra from both poor pixels are given in Figure 3.16. When compared with Figure 3.10, the timing spectrum from a typical pixel, the timing spectrum for pixel #44 appears normal. Furthermore, the two-peak feature in the energy spectrum appears at all depths in the detector. This indicates that the gain of the pixel may shift during acquisition. However, this effect was not observed when a test pulse was injected in the ASIC channel. Another possibility is the existence of a major defect just under the anode pixel contact. When the electron cloud avoids the defect, the full energy is observed; if the cloud loses electrons to the defect, only some of the energy will be observed. This could cause the behavior observed in the energy spectrum.

Unlike pixel #44, the timing spectrum of pixel #34 appears highly irregular. Some events have very long drift times (low timing spectrum numbers). Pixel #34 is a corner

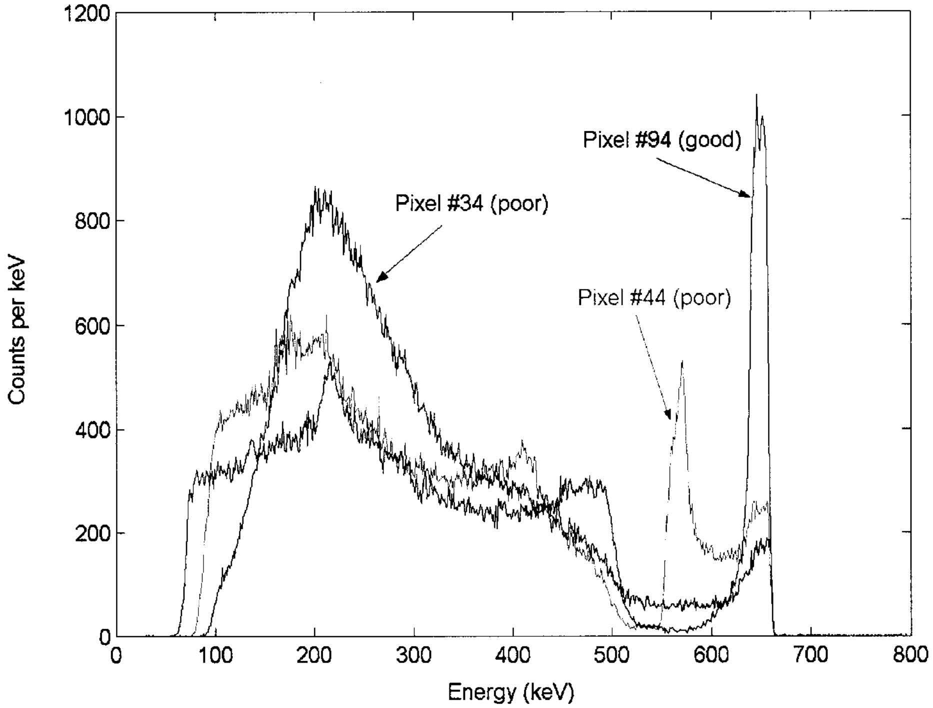

Figure 3.15. Energy spectra for one typical and two poor pixels after gain corrections and before depth correction. Pixel #44 exhibits a two-peak behavior, while the photopeak on pixel #34 has an extremely large low-energy tail.

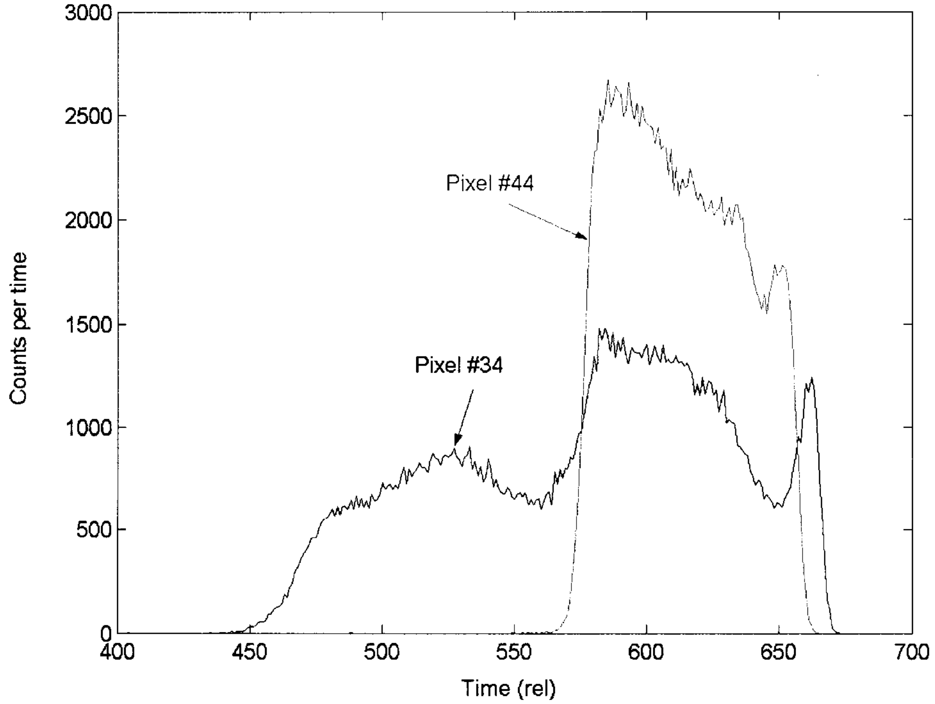

Figure 3.16. Timing spectra for pixels #34 and #44. Pixel #44 appears normal (compared with the typical spectrum shown in Figure 3.10).

pixel, and it is possible that surface defects can create a smaller electric field in this region. The electrons would then take a longer time to drift to the anode. Because of the reduced drift velocity, the electron trapping would increase. Evidence for this exists in the depth separated spectra for pixel #34, which show the poor spectroscopic performance worsening for depths near the cathode side.

Pixel #66, not shown in the previous figures, has normal timing and energy spectra. However, the 662 keV peak appears at a much lower channel before calibration than the peaks on other channels. This is not due to a low gain because the difference in channels between the peak and the Compton edge is the same as for other pixels. In other words, the spectrum is simply shifted to lower channel numbers. One possible explanation for this behavior is a high baseline due to leakage current. The baseline is subtracted from the signal during processing, which could cause events of given energies to appear at much lower channels. The energy spectrum for this pixel used to be normal; thus, there was obviously some degradation over time. The performance of this pixel is unpredictable and it was not used in measurements.

It is expected that corner pixels perform more poorly than pixels near the center of the detector due to surface defects from crystal polishing and handling. Electrons must travel a larger distance to reach the anode if they start under the boundary electrode than if they start directly under the pixel. This difference in drift time will create errors in depth determination and, hence, the depth-corrected spectrum. In fact, the worst resolution observed in the detector for a properly functioning pixel is the corner pixel at the top left of Figure 3.14. However, the performance on pixels #34 and #66 is much worse than the other two corner pixels, which have normal timing spectra and slightly broadened photopeaks in the energy spectra.

The three pixels with poor spectroscopic behavior are turned off in the measurements included in this work. There are two additional dead pixels, which totals five unused pixels. The remaining 116 anode pixels are used in the measurements of gamma-ray energies below 1 MeV.

3.5 VAS3/TAT3 System Performance

The VAS3/TAT3 system is used for high-energy measurements. For the experiments demonstrated later in this work, the dynamic range of the VAS2/TAT2 system (only 1 MeV) is insufficient for observing 2.2 MeV or 2.6 MeV gamma rays. The VAS3/TAT3 system, which is an updated version of the VAS2/TAT2 system, has a dynamic range of 1600 keV. Of course, a single event at 2.2 MeV cannot be observed even with the VAS3/TAT3 system, but Compton imaging relies on multiple events. It is possible for two events within the dynamic range to sum to 2.2 MeV. This is not true for the VAS2/TAT2 system.

The new system was connected to a different detector than the VAS2/TAT2 system. The detector was the same size and had the same anode structure as the previous detector. This detector required a -2200V cathode bias and -85V on the steering grid electrode. The calibration of the VAS3/TAT3 system was performed in the same manner as described in Section 3.2, but some high-energy sources are included. In addition to ^{133}Ba and ^{137}Cs, ^{60}Co (1173 and 1332 keV) and ^{232}Th (2614 keV + escape peaks) are used. The energy spectrum after calibration for all sources except thorium is shown in Figure 3.17. (The thorium spectrum, which has many low-energy gamma-ray lines, would obscure the other calibration energies.) A much poorer energy resolution is obtained with this system compared with the VAS2/TAT2 system. Single-pixel sequences display about 1.5% FWHM energy resolution at 662 keV, while the resolution for two- and three-pixel sequences are 3.1% and 4.8%, respectively, as shown in Figure 3.18. The poor resolution is caused by a flaw in the electronics design. The waveform output from the shaping amplifiers appear to have a stair-step response, rather than a

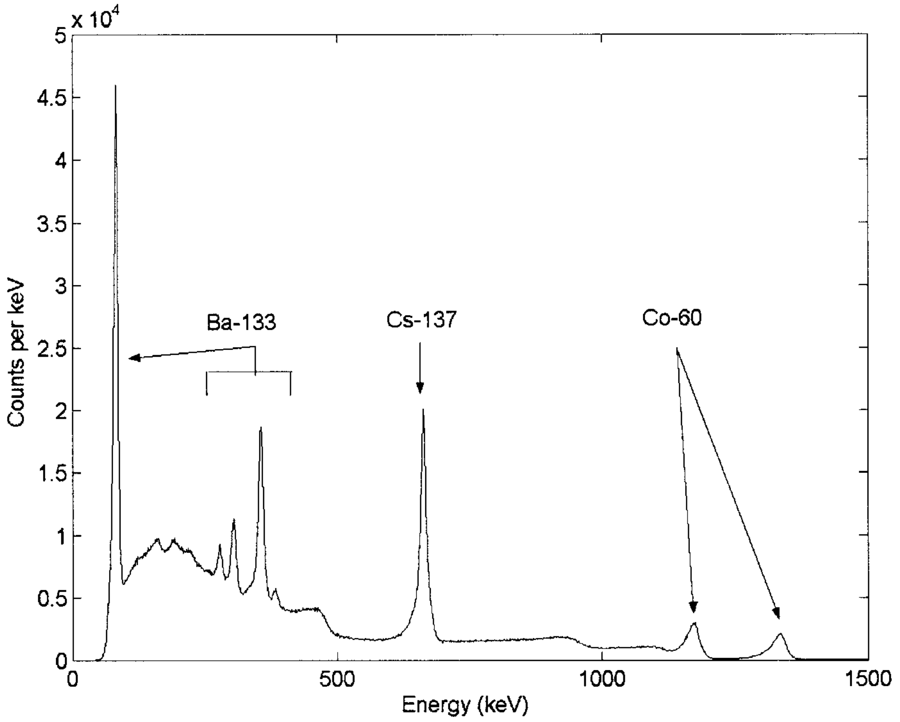

Figure 3.17. Total energy spectrum summed for all working pixels of ^{133}Ba, ^{137}Cs, and ^{60}Co from VAS3/TAT3 system after calibration.

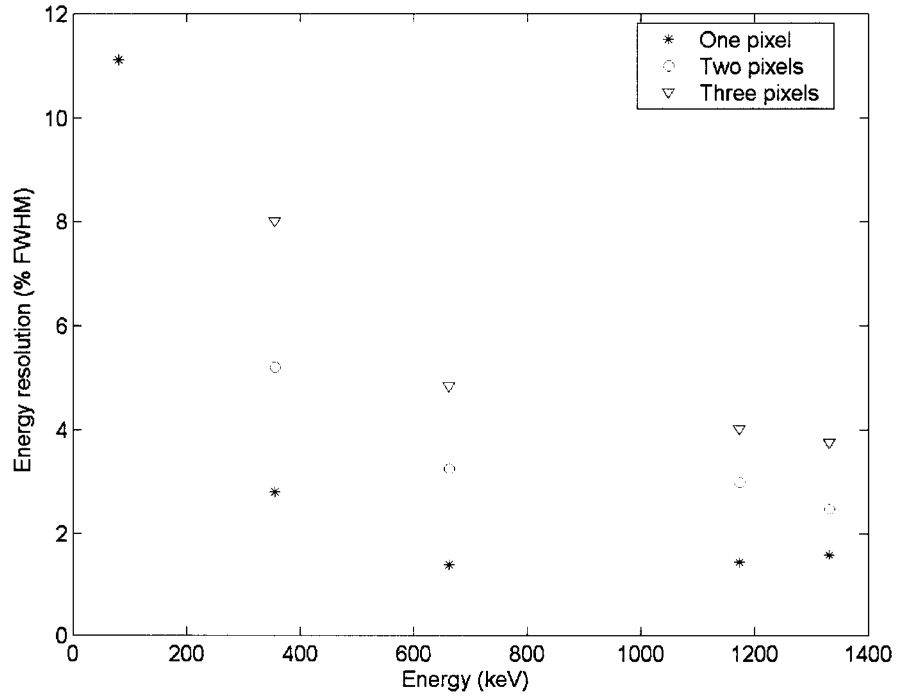

Figure 3.18. Energy resolution (in % FWHM) of the VAS3/TAT3 system at selected gamma-ray energies in one-, two-, and three-pixel sequences. Energy resolution is worse on this system compared with the VAS2/TAT2 system.

smooth shape. This creates problems for the peak-hold circuitry in the ASICs, and the signal pulse height is often incorrectly determined.

The energy resolution at 662 keV for single-pixel sequences is mapped in Figure 3.19. The resolution on the VAS3/TAT3 system is much more uniform than on the VAS2/TAT2 system, most likely due to using a higher quality detector crystal. For this system the electronics—and not the detector—limit the observable energy resolution. The only poor region of the detector is lower left corner in Figure 3.19, which shows poor energy resolution. The ^{137}Cs energy spectra after the gain correction (before depth correction) for a few pixels in that corner are given in Figure 3.20.

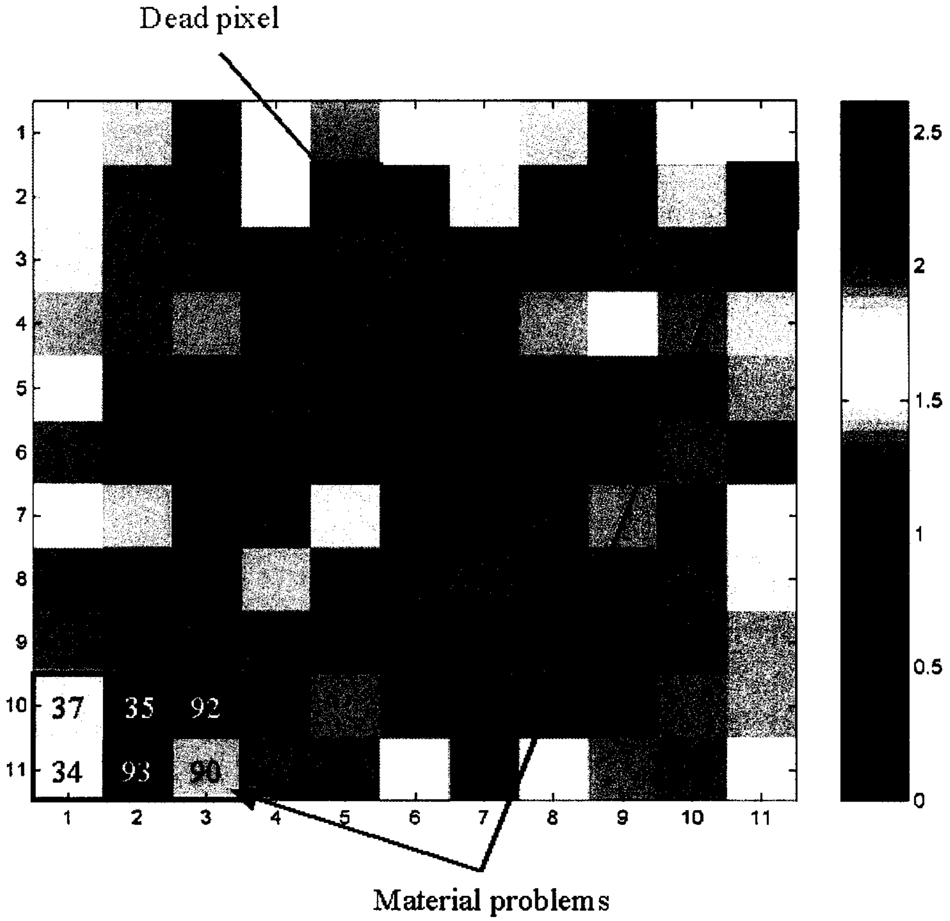

Figure 3.19. Energy resolution for each pixel in degrees FWHM for single-pixel sequences in VAS3/TAT3 system.

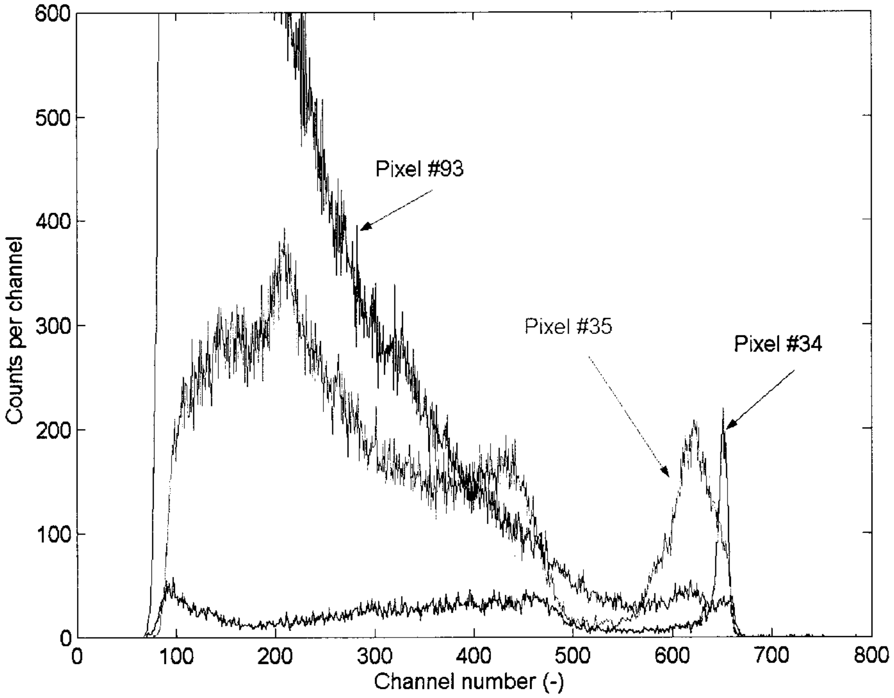

Figure 3.20. Energy spectra observed for three poor pixels in the lower left corner of Figure 3.19. Pixels #35, #92, and #90 have similar spectra, while the spectrum of pixel #37 is similar to that of pixel #93.

The energy spectrum for pixel #35 is similar to that for pixels #90 and #92 as well. The photopeak is very broad, but the spectrum looks otherwise normal. Pixel #34 exhibits a very low count rate. The timing spectrum, shown in Figure 3.21 along with the timing spectra for pixels #35, #92 and #93, shows a sharp peak rather than a broad distribution. Only events near the anode are being collected, indicating major defects in the crystal at that corner. The energy and timing spectra of pixel #37 are similar to those of pixel #93. There is a broad continuum in the energy spectrum with almost no photopeak present. The timing spectrum is extremely broad, indicating long collection times for events under this pixel. Pixel #93 shows a very large count rate, while the count rate of pixel #37 is similar to pixel #34. However, the timing spectrum for pixel #37 is broad, indicating that some events from all depths are being collected by the pixel. It is clear that there are some material problems in this corner of the crystal.

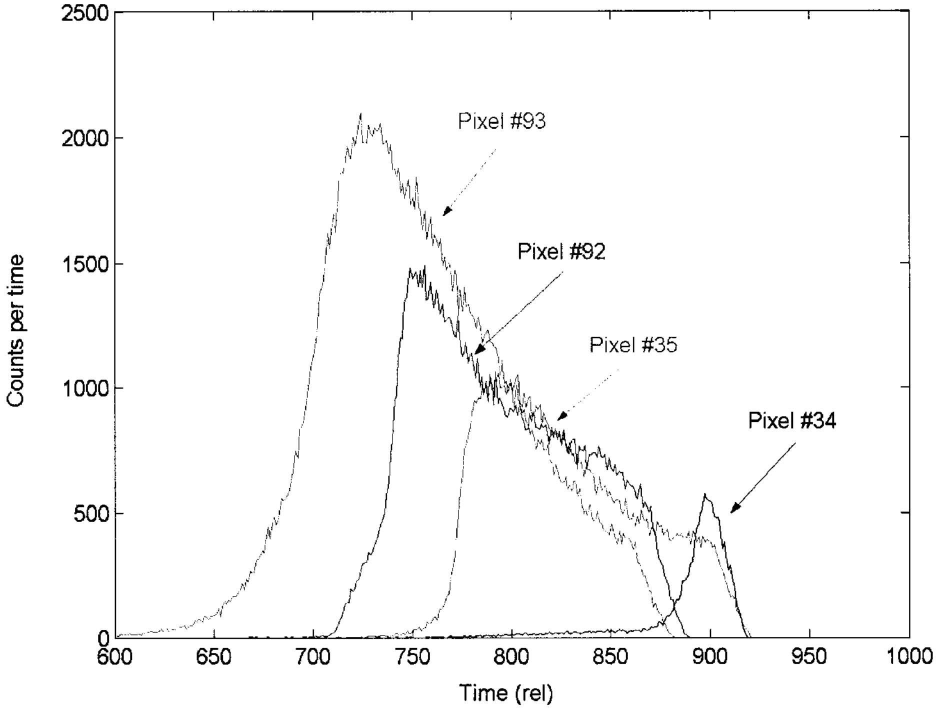

Figure 3.21. Timing spectra observed for four poor pixels in the lower left corner of Figure 3.19. Pixels #92 and #93 show longer drift times even for events near the cathode. The timing spectrum for pixel #34 contains only events from the anode side of the detector.

The six poor pixels and one dead channel total 7 excluded pixels. These ASIC TAT channels are turned off for data acquisition. The remaining 114 pixels are used for the high-energy measurements in this work.

The two detector systems discussed in this chapter are used to collect all data analyzed later in this work. The VAS2/TAT2 system is used for measuring energies below 1 MeV, while the VAS3/TAT3 system is used for high-energy measurements. Once the energies and interaction positions are determined for each event in the detector, it is necessary to reconstruct the sequence of events. This topic is discussed next in Chapter 4.

3.6 References

[1] K. B. Parnham, "Recent progress in Cd(1-x)Zn(x)Te radiation detectors," *Nuclear Instruments and Methods in Physics Research*, vol. A377, pp. 487-491, 1996.

[2] Y. Du, "Development of a prototype Compton scattering camera using 3-D position sensitive CZT detectors," in *Nuclear Engineering and Radiological Sciences*. Ann Arbor: University of Michigan, 2001, pp. 137.

[3] W. Li, Z. He, G.F. Knoll, D.K. Wehe, C.M. Stahle, "Spatial variation of energy resolution in 3-D position sensitive CZT gamma-ray spectrometers," *IEEE Transactions on Nuclear Science*, vol. 46, pp. 187-192, 1999.

CHAPTER 4

SEQUENCE RECONSTRUCTION

4.1 Introduction

The sequence of interactions in some types of Compton imagers is clearly defined. COMPTEL, for example, had two sets of detectors separated by a sufficient distance such that the timing between interactions in the first and second detector arrays could be measured[1]. Only gamma rays that first scattered in the plastic scintillators and then were absorbed in the NaI(Tl) back plane scintillators were accepted for imaging. In other designs, the back plane detector is shielded so that it does not receive direct irradiation. The design of the two-detector imager can then require the first detected event to occur in the front plane detector.

The 4π imager in this work consists of a single small detector. Time between events in the detector (less than 80 ps) is very small compared with the timing resolution of the system. Thus, all events for a given gamma ray appear to occur simultaneously. Neither shielding nor timing can help determine the sequence of events. The only information available on a sequence-by-sequence basis is the number of events and the positions and energies deposited for each event. The kinematics of Compton scattering provide some guidance to choosing the proper event order. In some applications, the initial gamma-ray energy or incident direction is known and the determination of interaction order becomes simpler and more precise. Except where indicated in the following discussion, the gamma-ray energy and incident direction are assumed to be unknown.

In the following discussion, “event” or “interaction” describes a single occurrence of a detectable photon interaction such as photoelectric absorption, Compton scatter, or pair production. A detectable interaction is one in which the energy deposited exceeds a given threshold. Except where explicitly stated, the detection threshold is 0 keV (i.e. a non-zero amount of energy must be deposited). For example, Rayleigh (coherent) scatter is not considered an event because the gamma ray deposits no energy and is therefore undetectable. A “sequence” or “track” is the series of interactions from a single gamma ray in the detector. Thus, a sequence consists of one or more events. Finally, “sequence reconstruction,” sometimes referred to as “gamma-ray tracking” in the literature, is the determination of the order of interactions in the detector.

Sequence reconstruction techniques differ according to the number of interactions observed. Figure 4.1 shows the simulated frequency of observing up to five-pixel full-energy sequences for selected energies between 300 keV and 2.5 MeV. Tracks that consist of only one event cannot be used for Compton imaging. At least two interactions must occur in the detector in order to determine the scatter angle and cone axis. This chapter discusses two- and three-event sequences in detail. A brief examination of 4+-event sequences is also given. The performance of each reconstruction method is analyzed using Monte Carlo simulations[2] (see Appendix), and the effectiveness is estimated for selected energies between 300 keV and 2.5 MeV.

4.2 Sequences with Two Interactions

Considering the curves in Figure 4.1, it is clear that two-pixel sequences will dominate Compton imaging with this detector. At all energies observed, two-pixel sequences occur with at least double the frequency of three-pixel sequences. It is therefore critical to correctly sequence two-event sequences.

Two interactions in the detector can consist of a scatter followed by an absorption, two scatter events, or a pair production followed by the scatter or absorption of one of the annihilation photons, as shown in Figure 4.2. (Pair production occurring after Compton scatter is also possible but rare.) Because the highest energy considered here is 2.6 MeV, pair production is typically neglected due to its low probability of occurrence relative to Compton scatter in CdZnTe. Although pair production is modeled in the simulations, when determining the sequence order, only scatter and photoelectric interactions are considered in the reconstruction process. When pair production does occur, it may or may not lead to incorrect choices for the sequence order, but it will lead to incorrect image reconstruction. The effect of pair production on Compton imaging is discussed in detail later in Chapter 6.

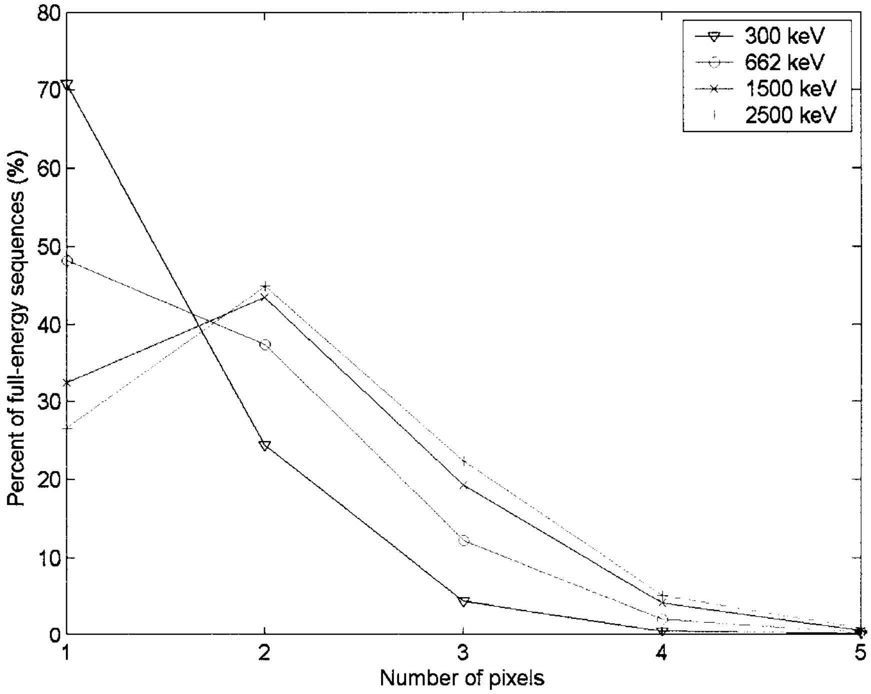

Figure 4.1. Frequency of observing the given number of pixels in full-energy sequences for selected incident gamma-ray energies.

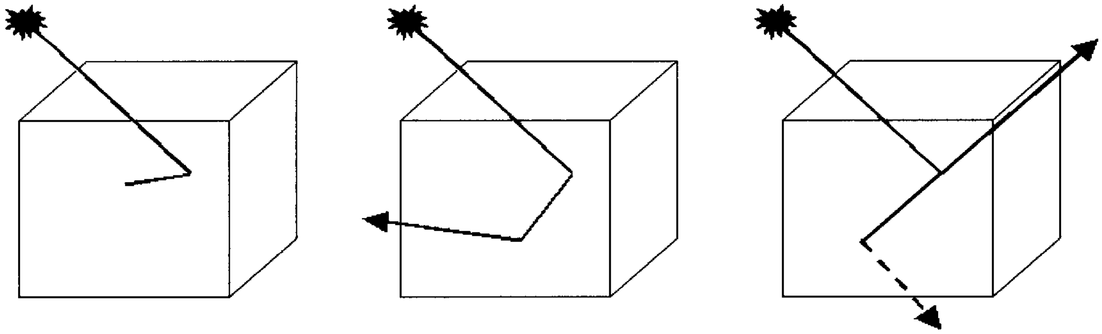

Figure 4.2. Illustration of possible two-event sequences: a) Compton scatter followed by photoelectric absorption, b) two Compton scatters, and c) pair production followed by the scatter (dashed blue line) or absorption (solid blue line) of one annihilation photon and the escape of the other (solid green line).

For tracks with two events, determining the order of interactions is for the most part educated guessing, where the method of guessing depends on the total observed energy. For initial gamma-ray energies below 256 keV the energy distribution of the deposited and scattered gamma-ray energies are distinct. This indicates that for a full-energy sequence in which the gamma ray is scattered and then absorbed in two interactions the sequence order is absolutely distinguishable. The first interaction always deposits less energy than the second. Figure 4.3 shows the deposited energy distributions for the scatter and absorption events, calculated using the Klein-Nishina differential Compton cross section [3] for 200 keV gamma rays. For gamma-ray energies above 256 keV the scatter and absorption distributions overlap, as shown in Figure 4.4 for 662 keV gamma rays. For these gamma rays the knowledge of the deposited energies is insufficient to determine the order of events absolutely.

From Figures 4.3 and 4.4 it is clear that there are some energies that are kinematically impossible to deposit via scatter processes given the incident gamma-ray energy. The Compton edge, corresponding to a backscatter event, is the highest energy that can be deposited in scatter by a gamma ray and is determined using the Compton scatter formula as in Equation 4.1. If the sequence order is known, then a sequence can be rejected if the first event deposits an energy higher than the Compton edge. This is called the Compton edge test.

$$E_{edge} = \frac{E_0}{1+\frac{m_e c^2}{E_0}(1-\cos\pi)} = \frac{E_0}{1+\frac{2m_e c^2}{E_0}} \qquad (4.1)$$

In any two-event sequence in which more than 256 keV is deposited at least one of the two potential sequence orders is kinematically possible. As a result, the Compton edge test cannot be used when the sequence order is unknown unless more information is available. Fortunately, as incident gamma-ray energy increases, the probability of the first event depositing more energy also increases. Shown in Figure 4.5 is the fraction of simulated events in which the first of two interactions deposited more energy. Notice that above 400 keV, there is a greater probability that the first event deposits more energy.

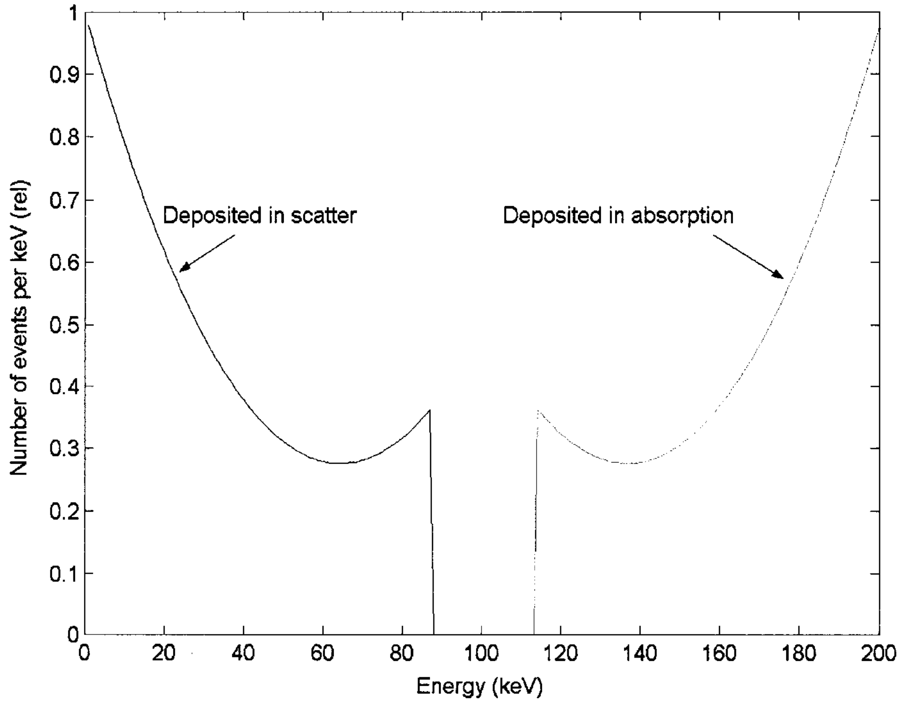

Figure 4.3. Energy deposition distributions for scatter and absorption of 200 keV photons in two-event sequences. For initial gamma-ray energies below 256 keV, the first of two events always deposits lower energy if the second event is an absorption.

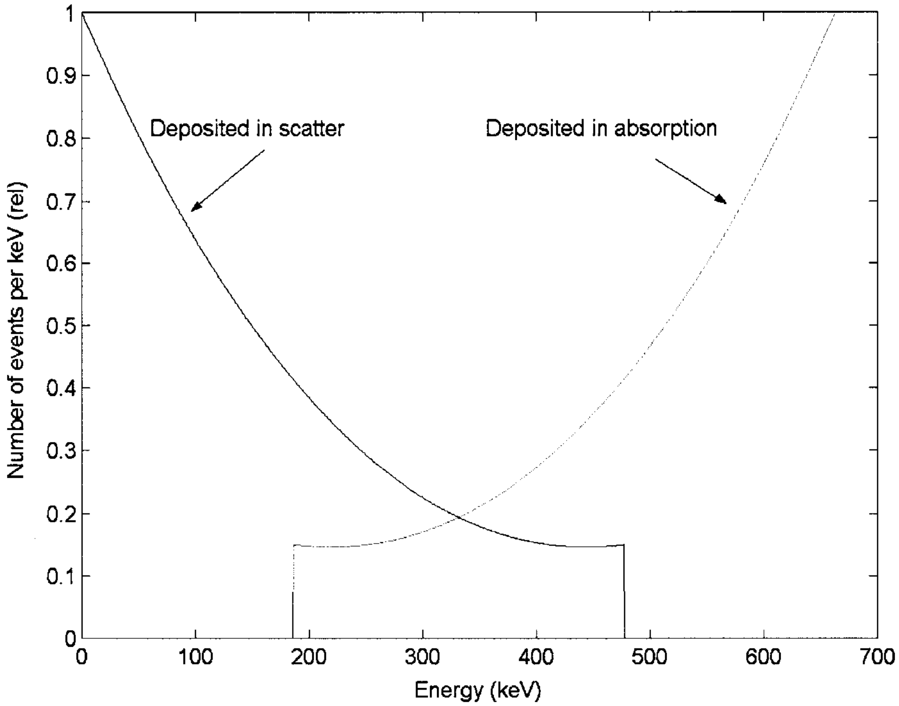

Figure 4.4. Energy deposition distributions for scatter and absorption of 662 keV photons in two-event sequences. For initial gamma-ray energies above 256 keV, the distributions always overlap.

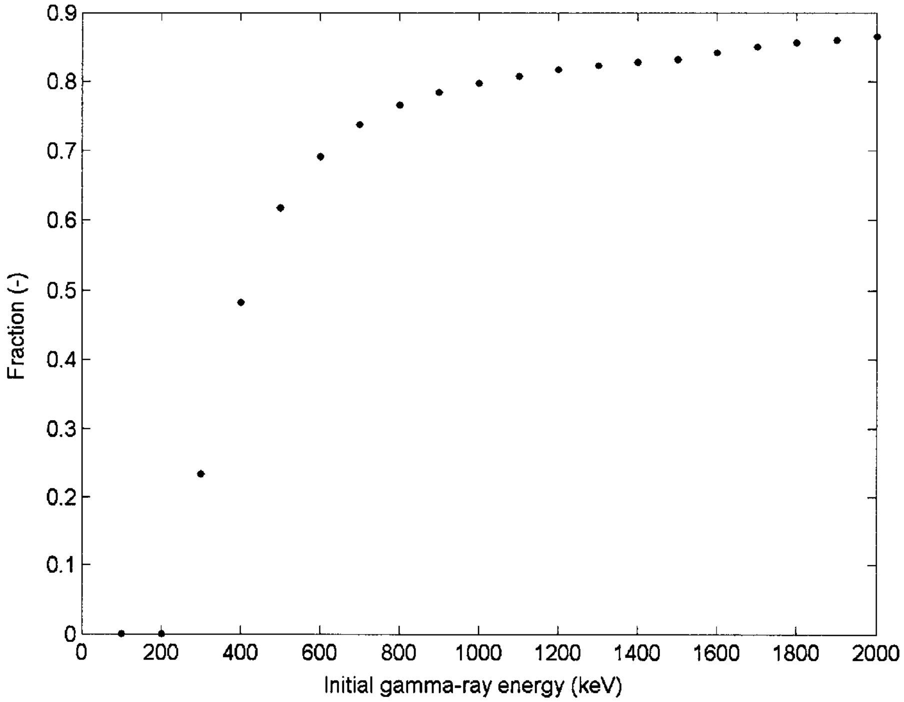

Figure 4.5. Fraction of simulated two-event tracks in which the first interaction deposits more energy than the second as a function of initial gamma-ray energy.

The probability is about 70% at 662 keV and approaches 85% at high energies. This suggests a simple way to determine which event in the sequence actually came first. If the total energy deposited is greater than 400 keV, the higher energy was most likely deposited first. If the total energy observed is below 400 keV the opposite assumption is made: the first interaction is the one that deposited less energy. Note that for full-energy sequences below 256 keV the probability of choosing the wrong track is zero (meaning that the sequence is always determined correctly), as explained via Figure 4.3.

Now that there is a simple sequence reconstruction technique for total deposited energies above 256 keV, the Compton edge test can be applied. If the chosen sequence is not kinematically possible, either the sequence order was incorrect or the full energy of the gamma ray was not deposited. When this occurs the track is rejected altogether. Using this method, many partial-energy sequences can be eliminated. As discussed in Chapter 5, only full-energy sequences will contribute to the correct source location during image reconstruction. Partial-energy sequences contribute to the background in the image, lowering the signal-to-noise ratio. Thus, the kinematics test can be used to eliminate some partial-energy sequences once a specific track order has been chosen, and better images can be produced.

Simulations were performed to test the performance of the two-pixel method (see Appendix). The interaction position and energies were recorded, along with the total number of interactions. The data were then "pixellated," meaning that the precise position of the interaction is replaced with the coordinate of the center of the pixel that would collect most of the electrons from the interaction site. The deposited energies were spread with a Gaussian distribution whose full-width at half-maximum (*FWHM*) is given by the empirical relation given in Equation 4.2 below. The Gaussian spread approximated the electronic noise and charge generation and collection statistics after data processing. Finite electron cloud size, charge sharing, and randomly coincident gamma rays were not considered.

$$FWHM = 4 + 0.129\sqrt{\Delta E} \quad (keV) \tag{4.2}$$

For the purposes of predicting the performance of the sequence reconstruction methods with simulations, a sequence is discarded ifn more than one interaction occurs under a single pixel. For example, if three events occur in the sequence and two of them are under a single pixel, only two events are observed. The number of apparent events is smaller than the actual number of events, and the track cannot be sequenced correctly. The impact of multiple interactions under a single pixel is shown in Table 4.1 for selected energies. The table shows the simulated fraction of two- and three-event sequences in which more than one interaction occurs under a single pixel. At 662 keV, nearly 24% of two-event sequences appear as a single event. That percentage decreases to 20% at 2500 keV. Because these tracks cannot be sequenced correctly, they are not useful for Compton imaging. There is no way to distinguish these from useful sequences using the current electronics, although digitization of the pulse shapes could provide more information. Sequences with multiple interactions under one pixels are excluded from the simulated data used throughout this chapter in order to test the performance of the sequence reconstruction methods on sequences that could possibly be reconstructed correctly. Thus, the performance is measured as a fraction of potentially useful Compton imaging sequences.

Table 4.1. Percentage of Sequences with Multiple Events under a Single Pixel

Energy (keV)	Two-Event Sequences	Three-Event Sequences
300	28.59%	54.51%
662	23.86%	46.08%
1500	22.69%	41.72%
2500	20.07%	37.91%

In measuring the overall performance of the two-pixel technique there are two considerations: a sequence must be both correctly determined and it must be accepted via the Compton edge test. A full-energy sequence will almost always be accepted if the sequence is correct. (The exceptions to this are the presence of a Rayleigh scatter in the track, which alters the direction but not the energy of the gamma ray, and finite energy resolution or Doppler broadening making a backscatter event deposit more energy than the Compton edge.) Also, as previously stated, a partial energy sequence may not be accepted even if the sequence is correct. Table 4.2 gives the percentage of useful two-event sequences that are accepted, are correct, and are both correct and accepted.

One significant result is that most of the full energy sequences are accepted and correctly reconstructed. Whereas for 2500 keV gammas the total accepted fraction is just over 60%, nearly all of the full-energy tracks are accepted. The poorest performance of the technique was at 662 keV where only 69% of full energy sequences and 48% of all sequences were determined correctly and accepted. The poorest performance is expected to occur for gamma rays near the 400 keV transition. Although 300 keV is closer to the transition point than 662 keV, the sequencing technique performs better at 300 keV due to the steep slope below 400 keV of the curve represented in Figure 4.5.

Table 4.2. Percentage of Useful Two-Event Sequences that are Correct and Accepted

Energy (keV)	All Sequences			Full Energy Sequences		
	Accepted	Correct	Correct & Accepted	Accepted	Correct	Correct & Accepted
300	93.0%	79.2%	76.0%	100%	87.1%	87.1%
662	76.4%	63.0%	47.5%	87.9%	72.6%	69.1%
1500	59.8%	85.8%	49.1%	96.2%	94.2%	91.1%
2500	61.2%	89.7%	52.4%	96.7%	97.6%	94.4%

It may be possible to use other available information to determine the sequence order. If, for example, the source direction were known, then knowing that low energy gamma rays will most likely interact near the surface of the detector would allow one to guess that the first interaction is nearest the source. In addition, the source energy and direction could be determined using spectroscopy and Compton imaging, respectively, and then that information could be fed back into determining which sequence is more likely. Such complex sequence reconstruction schemes are not used in this work.

In summary, for two-pixel sequences the first event is chosen to be one that deposits higher (lower) energy if the total deposited energy is above (below) 400 keV. The Compton edge test is then performed in an attempt to reject unwanted partial-energy tracks.

4.3 Sequences with Three Interactions

Traditional Compton imagers have not used three-interaction sequences for imaging. From Figure 4.1, it is clear that these tracks can contribute to a significant increase in efficiency, especially at high energies. Using both two- and three-event sequences at 662 keV can increase the efficiency by 30% if the sequence reconstruction performance for three-pixel tracks is at least as successful as two-pixel tracks. At 2500 keV, that increase jumps to 50%. It is important to correctly sequence as many of these tracks as possible.

When there are three events in the detector, there are six possible sequence orders as illustrated in Figure 4.6. Again, pair production is typically ignored (Section 6.2.2 discusses the effects of pair production on Compton imaging), and the sequence is assumed to consist of either three scatters or two scatters followed by photoelectric

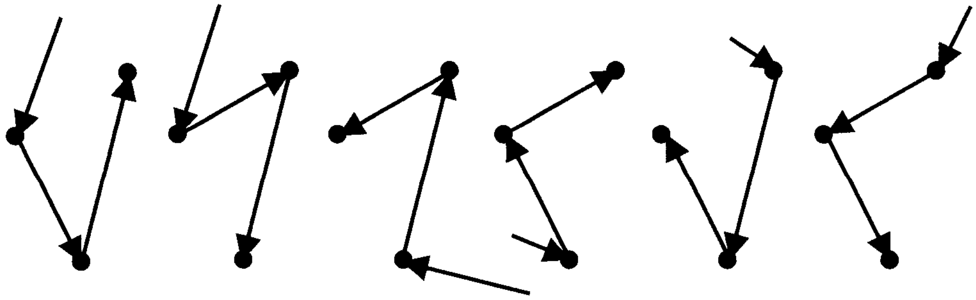

Figure 4.6. Illustration of the six possible sequences for three observed interactions.

absorption. Choosing between possible tracks requires a figure-of-merit (FOM) to be assigned to each track. The sequence with the best FOM is then chosen. Two FOMs have been proposed by other researchers: a chi-squared statistic relating the difference in the second scatter angle calculated using both deposited energies and known interaction positions ("minimum squared difference method") [4-7], and a likelihood function based on the Klein-Nishina scatter probability ("probabilistic method") [8, 9]. Both methods are investigated here. Simulations of a monoenergetic point source 10 cm from the detector were performed with Geant4[2] to determine which FOM is better at selected energies between 300 keV and 2.5 MeV.

4.3.1 Probabilistic method

The first step in the probabilistic method is to choose a sequence order and calculate the initial gamma-ray energy based on the observed energies and positions. From the Compton scatter formula, given in Equation 1.1, the energy of a gamma ray before the scatter, *E*, can be derived as in Equations 4.3 from ΔE, the energy deposited in the scatter at angle θ. The term $m_e c^2$ is the rest mass energy of an electron. The plus or minus in Equation 4.3 is a result of solving the quadratic equation. In reality, the initial gamma-ray energy cannot be less than the deposited energy, and only the positive root is used in the calculation.

$$\Delta E = E - \frac{E}{1 + \frac{E}{m_e c^2}(1-\cos\theta)}$$

$$\Delta E + \frac{\Delta E(1-\cos\theta)}{m_e c^2} E = \frac{(1-\cos\theta)}{m_e c^2} E^2$$

$$E = \frac{\Delta E}{2} \pm \frac{1}{2}\sqrt{\Delta E^2 + \frac{4 m_e c^2 \Delta E}{(1-\cos\theta)}} \tag{4.3}$$

In a sequence of three interactions, the second scatter angle is always known from the three interaction locations. Equation 4.3 can then be used to calculate the energy of the gamma ray before the second scatter. The initial gamma-ray energy is simply this energy plus the energy deposited in the first event. For deposited energies ΔE_1 and ΔE_2 in the first and second scatters, respectively, and scatter angle θ_2, initial energy E_0 can be calculated using Equation 4.4. This is sometimes referred to as "Three-Compton Reconstruction."

$$E_0 = \Delta E_1 + \frac{\Delta E_2}{2} + \frac{1}{2}\sqrt{\Delta E_2^2 + \frac{4m_e c^2 \Delta E_2}{(1-\cos\theta_2)}} \tag{4.4}$$

The second step in this method is to determine whether the chosen sequence is kinematically possible. In other words, the Compton edge test is performed for the first scatter event. If the energy deposited is higher than the Compton edge the sequence is discarded and a new one is examined. The final event in the sequence must either be a Compton scatter, requiring passing the Compton edge test, or a photoelectric absorption, in which case the sum of the deposited energies should equal the reconstructed energy from Equation 4.4. If the final event is not consistent with either a scatter or an absorption, then the sequence is discarded and a new one is examined.

If the sequence passes the kinematics tests, a figure-of-merit is assigned to the sequence based on the probability of observing the sequence. The probability is calculated using the Klein-Nishina differential cross section for Compton scatter[3], given the observed second scatter angle and deposited energies as in Equations 4.5 and 4.6, where Z is the atomic number of the scatter medium, r_0 is the classical electron radius, and E' is the gamma-ray energy after the first scatter, given by $E'=E_0-\Delta E_1$. Note that E' is solely a function of ΔE_2 and θ_2, in accordance with the Compton scatter formula. The product $2\pi r_0^2$ is a constant for all FOMs. Thus, the first term in Equation 4.6 is usually ignored.

$$FOM = \frac{d\sigma}{d\Omega}(\theta_2, E') \tag{4.5}$$

$$= 2\pi r_0^2 \left(\frac{1}{1 + \frac{E'}{m_e c^2}(1 - \cos\theta_2)} \right)^2 \left(\frac{1 + \cos^2\theta_2}{2} \right) \left(1 + \frac{\left[\frac{E'}{m_e c^2} \right]^2 [1 - \cos\theta_2]^2}{\left[1 + \cos^2\theta_2\right]\left[1 + \frac{E'}{m_e c^2}(1 - \cos\theta_2)\right]} \right) \tag{4.6}$$

After the FOM is assigned to the first track, the process is then repeated for the remaining sequences. Of the kinematically possible tracks, the one with the highest FOM is chosen as the correct sequence. Note that the sequences of opposite order will have the same FOM. For example, if the events are labeled A, B, or C, then the tracks B-A-C and C-A-B have the same ΔE_2 and θ_2, and therefore they have the same FOM. In many cases, only one of the two will be kinematically possible and there is no ambiguity. Sometimes it is possible for both sequences to occur. An additional parameter is used to help distinguish these sequences. If any of the six sequences has a total deposited energy equal to its reconstructed energy from Equation 4.4, then the FOM is increased by 10%. Kroeger *et al.* cite this as an effective way to improve the probability of getting full energy sequences correct, and they state that the performance of the algorithm is not significantly dependent on the value of the increase[8]. There may still be some cases in which the forward and backward sequences tie for the highest FOM. In these cases it is necessary to simply guess or to use additional information, such as distance between interactions[8]. For the CdZnTe detector when there is a tie for the highest FOM the correct sequence is chosen to be the one with the higher first deposited energy for total energies above 400 keV, as in the two-event case. Below 400 keV total deposited energy, the winning sequence in a tie is the one with the lower first deposited energy.

To test the probabilistic method data were simulated in the same manner as for two-pixel sequences. Again, sequences in which multiple interactions occur under a single pixel are excluded from this analysis, which reduces the number of observed three event sequences by 55% at 300 keV and by 38% at 2500 keV, as shown in Table 4.1. The performance of the probabilistic method for selected gamma-ray energies from 300 keV to 2.5 MeV is given in Table 4.3. Almost two-thirds of the sequences at 300 keV are incorrectly reconstructed. The algorithm improves as the incident gamma-ray energy increases, and at 2.5 MeV over half of the tracks are correctly identified. Note that the method is less successful for full-energy sequences compared with sequences at all energies, except at 300 keV where the success rates are nearly identical.

Table 4.3. Percentage of Useful Three-Event Sequences Correctly Determined by the Probabilistic Method

Energy (keV)	Total Correct	Full Energy Correct
300	33.5%	34.6%
662	40.1%	35.9%
1500	48.7%	41.2%
2500	50.3%	42.1%

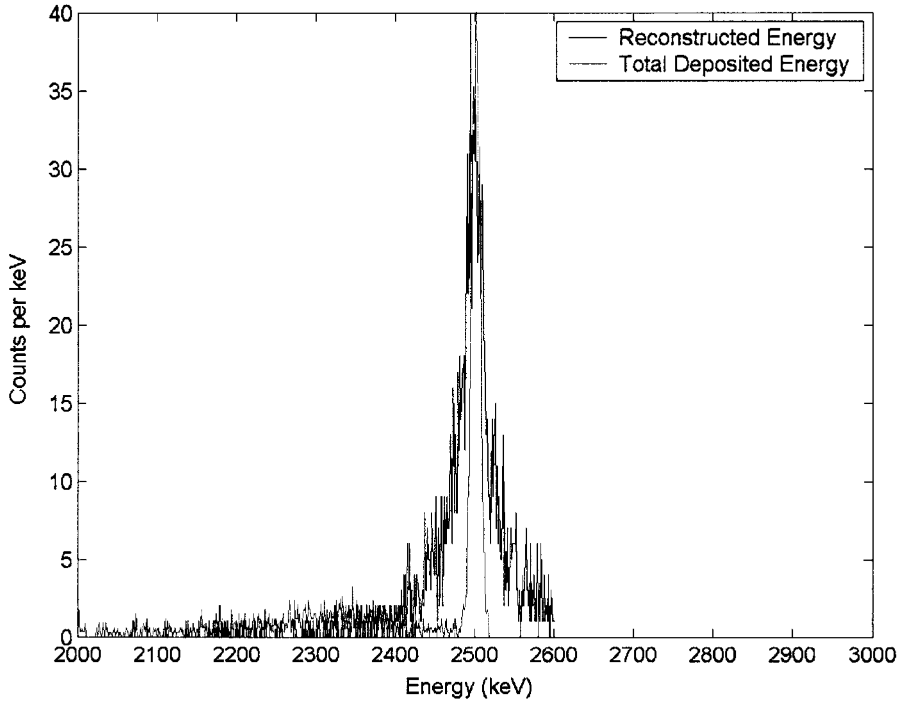

Figure 4.7. The distribution of reconstructed energies for full-energy sequences from simulated 2.5 MeV gamma rays using the three-Compton technique. Also shown is a normalized traditional spectrum that would be obtained by simply summing the energies of three-event sequences.

The probabilistic method shows poor performance (although it is still better than a random guess, for which one would expect 16.7% correct guesses). The poor position resolution leads to an incorrect value of $\cos\theta_2$, which is used in Equation 4.4 to calculate the initial gamma-ray energy. Figure 4.7 shows the distribution of reconstructed energies for full-energy sequences at 662 keV. Wulf *et al.* also demonstrate poor resolution in reconstructed spectra using this equation[10]. When the incident energy calculated using Equation 4.4 is significantly different than the actual incident energy, the calculation of probabilities will also be incorrect. Wulf *et al.* reported that the higher energies are favored in three-Compton reconstruction, but that effect was not observed here.

4.3.2 Minimum squared difference method

The minimum squared difference (MSD) method is the most common method of three-event sequence reconstruction. It first assumes that the full energy of the gamma ray has been deposited (i.e. the final event was a photoabsorption). In this case there are two ways to calculate the angle of the second Compton scatter: using the three measured positions r_1, r_2, and r_3 or using the final two observed energies ΔE_2 and ΔE_3, as in Equations 4.7 and 4.8.

$$\cos\theta_r = \frac{(\vec{r}_2 - \vec{r}_1) \bullet (\vec{r}_3 - \vec{r}_2)}{|(\vec{r}_2 - \vec{r}_1)||(\vec{r}_3 - \vec{r}_2)|} \tag{4.7}$$

$$\cos\theta_e = 1 - \frac{m_e c^2 \Delta E_2}{(\Delta E_2 + \Delta E_3)\Delta E_3} \tag{4.8}$$

$$FOM = \frac{(\cos\theta_e - \cos\theta_r)^2}{\sigma_e^2 + \sigma_r^2} \tag{4.9}$$

The figure-of-merit (FOM) is calculated according to Equation 4.9, where σ_r^2 and σ_e^2 are the variances of the cosines calculated in Equations 4.7 and 4.8, respectively. The sequence with the smallest FOM is chosen. The MSD method is occasionally referred to in the literature as a "chi-squared" analysis, but the algorithm is simply a minimization of the squared difference—adjusted for uncertainties—between cosines

Table 4.4. Percentage of Useful Three-Event Sequences Correctly Determined by the Minimum Squared Difference Method

Energy (keV)	Total Correct	Full Energy Correct
300	48.4%	57.2%
662	49.4%	50.7%
1500	47.3%	62.3%
2500	47.9%	63.6%

calculated using energies or positions of interactions. A chi-squared test is not actually performed. The variances in the cosines are calculated using the chain rule, as in Equations 4.10 and 4.11. The angular uncertainties $d\theta_r$ and $d\theta_e$ are defined in Section 5.2.4.

$$\sigma_r^2 = [d(\cos\theta_r)]^2 = \sin^2\theta_r(d\theta_r)^2 \tag{4.10}$$

$$\sigma_e^2 = [d(\cos\theta_e)]^2 = \sin^2\theta_e(d\theta_e)^2 \tag{4.11}$$

The percentage of useful sequences that are correctly determined by the minimum squared difference method is given in Table 4.4. Nearly half of all tracks are correctly sequenced. Full-energy tracks are sequenced correctly more often, up to 63% at 2.5 MeV.

The MSD method clearly outperforms the probabilistic method for all energies tested. More than half the full-energy sequences are correctly identified, and these tracks are chosen correctly more often than partial-energy tracks. This is no surprise, given that the algorithm assumes the full energy has been reconstructed.

4.3.3 Comparison of MSD and probabilistic methods

To directly compare the methods, the same simulated data were reconstructed using both the MSD and the probabilistic methods. A tally was made of the number of times a given pair of sequence orders was found. For example, MSD may select the sequence *213* while the probabilistic method may select *132*; in another sequence both methods may choose *123*, the correct sequence. The results are shown in Figures 4.8, 4.9, and 4.10 for 300 keV, 662 keV, and 2.5 MeV gamma rays, respectively. At 300 keV, the

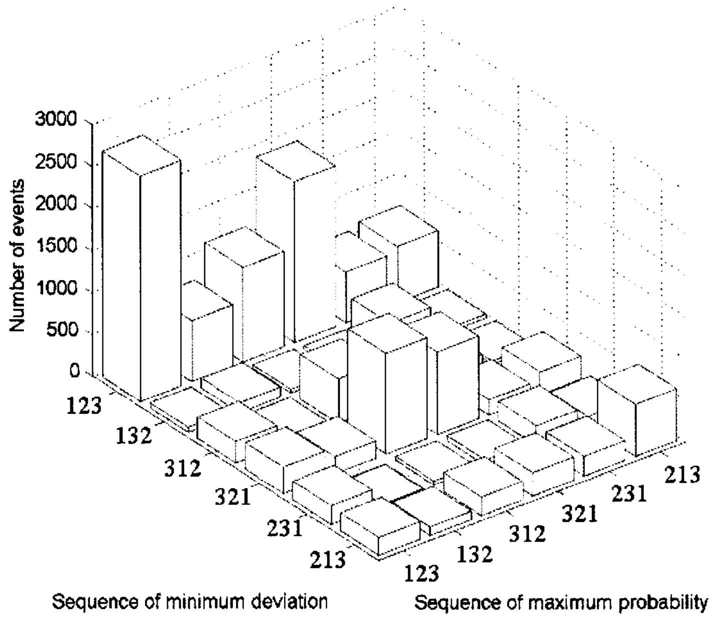

Figure 4.8. Comparison of sequence orders chosen by MSD and probabilistic methods for 300 keV gamma rays (all sequences). MSD chooses the correct sequence (*123*) with much higher frequency than the probabilistic method.

most common occurrence is both methods choosing the correct sequence (*123*), and it is clear that the MSD method performs better. When the order is chosen incorrectly, both methods select the reverse sequence (*321*) most often. There is no obvious correlation between the sequences chosen via MSD and the probabilistic method.

At 662 keV, it is evident that the probabilistic method performs better than at 300 keV. The performance of the MSD method is degraded somewhat, although still better than the probabilistic method. At 2.5 MeV, the MSD method correctly identifies fewer overall sequences than the probabilistic method, although more full energy tracks are correctly sequenced. Again, there is no obvious correlation between the two methods and the sequence orders chosen.

Due to its superior performance with full-energy sequences, the MSD method is the obvious choice for reconstructing three-pixel tracks in this detector. For the remainder of this work, the MSD method will be used to reconstruct sequences of three interactions.

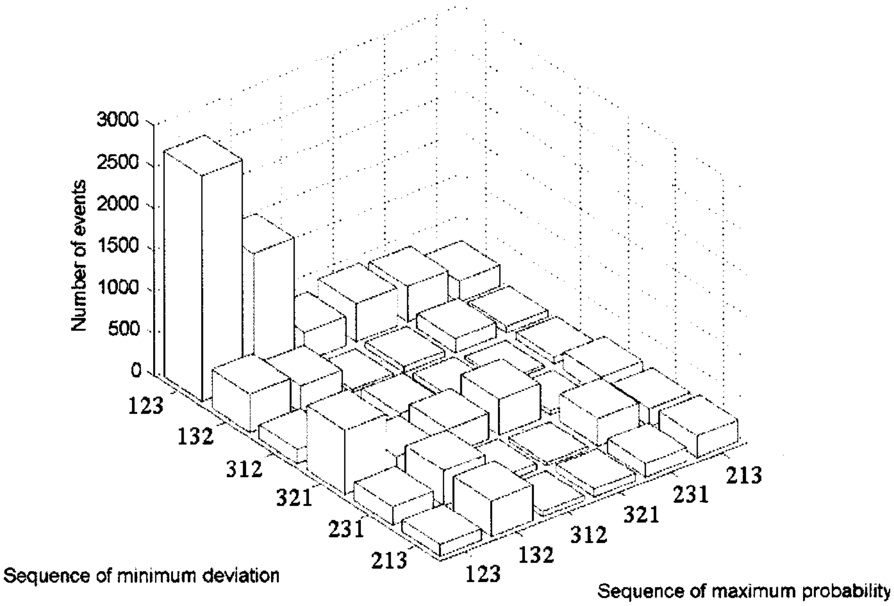

Figure 4.9. Comparison of sequence order chosen by MSD and probabilistic methods for 662 keV gamma rays (all sequences). The probabilistic method shows better performance than at 300 keV, although the MSD method is still superior.

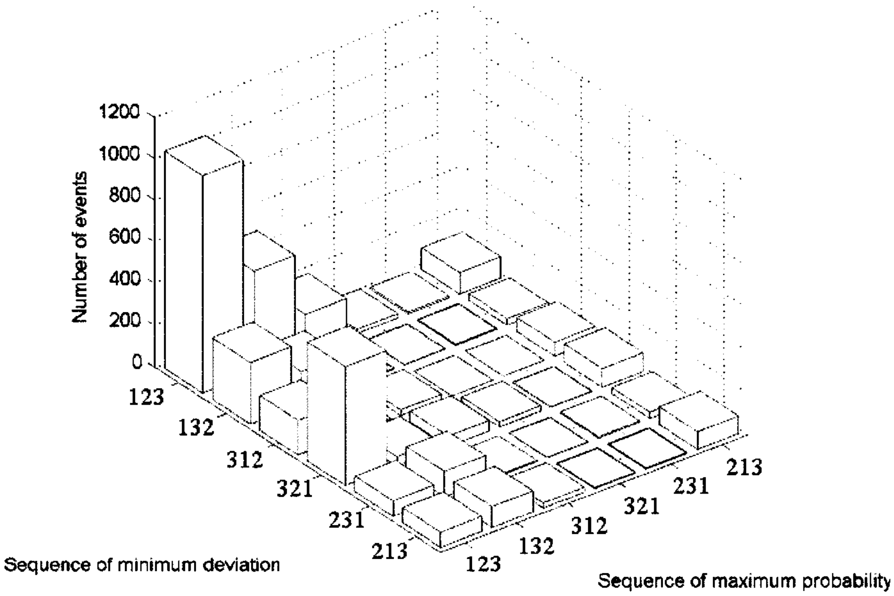

Figure 4.10. Comparison of sequence order chosen by MSD and probabilistic methods for 2.5 MeV gamma rays (all sequences). The probabilistic method shows better performance for all events, but the MSD method correctly identifies more full-energy sequences.

4.4 Sequences with Four or More Interactions

The process for determining the correct tracks for four or more interactions is similar to that for three interactions. Both the MSD and probabilistic methods are easily expandable. First, each possible track is separated into triplets. For example, the sequence *1234* has two triplets: *123* and *234*. The methods for three interactions are then used to reconstruct each triplet. Because the triplets actually overlap, there is redundant information. In this case, the scattered gamma-ray energy between interactions *2* and *3* should be the same for both *123* and *234*. This provides an additional constraint on the kinematics when four or more events are observed.

The figures-of-merit for each physically possible sequence is simply the sum of the FOMs of each triplet, as in Equation 4.12 for MSD and Equation 4.13 for the probabilistic method, where n is the number of triplets. The sequence order with the minimum (MSD) or maximum (probabilistic method) FOM is then selected.

$$FOM = \sum_{i=1}^{n} \frac{(\cos\theta_{ei} - \cos\theta_{ri})^2}{\sigma_{ei}^2 + \sigma_{ri}^2} \tag{4.12}$$

$$FOM = \sum_{i=1}^{n} \frac{d\sigma}{d\Omega}(\theta_{2i}, E_i') \tag{4.13}$$

Four-event tracks comprise only 1.5% of the total sequences at 662 keV, and most of them deposit the full gamma-ray energy. At 2.5 MeV, 2.5% of tracks have four interactions, although only 60% of these are usable for Compton imaging due to pair production and multiple interactions under a single pixel. For a detector larger than 2.25 cm^3 it may be necessary to include four-pixel tracks, but in this work these sequences are discarded in the interest of reducing computation time.

4.5 Sequence Reconstruction in This Work

Both two- and three-event tracks are used for Compton imaging. They comprise 33% of the total sequences (50% of full-energy sequences) at 662 keV and 25% of all sequences (67% of full-energy sequences) at 2.5 MeV. Tracks with four or more interactions occur with very low frequency and are not used in this work except where otherwise stated. Two-pixel sequences are reconstructed using the simple energy test: above 400 keV total energy deposited, the first interaction deposits more energy; below 400 keV the opposite is true. If the sequence is not kinematically possible, it is discarded. Three-pixel sequences are reconstructed via the Minimum Squared Difference method, which calculates the difference between the second scatter angle cosines using deposited energies and observed interaction positions.

It is important to note that the performance of these methods were evaluated using modified simulated data; sequences involving pair production and multiple interactions under a single pixel were known and discarded, and charge sharing was not considered. This was done to demonstrate the effectiveness of the methods for tracks that could possibly be determined correctly. Thus, although the MSD method reconstructs 49.4% of the useful three-pixel sequences correctly at 662 keV, only 53.9% of the three-event sequences are useful at that energy. Thus, of all the three-event tracks, only 26.6% will lead to correctly imaged sequences. Nearly 69% of full-energy two-event sequences are properly determined at 662 keV, but only 76% of sequences are useful. Therefore, 53% of full-energy two-event tracks will be correctly imaged. Clearly a reduction in efficiency results from these effects. The effect on imaging due to pair production, charge sharing, multiple events under a single pixel, and other factors is discussed in Chapter 6.

4.6 References

[1] V. Schonfelder, A. Hirner, K. Schneider, "A telescope for soft gamma ray astronomy," *Nuclear Instruments and Methods*, vol. 107, pp. 385-394, 1973.

[2] S. Agostinelli, J. Allison, K. Amako, J. Apostolakis, H. Araujo, P. Arce, M. Asai, D. Axen, S. Banerjee, G. Barrand, F. Behner, L. Bellegamba, J. Boudreau, L. Broglia, A. Brunengo, H. Burkhardt, S. Chauvie, J. Chuma, R. Chytracek, G. Cooperman, et al., "Geant4 - a simulation toolkit," *Nuclear Instruments and Methods in Physics Research*, vol. A506, pp. 250-303, 20003.

[3] G. F. Knoll, *Radiation Detection and Measurement*, 3rd ed. New York: John Wiley & Sons, Inc, 2000.

[4] G. J. Schmid, I.Y. Lee, M.A. Deleplanque, P. Hendriks, F.S. Stephens, K. Vetter, S.J. Asztalow, R.M. Clark, R.M. Diamond, P. Fallon, R. Kruecken, A.O. Macchiavelli, R.W. MacLeod, "Gamma-ray cluster identification in a spherical shell of highly segmented germanium detectors," *IEEE Transactions on Nuclear Science*, vol. 44, pp. 975-978, 1997.

[5] I. Y. Lee, "Gamma-ray tracking detectors," *Nuclear Instruments and Methods in Physics Research*, vol. A422, pp. 195-200, 1999.

[6] U. G. Oberlack, E. Aprile, A. Curioni, V. Egorov, K.L. Giboni, "Compton scattering sequence reconstruction algorithm for the liquid xenon gamma-ray imaging telescope (LXeGRIT)," *SPIE Proceedings*, vol. 4141, pp. 168-177, 2000.

[7] S. E. Boggs, and P. Jean, "Event reconstruction in high resolution Compton telescopes," *Astronomy & Astrophysics Supplement Series*, vol. 145, pp. 311-321, 2000.

[8] R. A. Kroeger, W.N. Johnson, J.D. Kurfess, B.F. Phlips, and E.A. Wulf, "Three-Compton telescope: Theory, simulations, and performance," *IEEE Transactions on Nuclear Science*, vol. 49, pp. 1887-1892, 2002.

[9] C. J. Pearson, J.J.V. Dobon, P.H. Regan, P.J. Sellin, E. Morton, P.J. Nolan, A. Boston, M. Descovich, J. Thornhill, J. Cresswell, I. Lazarus, and J. Simpson, "Digital gamma-ray tracking algorithms in segmented germanium detectors," *IEEE Transactions on Nuclear Science*, vol. 49, pp. 1209-1215, 2002.

[10] E. A. Wulf, B.F. Phlips, W.N. Johnson, R.A. Kroeger, J.D. Kurfess, E.I. Novikova, "Germanium strip detector Compton telescope using three-dimensional readout," *IEEE Transactions on Nuclear Science*, vol. 40, pp. 1182-1189, 2003.

CHAPTER 5

IMAGE RECONSTRUCTION

5.1 Introduction

Image reconstruction techniques typically fall into two categories: direct (Fourier) and iterative methods. Direct reconstruction uses approximate deterministic expressions to reconstruct an object from its forward projections. Iterative methods use statistical models and can more accurately treat the physics of gamma-ray detection and account for stochastic processes, although the iterative nature of the reconstruction necessitates longer computation times than the direct methods.

The two most popular methods for reconstructing images from Compton scatter data are backprojection and maximum likelihood estimation (ML). Backprojection is a direct reconstruction method relying on fast Fourier transforms and has been used extensively for 3-D tomographic imaging from x-ray projection data. It usually requires first a backprojection step to obtain a blurred estimate of the image and then a filtering step to remove the blurring. (Sometimes the filter is applied before the backprojection step.) Because the projections from Compton scatter data are not straight lines as in x-ray projections but rather conic sections, backprojection is not a precise image reconstruction technique for Compton imaging. As a result, maximum likelihood estimation—an iterative reconstruction method—has been used for Compton imaging since the 1980s with much success. It is the success of ML in planar Compton imaging that motivates the use of it in 4π imaging here.

5.2 Backprojection Reconstruction

Backprojection gained popularity in early Compton imagers because of its simplicity. The mathematics of backprojection were well understood in terms of tomography, where a 3-D image is reconstructed from its 2-D forward projections. In Compton imagers the forward projection is the observed data: deposited energies and interaction locations. As briefly described in Chapter 1, the observed energies are used to calculate the Compton angle for the first scatter in the detector. The initial direction of the gamma ray can be localized to within a cone of probability, where the vertex is at the first interaction location, and the half-angle is the calculated Compton angle. Reconstructing images requires summing the backprojected cones on a surface, as illustrated in Figure 5.1.

Usually, backprojection is performed in the source plane parallel to the front face of the detector. The source distance must be known *a priori*. For sources far from the

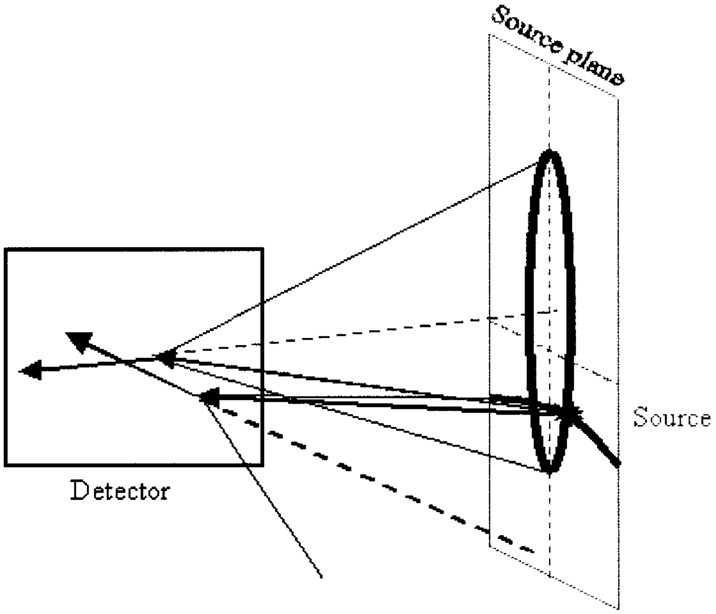

Figure 5.1. Illustration of backprojection imaging. Backprojected cones are summed in the source plane. After many events, the intersection of the cones indicates the source position.

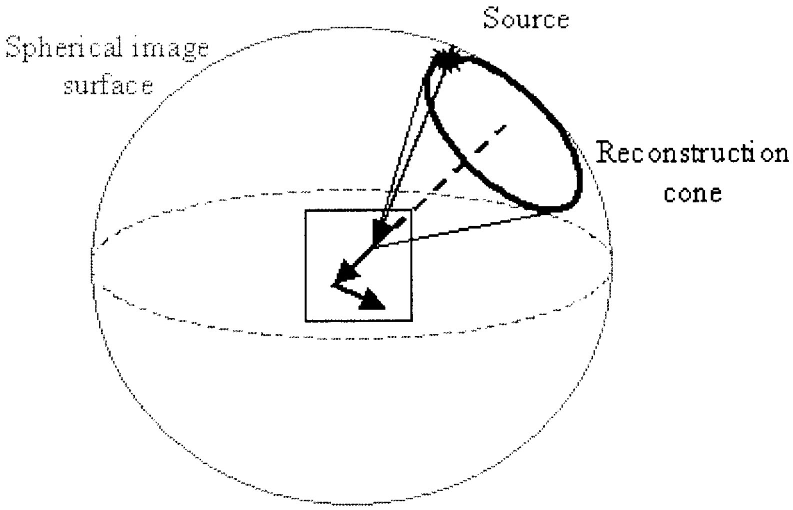

Figure 5.2. Illustration of 4π backprojection. The backprojected cones are summed on a spherical image surface that intersects the source location. As in planar imaging, the overlap of many cones indicates the source location.

detector ("far field imaging") the errors from incorrectly estimating the source distance are usually small. In 4π Compton imaging, the reconstruction surface is a sphere, as in Figure 5.2. The image sphere surrounds the detector, and gamma-rays from any direction can be used for imaging.

5.2.1 Event circle method

Backprojection is performed in the following manner. The axis of the Compton cone is determined by drawing a ray from the second interaction through the first interaction location. The cone vertex is the first interaction point, and the cone opens in the direction of the axis ray with a half-angle equal to the first Compton scatter angle. The cone has a finite width due to the uncertainty in both the axis direction and the calculated Compton angle (see Section 5.2.3 for a discussion of angular uncertainty). The projection of the cone shell on the image surface is determined by finding the image pixels that also lie on the cone. Wilderman, et al.,[1] describe a process for determining the proper backprojections with a planar image surface. Rohe, et al.,[2] describe the calculation for a spherical image volume inside a shell of detectors. Each image pixel that intersects the backprojection cone is then given a value of 1 for that gamma-ray sequence. All other pixels are assigned a value of 0. The image pixel values are then normalized such that the sum of the intensities for each pixel in the ring equals 1. The process is repeated for each set of measurements and the backprojections are summed. This is called the “event circle” method.

5.2.2 Far-field approximation

The calculation of the exact intersection of the backprojected cones and the image surface can be difficult and time consuming. To simplify the calculation, the cone vertex is approximated at the center of the detector, rather than the center of the voxel corresponding to the first interaction. In this way, the image sphere center coincides with the backprojection cone vertex. The cone axis, which should be a ray from the second through the first interaction, is then simply translated to the origin. This is known as the “far-field approximation.”

The effects of this approximation can be estimated as follows. Let R equal the (fixed) radius of the image sphere. Let d equal the separation distance between the true interaction location and the center of the detector. The angular difference φ on the image sphere between the true cone axis and the approximated cone axis can be estimated using Equation 5.1. An illustration of the geometry is shown in Figure 5.3.

$$\tan\varphi = \frac{d}{R} \tag{5.1}$$

The maximum difference in the intersection of the cone axis with the image surface was calculated for radii from 1 to 100 cm. As seen in Figure 5.4, for source-to-detector distances equal to or greater than 20 cm, the difference in the axes is less than 3.5°. By comparison, the average geometric uncertainty is about 5°. Thus, for source

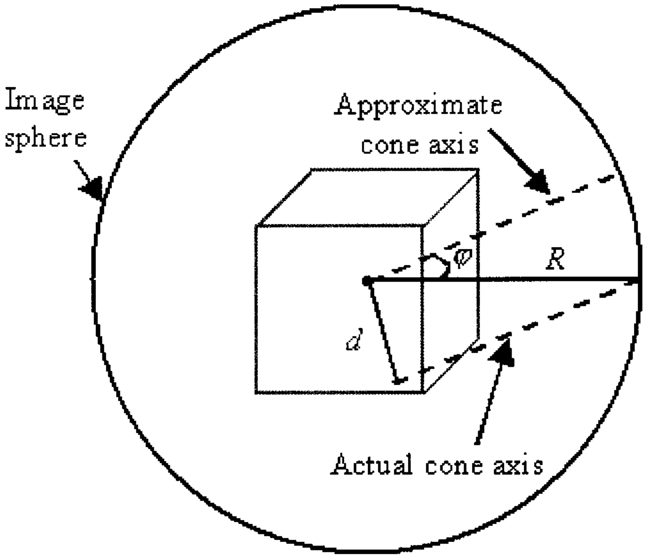

Figure 5.3. Illustration of the cone axis approximation. In the approximation the axis is translated to the origin of the detector, which is the center of the spherical image volume.

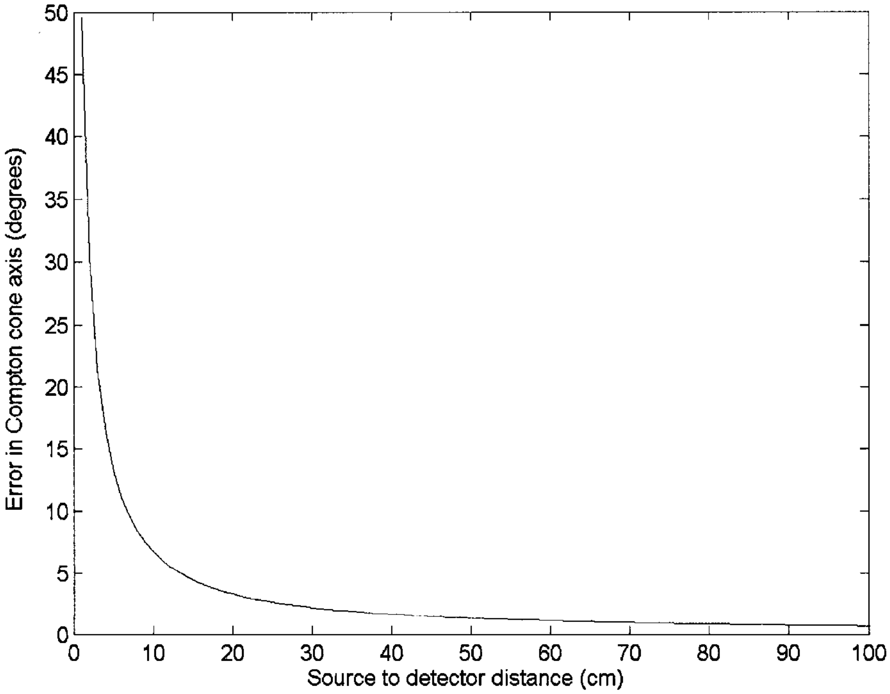

Figure 5.4. Calculated error in the Compton cone axis by relocating the vertex to the center of the image sphere. The effects are small for source distances above 20 cm.

distances greater than 20 cm, the far field approximation holds. Note that at 1 m the error is only 0.6°.

In addition to misregistration of the cone axis, the approximation also changes the shape of the intersection of the cone with the sphere. For a cone vertex at the center of the sphere, the intersection is always a circle. For a cone vertex located inside the sphere at another location, the intersection is slightly egg-shaped. Due to the large geometric uncertainties present in the 4π imager, the width of the cones is at least several degrees, and the differences in the reconstructed images should be minimal compared with the exact calculations. All backprojections performed in this work use the far field approximation.

5.2.3 Calculating angular uncertainty

The width of the backprojection cone is given by the estimated angular uncertainty. There are two independent components to the angular uncertainty: error in the Compton scatter angle, calculated using deposited energies, and error in the cone axis direction, calculated using interaction positions. The angular uncertainties due to energy and position can then be added in quadrature to yield the total angular uncertainty, and hence the width of the backprojection cone. Doppler broadening is not included in the estimate of angular uncertainty, but the effect is small due to the dominance of the position uncertainty contribution. Doppler broadening is discussed further in Chapter 6.

The uncertainty in angle calculated using energies, $d\theta_e$, is determined by applying error propagation to Equation 4.8, which assumes that the total initial gamma-ray energy is deposited. The angular uncertainty is calculated as in Equation 5.2, given the uncertainty dE_i in the energy ΔE_i, and is shown in Figure 5.5 for two-pixel sequences as a function of scatter angle for selected energies. The energy uncertainty is calculated as in Equation 4.2.

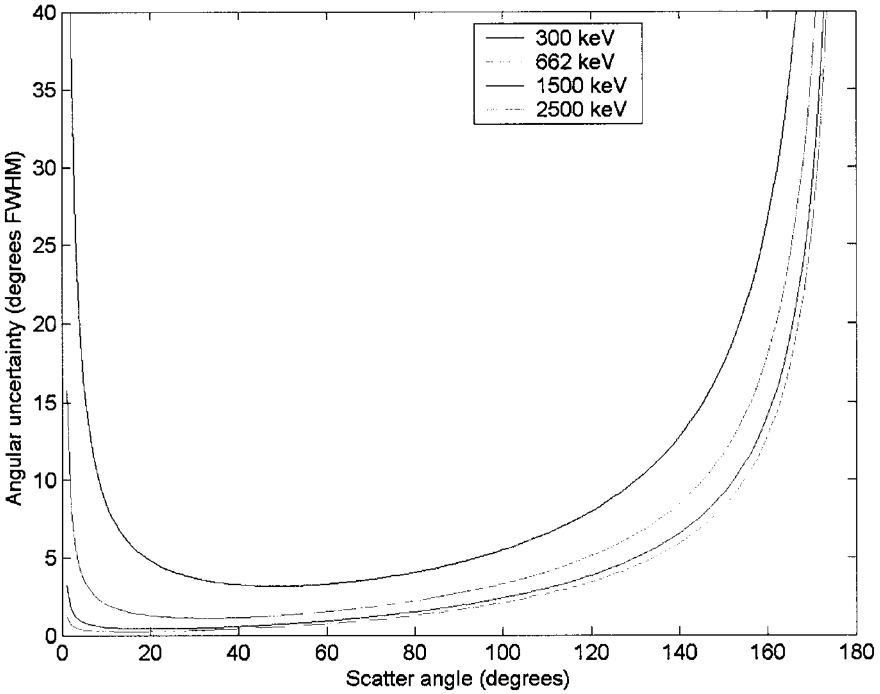

Figure 5.5. Angular uncertainty of two-pixel sequences due to energy resolution calculated as a function of scatter angle for selected energies.

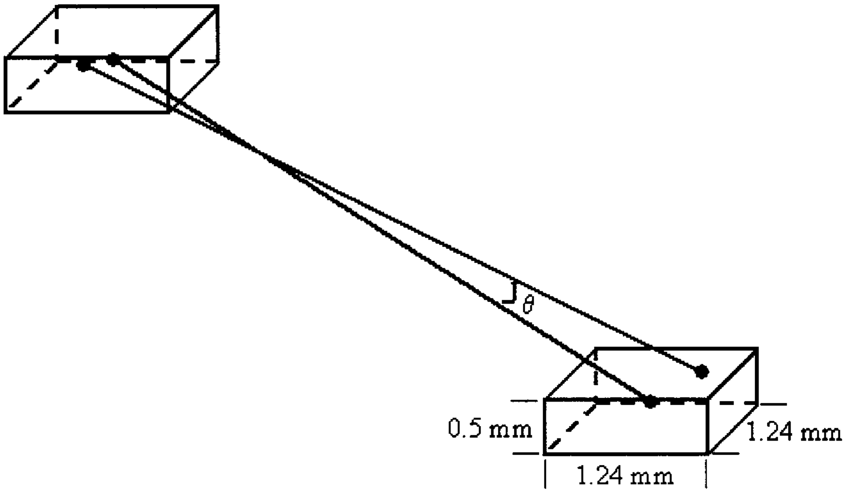

Figure 5.6. Illustration of the calculation of geometric uncertainty. A line connecting randomly chosen points within the voxels forms an angle with respect to the center line that is the angular deviation of the point from the voxel center. The geometric uncertainty is the average angular deviation calculated over many randomly chosen points.

$$d\theta_e = \frac{m_e c^2}{(\Delta E_0)^2 (\Delta E_0 - \Delta E_1)^2 \sin\theta} \sqrt{(\Delta E_0 - \Delta E_1)^4 (dE_1)^2 + [\Delta E_0^2 - (\Delta E_0 - \Delta E_1)^2]^2 \sum_{i>1} (dE_i)^2} \tag{5.2}$$

The angular uncertainty due to energy resolution becomes very large for both small and large scatter angles. For small scatter angles the first event deposits very little energy. In this case the error in the energy can be a large fraction of the deposited energy, and thus the angular uncertainty is also very large. For backscattered gamma rays, the deposited energy is not sensitive to large changes in scatter angles. As expected, the effect of energy resolution on the angular uncertainty is most profound for lower energy gamma rays.

Angular uncertainties based on interaction positions are estimated in the following manner. The two interactions are assumed to occur somewhere inside voxels with dimensions 1.24 mm × 1.24 mm × 0.5 mm, corresponding to the position uncertainties in *x*, *y*, and *z*. A point is randomly chosen inside each voxel and a vector is drawn between the points, as in Figure 5.6. The angular deviation of this vector from the line connecting the centers of the voxels can then be determined. For each possible pair of two interactions voxels, 10,000 points are randomly chosen within the voxel, and the angular deviation is calculated for each point. As an example, the distribution for two interactions separated by one pixel each in *x* and *y* and by 5 mm in *z* is given in Figure 5.7. The average of this distribution is considered to be the geometric uncertainty. The geometric uncertainties for all possible interaction pairs at the same depth is given in Figure 5.8, and for interactions separated by 5 mm in Figure 5.9.

The calculated geometric uncertainty is about 15° for the case where two interactions occur in neighboring pixels at the same depth. The maximum angular deviation for this case is nearly 90°. This method takes into account the fact that more volume is located near the line connecting the pixel centers than near the outer corners, where the angular deviation is large.

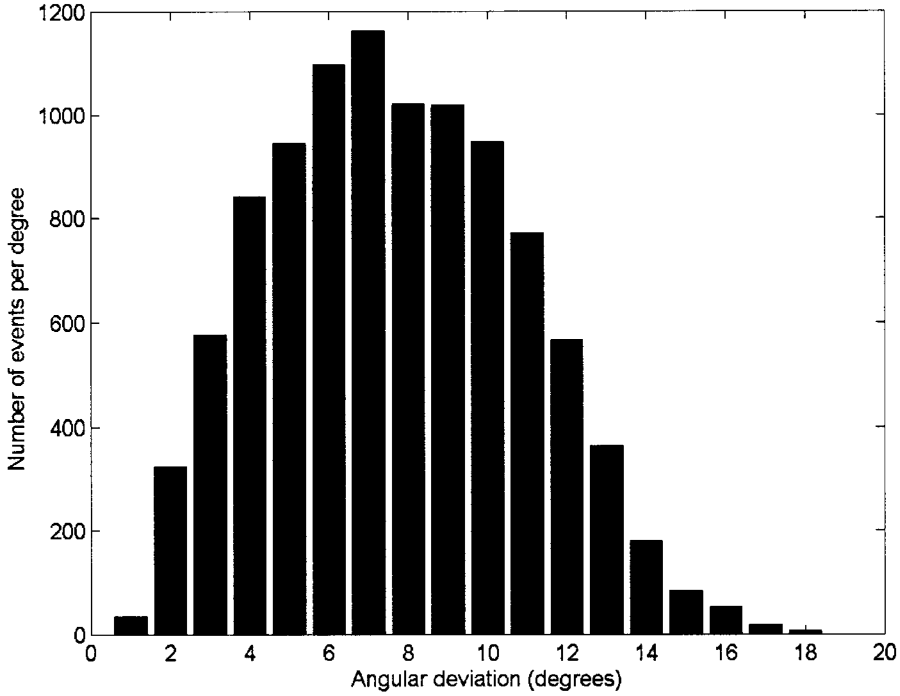

Figure 5.7. Distribution of angular deviation calculated for two points separated by 1 pixel each in *x* and *y* and by 5 mm in *z*. The average of this distribution is the calculated geometric uncertainty.

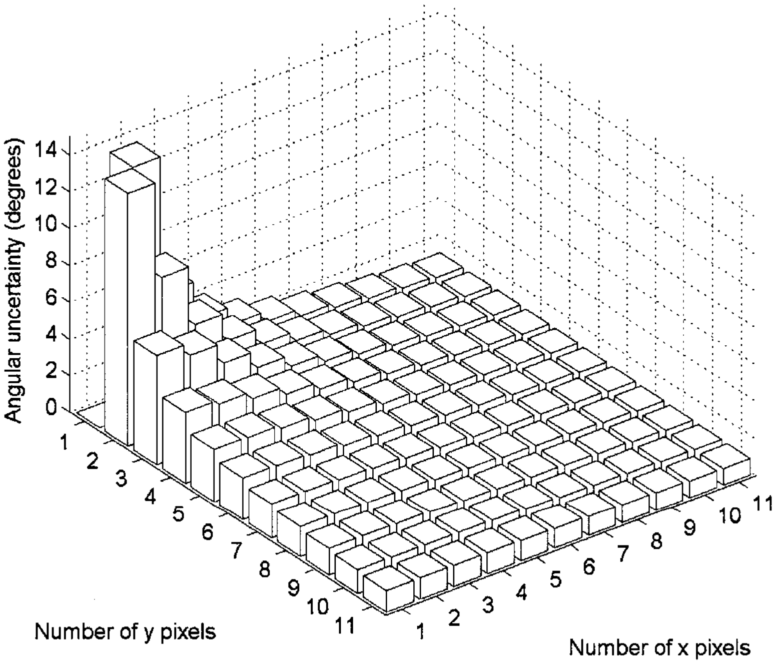

Figure 5.8. Angular uncertainties due to geometry for two events occurring at the same depth separated by the given number of *x* and *y* pixels.

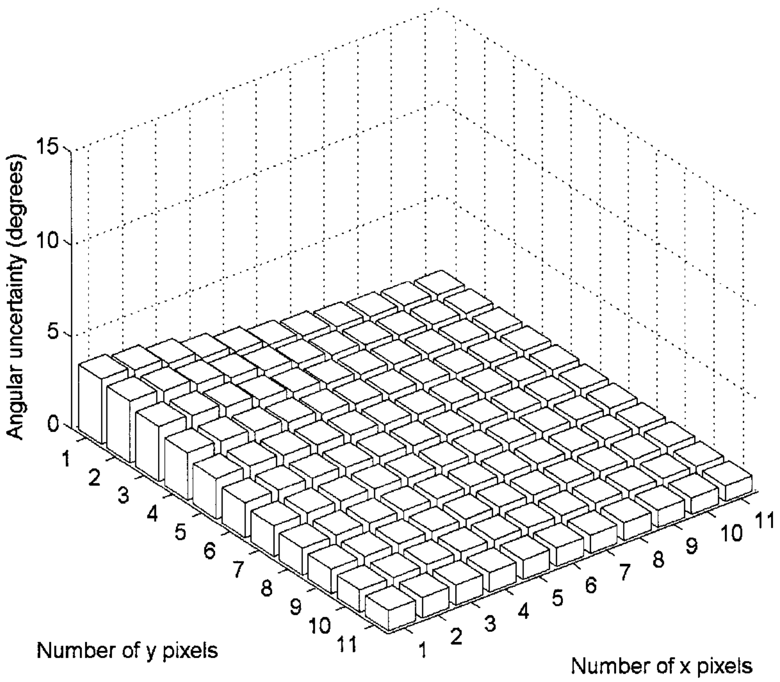

Figure 5.9. Angular uncertainties due to geometry for two events separated by 5 mm in depth and by the given number of *x* and *y* pixels.

The geometric angular uncertainty values are calculated in advance for the given geometry, tabulated, and stored for implementation in the image reconstruction program. Angular uncertainties due to energy are calculated for each sequence during image reconstruction.

5.2.4 Performance of backprojection reconstruction

A backprojection image of a simulated 662 keV point source is shown in Figure 5.10 for a source located above the detector. A slice through the center of the source in this image is shown in Figure 5.11. Figure 5.12 shows the image reconstructed from a source located to the side of the detector, and the central slice of this image is given in Figure 5.13. In each image, the full energy two- and three-pixel sequences are imaged. The slices show an angular resolution of 103° for the source above the detector and 55°

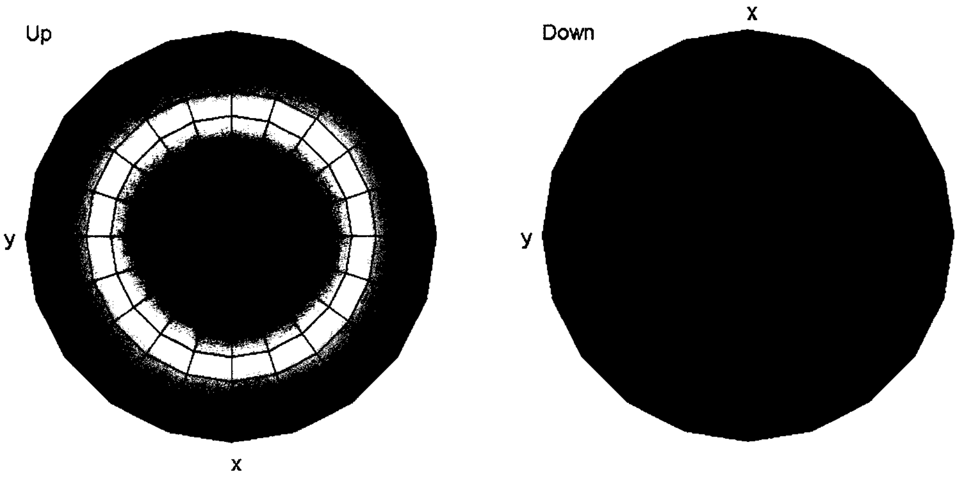

Figure 5.10. Backprojection image of simulated 662 keV point source located above the detector. Full-energy two- and three-pixel sequences are imaged.

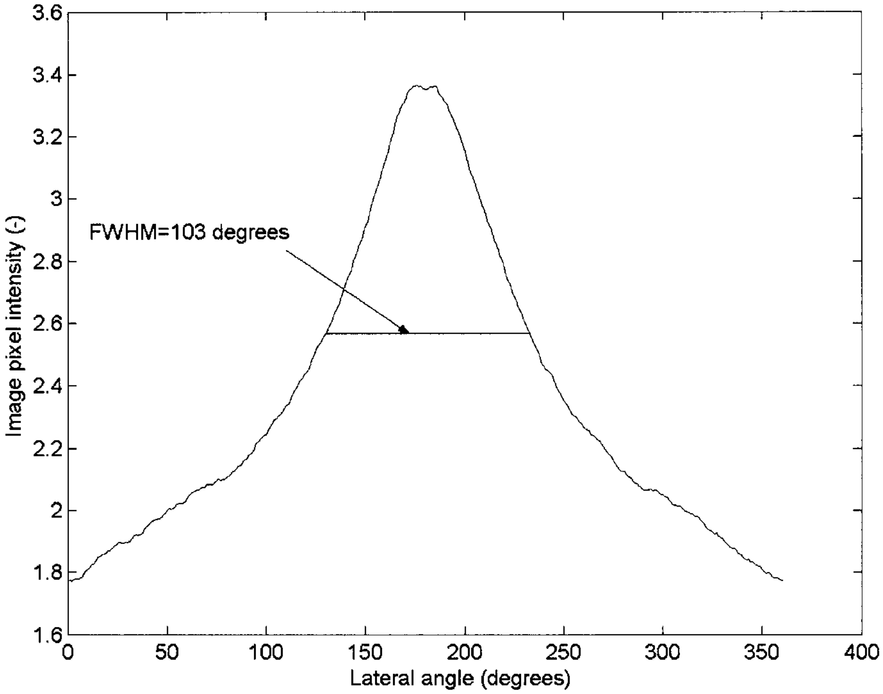

Figure 5.11. Central slice through the image in Figure 5.10. The estimated angular resolution is 103° FWHM.

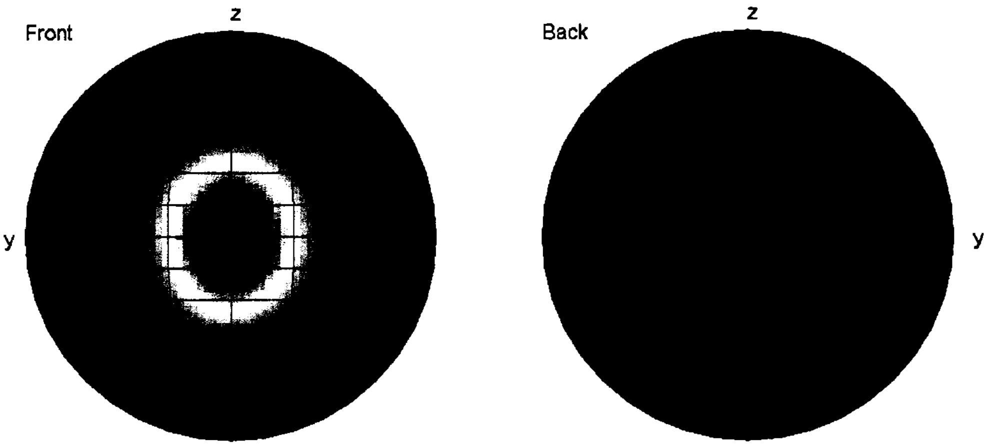

Figure 5.12. Backprojection image of simulated 662 keV point source located to the side of the detector. Full-energy two- and three-pixel sequences are imaged.

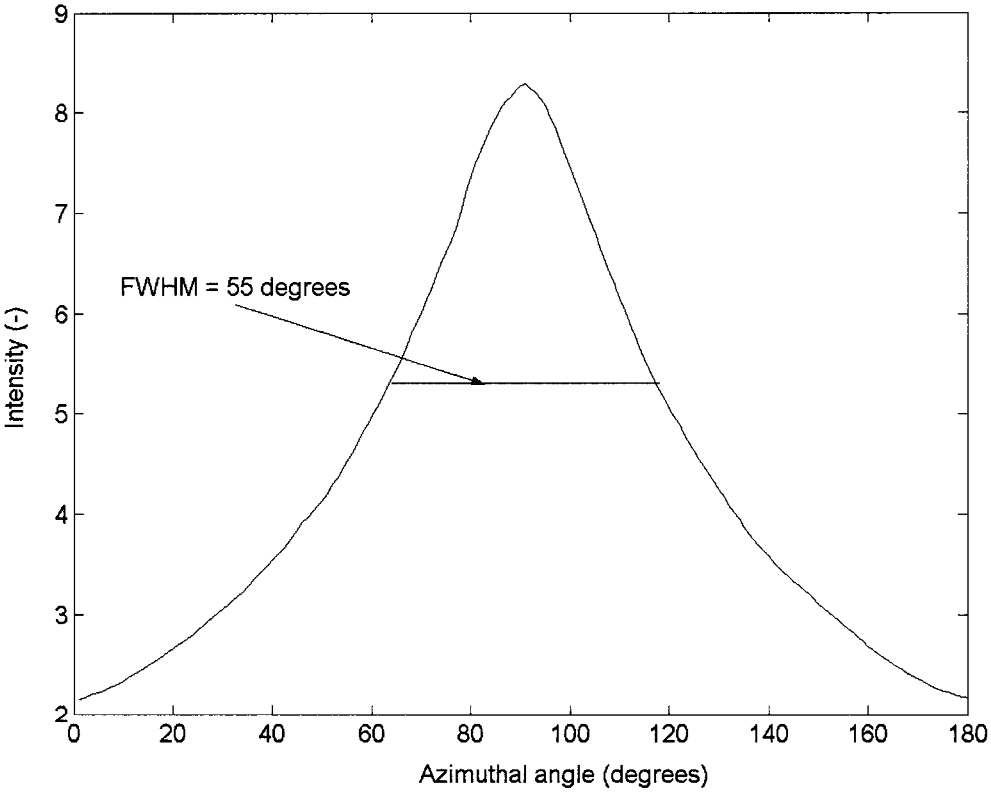

Figure 5.13. Vertical slice through the image in Figure 5.12. The estimated angular resolution is 55° FWHM.

for the source to side of the detector. The cause for the discrepancy between resolution of top and side images is discussed in Chapter 6. Despite the poor angular resolution, the location of the point source is correctly determined in 4π in both cases. For applications that do not require good imaging resolution, simply finding a point source may be sufficient.

The simulated intrinsic imaging efficiency (defined as the fraction of incident gamma rays that result in imageable full-energy sequences) is 4.4% for the source above the detector and 5.5% for a source to the side of the detector. The difference in efficiency is mostly due to the fact that the detector is not cubic. When a gamma ray is incident from the side there is 50% thicker material in which to undergo interactions compared with a gamma ray incident from the top. This effect alone would create nearly a 24% reduction in efficiency for a source above the detector compared with a source to the side. However, the track length of the scattered gamma rays relative to the dimensions of the detector should not be neglected. After the initial scatter, a gamma ray originally incident from the top will have a further distance in all dimensions to travel before escaping than an equivalently scattered gamma ray originally incident from the side. This will somewhat mitigate the effect of the non-cubic detector. As such, the total reduction in simulated efficiency for a source above the detector compared with a source to the side is 20%. Of course, if the detector were spherical, the efficiencies would be the same.

5.3 Maximum Likelihood Reconstruction

The goal of image reconstruction is to generate an estimate of the source distribution **f** given a set of N measured sequences. The measurements are denoted $\boldsymbol{A_1}$, $\boldsymbol{A_2}, \ldots, \boldsymbol{A_N}$, where the dimension of $\boldsymbol{A_i}$ is given by the number of parameters observed in each measurement. The task of maximum likelihood (ML) is to estimate the source distribution given a model for the detector system. The source estimate (image) is discretized into *M* pixels, and $p(A|j)$ denotes the system model, i.e. the probability of observing the measurement set *A* given a gamma ray originating from source pixel *j*.

Conventionally, the measurements *A* are also discretized. A given set of observed interaction locations and deposited energies for a measurement corresponds to one bin in $p(A|j)$. Many bins are required in order to account for all possible combinations of locations and energies; for *k* attributes in a given measurement with precision *b* measured in bits, at least 2^{kb} elements are required.[3] One research group estimated that over 2×10^{10} elements were required in the system model $p(A|j)$ *per source pixel* for their system.[4] At even 1 byte per integer value in the bin (counting up to 255 events in a single bin), the model would require nearly 20 GB of memory, which can be difficult to obtain and is certainly an inefficient way to store the data.

In list-mode, the measurements are stored in a list during acquisition. Each measured parameter is considered as a point in a continuous measurement space, and no binning of data is required. As a result, information is retained throughout the reconstruction that would otherwise be lost in the binning of positions and energies in conventional ML. The total number of memory elements required in list-mode is only *Nk*. Thus for large values of *k*, $2^{kb} >> Nk$, and list-mode reconstruction becomes much more efficient. The 4π Compton imager registers at least eight parameters per measurement: the 3-D positions of at least two interactions, plus the energies deposited at those locations. The number of detected sequences should be greater than 10^4 (see Section 5.3.2.) Thus, list-mode maximum likelihood reconstruction provides an increase in computation speed over conventional ML techniques for the 4π Compton imager.

5.3.1 List-mode maximum likelihood

The list-mode maximum likelihood equations are derived by Parra and Barrett[5]. Their notations and conventions are adopted here. Consider a source distribution $\mathbf{f} = [f_1,$

$f_2, \ldots, f_j, \ldots, f_M$], where f_j is the expected number of photons from source pixel j. Let s_j be the probability that a gamma ray from source pixel j is detected anywhere. Then, the probability of a detected gamma ray originating from source pixel j given the distribution **f** is given by Equation 5.3.

$$P(j \mid \mathbf{f}) = \frac{f_j s_j}{\sum_{n=1}^{M} f_n s_n} \tag{5.3}$$

The probability $p(A|\mathbf{f})$ of observing a measurement A due to a gamma ray that originated from anywhere in the distribution **f** is given in Equation 5.4, where $p(A|j)$ is the probability of observing a measurement A given that the gamma ray originated in source pixel j, also known as the system function or model.

$$p(\mathbf{A} \mid \mathbf{f}) = \sum_{j=1}^{M} p(\mathbf{A} \mid j) P(j \mid \mathbf{f}) \tag{5.4}$$

The goal of maximum likelihood reconstruction is to maximize the likelihood that the source estimate generated a given set of observed measurements. The log-likelihood of observing the measurements given the source distribution, $L(A_1, \ldots, A_N|\mathbf{f})$, is given in Equation 5.5.

$$L(\mathbf{A}_1, \ldots, \mathbf{A}_\mathrm{N} \mid \mathbf{f}) = \ln p(\mathbf{A}_1, \ldots, \mathbf{A}_\mathrm{N} \mid \mathbf{f}) = \sum_{i=1}^{N} \ln p(\mathbf{A}_i \mid \mathbf{f}) \tag{5.5}$$

After some algebra a detailed expression for the log-likelihood is obtained as in Equation 5.6.

$$L(\mathbf{A}_1, \ldots, \mathbf{A}_\mathrm{N} \mid \mathbf{f}) = \sum_{i=1}^{N} \ln\left(\sum_{j=1}^{M} p(\mathbf{A}_i \mid j) f_j s_j \right) - N \ln \sum_{j=1}^{M} f_j s_j \tag{5.6}$$

When the data are collected, typically the measurement time T is fixed and the number of detected sequences N becomes a random variable that is drawn from a Poisson distribution as in Equations 5.7 and 5.8.

$$P(N \mid T, \mathbf{f}) = \frac{(\lambda T)^N \exp(-\lambda T)}{N!} \tag{5.7}$$

$$\lambda = \sum_{j=1}^{M} s_j f_j \tag{5.8}$$

Then the likelihood function is calculated via the product of the independent likelihoods of observing A and N, as in Equation 5.9.

$$L(\mathbf{A}_1,\ldots,\mathbf{A}_N,N\,|\,T,\mathbf{f}) = \ln\left[p(\mathbf{A}_1,\ldots,\mathbf{A}_N\,|\,\mathbf{f})P(N\,|\,T,\mathbf{f})\right] \tag{5.9}$$

The likelihood function is then maximized with respect to the source distribution **f**. Since **f** is unknown, an iterative process must be used to determine the estimate of **f** that maximizes the likelihood of observing the given data. Various maximization procedures can be used, but the expectation-maximum technique is used most often with maximum likelihood reconstruction.

5.3.2 Expectation-maximum algorithm

The key principle for the expectation-maximum (EM) algorithm is the assumption that the observed data are incomplete and are drawn from a set of (unknown) complete data. Two assumptions are required: the source distribution is "*a priori* independent of the parameters of the missing data process, and the missing data are missing at random" [6]. The log-likelihood function of the complete data then provides all information necessary to exactly reconstruct the source distribution. However, the complete data set is unknown and it cannot be sampled. Instead, the expectation value of the log-likelihood function is calculated based on the current estimate of the source distribution and the observed data. The source distribution that maximizes the expected value of the log-likelihood then becomes the current estimate, and the process is repeated until the log-likelihood function converges or the process is artificially stopped. Thus the two steps in the EM algorithm are first a calculation of the expectation of the log-likelihood function based on the current source estimate and then a calculation of the source estimate that maximizes the calculated log-likelihood function.

Suppose the observed data is expanded by the unobserved variables z_{ij}, given in Equation 5.10. In other words, assume there are some gamma rays emitted from the source that were not detected. It is clear that z_{ij} has only one non-zero entry in each row because a gamma ray can originate from only one source pixel.

$$z_{ij} = \begin{cases} 1, & \text{if event } i \text{ originated in pixel } j \\ 0, & \text{otherwise} \end{cases} \tag{5.10}$$

The probability of observing measurement $\mathbf{z}_i$ is then determined by Equation 5.11.

$$P(\mathbf{z}_i \mid \mathbf{f}) = \sum_{j=1}^{M} p(\mathbf{z}_i \mid j) P(j \mid \mathbf{f}) = \sum_{j=1}^{M} z_{ij} P(j \mid \mathbf{f}) \tag{5.11}$$

The log-likelihood function for the complete data is then given by Equations 5.12 and 5.13, which reduces to the expression in Equation 5.14.

$$L(\mathbf{A}_1, \mathbf{z}_1, \ldots, \mathbf{A}_N, \mathbf{z}_N, N \mid T, \mathbf{f}) = \ln p(\mathbf{A}_1, \mathbf{z}_1, \ldots, \mathbf{A}_N, \mathbf{z}_N, N \mid T, \mathbf{f}) \tag{5.12}$$

$$L(\mathbf{A}_1, \mathbf{z}_1, \ldots, \mathbf{A}_N, \mathbf{z}_N, N \mid T, \mathbf{f}) = \sum_{i=1}^{N} \ln p(\mathbf{A}_i, \mathbf{z}_i \mid \mathbf{f}) + \ln P(N \mid T, \mathbf{f}) \tag{5.13}$$

$$L(\mathbf{A}_1, \mathbf{z}_1, \ldots, \mathbf{A}_N, \mathbf{z}_N, N \mid T, \mathbf{f}) = \sum_{i=1}^{N} \ln\left(\sum_{j=1}^{M} z_{ij} P(j \mid \mathbf{f}) \right) + \sum_{i=1}^{N} \ln\left(\sum_{j=1}^{M} z_{ij} p(\mathbf{A}_i \mid j) \right) + \ln P(N \mid T, \mathbf{f}) \tag{5.14}$$

Since only one element per row of z_{ij} is nonzero, the expressions inside the summation over pixel number are only nonzero for one value of j. In addition, the nonzero entries of z_{ij} are all equal to 1. This leads to the further simplification in Equation 5.15.

$$L(\mathbf{A}_1, \mathbf{z}_1, \ldots, \mathbf{A}_N, \mathbf{z}_N, N \mid T, \mathbf{f}) = \sum_{i=1}^{N} \sum_{j=1}^{M} z_{ij} \left(\ln P(j \mid \mathbf{f}) + \ln p(\mathbf{A}_i \mid j) \right) + \ln P(N \mid T, \mathbf{f}) \tag{5.15}$$

As previously stated, the unknown data z_{ij} cannot be sampled. Thus, in the expectation step of the EM algorithm, the expected value $Q(\mathbf{f} \mid \mathbf{f}^{(t)})$ of the log-likelihood function (defined in Equation 5.16) is calculated based on the measured data $\mathbf{A}_1, \ldots, \mathbf{A}_N$ and the (fixed) current estimate $\mathbf{f}^{(t)}$ of the source distribution $\mathbf{f}$, where t indicates the iteration number. The calculation involves simply replacing z_{ij} with its expected value, given in Equation 5.17.

$$Q(\mathbf{f} \mid \mathbf{f}^{(t)}) = E\left[L(\mathbf{A}_1, \mathbf{z}_1, \ldots, \mathbf{A}_N, \mathbf{z}_N, N \mid T, \mathbf{f}) \mid \mathbf{A}_1, \ldots, \mathbf{A}_N, N, \mathbf{f}^{(t)} \right] \tag{5.16}$$

$$\bar{z}_{ij}(\mathbf{f}^{(t)}) = P(j \mid \mathbf{A}_i, \mathbf{f}^{(t)}) = \frac{P(j \mid \mathbf{f}^{(t)})\, p(\mathbf{A}_i \mid j)}{\sum_{k=1}^{M} P(k \mid \mathbf{f}^{(t)})\, p(\mathbf{A}_i \mid k)} \tag{5.17}$$

After the expectation step is complete the derivative of the expected value of the likelihood is set to zero, while $\mathbf{f}^{(t)}$ is fixed.

$$\frac{\partial Q(\mathbf{f} \mid \mathbf{f}^{(t)})}{\partial f_l} = \frac{\partial}{\partial f_l} \sum_{i=1}^{N} \sum_{j=1}^{M} \bar{z}_{ij}(\mathbf{f}^{(t)}) \ln \frac{f_j s_j}{\sum_{k=1}^{M} f_k s_k} + \frac{\partial}{\partial f_l} \left[N \ln\left(T \sum_{k=1}^{M} f_k s_k \right) - T \sum_{k=1}^{M} f_k s_k \right] \tag{5.18}$$

$$\frac{\partial Q(\mathbf{f} \mid \mathbf{f}^{(t)})}{\partial f_l} = \sum_{i=1}^{N} \bar{z}_{il} s_l \left(\frac{1}{f_l s_l} - \frac{1}{\sum_{k=1}^{M} f_k s_k} \right) + \frac{N s_l}{\sum_{k=1}^{M} f_k s_k} - T s_l = 0 \tag{5.19}$$

The two inner terms in Equation 5.19 cancel because $\sum_{i=1}^{N} \bar{z}_{il} s_l = N s_l$, and Equations 5.20 and 5.21 are obtained for the update algorithm.

$$f_j^{(t+1)} = \sum_{i=1}^{N} \frac{\bar{z}_{ij}(\mathbf{f}^{(t)})}{T s_j} \tag{5.20}$$

$$f_j^{(t+1)} = \frac{f_j^{(t)}}{T} \sum_{i=1}^{N} \frac{p(\mathbf{A}_i \mid j)}{\sum_{k=1}^{M} p(\mathbf{A}_i \mid k) f_k^{(t)} s_k} \tag{5.21}$$

Thus, given any initial estimate $\mathbf{f}^{(0)}$ a new source estimate can be calculated from the system model and the sensitivity of the device. In practice only the update expression is required and the expectation and maximization steps are performed simultaneously. The initial estimate $\mathbf{f}^{(0)}$ used in this work is always a uniform field.

Some authors [4, 7, 8] have performed the expectation step on the complete data, rather than the likelihood function. Shepp and Vardi [7] have shown that this method also converges to a maximum likelihood point. However, it leads to a slightly different result for the iteration expression [4, 8] as given in Equation 5.22.

$$f_j^{(t+1)} = \frac{f_j^{(t)}}{T s_j} \sum_{i=1}^{N} \frac{p(\mathbf{A}_i \mid j)}{\sum_{k=1}^{M} p(\mathbf{A}_i \mid k) f_k^{(t)}} \tag{5.22}$$

The sensitivities s_j are moved outside the summations. (The original MLEM algorithm by Dempster, Laird, and Rubin[6]—which is nearly always cited as the original reference—uses the expectation of the likelihood function, except in the special case of exponential families where the vector of sufficient statistics is used.) It is believed that there may be some small differences in the two methods, especially for systems in which the sensitivity widely varies from pixel to pixel. Wilderman *et al.*[9] calculate sensitivity based on the solid angle subtended by the scatter detector and the probability of the gamma ray interacting inside it. Since the 4π imager is nearly a cube, the sensitivity should not vary significantly for sources from different image pixel locations, and the difference between the two EM algorithms should not be significant.

The EM algorithm has several advantages over other maximization procedures. Dempster, Laird, and Rubin[6] showed that the likelihood after each step is nondecreasing, meaning that successive iterations lead to a source estimate that is at least as likely as the previous estimate to have produced the observed data. Any positive initial source estimate automatically results in non-negative subsequent estimates[8]. Furthermore, under some reasonable conditions (such as $N \geq M$: the number of observed sequences is greater than or equal to the number of image pixels) the log-likelihood function is strictly convex and necessarily has a single global maximum[5]. In this case, it has been proven that successive iterations of the expectation and maximization steps will lead to global convergence[8]. Convergence is achieved when the global maximum of the likelihood function has been reached. Lange and Carson proved that the image obtained after convergence is independent of the choice of initial estimate $\mathbf{f}^{(0)}$[8]. In practice, image reconstruction is rarely computed through all the iterations required to achieve convergence, and stopping rules and other justifications for early termination of the algorithm are often applied (see Section 5.3.4).

5.3.3 Weighted list-mode maximum likelihood

Wilderman *et al.*[9] have proposed an analytical system model for list-mode maximum likelihood of Compton scatter images. A value for $P(A|j)$ that can be calculated on the fly is advantageous and preferable to a system matrix that bins the data (resulting in lost information) and requires dedicated memory or a table look-up (resulting in lengthy reconstruction times). The probability of observing a given measurement $A=[E_0,E',E'',...,r_{01},r_{12},r_{23},...]$ given a gamma ray incident from pixel j is then given by Equation 5.23.

$$P(\mathbf{A}\,|\,j)=\exp(-\sigma_t(E_0)r_{01})\frac{d\sigma_C}{d\Omega}\exp(-\sigma_t(E')r_{12}) \tag{5.23}$$

where $\sigma_t(E)$ is the total absorption cross section at energy E, E_0 and E' are the initial and scattered gamma-ray energies, respectively, r_{01} is the attenuation distance between the source pixel and the first interaction, r_{12} is the attenuation distance between the first and second interactions, and $d\sigma_C/d\Omega$ is differential Compton cross section, which is approximated by the Klein-Nishina cross section divided by r_{12}^2. Thus the system model is the product of the probabilities of survival of the initial gamma ray to the first interaction point, scatter at the observed angle θ, and survival of the scattered gamma ray to the second interaction location. The Klein-Nishina cross section is given in Equation 5.24 [10], where $\alpha=E_0/m_ec^2$ is the ratio of the initial gamma-ray energy to the rest mass energy of an electron.

$$\frac{d\sigma_C}{d\Omega}\propto\left[\frac{1}{1+\alpha(1-\cos\theta)}\right]^2\left(\frac{1+\cos^2\theta}{2}\right)\left[1+\frac{\alpha^2(1-\cos\theta)^2}{(1+\cos^2\theta)[1+\alpha(1-\cos\theta)]}\right] \tag{5.24}$$

In the above calculation, θ is the angle of scatter that would be observed if the gamma ray were incident from pixel j and interacted at the measured locations r_1 and r_2.

It is clear from the above discussion that higher probabilities are assigned to measurements in which the interaction distances are small. Furthermore, image pixels that lead to smaller apparent Compton angles, where the Klein-Nishina formula is peaked over the energy range of interest for Compton imagers, are also assigned a higher probability. Thus the product $f_jP(A|j)$ is the forward projection and should produce the measurements most likely to be observed. However, the most likely measurements are also those with the most uncertainty. Small distances between interactions result in very large geometric uncertainties. Forward scattered gamma rays lose a small fraction of their energies, leading to large energy uncertainties as well. Thus, the reconstructed angular uncertainties for the most likely sequences will be large.

Ideally, the sequences leading to high angular uncertainty should be weighted less than those that lead to low uncertainty. A more accurate knowledge of the source location should be possible through such weighting. To determine a proper weighting system, it is first necessary to revisit conventional maximum likelihood estimation.

In the non-list-mode MLEM reconstruction, the update algorithm is given by Equation 5.25[9], where Y_i is the number of times (binned) measurement $\boldsymbol{A}_i$ is observed. Thus, the list-mode and conventional algorithms differ by a factor of Y_i in the numerator of the summation over events. In list-mode each measurement is observed only once due to the continuous measurement space, and Y_i is essentially set to 1.

$$f_j^{(t+1)} = \frac{f_j^{(t)}}{Ts_j} \sum_{i=1}^{N} \frac{Y_i p(\mathbf{A}_i \mid j)}{\sum_{k=1}^{M} p(\mathbf{A}_i \mid k) f_k^{(t)}} \tag{5.25}$$

Using Y_i to weight sequences appropriately seems an obvious choice. As given in Equation 5.26, the Y_i are the inverse of the estimated angular uncertainties $\Delta\theta_i$, which are calculated as the quadratic sum of the energy and position components discussed in Section 5.2.3.

$$Y_i = \frac{1}{\Delta\theta_i} \tag{5.26}$$

The image must then be normalized to preserve absolute source intensity information, as in Equation 5.27.

$$f_j^{(t+1)} = \frac{N f_j^{(t)}}{Ts_j \sum_{i=1}^{N} (\Delta\theta_i)^{-1}} \sum_{i=1}^{N} \frac{(\Delta\theta_i)^{-1} p(\mathbf{A}_i \mid j)}{\sum_{k=1}^{M} p(\mathbf{A}_i \mid k) f_k^{(t)}} \tag{5.27}$$

5.3.4 Convergence and early termination

In practice, iterations of the MLEM algorithm are usually terminated before convergence is reached. Images resulting from convergence of the likelihood function are noisy because the data creating them is noisy[11]. Veklerov, Llacer, and Hoffman state that because of the inherent statistical processes involved in radiation emission and measurement “a source distribution identical to the recovered image could not have possibly generated the data[12].” When Equation 5.22 or 5.27 is iterated until the maximum likelihood solution is reached, the resulting image becomes unacceptably noisy. Typically, the reconstruction process is stopped while the image is still relatively smooth.

One possible way to determine the proper number of iterations is to monitor the progress of the reconstructed image with increasing iterations. When the image begins to degrade rather than improve, the user could stop the reconstruction process. This is a dissatisfying method for early termination because it is user dependent. It is preferable to use a statistical or at least disciplined method for determining the stopping point. One simple method involves simply terminating the reconstruction after a given number of iterations. However, the rate of convergence depends upon both the number of observed events in the detector and the spatial distribution of the source[13]. Therefore, using the same number of iterations for all source distributions will yield widely variable results. It is necessary to determine an independent, case-specific stopping criterion. Several such methods have been proposed.

In 1988, Veklerov, Llacer, and Hoffman proposed a method based on the Poisson nature of radiation measurements[12]. After each iteration, the hypothesis that the observed data are a Poisson sample drawn from the source distribution given in the image is tested. If the hypothesis cannot be rejected, then the iterations are stopped. For a small number of iterations, the image does not sufficiently fit the observed data; for a large number of iterations, the image becomes too noisy to have generated the data. In this way, the reconstructed image passes through a region of acceptable images which they call "feasible images"[14]. For computer generated Poisson random data the authors have observed that the iterative process consistently passes through such a region. Choosing any of the images in the region is acceptable, although with the test outlined above the first image to satisfy the criterion is chosen.

The authors observed for real PET imaging data that a feasible image was never found. With the computer generated data the same system function is used to perform the generation and reconstruction of the data; this is not necessarily the case for real imaging data. The system function used in the maximum likelihood estimation has some uncertainty associated with it. This observation led to a weaker stopping criterion based on the variance of the observed data and the reconstructed image[14]. This weaker stopping criterion was found to be more robust and led to acceptable images from real PET data.

Kadrmas uses a different statistic to test the nearness of the observed data with the predicted data given the current image estimate[15]. He assumes that the difference between the two sets of data should be Gaussian distributed. Then a two-tailed *t*-test can be performed on the data. When a given pixel in the image demonstrates a statistically significant difference between the observed and predicted data, its value is updated using Equations 5.22 or 5.27. This is called "spatially adaptive updating," and results in an effective regularization of the reconstruction.

Another possible stopping criterion is to choose a solution near the maximum likelihood solution. Vardi, Shepp, and Kaufman[16] have suggested calculating the change in the likelihood value between iterations, and terminating the reconstruction when the difference is small (i.e. convergence is near). Thus, a sort of diminishing returns approach can be used.

Kontaxakis and Tzanakos proposed a different stopping criterion based on the factor that is multiplied by $f_j^{(i)}$ in Equation 5.25[17]. This factor approaches 1.0 as the image approaches the maximum likelihood estimate. The authors state that a value of 0.8 produces images that are close to the optimal image, "independently of image shape, the number of counts in the image, and the system configuration." The optimal image is defined as having the minimum RMS error and also minimizing a χ^2 distribution similar to that used by Veklerov. There is no mention of the dependence on the initial source estimate.

A reconstruction method which maximizes the likelihood and then terminates the iterations before that maximum likelihood solution is obtained can be conceptually difficult to accept, regardless of the way in which the stopping point is chosen[11]. The maximum likelihood image does not depend on the choice of initial source estimate, but if the reconstruction is halted early the independence will no longer hold. As a result, there is still much debate about the use of maximum likelihood estimators for reconstructing Compton imaging, emission tomography, and PET imaging data. Using a stopping criterion with MLEM may not be the theoretically optimal reconstruction method, but it has been shown via simulations and experiments to produce low-noise, high-resolution images.

In this work, the controversy of using MLEM without requiring full convergence is acknowledged. To limit the bias introduced by early termination, the initial source estimate used here is always a uniform field. Further, although it is recognized that a scientifically defensible termination criterion is important, none of the above termination criteria is implemented in this work. A constant number of iterations is always performed on the simulated and measured point source data. The effect of the number of iterations on the image of a point source is demonstrated in the next section.

5.3.5 Performance of maximum likelihood reconstruction

The simulated data used previously for reconstructing backprojection images were used with maximum likelihood reconstruction. Figure 5.14 shows the image of a 662 keV source located along the x-axis after 1, 5, 10, and 20 iterations of list-mode maximum likelihood. Figure 5.15 shows the same data reconstructed using weighted list-mode maximum likelihood. The weighted method converges faster than the traditional method. Figure 5.16 provides a comparison of the two methods in terms of the central slice of the image obtained after 10 iterations. The traditional method yields an angular resolution of 18° FWHM, whereas the weighted method improves this to 16° FWHM. It

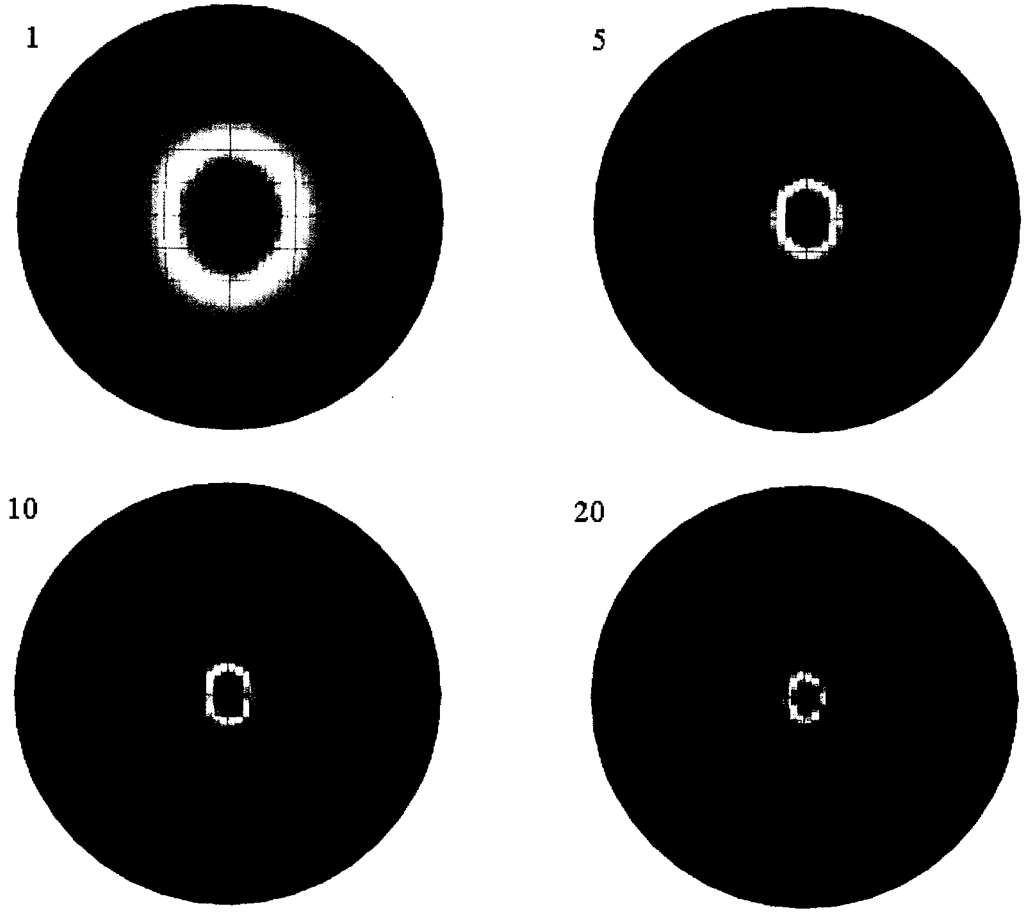

Figure 5.14. Images of a simulated 662 keV point source reconstructed using MLEM after 1, 5, 10, and 20 iterations.

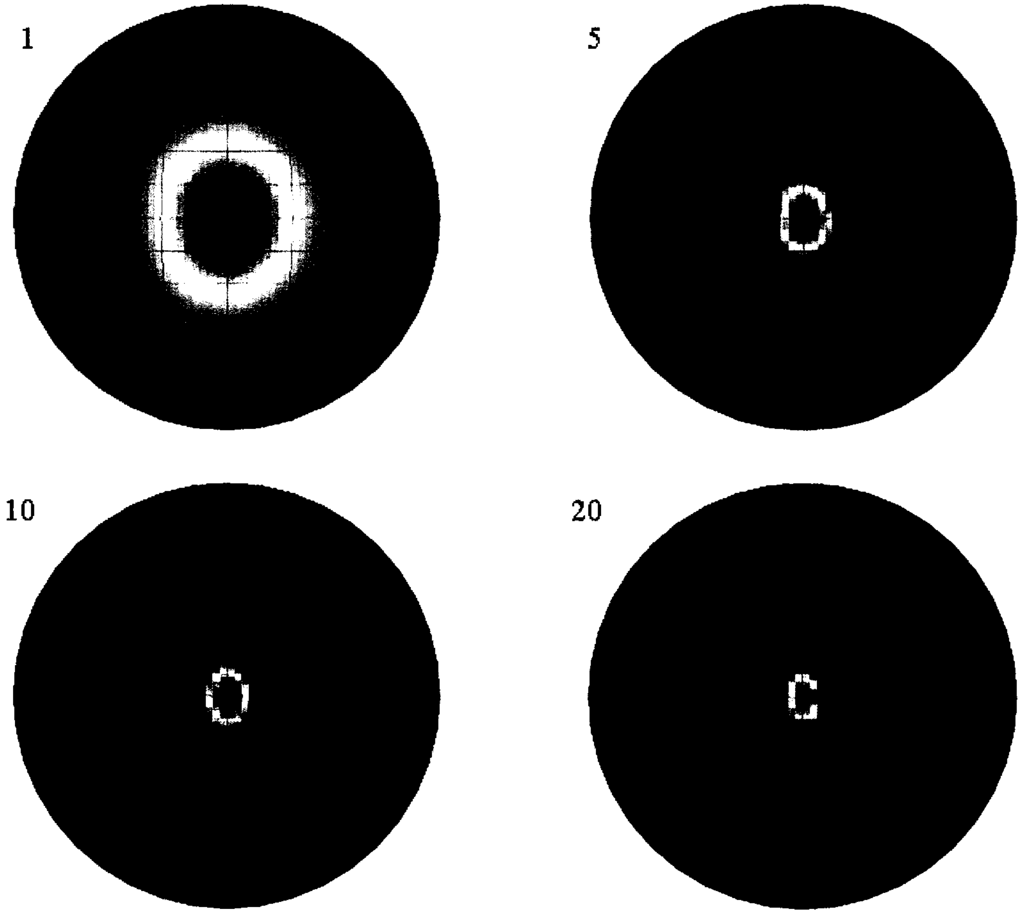

Figure 5.15. Images of a simulated 662 keV point source reconstructed using WMLEM after 1, 5, 10, and 20 iterations.

would take 15 total iterations of traditional MLEM reconstruction in order to obtain the same angular resolution as 10 iterations of weighted MLEM.

Determining the number of iterations is important. The FWHM of the central slice of the image as a function of iteration number for the traditional and weighted maximum likelihood reconstruction methods is shown in Figure 5.17. As the iterations progress, the angular resolution improves from 53° after 1 iteration to 13° FWHM after 20 iterations of WMLEM, while the traditional MLEM improvement is from 53° to 15°. The rate of improvement diminishes with increasing iteration number, leading to the exponential

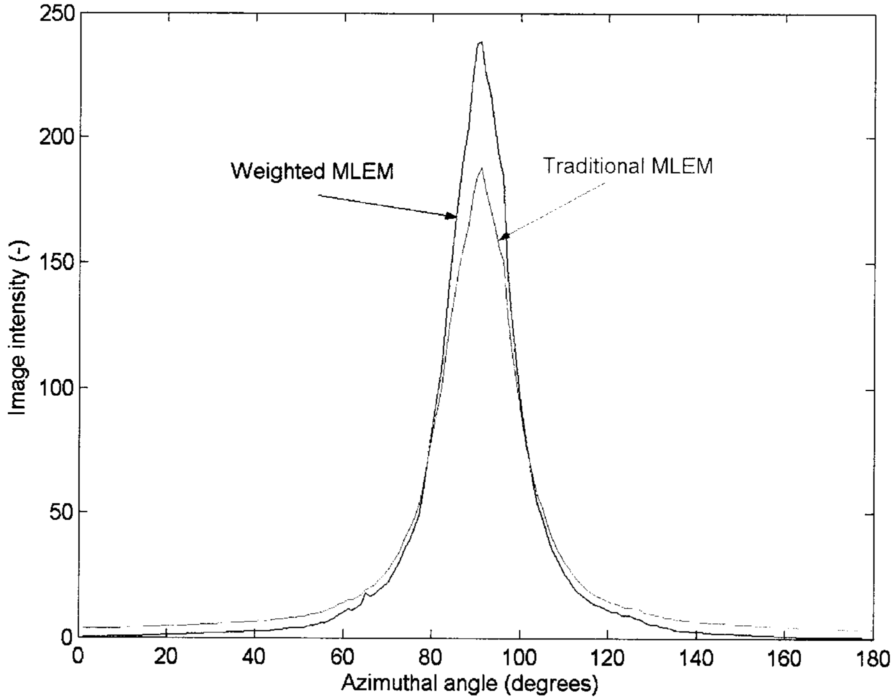

Figure 5.16. Comparison of the central slices of images calculated with traditional and weighted maximum likelihood reconstruction after 10 iterations for a simulated 662 keV point source.

shape observed. If a statistically defensible convergence criterion is not being used, it is necessary to make a value judgment on the improvement in the image compared with the reconstruction time. The speed of the maximum likelihood reconstruction program is approximately 9.6 sequences per second per iteration on a personal computer with a 1.1 GHz Pentium III processor. With a minimum requirement of 32,400 sequences (the number of sequences must be greater than or equal to the number of pixels in the 180×180 image, as stated in Section 5.3.2), each iteration requires a minimum of 56 minutes. Because the improvement in angular resolution between 10 and 20 iterations is only 3° with the weighted MLEM method, the improvement in the image is not considered to be worth the extra 10 hours of computation time. For all weighted MLEM reconstructed images in this work, a total of 10 iterations are performed.

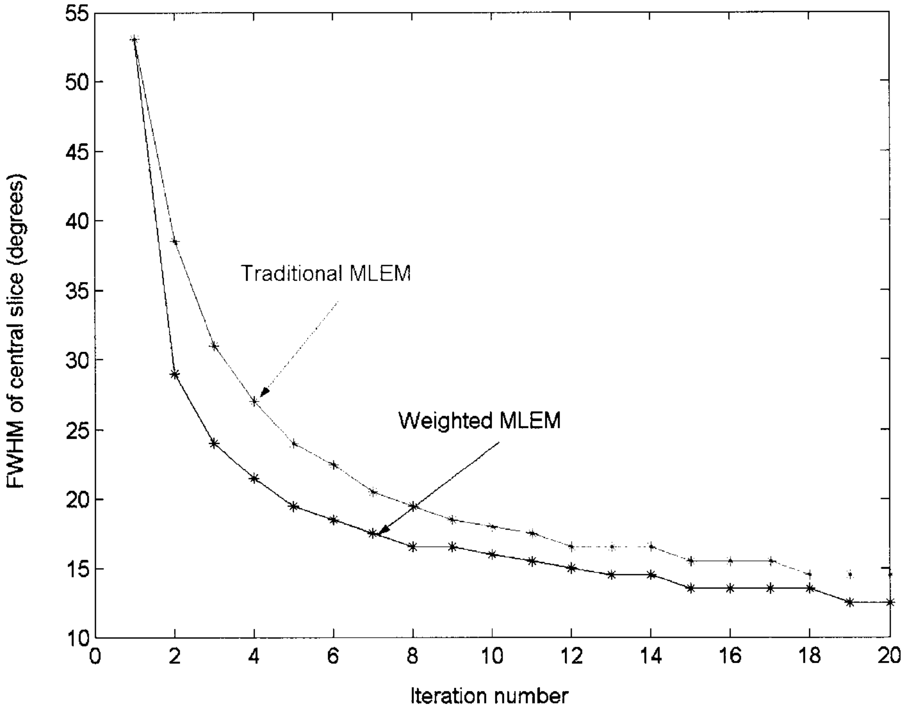

Figure 5.17. FWHM of the central slice of the image as a function of iteration number of simulated 662 keV source reconstructed using WMLEM. The angular resolution improves with iteration number.

Requiring at least 32,400 sequences can be prohibitive in some applications. It may require counting for a long time or reducing the number of pixels in the image (resulting in a smaller required number of sequences) in order to perform maximum likelihood reconstruction. In reality the images are improved relative to backprojection even if only 1000 sequences are used with the 180×180 image surface, and it may be tempting to use MLEM or WMLEM for low-count imaging measurements. One must be careful, however, because global convergence is no longer ensured with a small number of sequences.

5.4 References

[1] S. J. Wilderman, W.L. Rogers, G.F. Knoll, J.C. Engdahl, "Fast algorithm for list mode back-projection of Compton scatter camera data," *IEEE Transactions on Nuclear Science*, vol. 45, pp. 957-962, 1998.

[2] R. C. Rohe, M.M. Sharfi, K.A. Kecevar, J.D. Valentine, C. Bonnerave, "The spatially-variant backprojection point kernel function of an energy-subtraction Compton scatter camera for medical imaging," *IEEE Transactions on Nuclear Science*, vol. 44, pp. 2477-2482, 1997.

[3] H. H. Barrett, T. White, L.C. Parra, "List-mode likelihood," *J. Opt. Soc. Am.*, vol. A14, pp. 2914-2923, 1997.

[4] S. J. Wilderman, N.H. Clinthorne, J.A. Fessler, W.L. Rogers, "List-mode likelihood reconstruction of Compton scatter camera images in nuclear medicine," *IEEE Nuclear Science Symposium Conference Record*, pp. 1716-1720, 1999.

[5] L. Parra, H.H. Barrett, "List-mode likelihood: EM algorithm and image quality estimation demonstrated on 2-D PET," *IEEE Transactions on Nuclear Science*, vol. 17, pp. 228-235, 1998.

[6] A. P. Dempster, N.M. Laird, D.B. Rubin, "Maximum likelihood from incomplete data via the EM algorithm," *Journal of the Royal Stastistical Society*, vol. B39, pp. 1-38, 1977.

[7] L. A. Shepp, Y. Vardi, "Maximum likelihood reconstruction for emission tomography," *IEEE Transactions on Nuclear Science*, vol. 1, pp. 113-122, 1982.

[8] K. Lange, R. Carson, "EM Reconstruction algorithms for emission and transmission tomography," *Journal of Computer Assisted Tomography*, vol. 8, pp. 306-316, 1984.

[9] S. J. Wilderman, J.A. Fessler, N.H. Clinthorne, J.W. LeBlanc, W.L. Rogers, "Improved modeling of system response in list mode EM reconstruction of Compton scatter camera images," *IEEE Transactions on Nuclear Science*, vol. 48, pp. 111-115, 2001.

[10] G. F. Knoll, *Radiation Detection and Measurement*, 3rd ed. New York: John Wiley & Sons, Inc, 2000.

[11] L. Shepp, "From convolution algorithms to maximum likelihood," *IEEE Nuclear Science Symposium Conference Record*, pp. 1441-1444, 1990.

[12] E. Veklerov, J. Llacer, E.J. Hoffman, "MLE reconstruction of a brain phantom using a Monte Carlo transition matrix and a statistical stopping rule," *IEEE Transactions on Nuclear Science*, vol. 35, pp. 603-607, 1988.

[13] T. Hebert, R. Leahy, M. Singh, "Fast MLE for SPECT using an intermediate polar representation and a stopping criterion," *IEEE Transactions on Nuclear Science*, vol. 35, pp. 615-619, 1988.

[14] J. Llacer, E. Veklerov, "Feasible images and practical stopping rules for iterative algorithms in emission tomography," *IEEE Transactions on Nuclear Science*, vol. 8, pp. 186-193, 1989.

[15] D. J. Kadrmas, "Statistically regulated and adaptive EM reconstruction for emission computed tomography," *IEEE Transactions on Nuclear Science*, vol. 48, pp. 790-798, 2001.

[16] Y. Vardi, L.A. Shepp, L. Kaufman, "A statistical model for positron emission tomography (with discussion)," *Journal of the American Statistical Association*, vol. 80, pp. 8:37, 1985.

[17] G. N. Kontaxakis, G.S. Tzanakos, "Practical application of a new stopping criterion for the EM-MLE image reconstruction for PET," *Proceedings of the 18th Annual International Conference of the IEEE Engineering in Medicine and Biology Society*, pp. 848-849, 1996.

CHAPTER 6

FACTORS THAT DEGRADE IMAGING EFFICIENCY AND RESOLUTION OF THE 4π COMPTON IMAGER

6.1 Introduction

There are several factors that can degrade the image quality or efficiency of the 4π Compton imager. Some of these are physics related, such as Doppler broadening or the occurrence of pair production or coherent scattering. Others are caused by the detector system itself. The geometry of the anode structure, which allows multiple interactions to occur under a single pixel, reduces the observed number of events in a sequence. Charge sharing between pixels can have the opposite effect and make one interaction appear as multiple events. The anode threshold reduces the efficiency of the imager by requiring at least 100 keV be deposited in each event. Furthermore, the dynamic range of the ASICs limits the observable energies to less than 1 MeV with the VAS2/TAT2 system and 1.6 MeV with VAS3/TAT3 system. In addition, the imaging reconstruction methods can cause degradation in the efficiency and resolution of the imager. The techniques used for reconstructing sequence orders limit the observable scatter angles and introduce artifacts in the image. Finally, there is some anisotropy in the backprojection image, such that an image of a source located above the detector appears different than a source to the side. The effects of these phenomena on the performance of the Compton imager are tested using Monte Carlo simulations (see Appendix). Finally, the imaging resolution and efficiency are predicted.

6.2 Physics Processes

6.2.1 Doppler broadening

The Compton scatter formula (given in Chapter 1) was used for determining the sequences order of three or more events (as described in Chapter 4) and for calculating the opening angle of the backprojection cone (as in Chapter 5). This formula is derived under the conditions that the electron is unbound and at rest. However, these assumptions are typically false. The impact of electron binding and motion is discussed in this section.

The assumption of free electrons has very little effect on Compton imaging. The effect of including the binding energy is to restrict Compton scatter to only those electrons whose binding energy can be overcome by the energy deposited in the scatter event. A reduction in the electron shell cross section results, and the electron kinetic energy is reduced by the binding energy of the shell. A deexcitation x-ray is emitted from the atom with an energy equal to the binding energy. In CdZnTe, the highest energy shell is only 31.8 keV. With pixel sizes of 1 mm very little x-ray escape is predicted, and the total energy lost by the gamma ray is same as the total energy deposited under the pixel from the initial ejected electron and the absorption of the x-ray. In this way, the energy observed under one pixel is equal to the recoil electron energy calculated using the Compton scatter formula.

The momentum of the electron before the scatter, on the other hand, has a much more significant effect on Compton imaging. The Compton scatter formula predicts a one-to-one relationship between the scatter angle and the scattered gamma-ray energy. If the finite electron momentum is included, for a fixed scatter angle the scattered gamma-ray energy will deviate from that predicted by the Compton scatter formula. The relationship between the initial gamma-ray energy E_0, scattered gamma-ray energy E', the scatter angle θ, and the electron momentum in the scatter plane p_z is given in Equation 6.1[1, 2].

$$p_z = -mc\frac{E_0 - E' - E_0E'(1-\cos\theta)/mc^2}{\sqrt{E_0^2 + E'^2 - 2E_0E'\cos\theta}} \tag{6.1}$$

If the initial electron momentum were known, then Equation 6.1 could be used in place of the Compton scatter formula to calculate the precise scatter angle. However, the initial electron momentum cannot be known *a priori*. It may be possible in some detector designs to measure the electron momentum after the scatter and deduce the initial momentum from the measured energies, but this is not possible in the CdZnTe detector used in this work. As a result, there is no recourse except to use the Compton scatter formula given in Chapter 1 and account for the additional uncertainty due to the motion of the electron in the calculated scatter angle.

The electron momentum vector can be oriented in any direction. In some scatters it will have an additive effect, increasing the scattered gamma-ray energy; in others it will reduce the scattered gamma-ray energy. The result is a distribution of possible energies centered about the value predicted by the Compton scatter formula. Similarly, for a fixed deposited energy the actual Compton scatter angle will also vary about the mean predicted value. This is called "Doppler broadening."

The effect of Doppler broadening is to degrade the angular resolution of the instrument. Doppler broadening is most severe for high electron momentum, which occurs in materials with high atomic numbers. Figure 6.1 shows the scattered gamma-ray energy distribution in several detection materials for a 90° scatter of 662 keV photons. Shown in Figure 6.2 is the scatter angle distribution for a scattered gamma-ray energy of 288 keV (corresponding to 90° scatter). These distributions are calculated analytically using Equation 6.1 and the Hartree-Fock Compton profiles[3], using the method described by Ribberfors and Berggren[2]. The Compton profile for each element is the average of the profiles for each atomic shell weighted by the number of electrons in the

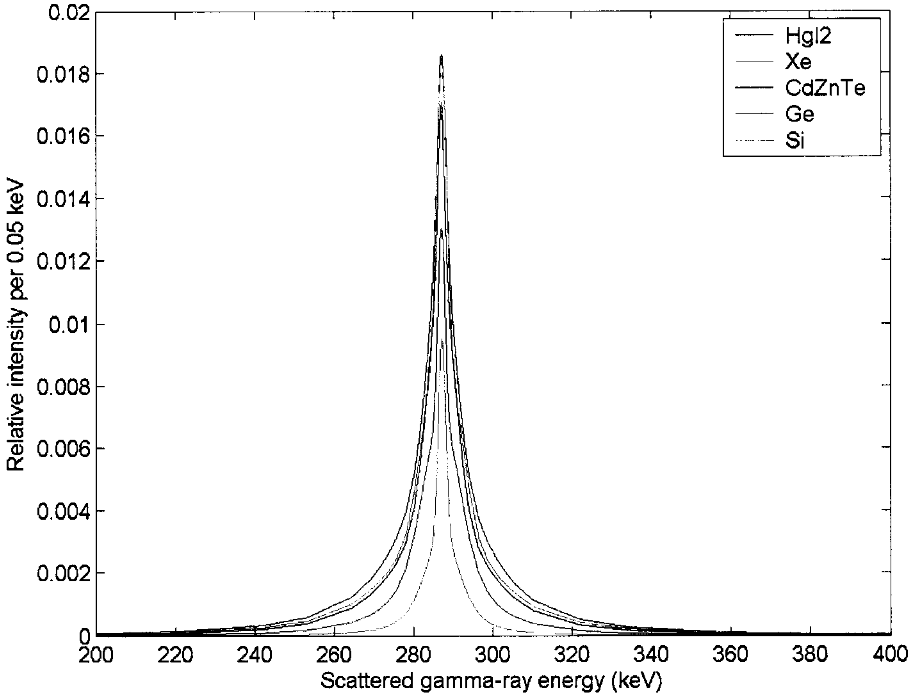

Figure 6.1. Scattered gamma-ray energy distribution due to Doppler broadening of a 662 keV photon at 90° in selected detector materials.

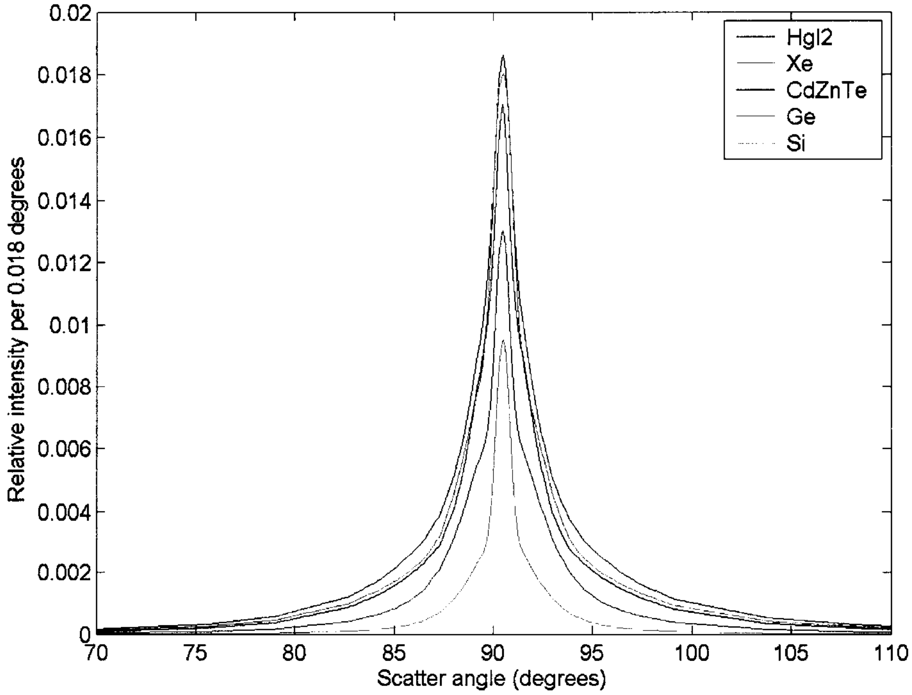

Figure 6.2. Scatter angle distribution due to Doppler broadening of a 662 keV photon depositing 374 keV in selected detector materials.

shell, and the total $Cd_{0.9}Zn_{0.1}Te_{1.0}$ and HgI_2 profiles are the averages of the elemental profiles weighted by the atom fractions.

Due to their similar atomic numbers, Doppler broadening in CdZnTe and Xe is about the same. HgI_2 has a slightly wider profile due to the 80 protons present in the Hg nucleus. With low atomic numbers Ge and Si demonstrate less variation in the scattered gamma-ray energy. Also, the shape of the distribution for each material is dependent upon the filled electron levels in the atom. For example, consider the shapes of the curves for Ge and Xe in Figure 6.2. All electron levels through the *5p* shell are filled in Xe, whereas Ge has a partially filled *4p* shell. The Ge curve has wide "shoulders" from 88 – 92°; this phenomenon is not observed in the Xe curve. This is clear evidence that the shape of the Doppler broadened distribution varies by the element involved in the scatter.

Also evident from the distributions in Figure 6.1 and 6.2 is that the Doppler broadening is not a Gaussian effect. Although the Compton profile of each electron shell is Gaussian, the total atomic distribution is the weighted sum of the profiles and not the convolution of them. As such, using a full-width at half-maximum (FWHM) value to estimate the uncertainty due to Doppler broadening will greatly underestimate the effect. In addition, because the profiles differ for each element the FWHM will result in a variable measure of the Doppler broadening effect. In a Gaussian distribution, 68% of the distribution is contained within the FWHM. For the non-Gaussian distributions from Doppler broadening a 68% containment value can also be reported[4]. Fig 6.3 shows the estimated energy uncertainty due to Doppler broadening reported as the FWHM and as the 68% containment value as a function of scatter angle for CdZnTe. Figure 6.4 shows the estimated angular uncertainty due to Doppler reported in the same manner. The choice of uncertainty metric is somewhat arbitrary, but it is clear that the FWHM will underestimate the Doppler broadening contribution. As such, a 68% containment value for the angular uncertainty due to Doppler will be considered equivalent to the FWHM angular uncertainty values reported for the position and energy resolution contributions.

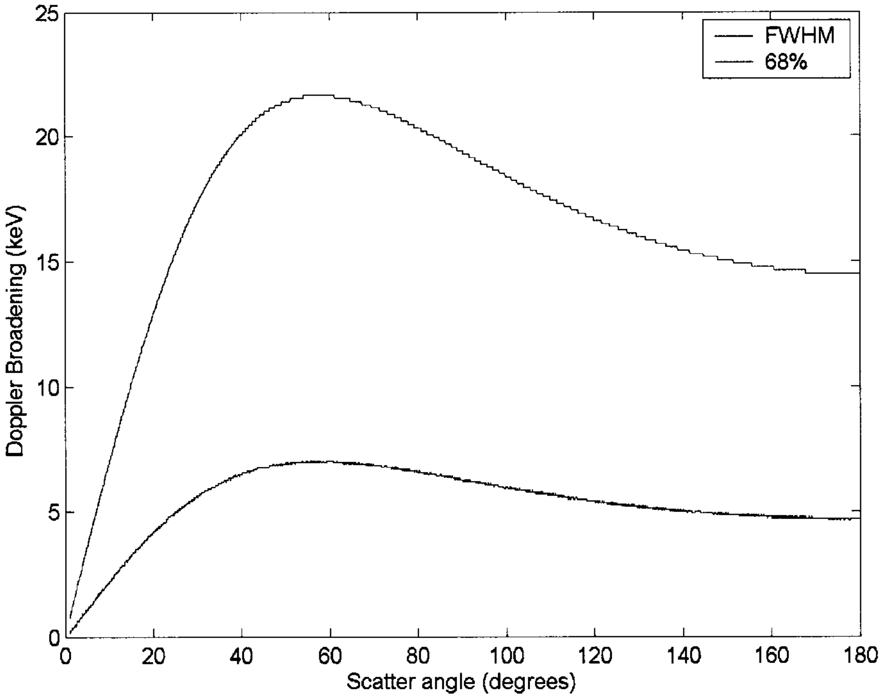

Figure 6.3. Doppler broadening in CdZnTe of observed energies as a function of scatter angle for 662 keV photons measured using FWHM and 68% containment.

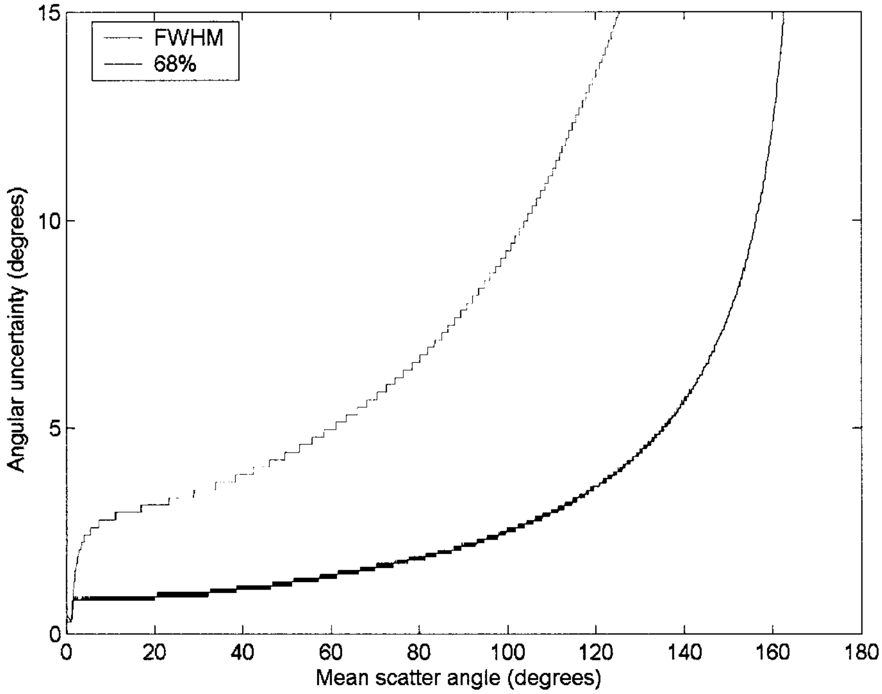

Figure 6.4. Angular uncertainty in CdZnTe due to Doppler broadening as a function of mean scatter angle for 662 keV photons measured using FWHM and 68% containment.

The 68% containment curve in Figure 6.4 demonstrates that the minimum angular uncertainty achievable with CdZnTe is at least several degrees, even if the scatter angles are limited.

6.2.2 Pair production

Pair production is the conversion of a gamma-ray to an electron-positron pair. Sequences involving pair production are not useful for Compton imaging. According to Geant4[5] simulations (see Appendix), pair production occurs in the detector in 19% of the two-event sequences at 2.5 MeV. (At 1.5 MeV, it occurs in less than 2.5% of two-event sequences.) A two-pixel sequence involving pair production includes the conversion event plus the scatter or absorption of one of the annihilation photons. If the annihilation photon is absorbed, then the presence of the 511 keV energy deposition can indicate that a pair production occurred. The sequence can then be rejected. Only 23% of two-pixel pair production sequences at 2.5 MeV involve the absorption of an annihilation photon. Thus, in 15% of two-pixel tracks, pair production is not identifiable and will contribute to the image background.

In three-event sequences the fraction of pair production events for 2.5 MeV gamma rays incident on the detector increases to 28%. In over half (53%) of these sequences, one of the annihilation photons deposits full energy. These can be identified. Thus, 13% of three-event sequences will result from unidentifiable pair production processes and will be reconstructed incorrectly.

All full-energy pair production sequences are identifiable because both annihilation photons are absorbed. Clearly, if the gamma-ray energy is known and only full-energy sequences are imaged, then unidentifiable pair production sequences from this gamma-ray energy cannot contribute to the image. All unidentifiable sequences deposit only partial energy. However, if either the gamma-ray energy is unknown or

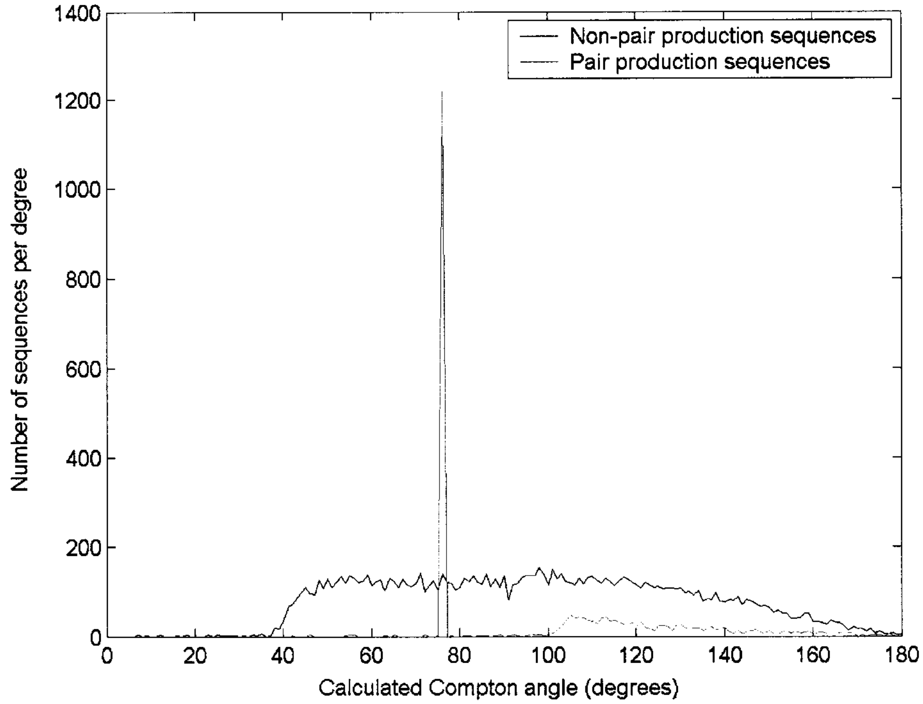

Figure 6.5. Comparison of calculated Compton angle distributions for simulated pair production and non-pair production two-pixel sequences at 2.5 MeV. The spike corresponds to identifiable sequences (511 keV is deposited).

multiple gamma-ray energies are present in the source spectrum, then unidentifiable pair production events will contribute to the background of the image. The pair production contribution to the image is not necessarily diffuse.

When unidentifiable pair production sequences occur (or if no attempt is made to discard pair production sequences) then the sequence will be reconstructed according to the rules outlined in Chapter 4 and then imaged using the process described in Chapter 5. A Compton scatter angle will be erroneously calculated. The distribution of calculated Compton angles for pair production and non-pair production two-pixel sequences is given in Figure 6.5. The low-angle cutoff near 40° in the non-pair production distribution is due to the sequence reconstruction method for two-pixel events, as discussed later in Section 6.4.1. The spike in the pair production distribution is due to sequences in which one of the annihilation photons is directly absorbed. (These can be identifiable.) In fact,

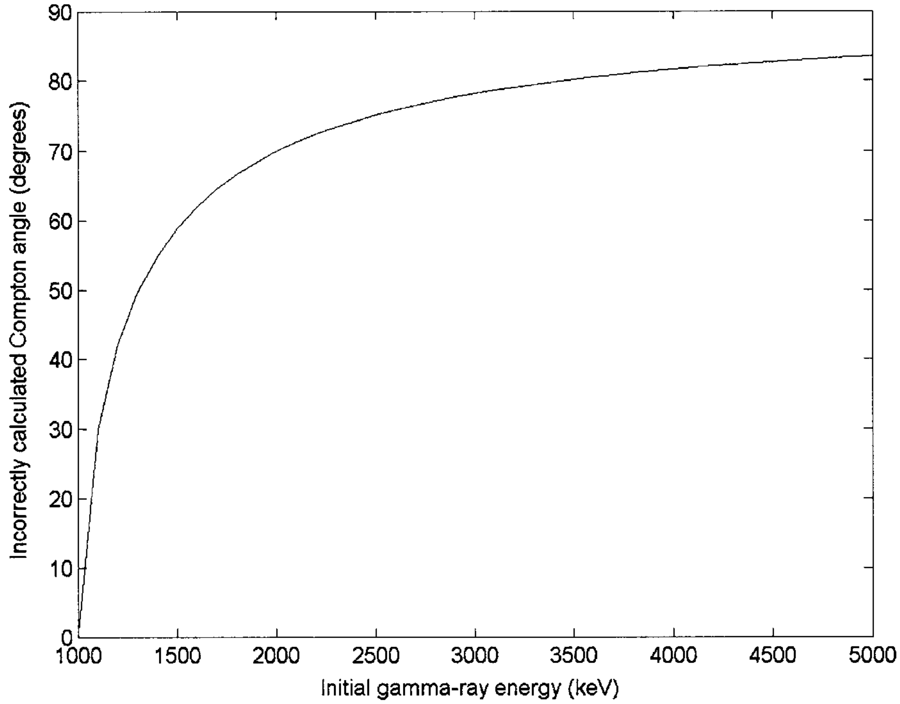

Figure 6.6. Compton angles (incorrectly) calculated for simulated two-pixel sequences in which pair production is followed by the absorption of an annihilation photon. This determines the location of the spike in Figure 6.5 for 2.5 MeV.

the location of the spike yields information about the initial gamma-ray energy. Figure 6.6 shows for gamma-ray energies up to 5 MeV the location of spike in the distribution of calculated Compton angles. The remainder of the pair production distribution in Figure 6.5 consists of sequences in which the photon is scattered and escapes, depositing a maximum of 340 keV in a backscatter event. In this case, the total energy deposited in the detector is (2500 – 1022) + 340 = 1819 keV. The pair production event deposits more energy than the photon scatter event, and is therefore decided to be the first event according to the two-pixel sequencing technique discussed in Chapter 4. The calculated Compton angle for this sequence is then 102°, corresponding to the minimum angle of the broad pair production distribution in Figure 6.5.

The unidentifiable pair production sequences can be eliminated, then, by excluding calculated Compton scatter angles above a given threshold. Figure 6.7 shows

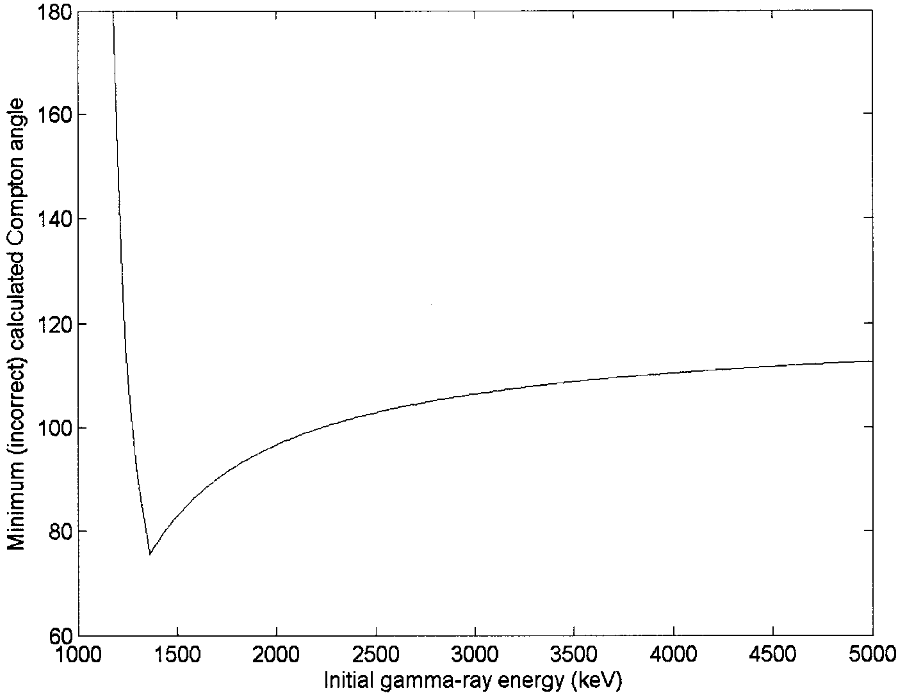

Figure 6.7. Minimum (incorrect) calculated Compton angle for simulated unidentifiable two-pixel pair production sequences as a function of incident gamma-ray energy. Excluding sequences with scatter angles above this threshold will eliminate all otherwise unidentifiable pair production sequences, but will also reduce imaging efficiency.

for gamma-ray energies up to 5 MeV the apparent minimum scatter angle due to unidentifiable pair production events. There is a sharp spike in the function at 1362 keV. This is the gamma-ray energy at which the energy deposited in the backscatter of an annihilation photon is greater than the energy deposited in the pair production event itself. Thus, the sequence order switches, and the backscatter is considered to occur first. By excluding all sequences with a calculated Compton angle above 80°, it is possible to eliminate all otherwise unidentifiable pair production sequences. Or, given that pair production does not frequently occur at the lower energies, the threshold could be increased to 90° or even 100°. Of course, this will also eliminate useful events and reduce the efficiency of the system. If sequences with a calculated scatter angle greater than 100°

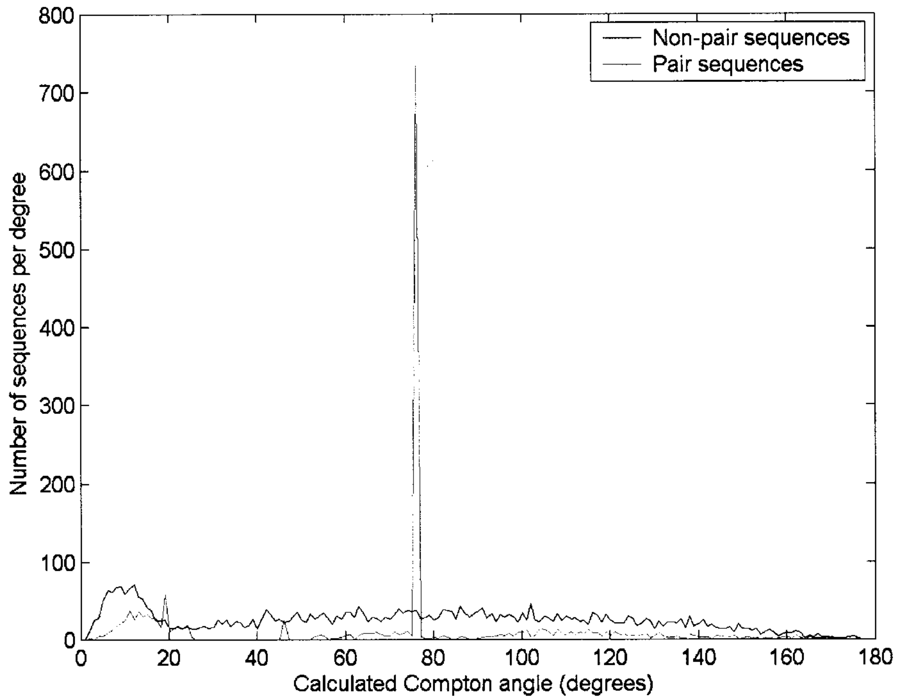

Figure 6.8. Comparison of calculated Compton angle distributions for simulated pair production and non-pair production three-pixel sequences at 2.5 MeV. The spike corresponds to identifiable sequences (511 keV is deposited in two events).

are eliminated, then the efficiency at 2.5 MeV for two-pixel sequences decreases by about half (see Figure 6.5).

The situation for three-pixel sequences is not as clear cut as for two-pixel sequences. Figure 6.8 shows the calculated Compton angles at 2.5 MeV for three-pixel sequences with and without pair production. Sequences in which one annihilation photon is absorbed in one or two events are identifiable. The spike in Figure 6.8 is due to those in which one annihilation photon scatters and then is absorbed. This is the same calculated angle as for two-pixel sequences in which the photon is absorbed. When one annihilation photon is absorbed immediately and the other scatters, the sequence can be identified as containing pair production due to the observance of a 511 keV event, although there is no correlation between the Compton angles calculated from these sequences. Three-pixel sequences in which neither photon is ultimately absorbed also result in a broad distribution of scatter angles. There is no way to clearly identify these sequences as involving pair production.

A backprojection image was generated using only unidentifiable pair production sequences for a 2.5 MeV source located above the detector. No energy or position cuts were made. The result is shown in Figure 6.9. The image, which contains about 2500 sequences, is not a diffuse background; it has high intensities in some regions, and low intensities along the *-z* and *+z* directions (where the source is located). Compare Figure 6.9 with the image reconstructed from non-pair sequences (about 16000 sequences) under the same conditions in Figure 6.10. Figure 6.9 demonstrates that pair production sequences can interfere in the image reconstruction of high-energy gamma-ray sources. The degree of this interference is application specific, depending on the source spectrum and the reconstruction parameters.

In this work, identifiable pair production sequences are sought and discarded when the initial gamma-ray energy is known to be above 2 MeV. Unidentifiable pair production sequences, which do not deposit the full gamma-ray energy, are discarded through full-energy windowing.

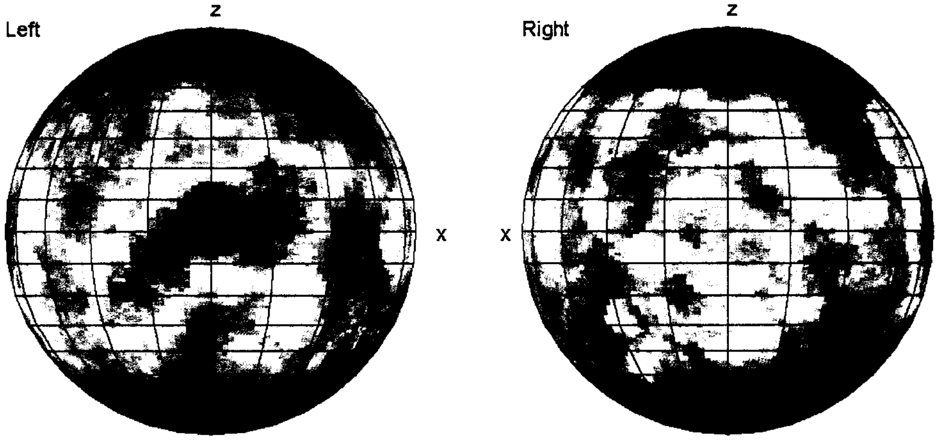

Figure 6.9. Backprojection image of simulated unidentifiable pair production sequences using two- and three-pixel sequences without energy or position cuts for 2.5 MeV gamma rays.

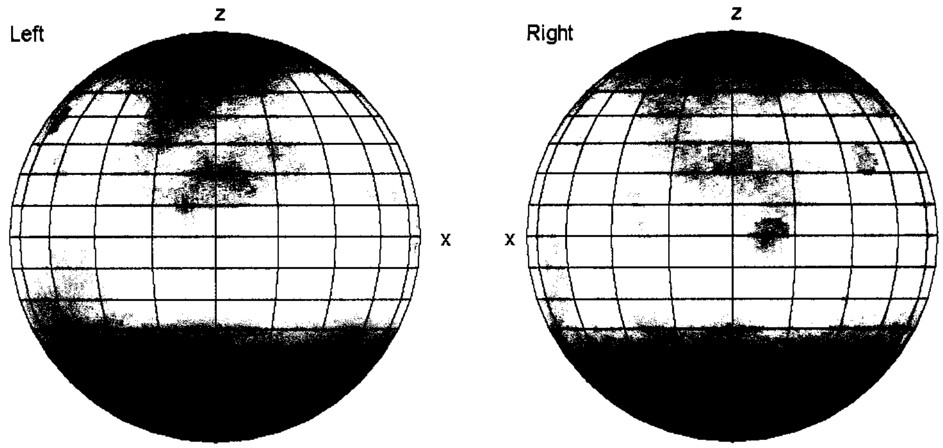

Figure 6.10. Backprojection image of simulated non-pair production sequences under the same conditions as in Figure 6.9.

6.2.3 Coherent scatter

Coherent (or Rayleigh) scatter occurs when a photon scatters from an atom and changes direction without losing any energy. The coherent scattering cross section decreases with increasing energy, as shown in Figure 6.11[6]. Also shown are the cross sections for photoelectric absorption, Compton scatter, and pair production. The coherent scattering cross section is nearly equal to the Compton scattering cross section for 100 keV photons in CdZnTe. Therefore, for gamma-rays with energies up to a few hundred keV, coherent scatter can occur with non-negligible frequency. The energy range of interest for gamma-ray imaging in this work is from 300 keV to 2.5 MeV. Coherent scatter is not common for gamma rays in this energy range. However, these gamma rays will Compton scatter into lower energies where coherent scatter is common. When a gamma-ray Compton scatters, coherent scatters, and then is absorbed, the full energy of the gamma-ray is deposited, and the Compton scatter angle is correctly determined from energies. However, the cone axis is incorrectly determined from the two observable

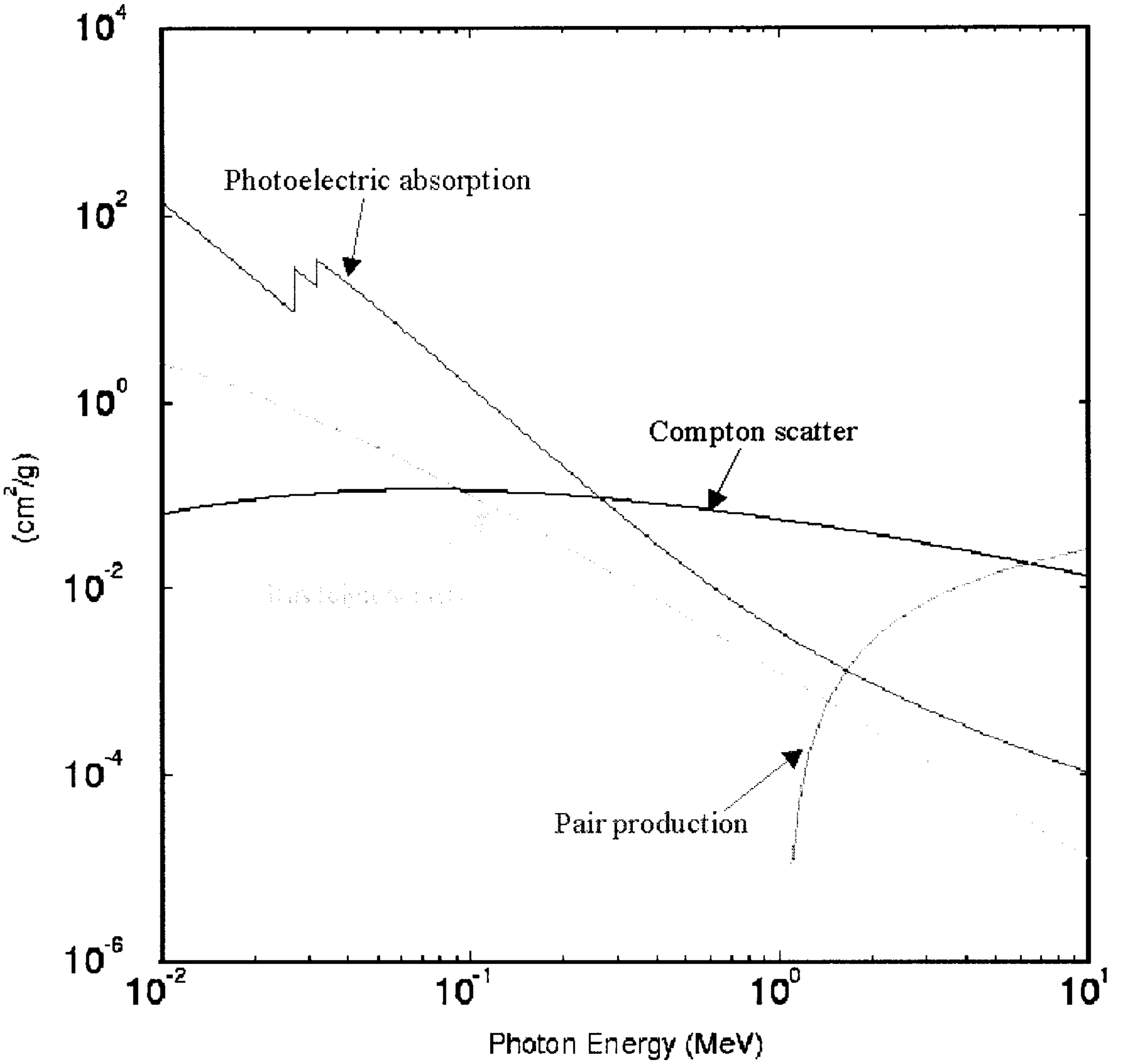

Figure 6.11. Interaction cross sections for gamma rays between 10 keV and 10 MeV in CdZnTe. Rayleigh scatter can be important for gamma rays with energies below several hundred keV.

interaction locations because the Rayleigh scatter changes the direction of the gamma ray between the scatter and absorption events.

If two events occur in the detector and deposit the full gamma-ray energy, the backprojection will be incorrect regardless of when the coherent scatter occurs in the sequence. For three events, however, if the coherent scatter occurs between the second and third events, it is still possible to get the sequence correct. The first scatter angle will be correctly determined from energies, and if the sequence is correct, the cone axis connecting the first and second interaction locations will also be correct. Only if the Rayleigh scatter occurs before the second interaction will the sequence always yield the improper backprojection. Table 6.1 gives for selected gamma-ray energies the fraction of full-energy two-pixel sequences involving Rayleigh scatter and the fraction of full-energy three-pixel sequences in which the Rayleigh scatter occurs before the second interaction.

Sequences in which coherent scatter occurs before the second interaction do not necessarily result in lost efficiency. The distribution of coherent scatter angles observed in sequences of 662 keV photons is given in Figure 6.12. For most of these sequences the scatter angles are small (<10°). In this case the observed gamma-ray direction is not too different from the actual gamma-ray direction, and the gamma-ray source location can still be determined. Figure 6.13 shows the image generated from two- and three-pixel sequences in which coherent scatter occurs for a 662 keV source located above the detector. As expected, the true source location is found.

Coherent scatter is always included in the simulations in this work. Although coherent scatter cannot be observed in a sequence, the scatter event does change the direction of the gamma-ray which results in an incorrect cone axis. Fortunately, the scatter angles are relatively small, deflecting the gamma rays only slightly. The correct source location can still be identified.

Table 6.1. Percentage of Full-Energy Sequences with Coherent Scatter before the Second Interaction

Energy (keV)	Two Events	Three Events
300	7.5%	7.2%
662	3.5%	4.0%
1500	2.2%	2.1%
2500	1.4%	1.4%

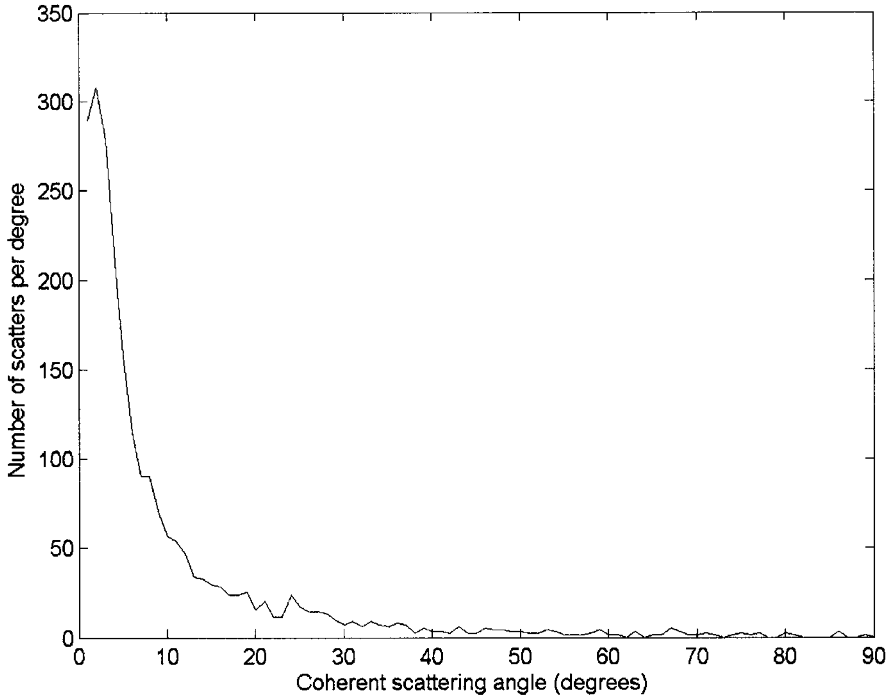

Figure 6.12. Distribution of coherent scattering angles for simulated sequences of 662 keV photons.

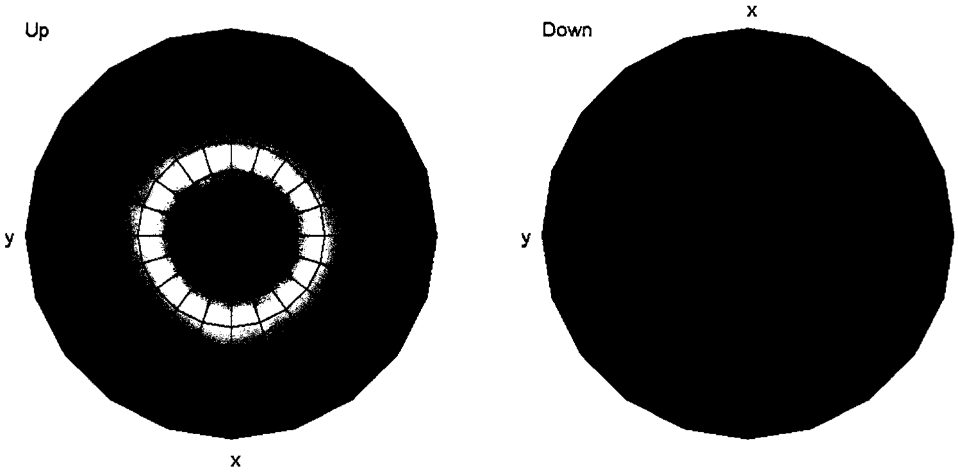

Figure 6.13. Simulated backprojection image of full-energy sequences involving Rayleigh scatter for 662 keV photons. The correct source location can still be found.

6.3 Detector System

6.3.1 Multiple interactions under one pixel

The sequence reconstruction techniques discussed in Chapter 4 were tested using simulated data in which sequences were discarded if more than one interaction occurred under the same pixel. The fraction of two- and three-event sequences in which this occurs was given in Chapter 4: 24% of two-event sequences and 46% of three-event sequences for 662 keV gamma rays. The effect on image reconstruction due to these sequences is examined here.

When both events of a two-event sequence occur underneath the same pixel, the track is observed as a single event with the summed energy and averaged depth. This track cannot be used for Compton imaging, which results in loss of efficiency. When two events of a three-event sequence occur underneath the same pixel, only two events are observed. Figure 6.14 shows the image of full-energy two-pixel sequences resulting from three-event sequences for a 662 keV source above the detector. The backprojection yields the correct source location even though the sequencing was wrong.

Figure 6.15 shows a similar image for a point source located in front of the detector. In this case the source location is also correctly determined. (The source distribution above the detector appears broader than when the source is located to the side of the detector. This effect is discussed in Section 6.4.2.) To explain why the source is still correctly located, it is necessary to examine the difference in depths of interaction when more than one event occurs under a pixel. The distribution for top irradiation is shown in Figure 6.16. In nearly 90% of sequences, the two events under the same pixel are separated by 1.5 mm or less. With a depth resolution of about 1 mm, these events appear to occur at virtually the same position (see Figure 6.17). Consider a sequence consisting of a two scatters followed by a photoelectric event in which the last two interactions occur under the same pixel. This appears as a two-pixel event. If the first interaction deposits more than half the gamma-ray energy, the sequence order selection rules state to choose (correctly) this event as the first. The calculated cone axis will be almost correctly determined, while the cone angle (which depends only on the energy deposited in the first event and the total energy) will be truly correct. Nearly 50% of sequences with multiple interactions under a pixel resemble this case. If the first events in these sequences deposit more than half the gamma-ray energy, then the sequences will be determined correctly and the backprojection cones will include the correct source location. There are two other possibilities for a three-event sequence. Either the first and second events or the first and third events can occur under the same pixel. In the former case, the correct source location will only be found if one of the deposited energies is low such that the error in using the summed energies to calculate the scatter angle is small. When this is true, both the calculated Compton angle and the cone axis are wrong, but within the limits of the uncertainties. In the latter case, the correct source location cannot be found.

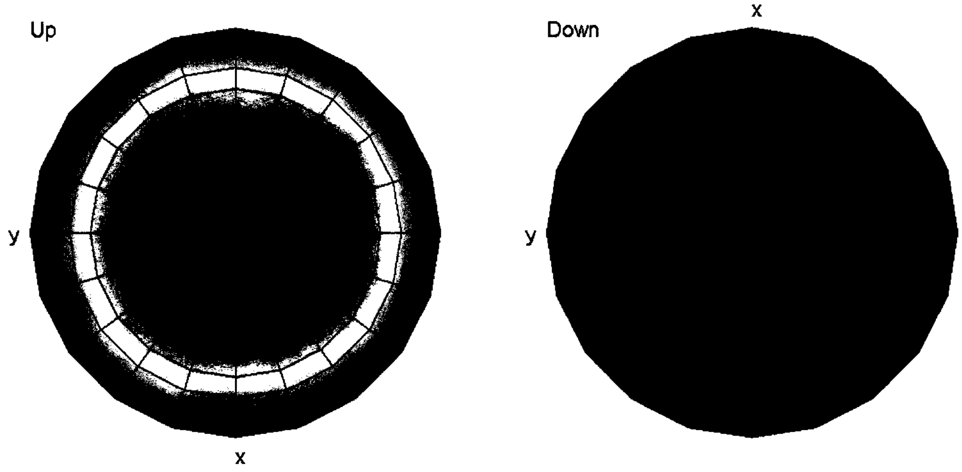

Figure 6.14. Backprojection image of 662 keV source located on top of the detector using simulated full-energy three-event sequences in which more than one interaction occurs under a single pixel, resulting in an observed two-pixel sequence. Despite the incorrect sequence reconstruction, the source location can still be found.

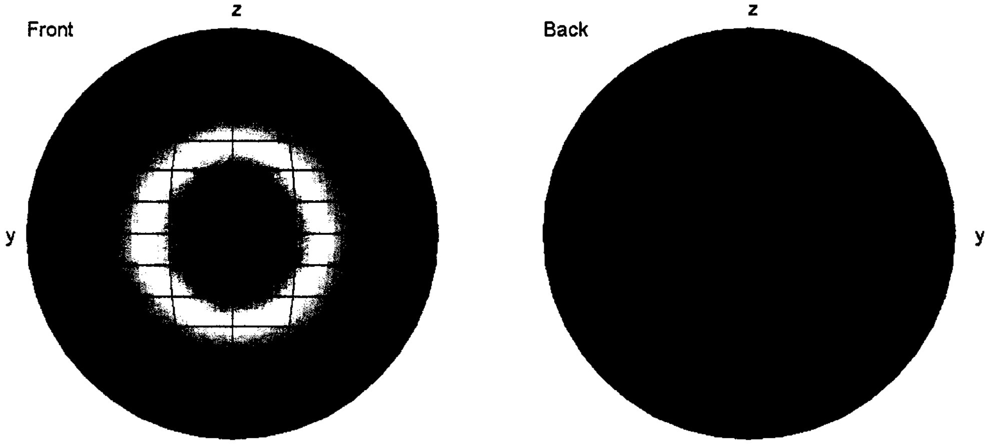

Figure 6.15. Backprojection image of 662 keV source located in front of the detector using simulated full-energy three-event sequences in which more than one interaction occurs under a single pixel, resulting in an observed two pixel sequence. Despite the incorrect sequence reconstruction, the source location can still be found.

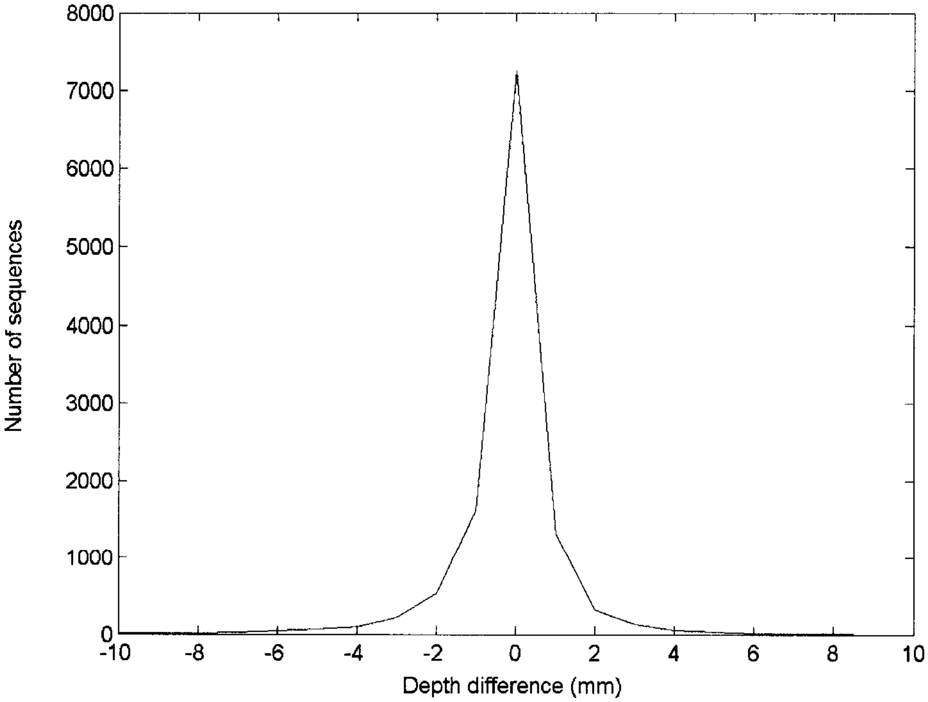

Figure 6.16. Simulated difference in interaction depths observed when multiple interactions occur under one pixel.

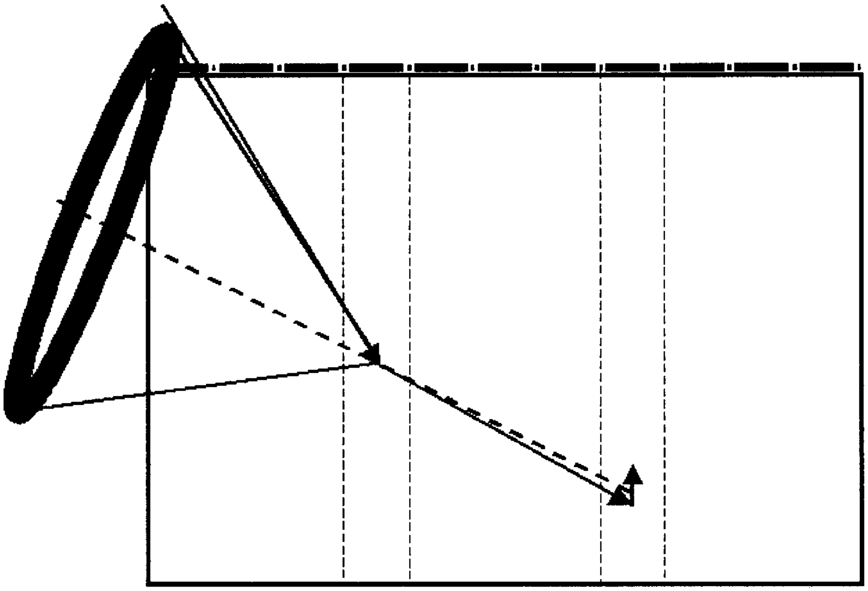

Figure 6.17. Illustration of a sequence with multiple interactions under one pixel that will contribute to the gamma-ray source location in the image due to the small difference in depth between the second and third interactions.

When multiple interactions occur under one pixel, there is no recourse. The sequences cannot be identified, and the only way to reduce the frequency of occurrence is to decrease the pixel pitch of the anodes. From the above results, however, this effect is not crucial because many sequences can still reconstruct to the correct source location.

6.3.2 Charge sharing between pixels

In the simulations used in this work, only the deposited energies have been considered. The finite extent of the charge cloud has not been considered. In the actual detector, as the deposited energy increases, the size of the charge cloud (which is subject to the range of the recoil electron and diffusion through the material) also increases, and there is a higher probability that an electron cloud near the pixel edge will split and be collected by two neighboring pixels. This is illustrated in Figure 6.18. In this case, a single event is observed as two or more.

Multiple-pixel sequences due to charge sharing can be distinguished from actual multiple-event sequences in some instances by comparing the depths of interactions. Events resulting from charge sharing should share the same depth, while true multiple-event sequences will have varying depths. Figure 6.19 shows the measured difference in depths for the events in two-pixel sequences in which the pixels collecting charge are neighbors. Also included on the graph is a similar curve from simulations, normalized to the same total number of sequences as the first curve. The measured curve shows a narrower peak at small depth differences, which is an indication of charge sharing.

One way to reduce charge sharing is to increase the size of the anode pixels. If the pixel pitch is increased, however, the position resolution worsens and the frequency of multiple interactions occurring under a single pixel will increase. Thus there is a tradeoff that must be made in designing the anode structure to balance the competing effects of

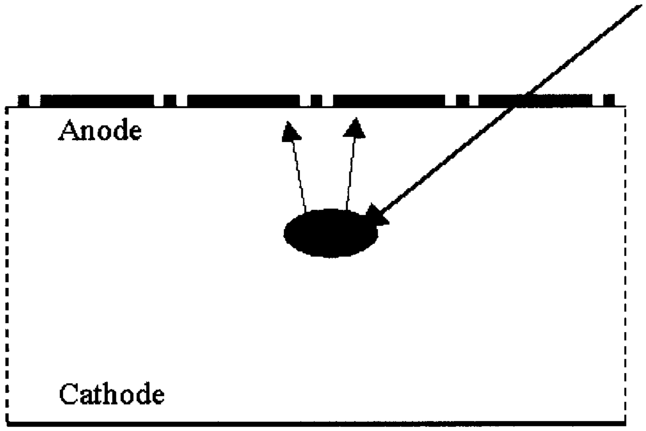

Figure 6.18. Illustration of charge sharing. When the electron charge cloud is large, it can be split and collected by two neighboring pixels. In this case, a single event appears as two.

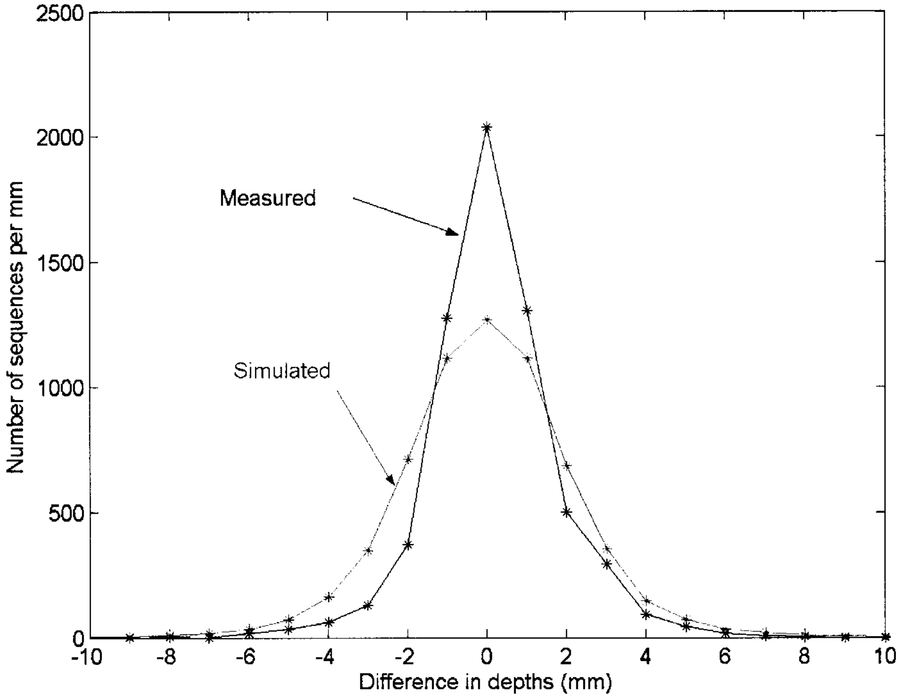

Figure 6.19. Comparison of simulated and measured interaction depth differences for two-pixel sequences in which neighboring pixels collect charge (normalized to the same number of sequences).

charge sharing and multiple events. Du *et al.* have shown the effect of pixel size on charge sharing and multiple events under one pixel in CdZnTe detectors [7]. They estimate that at 662 keV a 1.3 mm pixel pitch leads to charge sharing in 18% of single events. About 23% of all full-energy sequences involve more than one interaction under a single pixel at that size. As was shown in the previous section, sequences with multiple events under one pixel are not necessarily destructive to the Compton imaging process. Thus, in designing the anode structure for medium-energy applications it would be beneficial to err on the side of less charge sharing, and a 1.3 mm pixel pitch is sufficient according to the calculations of Du *et al.* For higher energy applications, a larger pixel size would be necessary. The anode pixel design should be tailored to the desired energy range of the imager.

In order to eliminate the effects of charge sharing in a detector with a given pixel size, it is necessary to exclude sequences in which nearest neighbor pixels both collect charge. This will also eliminate some useful events, thereby reducing the efficiency of system. The simulated fractions of useful full-energy sequences lost by requiring anticoincidence with four nearest and eight nearest neighbors for the current anode configuration are given in Table 6.2 for selected incident gamma-ray energies. The reduction in efficiency is almost uniform across energies: between 15-19% if only the nearest four neighbors are rejected, and almost 30% if the nearest eight neighbors are included in the comparison. In this work for 662 keV gamma rays the efficiency is more important than reducing charge sharing sequences by rejecting sequences in which neighboring pixels collect charge. Only at high energies (greater than 2 MeV) are attempts made to reject charge sharing sequences.

Table 6.2. Percentage of Useful Full-Energy Sequences Lost by Requiring Anticoincidence with Nearest Four and Nearest Eight Neighbor Pixels

Energy (keV)	Nearest Four Pixels	Nearest Eight Pixels
300	15.3%	25.0%
662	18.5%	28.5%
1500	18.5%	29.5%
2500	15.9%	27.2%

6.3.3 Anode threshold

The threshold on the anodes of the VAS2/TAT2 system is approximately 100 keV. As discussed in Chapter 3, if a pulse with amplitude greater than about 100 keV is observed on a pixel, the system is triggered to hold the signal and register the event. If less than 100 keV is deposited under a pixel, the system will not trigger. The threshold varies from pixel to pixel, but in this section it will be assumed that each anode has the same threshold.

The effect of this threshold can be significant. Imaging 300 keV gamma rays, for example, cannot be done with three or more events if 100 keV is required in each event. Furthermore, only two-event sequences in which both events deposit at least 100 keV will register as two-pixel events; all others are observed as single-pixel tracks and are not imageable. Sequences in which only two of three events are observed cannot be excluded except through full-energy windowing. If only full-energy sequences are imaged, the effect of the threshold is to decrease the imaging efficiency. The loss in efficiency is calculated for 300, 662, 1500, and 2500 keV, and is tabulated in Table 6.3. Not surprisingly, the greatest reduction in efficiency occurs for 300 keV gamma rays, where none of the three-pixel sequences can be observed with a 100 keV threshold. A total reduction of about 54% was observed at this energy. For 662 keV, about 15% of efficiency is lost due to the high anode threshold. This percentage decreases to about 7% for 2500 keV gamma rays. Note that for full-energy two-pixel sequences, only the first event can deposit less than 100 keV at any of the energies tested. For gamma-ray energies above 400 keV, this means that the two-pixel sequences lost are those that would be incorrectly sequenced.

Table 6.3. Percentage Reduction in Efficiency Due to 100 keV Anode Threshold

Energy (keV)	Efficiency Reduction
300	53.9%
662	14.7%
1500	7.45%
2500	7.44%

Figure 6.20 shows the expected reduction in efficiency for 662 keV gamma rays given various threshold levels. The VAS3/TAT3 system, for example, has an anode threshold of about 60 keV. This means that only 8% reduction in efficiency should be observed at 662 keV. This is an improvement over the VAS2/TAT2 system. If the anode

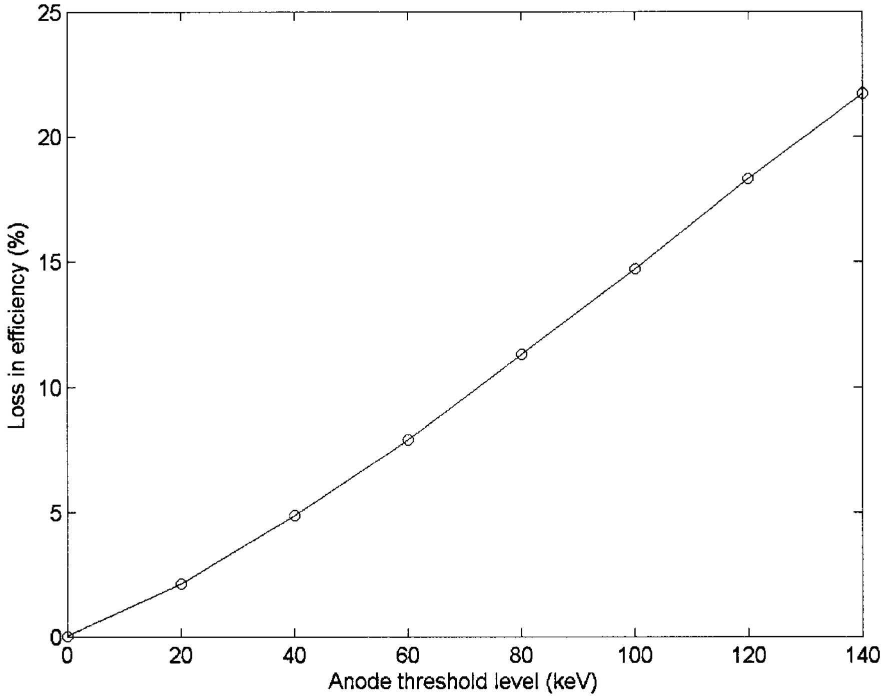

Figure 6.20. Simulated reduction in efficiency for 662 keV gamma rays due to the given anode threshold levels. The VAS3 system has a threshold near 60 keV, while the VAS2 system threshold is about 100 keV.

thresholds could be reduced even further to 30 keV, then the efficiency loss would be reduced to only 4%.

6.3.4 Dynamic range of the ASICs

As discussed in Chapter 3, the application-specific integrated circuits (ASICs) used to measure the voltage and timing information for each anode pixel have a limited dynamic range. If the voltage signal from a pixel is sufficiently high, the corresponding channel in the ASIC will saturate. In the VAS2/TAT2 system, the maximum energy that can correctly be measured is about 1000 keV. In the VAS3/TAT3 system the range is increased to 1600 keV. The limited dynamic range does not affect imaging for gamma-ray energies within the range, for example 662 keV. As the gamma-ray energy increases, however, the dynamic range can have a major impact on the image reconstruction.

The most significant effect of the limited dynamic range is to limit the observable energies in a full-energy two-pixel sequence. For example, consider a source of 2.5 MeV gamma rays. If one event deposits a maximum of 1600 keV, the other event must deposit a minimum 900 keV if the gamma-ray deposits its full energy. Only gamma-ray interactions that deposit between 900 and 1600 keV can contribute to the photopeak of the two-pixel energy spectrum, as illustrated in Figure 6.21. The figure shows the distribution of energy deposited in the first and second events for simulated full-energy two-pixel sequences. There is a 96% reduction in observable two-pixel sequences at 2.5 MeV due to the limited dynamic range. In addition, energy distributions of the first and second event overlap in this range. Rather than correctly choosing the event order in 97% of sequences at 2.5 MeV, the two-pixel sequencing technique succeeds in only 65% of simulated sequences observed due to the limited dynamic range.

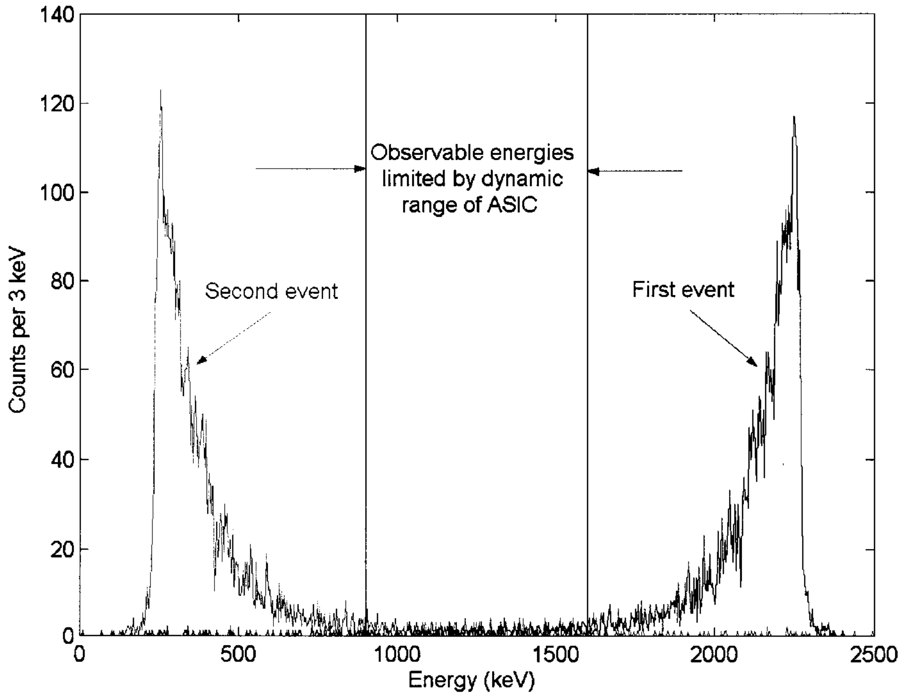

Figure 6.21. Distribution of simulated first and second energy depositions in full-energy two-pixel sequences. The 1600 keV dynamic range on the VAS3 system reduces the useful energy region to 900-1600 keV.

As a result of the reduced energy range, there is also a limitation on the observable scatter angles for two-pixel sequences. If the first event deposits 900 keV, the Compton scatter angle is approximately 27°. Likewise, a scatter angle of 50° corresponds to 1600 keV deposited in the first event. Only scatter angles between 27°-50° can lead to observable full-energy sequences, as shown in Figure 6.22. Furthermore the event ordering algorithm for two-pixel sequences limits the calculated Compton angles to the range 39°-50° (see Section 6.4.1). The resulting backprojection image from full-energy two-pixel sequences of a 2.5 MeV point source located above the detector is shown in Figure 6.23. The granularity in the image results from the poor statistics (only 232 sequences). The source location can still be found.

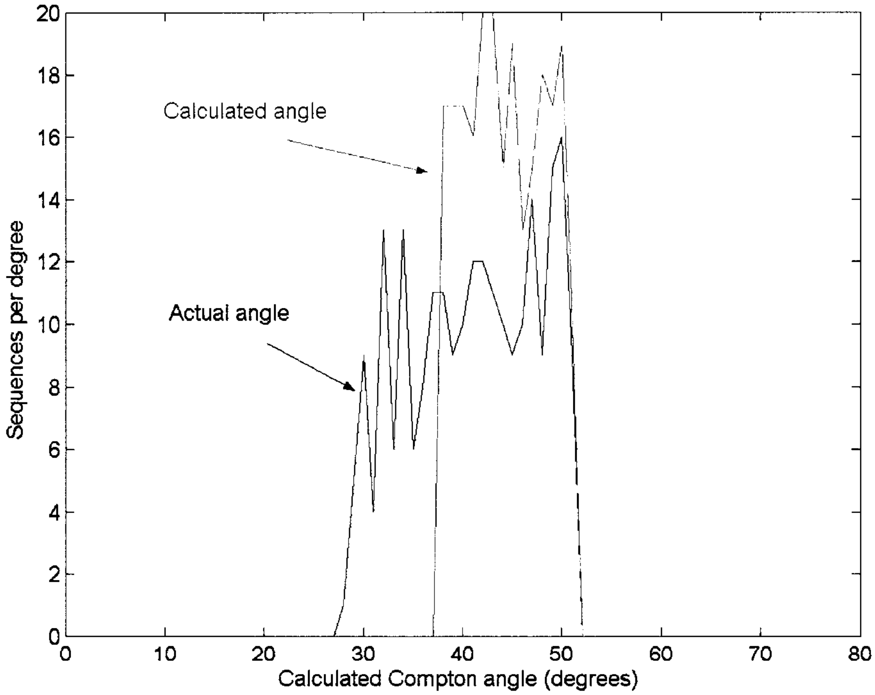

Figure 6.22. Distribution of actual and calculated Compton scatter angle in simulated full-energy two-pixel sequences at 2500 keV. The ASIC dynamic range and sequence reconstruction method limit the observable scatter angles to 39°-50°.

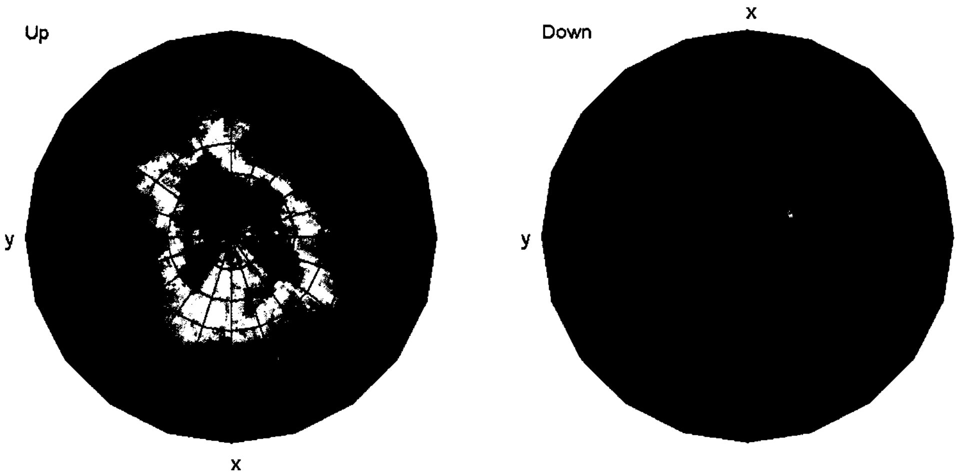

Figure 6.23. Backprojection image of simulated full-energy two-pixel sequences for a 2.5 MeV point source above the detector. The limited dynamic range results in an efficiency loss of 96% of two-pixel sequences.

6.4 Image Reconstruction Methods

6.4.1 Sequence reconstruction techniques

For two-pixel sequences, the sequence reconstruction method can have a significant effect on the image. A minimum allowable scatter angle is artificially set by requiring that the first interaction deposit more energy than the second interaction for two-pixel sequences depositing a total energy above 400 keV. For example, at 662 keV the minimum amount of energy deposited in the first event of a full energy sequence is 331 keV. If less energy than this is deposited in the first event, the order of the two events is reversed, and the higher energy is assumed to be deposited first. The minimum scatter angle is then 76°. This is observed in Figure 6.24, where the simulated distribution of calculated scatter angles is plotted for correctly sequenced tracks and for tracks sequenced using the two-pixel rules outlined in Chapter 4. As the incident gamma-ray energy increases, the minimum allowable scatter angle decreases, as shown in Figure 6.25. Below 400 keV, the sequence order rules change, and the first interaction must

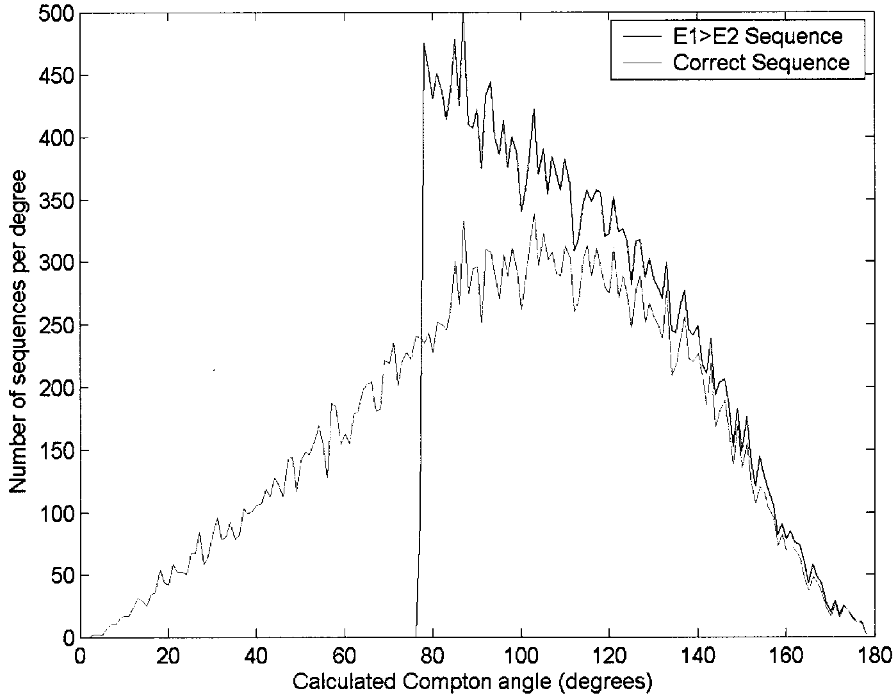

Figure 6.24. Simulated distributions of calculated Compton angles for simulated two-pixel sequences at 662 keV that deposit full energy using both two-pixel tracking rules and the correct sequences. When the first event must deposit at least half the gamma-ray energy, a minimum observable scatter angle is set.

deposit less energy than the second. In this case, there is a maximum observable scatter angle imposed. Note that below 256 keV, where the sequence can be absolutely determined, all scatter angles are allowed.

The effect of the two-pixel sequencing technique is to limit the allowable scatter angle, and to reduce the imaging efficiency. Figure 6.26 shows the backprojection image that results from incorrectly sequencing the tracks in which the first event deposits less energy than the second. The backprojection image from correctly sequencing these tracks is shown in Figure 6.27. Figure 6.28 shows an image similar to Figure 6.26 for a source to the side of the detector. In both 662 keV source geometries, the result of guessing the wrong sequence is a ring-shaped hot spot in the correct hemisphere. (The differences

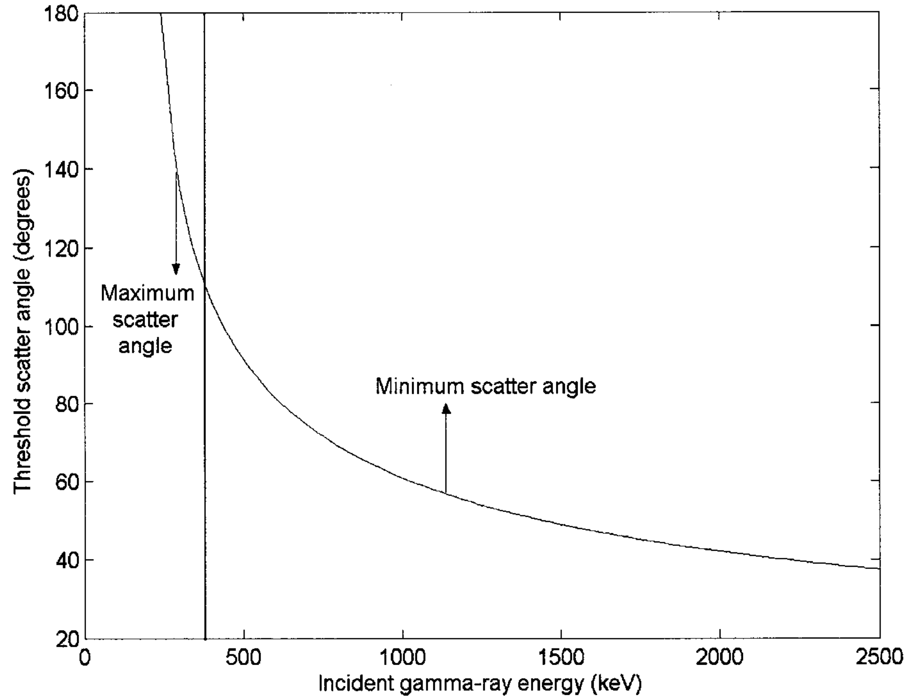

Figure 6.25. Threshold scatter angles for two-pixel sequences as a function of incident gamma-ray energy. Below 400 keV, the sequence selection rules dictate a maximum scatter observable scatter angle; above 400 keV, a minimum angle is imposed.

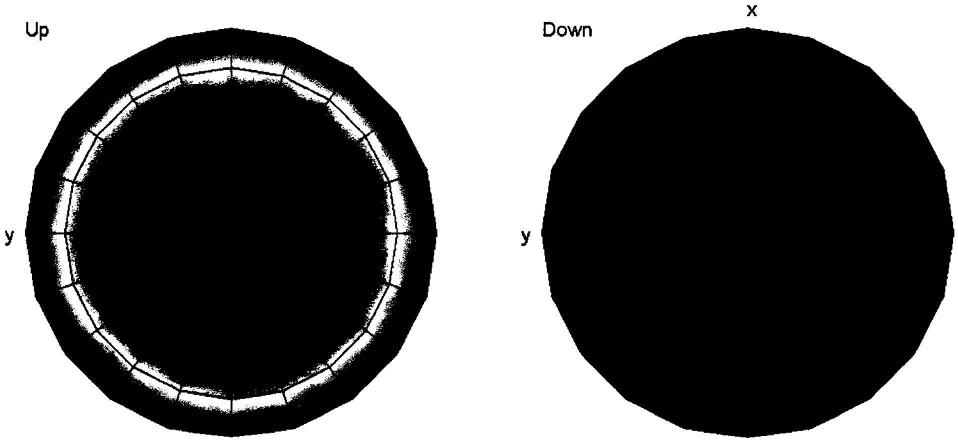

Figure 6.26. Simulated backprojection for incorrectly sequenced full-energy two-pixel sequences at 662 keV in which the first event deposits less energy than the second event (source above the detector).

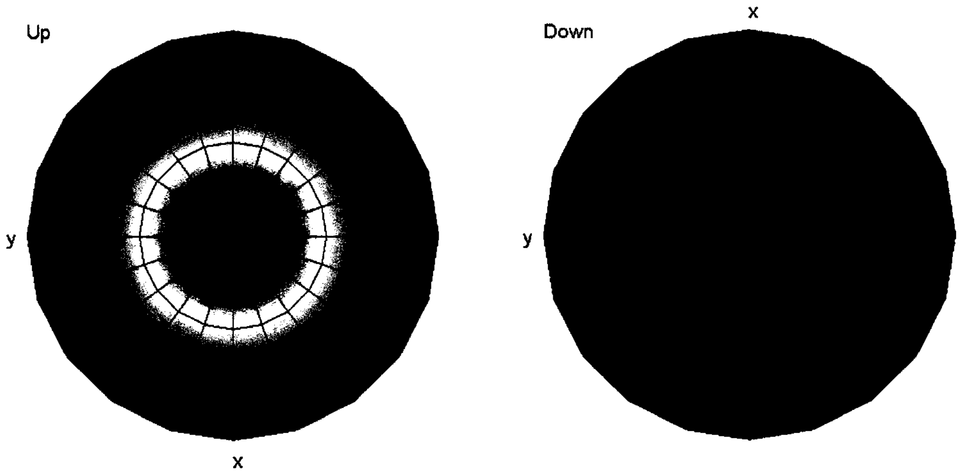

Figure 6.27. Simulated backprojection image for correctly sequenced full-energy two-pixel sequences at 662 keV in which the first event deposits less energy than the second event (source above the detector).

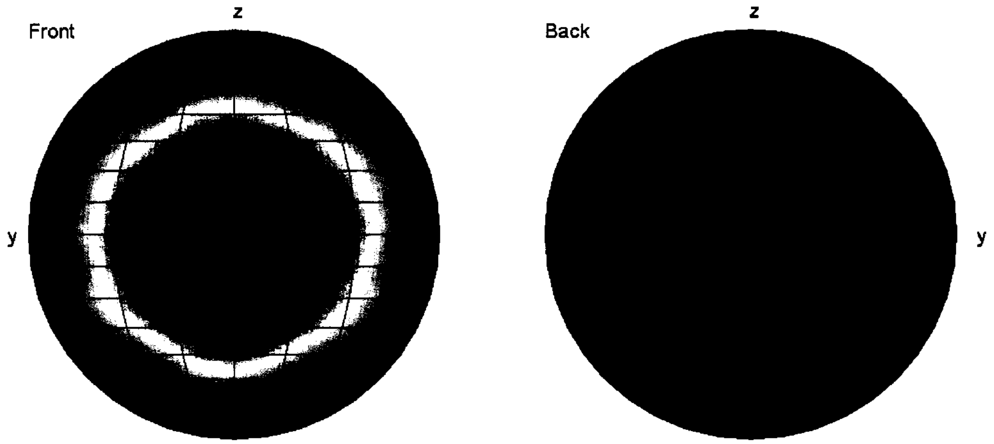

Figure 6.28. Simulated backprojection image for incorrectly sequenced full-energy two-pixel sequences at 662 keV in which the first event deposits less energy than the second event (source to the side of the detector).

observed between the image shown in Figure 6.26 and that shown in Figure 6.28 are due to the anisotropy of the backprojection process, which is discussed later in Section 6.4.2.)

When the sequence order is wrong, the cone axis points opposite of the correct direction. However, the calculated Compton angle is also incorrect. In a full-energy sequence for 662 keV gamma rays if the first energy is less than 287 keV (less than 65° scatter angle), the Compton angle is calculated to be greater than 90°. In this case, the incorrect cone axis direction and the obtuse Compton angle combine to put the cone in the correct hemisphere of the image. For example, if the first event deposits 250 keV and the second event deposits 412 keV, the correct scatter angle is 57.9°. Reversing the sequence order results in a calculated scatter angle of 105.8°. The difference in the backprojection cones is only 17.4°. The two effects do not exactly cancel, which causes the ring shape in Figures 6.26 and 6.28.

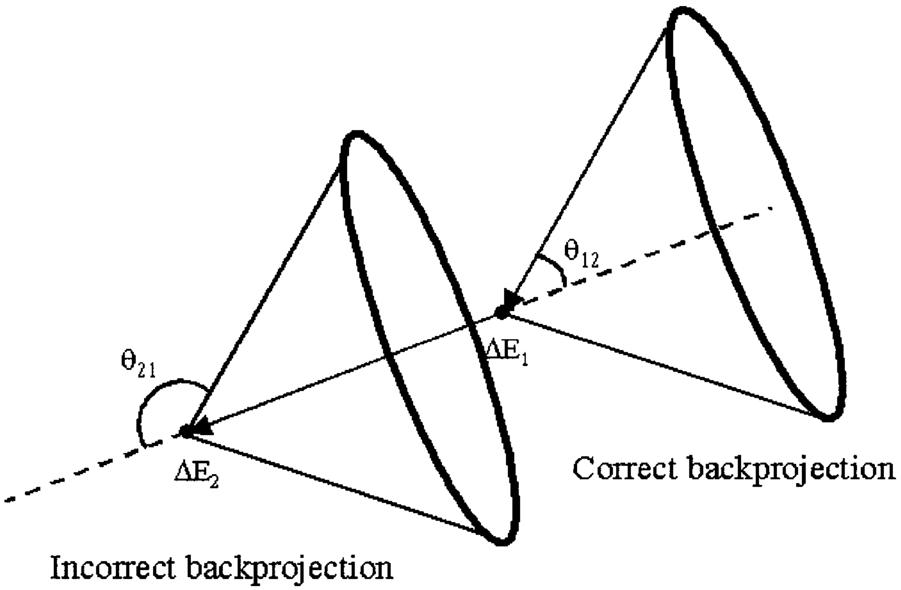

Figure 6.29. Illustration of a two-pixel sequence where the incorrect sequence order yields the same backprojection cone as the correct sequence order. This occurs only for some sequences from 511 keV photons if the far-field approximation is used for backprojection.

There is a single exception to the above case. For 511 keV gamma rays, the sequencing error for two-pixel tracks is almost exactly offset by error in the cone axis, and the source location is almost correctly reconstructed even when the sequencing algorithm fails. The sequencing error causes a 180° rotation of the Compton cone axis. Thus, to obtain the same backprojection cone for the correct and incorrect sequences, the two Compton angles must sum to 180°, as shown in Figure 6.29. This is only true for far-field imaging, where the backprojection cones for the two sequence orders have the same vertex. Figure 6.30 shows the sum of the correct and incorrect calculated Compton angles for full-energy 511 keV sequences over the energy range in which both angles are defined.

For deposited energies near 256 keV, which corresponds to a 90° scatter, the correct and incorrect sequence orders will result in nearly the same backprojection cone. If the first event deposits at least 200 keV, then the error is less than 10°. The sequence is rejected if the first event deposits less than 170 keV due to the Compton edge test as discussed in Chapter 4, and if the first event deposits more than 256 keV, the sequence is correctly determined. Thus, only if the first interaction deposits between 170 – 200 keV will the incorrect sequencing significantly detract from imaging the 511 keV photon source. The image from incorrectly determining the sequence order is given in Figure 6.31. Figure 6.32 shows the image generated if the tracks are correctly sequenced.

When the sequence order is wrong, the hot spot in the image is more diffuse, incorporating 30-40° from the pole center. The extent of the hot spot is only 10-20° when the sequences are correctly determined. Thus, although only 60% of two-pixel sequences are correctly determined at 511 keV, the other 40% still contribute to the correct source position with marginal blurring of the true source location.

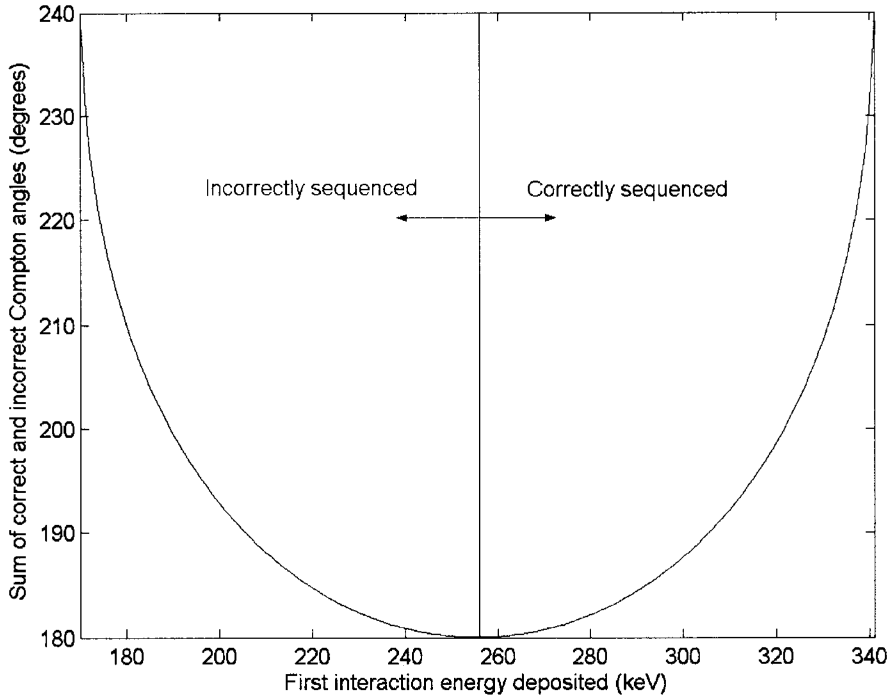

Figure 6.30. Sum of correct and incorrect Compton scatter angles for two-pixel full-energy sequences of 511 keV photons. When the first energy is lower than 256 keV, the sequence is incorrectly reconstructed, but the error in the backprojection cone can be small.

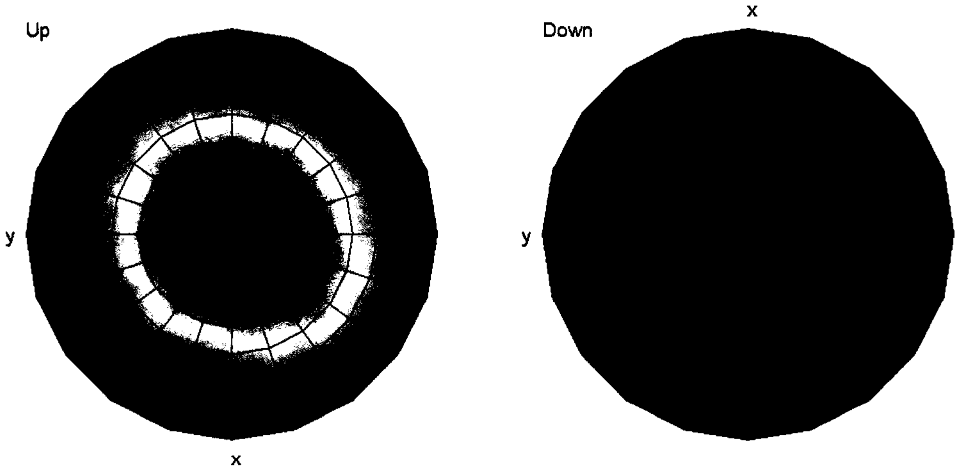

Figure 6.31. Simulated backprojection image for 511 keV photons of incorrectly sequenced full-energy two-pixel sequences in which the first event deposits less energy than the second event.

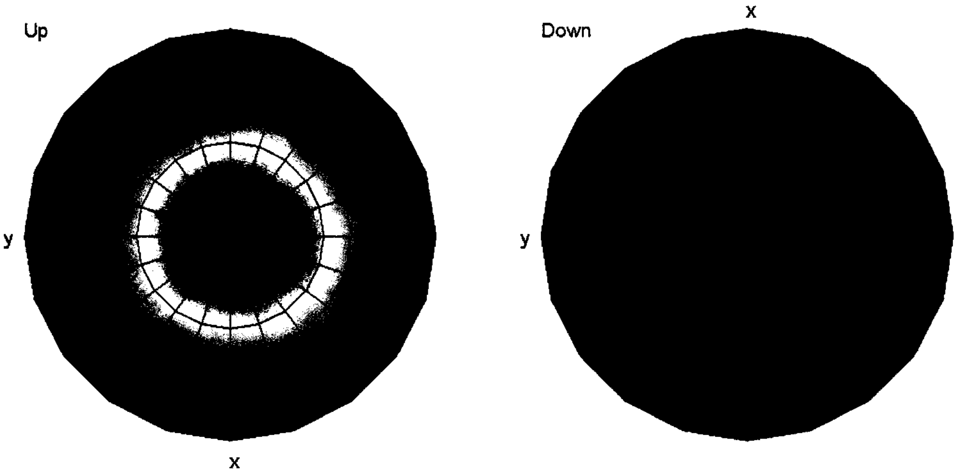

Figure 6.32. Simulated backprojection image for 511 keV photons of correctly sequenced full-energy two-pixel sequences in which the first event deposits less energy than the second event.

For other gamma-ray energies, the location of the incorrectly reconstructed ring, as in Figures 6.26 and 6.28 for 662 keV, is solely a function of the incident gamma-ray energy and can be predicted. For full-energy sequences in which an equal amount of energy is deposited in the first and second interaction, the sum of the calculated Compton angles for the two possible sequence order is greater than 180° for gamma-ray energies below 511 keV. The opposite is true for gamma-ray energies above 511 keV. The difference between this angle sum and 180° gives the location of the ring artifact for incorrectly sequenced events. Figure 6.33 shows the predicted location of the ring for gamma-ray energies from 260 – 2500 keV, measured in degrees from the true source location. For 662 keV gamma rays, the predicted ring position is about 30° from the source location, which is confirmed by examination of Figures 6.26 and 6.28. For gamma-ray energies above 1760 keV, the ring artifact appears in the hemisphere opposite the true source location. Fortunately, as the incident gamma-ray energy increases, the probability of correctly sequencing two-pixel sequences increases, and the relative effect of reconstructing the wrong sequences is small. At the same time, the two-pixel sequencing technique has the poorest performance for medium energies. Thus, for imaging gamma-ray energies near 511 keV, this artifact can help increase the effective efficiency of the imager. Of course, the imaging resolution will become poorer as was observed even for 511 keV gamma rays.

The sequence reconstruction method for determining the order of three observed events in the detector can also affect the imaging performance. Shown in Figure 6.34 are the distributions of calculated Compton scatter angles using the reconstructed and correct sequence orders for 662 keV. The sequencing technique tends to overestimate the contribution of small-angle scattering, specifically at angles less than 45°. Unlike two-pixel sequencing, there is no limit on the observable scatter angles. An image of full-energy three-pixel sequences was created using the MSD sequencing method outlined in Chapter 4; this is shown in Figure 6.35. Figure 6.36 shows the image generated using the

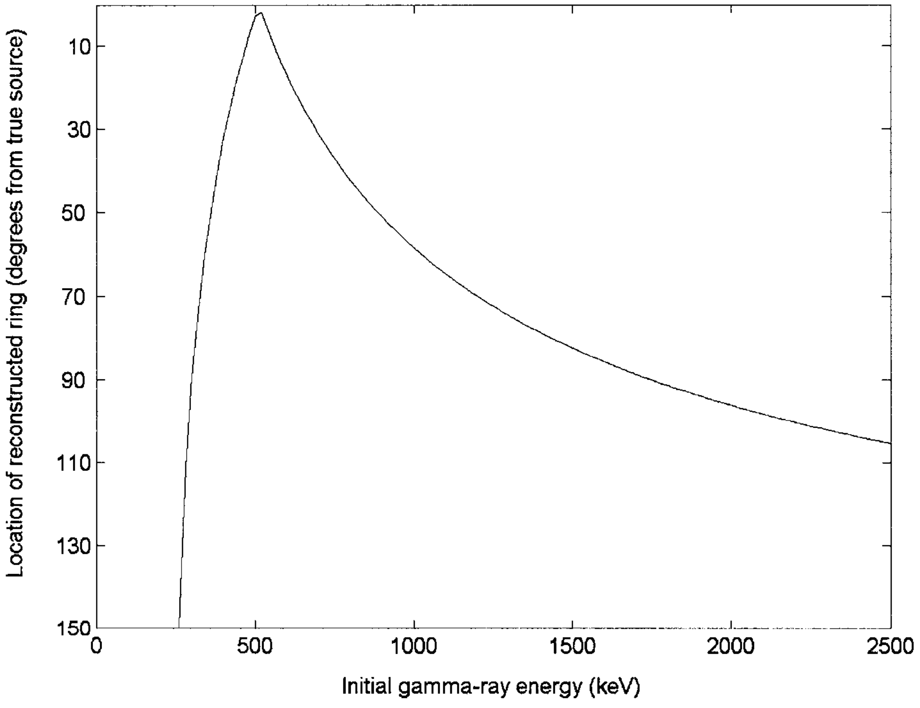

Figure 6.33. Location (measured in degrees from the true source location) of reconstructed ring due to incorrectly sequencing full-energy two-pixel events.

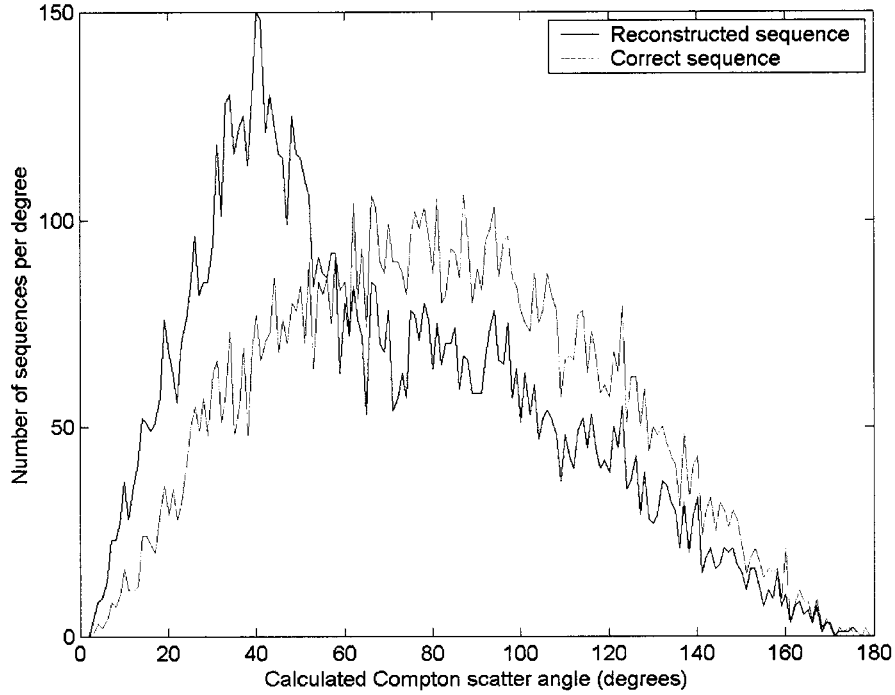

Figure 6.34. Simulated distributions of calculated Compton scatter angles using the reconstructed sequence order and the correct sequence order for full-energy three-pixel tracks at 662 keV.

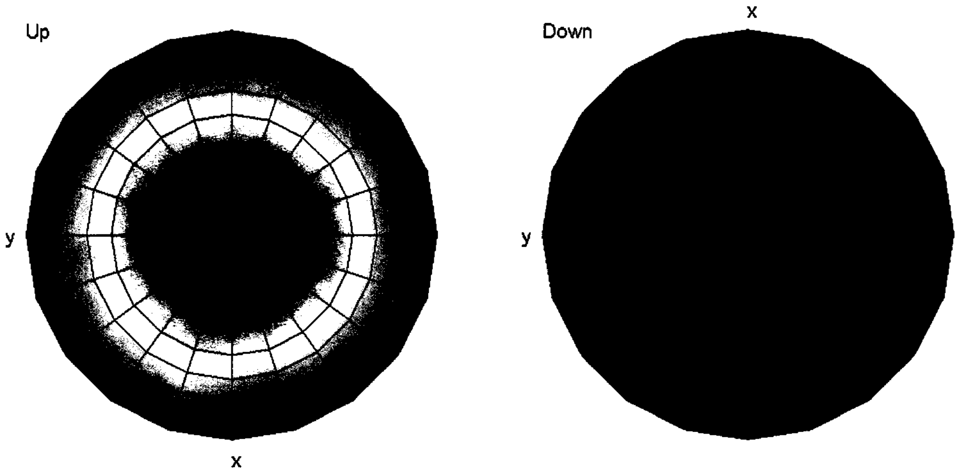

Figure 6.35. Simulated backprojection image of full-energy three-pixel sequences at 662 keV using the MSD sequence order technique.

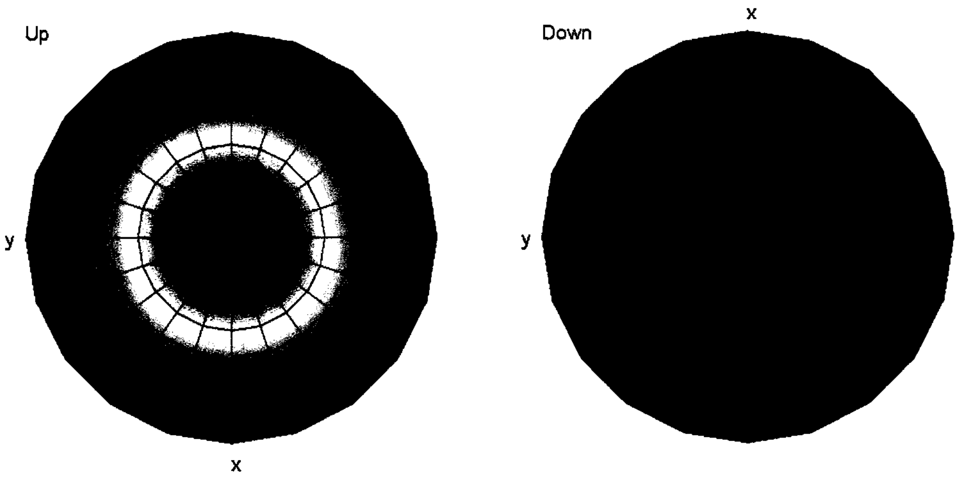

Figure 6.36. Simulated backprojection image of full-energy three-pixel sequences at 662 keV using the correct sequence orders.

correct sequence orders. The image quality is slightly better (especially in the tails of the source distribution) when the correct sequences are used, as the addition of incorrect sequences blurs the source location.

6.4.2 Backprojection image anisotropy

There are significant differences observed in the backprojection image resolution for point sources located to the side of the detector compared with sources located above or below the detector. (This effect is not observed for WMLEM reconstructed images.) Compare, for example, Figure 6.37 and Figure 6.38, which show backprojection images from simulated 662 keV point sources above and to the side of the detector, respectively, using the known correct sequence orders. The image of the source at the top of the sphere (Figure 6.37) has much poorer quality than the image where the source is along the equator (Figure 6.38). The source appears to be larger in the first image.

The difference in appearance is due to the choice of normalization in the backprojection process. As discussed in Chapter 5 for an observed sequence the value of the image pixels intersecting the backprojection cone are normalized such that the total

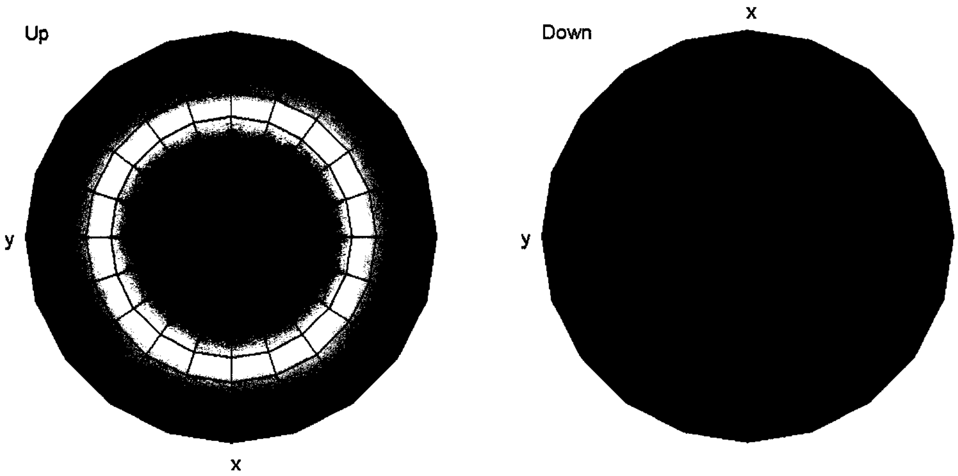

Figure 6.37. Simulated backprojection image of full-energy two-pixel sequences (with known sequence orders) at 662 keV with the source located above the detector.

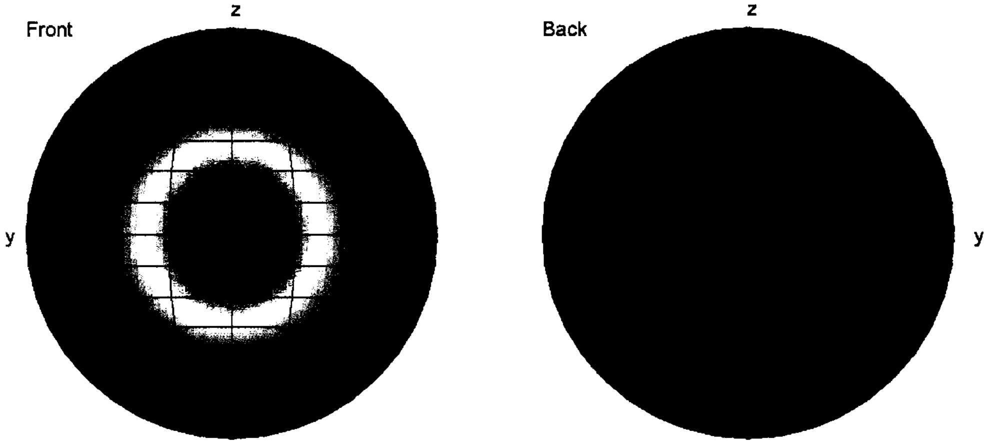

Figure 6.38. Simulated backprojection image of a full-energy two-pixel sequences (with known sequence orders) at 662 keV with the source located to the side of the detector.

ring sums to one. In this way the sum over all pixels in the image yields the total number of sequences observed. This is a "conservation of sequences" normalization. There are at least two other options that could be used.

If normalization is not performed at all, image pixels on the cone are set to a value of 1 regardless of the number of pixels involved. The resulting image using the same simulated data is shown in Figure 6.39 for a source located above the detector. This image is very similar to the image shown in Figure 6.38 for a source to the side of the detector. However, the image for a source to the side of the detector when there is no normalization, shown in Figure 6.40, does not appear similar to Figures 6.38 and 6.39. In fact, the hotspot in Figure 6.40 is elliptical in shape. This is actually a result of the pixellation in the detector. Two events occurring under the same pixel cannot be distinguished, and thus the backprojection cone axis can never be pointed directly up or down. When the same simulated data with exact positions are reconstructed, the result is a circular image, as shown in Figure 6.41. If a minimum distance of 1.3 mm is required for the lateral coordinates (forcing events to occur under different pixels) but exact position data is still used, the result is peanut-shaped image as shown in Figure 6.42. Additional blurring of the position data would produce an image similar to that in Figure 6.40. (See Section 7.5.2 for an example of this effect at high energies.)

Another normalization option is "conservation of information." In this case, the value given to the image pixels that intersect the backprojection cone are normalized by the total area of the intersected pixels. There would be more confidence that a source is located at a particular image pixel if the ring is small (i.e. there is more information about the source location). The small ring would therefore be given a higher weight than a large ring. The resulting image for a source above the detector is shown in Figure 6.43. Figure 6.44 shows the corresponding image for a source to the side of the detector.

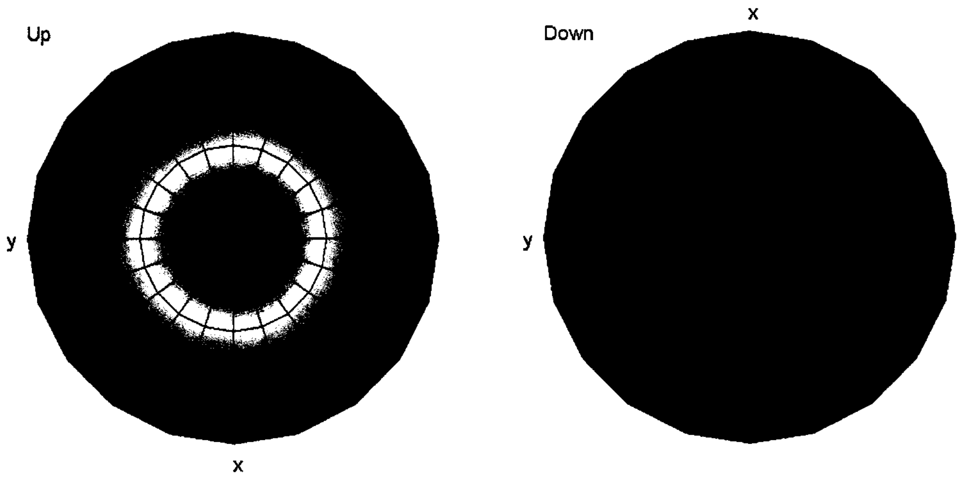

Figure 6.39. Simulated backprojection image using the reconstruction parameters from Figure 6.37 except without backprojection ring normalization. The resolution improves when no normalization is performed.

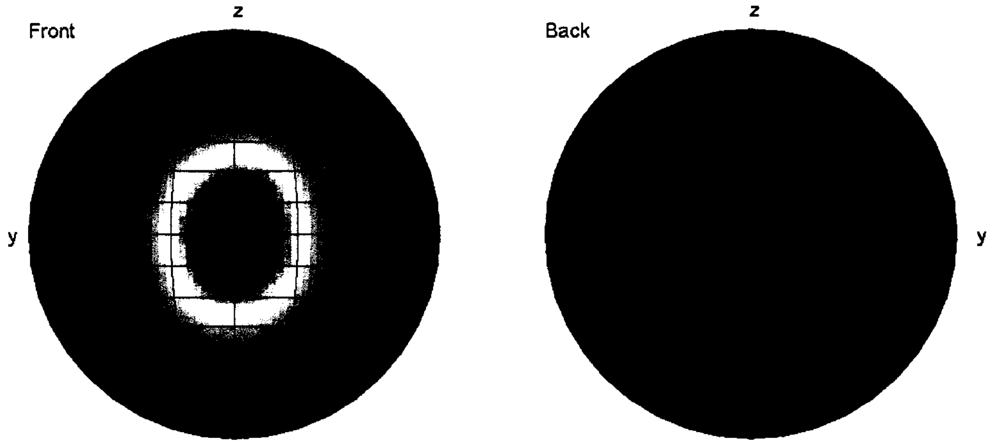

Figure 6.40. Simulated backprojection image using the reconstruction parameters from Figure 6.38 except without backprojection ring normalization. The hotspot appears elliptical.

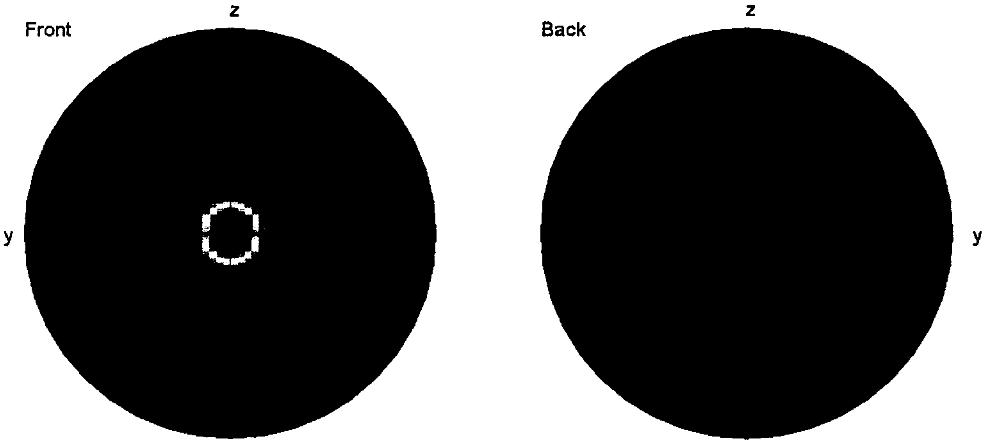

Figure 6.41. Simulated backprojection image using the reconstruction parameters from Figure 6.40 except using exact interaction locations. The hotspot appears circular when exact position data is used.

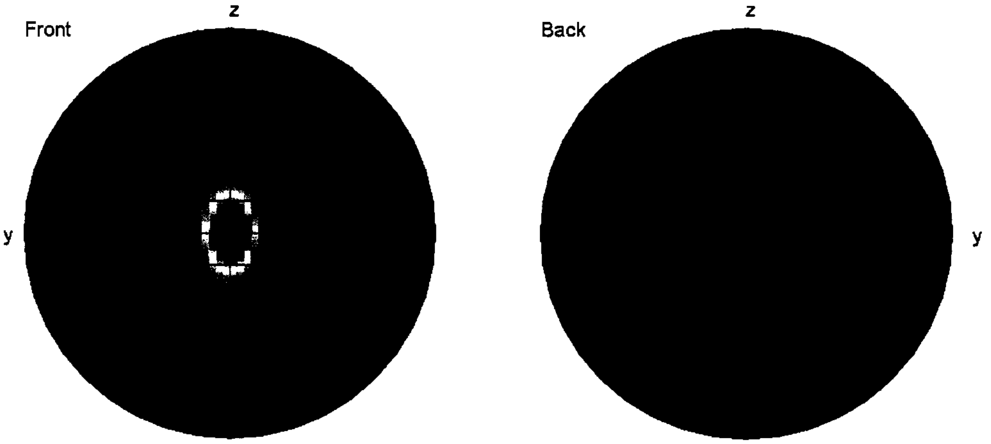

Figure 6.42. Simulated backprojection image using the reconstruction parameters from Figure 6.41 except events are required to occur at least 1.3 mm apart in the lateral dimension. The hotspot appears peanut shaped.

As observed with no normalization, the conservation of information method produces an elongated image when the source is located to the side of the detector, but a circular image when the source is located above the detector. This shape is attributed to the pixellation in the detector. It may also be due to the use of a symmetric angular uncertainty in conjunction with the detector pixellation. The assumption made in Chapter 5 is that the angular uncertainty is symmetric about the backprojection cone axis. This means that the width of the cone in the azimuthal direction is the same as that in lateral direction. However, this may not be a proper representation of the backprojection cone[8]. It may be appropriate to assign different widths to the cone in each direction. This issue warrants further investigation.

The conservation of sequences normalization does not show an elongated image for a source to the side of the detector despite the pixellation effects in the detector. This is due to the varying pixel sizes on the image sphere. Pixels are smaller at the top of the image than near the equator. When a ring intersects at the zenith, more pixels are intersected than at the equator, and the normalization results in a lower weight being assigned to the ring. This reduced weighting near the poles counteracts the elongation of the hotspot in the image to produce a circular image. When the image sphere is rotated by 90° such that the poles are located along the $+x$ and $-x$ axes (and the detector position is held constant), an elliptical source distribution is observed, as shown in Figure 6.45 for a source located to the side of the detector.

Regardless of the choice of backprojection normalization, there exists an anisotropy between sources imaged above the detector and those imaged to the side of the detector. It may be preferable to use the conservation of information normalization; although it produces elongated hotspots for sources near the equator, it results in the best resolution. Due to the poor overall resolution, backprojection is typically not used to determine the spatial distribution of a source—only the presence or absence of the source.

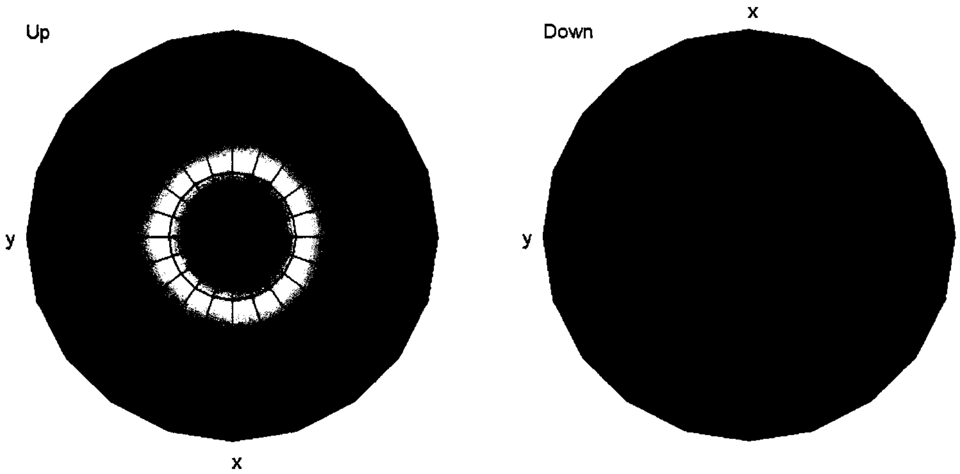

Figure 6.43. Simulated backprojection image using the reconstruction parameters from Figure 6.37 except with normalization by image pixel area.

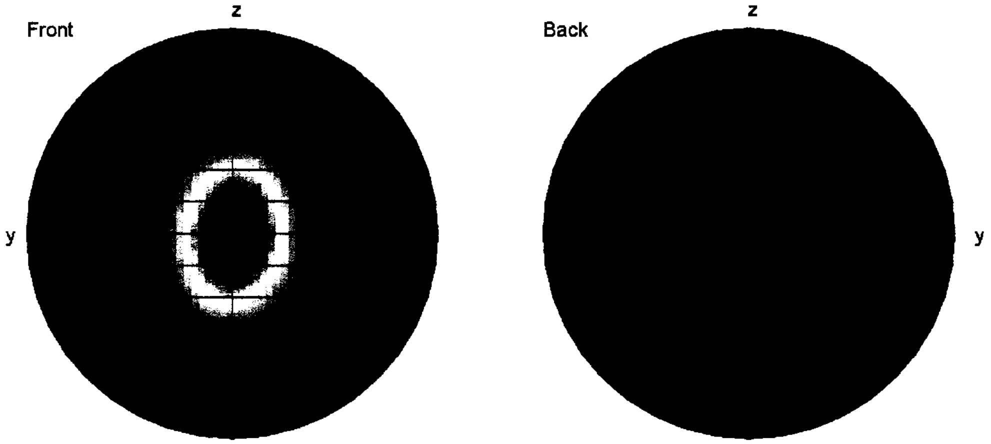

Figure 6.44. Simulated backprojection image using the reconstruction parameters from Figure 6.38 except with normalization by image pixel area.

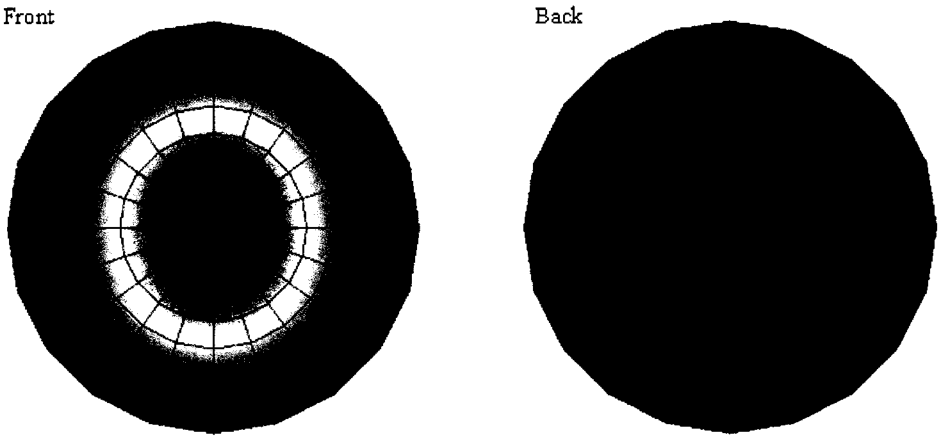

Figure 6.45. Simulated backprojection image using the reconstruction parameters from Figure 6.38 except with the image sphere rotated by 90°.

In this case the shape of the response, whether it is circular or elliptical—is less important than the ability to distinguish two sources, and the method that produces the best resolution should be chosen. However, the conservation of sequences normalization is used throughout the backprojection reconstruction in this work, and it is recognized that the resulting resolutions are therefore conservative. Furthermore, the preceding analyses regarding other factors that degrade the performance of the imager are unaffected by the shape of the point source response, and can be illustrated with any of the backprojection normalization methods.

6.5 Predicted Performance of the 4π Compton Imager

6.5.1 Imaging resolution

Most of the factors discussed in this chapter were taken into account in generating the images shown in Chapter 5, and the imaging resolutions presented there (55° FWHM for backprojection and 16° FWHM for 10 iterations of WMLEM at 662 keV) should nearly predict the performance of the 4π Compton imager. Doppler broadening, pair production, and Rayleigh scatter were modeled in the simulations. When multiple interactions occurred under a single pixel, the energies were summed and the depths were averaged such that the two events appear as one. The true sequence orders from the simulated data were ignored, and sequence reconstruction techniques were used to determine the order of events. The anode threshold and limited dynamic range were not modeled in Chapter 5, and those effects are examined here. In addition the imaging resolution is predicted at other gamma-ray energies.

Table 6.4. Backprojection Imaging Resolution in Degrees FWHM for Simulated Source to the Side of the Detector with the Given Anode Threshold/Dynamic Range

Energy (keV)	0 keV/unlimited	100 keV/1600 keV
300	44.5°	47.0°
662	57.0°	61.5°
1500	40.5°	44.0°
2500	39.5°	27.0°

Table 6.5. Weighted MLEM Imaging Resolution in Degrees FWHM for Simulated Source to the Side of the Detector with the Given Anode Threshold/Dynamic Range

Energy (keV)	0 keV/unlimited	100 keV/1600 keV
300	14.5°	24.5°
662	16.0°	16.0°
1500	15.0°	10.5°
2500	15.5°	6.0°

Backprojection imaging resolutions, given in Table 6.4, were calculated for a simulated source to the side of the detector given 0 keV anode thresholds and unlimited dynamic range as well as 100 keV anode threshold and a 1600 keV dynamic range. The worst performance was 62° at 662 keV, where backprojecting the incorrect two-pixel sequence orders creates a ring around the true source location and widens the point source response. In most cases the imaging resolution was worsened when the anode threshold was considered. The best simulated resolution occurred at 2.5 MeV, where the backprojection imaging resolution was 27°. In this case the limited dynamic range prevents the large scatter angle sequences from being observed. The backscatter sequences have high uncertainty, as previously discussed in Chapter 5. Eliminating these sequences actually improves the angular resolution, although the imaging efficiency is greatly reduced.

The imaging resolutions calculated for the same data reconstructed with the weighted maximum likelihood method after 10 iterations are given in Table 6.5. These resolutions are calculated for a constant source strength, not a constant count rate. Thus, the predicted value is the imaging resolution that can be expected for sources with the same gamma-ray emission rate at a constant distance from the detector for the same amount of acquisition time. As discussed in Chapter 5, the convergence speed of the image using maximum likelihood is dependent on the number of counts in the image. Comparable resolutions are obtained at all energies with no threshold and unlimited dynamic range, despite the fact that more sequences are included in the 300 keV image than in the 2500 keV image.

At 1500 keV the resolution improved from 15.0° to 10.5° when the 100 keV threshold was considered. At 2500 keV the improvement was even more drastic: from 15.5° to 6° FWHM. With fewer counts in the image, it is expected that the resolution should improve: fewer counts result in faster convergence. At 662 keV the limiting factor is the backprojection of incorrectly sequenced events, and no change was observed with and without accounting for the anode threshold.

The surprising result is at 300 keV, where the resolution worsened despite the decrease in the number of events. The unobservable events are those in which the first interaction deposits less than 100 keV. Thus, the only two-pixel sequences that are observed and correctly sequenced are those in which the first scatter deposits between 100 and 150 keV, corresponding to a range of scatter angles from 81° to 135°. The 200 keV scattered gamma-ray will not travel far, and will most likely be absorbed in one the eight surrounding pixels. The geometric uncertainty for these sequences is about 15°, with a minimum added energy contribution of 5° FWHM, as seen in Section 5.2.3. For larger scatter angles, the energy uncertainty quickly increases and dominates the total angular uncertainty for 300 keV gamma rays. The backprojection imaging resolution is too poor to see a dramatic effect, although it did worsen somewhat when the threshold was considered.

6.5.2 Imaging efficiency

The concept of imaging efficiency for this detector is not straightforward. Typically, the intrinsic efficiency is defined as the fraction of incident gamma rays that contribute to the image. In the case of the 4π Compton imager, some sequences result in an incorrect backprojection cone due to charge sharing, multiple events, incorrect event sequencing, etc.; these sequences are still imaged. It is possible to count instead the number of backprojection cones that intersect the true source location. However, even when the backprojection cone is not correctly determined it is possible for the ring in the image to accidentally intersect at the true source location. This effect is especially pronounced for physically large sources and for high-uncertainty sequences, where either the object or the backprojected cone subtend a significant fraction of the field-of-view. Furthermore, each correctly backprojected sequence also contributes to noise in the image outside of the true source location. If the sequence order were known, the pixel size were small, the anode threshold were very low, and the dynamic range of the ASICs were infinite, then almost all sequences would be correctly imaged, and it would be sufficient to predict the fraction of incident gamma rays that yield full-energy two- or three-pixel sequences. In reality this will overestimate the performance of the imager.

In this work efficiency losses calculated in simulations have been discussed as fractions of what would otherwise have been useful sequences. It is possible to adopt a strict definition of imaging efficiency: the fraction of incident gamma rays that result in useful sequences. A useful sequence would be one in which the full gamma-ray energy is deposited, the sequence order is correctly determined, pair production does not occur, the effect of multiple interactions under one pixel is small, there is no charge sharing, and all events deposit energies between the anode threshold and the maximum observable energy due to the ASIC dynamic range. In reality it is impossible to determine if the correct sequence order was chosen, if the gamma ray interacted more than once under one pixel, or if charge sharing occurred. If the gamma-ray energy is known, all that can be determined absolutely is that the total energy was deposited in the observed events, no pair production occurred, and the sequence passed the Compton edge test. Thus, the intrinsic imaging efficiency must be defined as the fraction of incident gamma rays that satisfy those three criteria. This provides the best measurable metric for efficiency, and in fact is identical to the first definition of intrinsic efficiency discussed in this section. Only sequences that satisfy the three criteria are imaged, and thus the fraction of incident gamma rays resulting in imaged sequences is the intrinsic imaging efficiency.

Table 6.6. Intrinsic Imaging Efficiency for Simulated Source to the Side of the Detector with the Given Anode Threshold/Dynamic Range

Energy (keV)	0 keV/unlimited	100 keV/1600 keV
300	14.2%	6.3%
662	5.5%	4.6%
1500	2.4%	2.2%
2500	1.4%	0.14%

Efficiencies are calculated for the 4π imager assuming 0 keV threshold and unlimited dynamic range as well as 100 keV threshold and 1600 keV dynamic range. The latter represents the current detector design, while the former represents what the imager is capable of if the electronics were perfect. The intrinsic imaging efficiencies are listed for selected energies in Table 6.6. At 300 keV, the anode threshold is the main cause for the reduction in efficiency from 14% to 6%. At 2500 keV, the loss in efficiency is a direct result of the limited dynamic range. At 662 keV, the 4π Compton imager is expected to have an intrinsic imaging efficiency of 4.6% for a source to the side of the detector.

6.6 References

[1] R. Cesareo, A.L. Hanson, G.E. Gigante, L.J. Pedraza, S.Q.G Mahtaboally, "Interaction of keV photons with matter and new applications," *Physics Reports*, vol. 213, pp. 117-178, 1992.

[2] R. Ribberfors, K.-F. Berggren, "Incoherent x-ray scattering functions and cross sections by means of a pocket calculator," *Physical Review A*, vol. 26, pp. 3325-3333, 1982.

[3] F. Biggs, L.B. Mendelsohn, J.B. Mann, "Hartree-Fock Compton profiles for the elements," *Atomic Data and Nuclear Data Tables*, vol. 16, pp. 201-309, 1975.

[4] E. Novikova, "Testing LECS: Doppler Broadening Extension of Geant4," *Unpublished* 2003.

[5] S. Agostinelli, J. Allison, K. Amako, J. Apostolakis, H. Araujo, P. Arce, M. Asai, D. Axen, S. Banerjee, G. Barrand, F. Behner, L. Bellegamba, J. Boudreau, L. Broglia, A. Brunengo, H. Burkhardt, S. Chauvie, J. Chuma, R. Chytracek, G. Cooperman, et al., "Geant4 - a simulation toolkit," *Nuclear Instruments and Methods in Physics Research*, vol. A506, pp. 250-303, 20003.

[6] M. J. Berger, J.H. Hubbell, S.M. Seltzer, J.S. Coursey, D.S. Zucker, "XCOM: Photon cross sections database," [Online], 2004.

[7] Y. F. Du, Z. He, W. Li, G.F. Knoll, D.K. Wehe, "Monte Carlo investigation of the charge sharing effects in 3-D position-sensitive CdZnTe gamma ray spectrometers," *IEEE Transactions on Nuclear Science*, vol. 46, pp. 844-847, 1999.

[8] D. Xu, personal communication, January 2004.

CHAPTER 7

MEASURED PERFORMANCE OF THE 4π COMPTON IMAGER

7.1 Introduction

The performance of the 4π Compton imager was measured using sealed point-like radiation sources with gamma-ray energies ranging from 276 keV to 835 keV. These sources were used individually to measure imaging efficiency and resolution as well as combined to test the response of the imager to multiple sources. In addition, a Th disk source (2.6 MeV) was also imaged to test the high-energy imaging capabilities. Finally, a large $^{1}H(n,\gamma)^{2}H$ spherical gamma-ray source (2.2 MeV) was used for demonstrating imaging of extended sources. This chapter describes the experiments performed and characterizes the measured performance of the imager.

7.2 Intrinsic Imaging Efficiency

The intrinsic imaging efficiency was measured using calibrated sealed ^{133}Ba, ^{22}Na, ^{137}Cs, and ^{54}Mn sources placed to the side of the detector. The known activities of the sources were used with the geometric efficiency to determine the rate at which gamma rays are incident on the detector. The fraction of incident gamma rays that are imageable (i.e. all the energy is deposited and the sequence passes the Compton edge test) is the measured intrinsic efficiency. The geometric efficiency ($\Omega/4\pi$) is calculated from Equation 7.1 for a detector width and depth specified by $2x$ and $2z$, respectively, and a source-to-detector spacing of d. This equation can be derived from basic geometry considerations.

$$\frac{\Omega}{4\pi} = \frac{1}{\pi}\tan^{-1}\left[\frac{xz}{d\sqrt{x^2 + z^2 + d^2}}\right] \tag{7.1}$$

The geometric efficiency for a point source 20 cm from the 1.5 cm × 1.0 cm side of the detector is 0.03%. The measured intrinsic imaging efficiencies are given in Table 7.1 for selected energies. At 662 keV, the efficiency is 1.84%. This is much larger than that of the previous two-detector design, which had an efficiency of 0.00153%[1]. However, the measured efficiency is less than half the predicted value of 4.6% (discussed in Chapter 6). Charge sharing, which was discussed in Chapter 6 but not taken into account in estimating the efficiencies, should cause a reduction in efficiency (due to two- and three-pixel sequences appearing as four or more events) on the order of 18%, not 60% as observed here.

Table 7.1. Measured Intrinsic Imaging Efficiency for Source to the Side of the Detector

Energy (keV)	Efficiency
356	3.07%
511	2.45%
662	1.84%
835	1.28%

There are six unused channels on this detector. When these pixels are taken into account in the simulated data, the predicted efficiency at 662 keV reduces by 10% of the previous value to 4.2%. There is still a 56% discrepancy between the measured and predicted values for efficiency.

A predicted 86% of sequences should be imageable (i.e. pass the Compton edge test after sequencing). In the measured data only 78.1% of observed sequences were imageable. If the same number of sequences were observed for both simulated and measured data, this difference would account for a 9% difference in efficiency. However, the same number of sequences was not observed in the measured and predicted data. In measurements only 18254 two-pixel and 4287 three-pixel full-energy 662 keV sequences were observed in 10800 seconds. For the given source strength (349.4 kBq), geometric efficiency, and acquisition time, simulations predict 42537 and 6427 counts, respectively, for two- and three-pixel full energy sequences (taking into account the anode threshold and unused pixels). The total reduction in observed two- and three-pixel sequences from simulation to measurement is 54% of the predicted value. This decrease in observed events—and not any sequencing or image reconstruction process—accounts for most of the 56% discrepancy in the predicted and measured efficiencies.

In fact comparing the intrinsic peak efficiencies between simulations and measurements also yields a large discrepancy. This efficiency includes all observed full-energy sequences, regardless of the number of interactions or imageability. The simulated intrinsic peak efficiency was 11.8%, while a value of 4.4% was measured. However, the intrinsic total efficiencies (number of sequences at all energies) are comparable at 33.8% simulated and 35.8% measured. Total efficiencies are highly subject to surrounding material in which the gamma rays may scatter before interacting in the detector; no surrounding materials were included in the simulations. Furthermore, these external scatter sites only add to the total observed count rates. If surrounding materials were included in the simulations, the simulated total efficiency would increase, resulting in a higher estimated efficiency than the measured efficiency, as is the case with the peak efficiency and the imaging efficiency discussed above.

The reduction in events may be partly due to the material between the source and detector, which was not modeled in the simulations. The detector is encased in an aluminum box approximately 2 mm thick. This expected attenuation of 662 keV gamma rays through the box is less than 4%. For stability the detector is anchored to the hybrid card with a polyvinyl chloride (PVC) mounting structure that is approximately 4 cm thick. Very little attenuation of gamma rays is expected in the material due to the low atomic numbers (C_2H_3Cl) and low density (~1.4 g/cm^3). Upon further investigation, it was discovered that the PVC may include a Pb additive for stability and rigidity. The concentration of lead in the PVC is unknown, but would be typically below 10%. In the worst case, the attenuation coefficient of the lead filled PVC is 0.0824 cm^2/g at 662 keV[2], and the expected loss of gamma rays in the mount is about 37%.

If the PVC were the main cause for the reduced efficiency, the effect would be more pronounced for low energy gamma rays. However, this is not observed. At 356 keV, lead-filled PVC would have an attenuation coefficient of 0.122 cm^2/g. The expected reduction in gamma-ray flux at this energy is nearly 50%, compared with 37% for 662 keV photons. The difference between the predicted and measured efficiencies should therefore be more than that observed at 662 keV. At 300 keV, the predicted efficiency was 6.3%, while the measured efficiency at 356 keV was 3.07%, resulting in an estimated discrepancy of 52% before taking into account charge sharing and the six unused pixels. This is less than the 56% discrepancy at 662 keV, indicating that the PVC may not be the most significant factor.

In addition, as shown previously in Figure 3.4, the PVC mount does not completely encase the detector. There is a circular hole in the mount at the top such that the cathode surface is visible. This hole exposes only 35% of the cathode surface, but the thickness of PVC near the edges of the detector is only 5 mm when the detector is irradiated from the top. Thus, a comparison between calculated and measured efficiencies can be made using a source above the detector. The predicted efficiency is 3.8%, but an efficiency of 1.9% is measured. Only an estimated 5% of gamma rays could be attenuated in the lead-filled PVC, and yet the measured efficiency is still only half of the predicted value (before charge sharing and unused pixels are taken into account).

Another possible cause for the difference between simulated and observed efficiencies is the estimated density of the material. A value of 6 g/cm^3 was used in simulation, but the true density of the CdZnTe crystal used in the detector is not known. However, a 10% error in the density causes only a 4% error in the attenuation of gamma rays through the detector. This cannot be the full cause for the discrepancy, although it may make a small contribution.

It is also possible that some events, particularly those near the anode surface, are not measured. As discussed in Chapter 2, when an interaction occurs very close to the anode, the signal measured on the anode will be small. If the anode timing signal does not exceed the set threshold, it will not trigger, and the event will not be registered. For the maximum observable energy in a Compton event (477 keV for 662 keV photons) the 0.2 mm nearest the anode are unusable. This decreases the total detector volume by 2%. For a 200 keV energy deposition, the final 0.5 mm are unusable, resulting in a volume decrease of 5%. This effect cannot account for the discrepancy alone.

In the end it is difficult to explain why the measured efficiency is less than half the predicted efficiency at all energies. This effect was observed for sources both above and to the side of the detector. It is clear that the major culprit is the loss of two- and three-pixel sequences overall, and the discrepancy was not caused by the sequencing or image reconstruction techniques.

7.3 Imaging Resolution

The imaging resolution at different energies was tested with standard sealed sources: ^{137}Cs, ^{133}Ba, ^{22}Na, and ^{54}Mn. The sources were placed 20 cm from the detector along the *x*-axis. The backprojection image of the ^{137}Cs point source (662 keV) is shown in Figure 7.1, and the weighted maximum likelihood (WMLEM) image after 10 iterations is shown in Figure 7.2. Full-energy two- and three-pixel sequences were imaged. The imaging resolution is given by the full-width at half-maximum (FWHM) of a slice through the center of the image in the *x-z* plane. The measured imaging resolutions were 68° FWHM and 17° FWHM, respectively, for backprojection and WMLEM. The

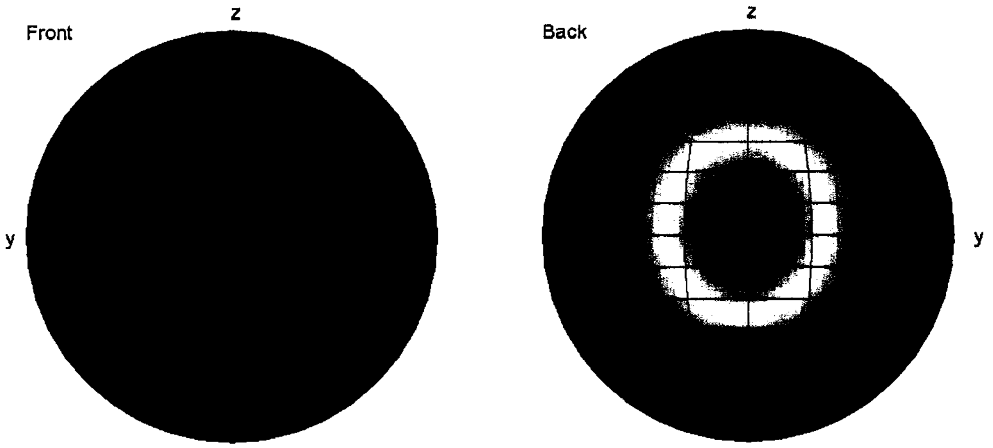

Figure 7.1. Backprojection image of measured ^{137}Cs source. Full-energy two- and three-pixel sequences are imaged.

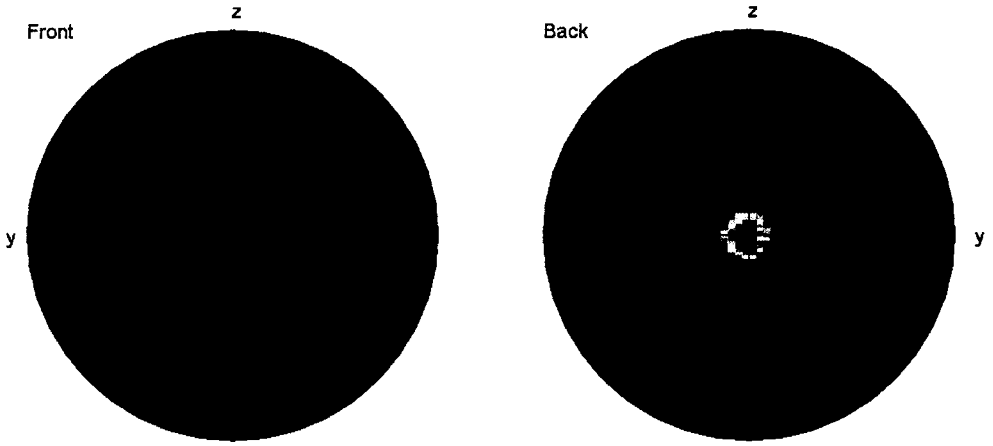

Figure 7.2. Weighted maximum likelihood image of measured ^{137}Cs source. Full-energy two- and three-pixel sequences are imaged.

Table 7.2. Measured Imaging Resolution in Degrees FWHM using Backprojection and WMLEM for Source to the Side of the Detector

Energy (keV)	Backprojection	WMLEM
356	39.5°	17.0°
511	69.5°	19.0°
662	68.0°	17.0°
835	60.5°	14.5°

backprojection resolution is worse than the predicted value of 61.5° (discussed in Chapter 6), although the measured WMLEM image is close to the predicted 16° resolution. As discussed in Chapter 5 the convergence speed of any MLEM reconstruction algorithm is dependent on the source distribution and the number of events in the image. The predicted resolutions in Chapter 6 were calculated for a constant gamma-ray emission rate, source distance, and acquisition time. In the measurements performed here the acquisition time is adjusted to account for the variability in the gamma-ray emission rates of each source. The source distance is held constant at 20 cm. The measured imaging resolutions for selected gamma-ray energies are given in Table 7.2 for backprojection and weighted maximum likelihood.

The worst imaging resolutions for both backprojection (69.5° FWHM) and WMLEM (19.0° FWHM) were measured at 511 keV. This is not surprising because many sequences are incorrectly ordered, and the result is a broadening of point source response, as discussed in Chapter 6. The best performance for backprojection was observed for 356 keV photons from ^{133}Ba. This is predicted from simulations where the lowest gamma-ray energy tested resulted in the best backprojection performance. The best WMLEM imaging resolution was 14.5° observed for ^{54}Mn at 835 keV, again following the predicted behavior that the highest energy tested yields the best imaging resolution for WMLEM.

7.4 Multiple Gamma-Ray Sources

7.4.1 Two-source resolution test

The resolutions measured in the previous section were calculated using the point source response of the system. To test the measured resolution at 662 keV two ^{137}Cs sources were placed 9° degrees on either side of the *x*-axis at 20 cm from the detector for a total of 18° separation. The backprojection image is not expected to resolve the two sources, and as shown in Figure 7.3 the sources cannot be distinguished. The WMLEM reconstructed image is shown in Figure 7.4, and the two sources are just barely resolved. The source on the right in the image has a higher activity than the source on the left, and this is reflected in the brightness of each source. A slice through the center of the image, shown in Figure 7.5, shows that the two sources are just barely resolved.

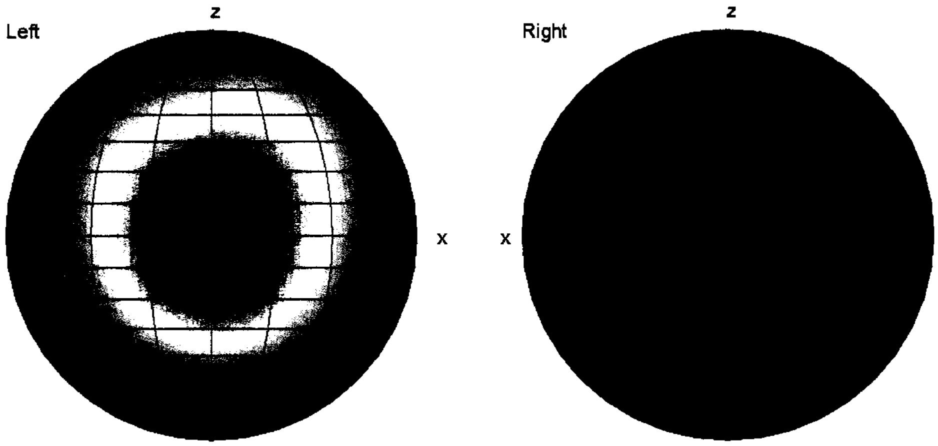

Figure 7.3. Backprojection image of two ^{137}Cs sources separated by 18° at 20 cm from the detector. The two sources cannot be resolved.

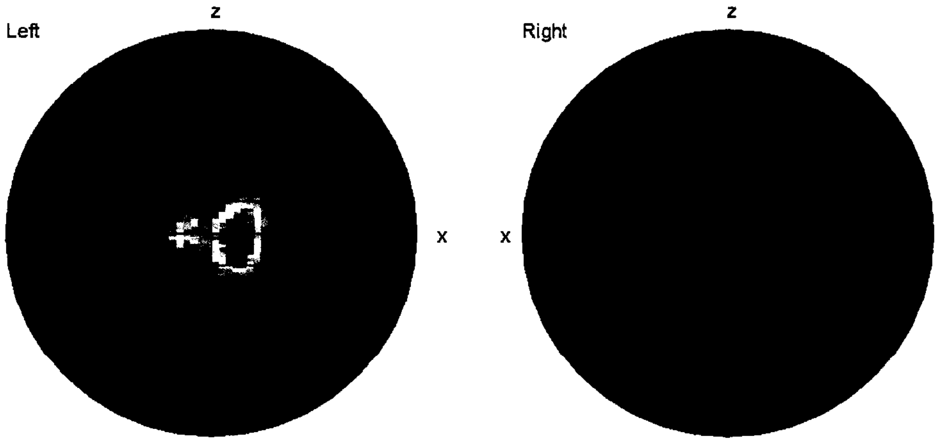

Figure 7.4 WMLEM image of two ^{137}Cs sources separated by 18° at 20 cm from the detector. The two sources can be resolved.

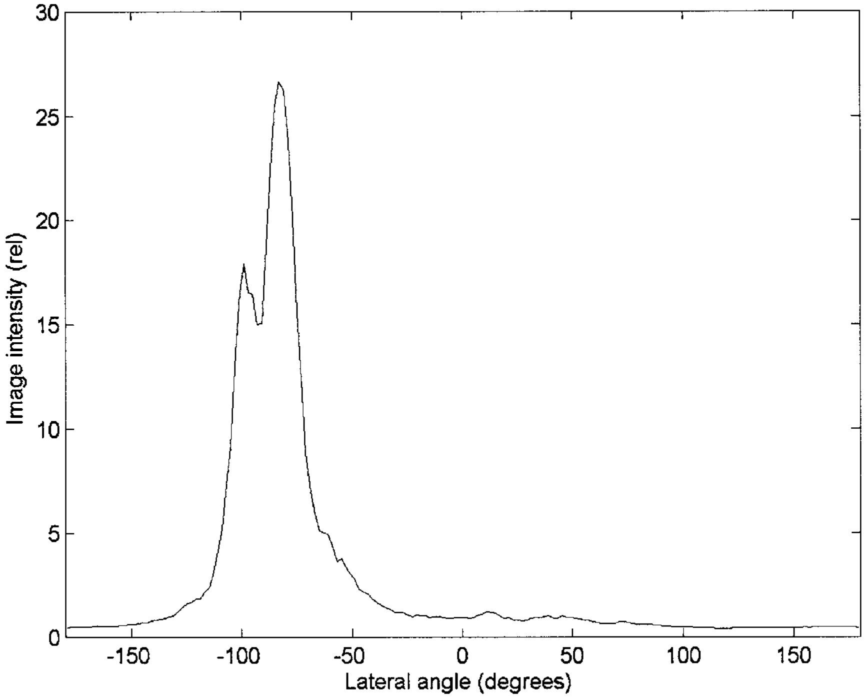

Figure 7.5. Slice of the WMLEM image shown in Figure 7.4. The two sources can be resolved.

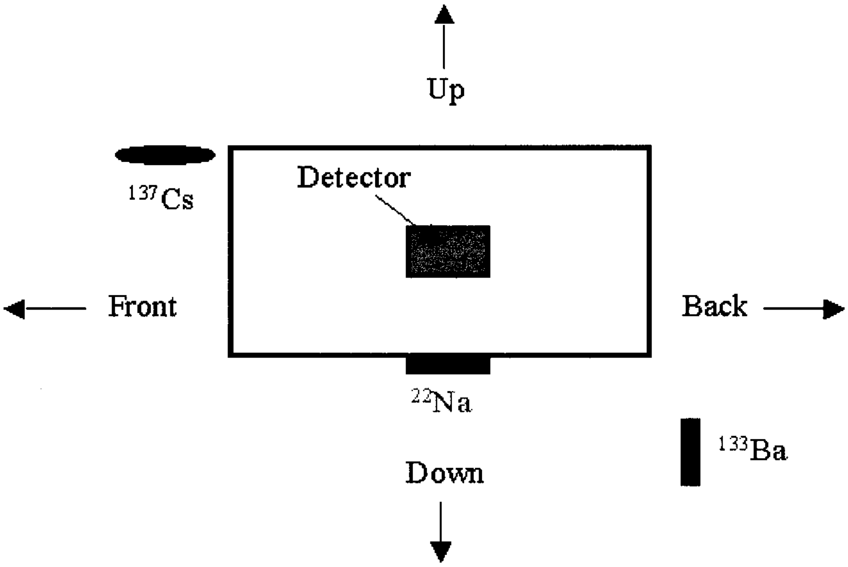

Figure 7.6. Illustration of source configuration for multiple source imaging.

7.4.2 Multiple gamma-ray energies

Three sources (^{137}Cs, ^{22}Na, and ^{133}Ba) were placed near the detector in the configuration shown in Figure 7.6. The backprojection image generated using all imageable events is shown in Figure 7.7. No energy windows are used. The ^{137}Cs source to the front of the detector appears much brighter than the other sources, due to a difference in source activities and the anisotropy discussed in Chapter 6, but all sources are visible.

Separate images can be generated for each isotope by only reconstructing the appropriate full energy windows. Figures 7.8 and 7.9 show the three images generated by simple backprojection and WMLEM, respectively, using energy windows of 340-370 keV (^{133}Ba: 356 keV), 480-450 keV (^{22}Na: 511 keV), and 630-700 keV (^{137}Cs: 662 keV). Each source is easily identified when only the photopeaks are reconstructed in separate images. The WMLEM image in Figure 7.9 shows better imaging resolution, for all sources, as expected. The ^{22}Na source below the detector appears slightly broadened compared with the other two sources.

This analysis indicates that the preferred method of imaging sources with varying activities and energies may be to generate a three-dimensional backprojection image using the two angular coordinates that define a sphere and an additional energy coordinate based on the observed total energy in the sequence. Each backprojection ring would contribute to only one energy coordinate. Summing over all energies would yield an image similar to that shown in Figure 7.7. It would also be possible to sum over a small range of energies and achieve the images shown in Figures 7.8 and 7.9 without requiring that the data be reconstructed individually for each energy. A similar concept has been proposed for coded aperture imaging[3].

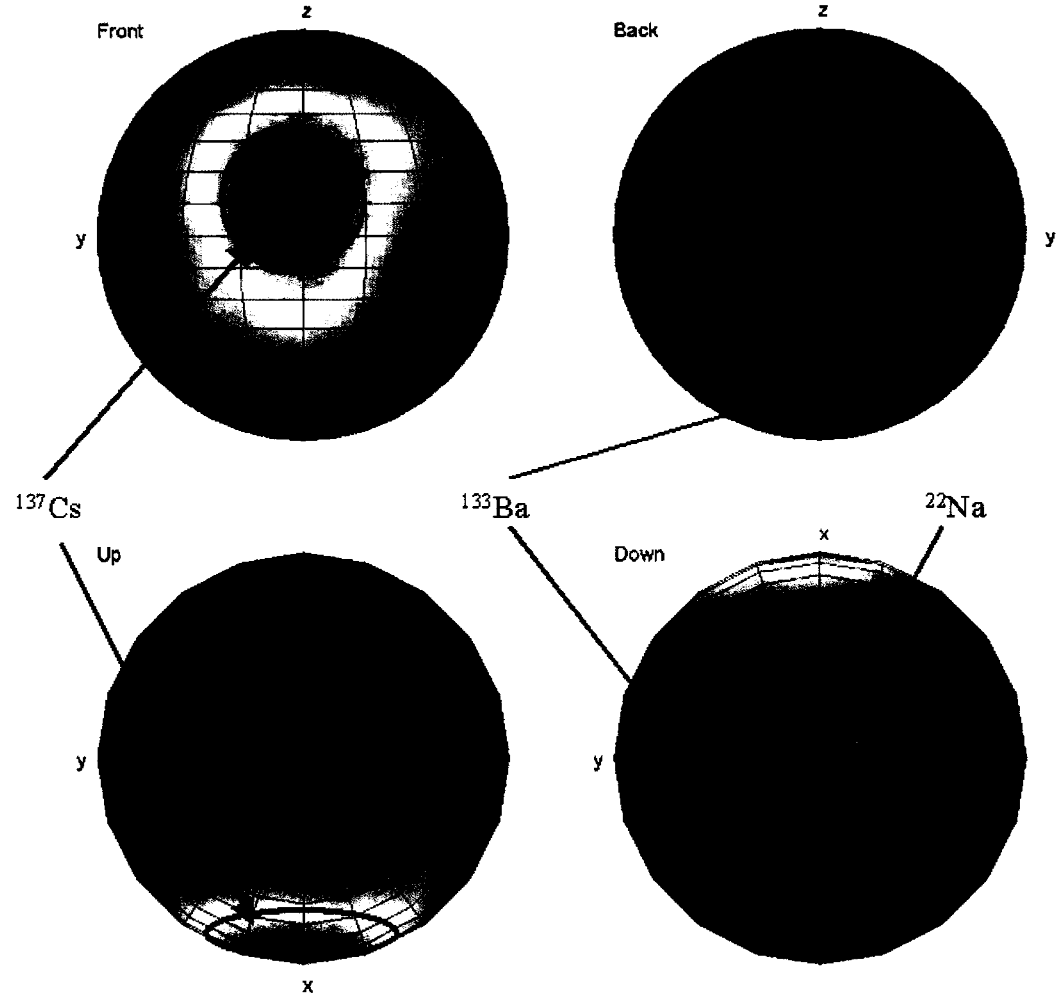

Figure 7.7. Backprojection image of multiple sources without energy selection viewing a) the front and back and b) the top and bottom of the detector.

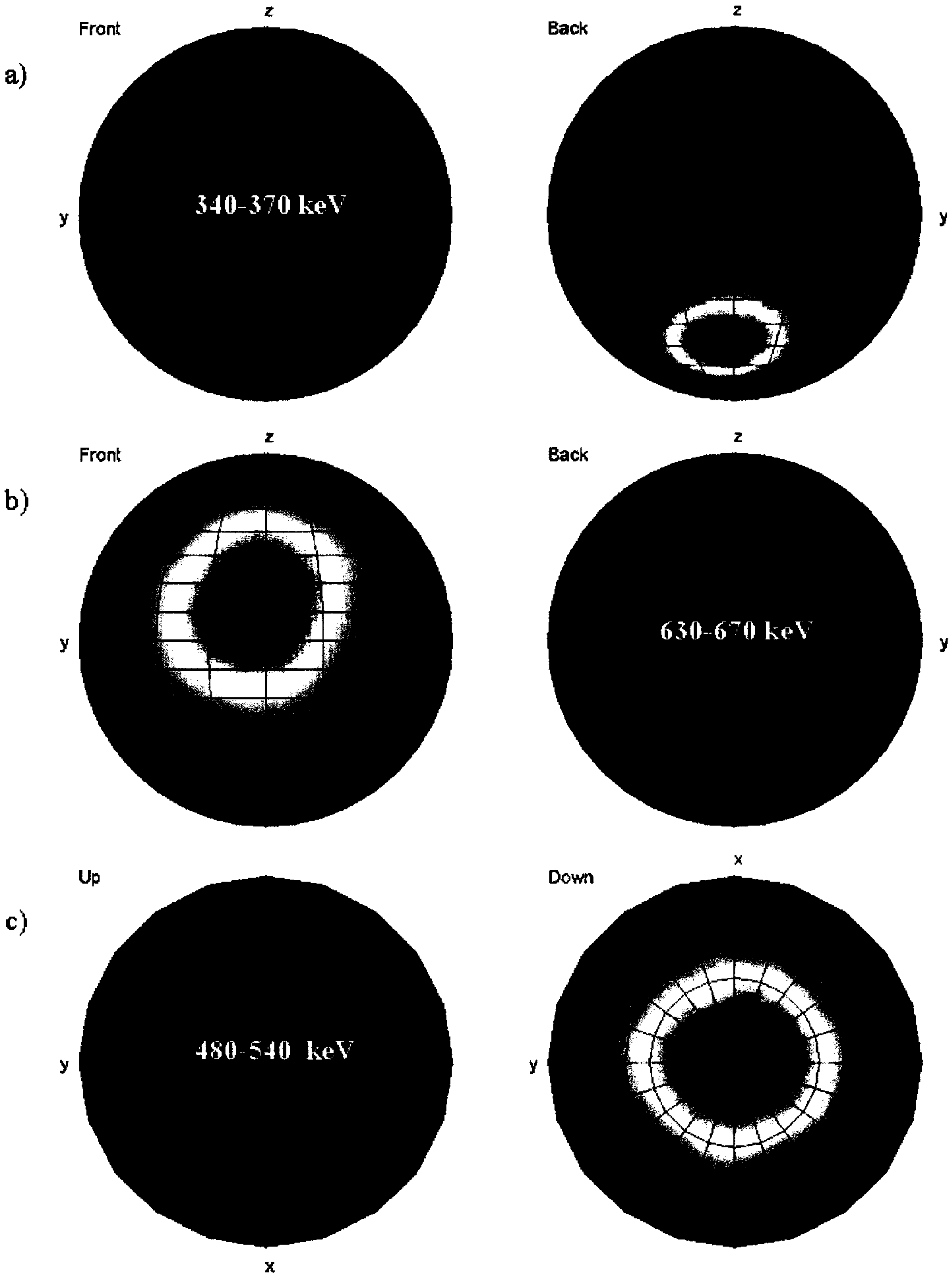

Figure 7.8. Backprojection image of multiple source data reconstructed separately with different energy windows: a) 340-370 keV, b) 630-670 keV, and c) 480-540 keV.

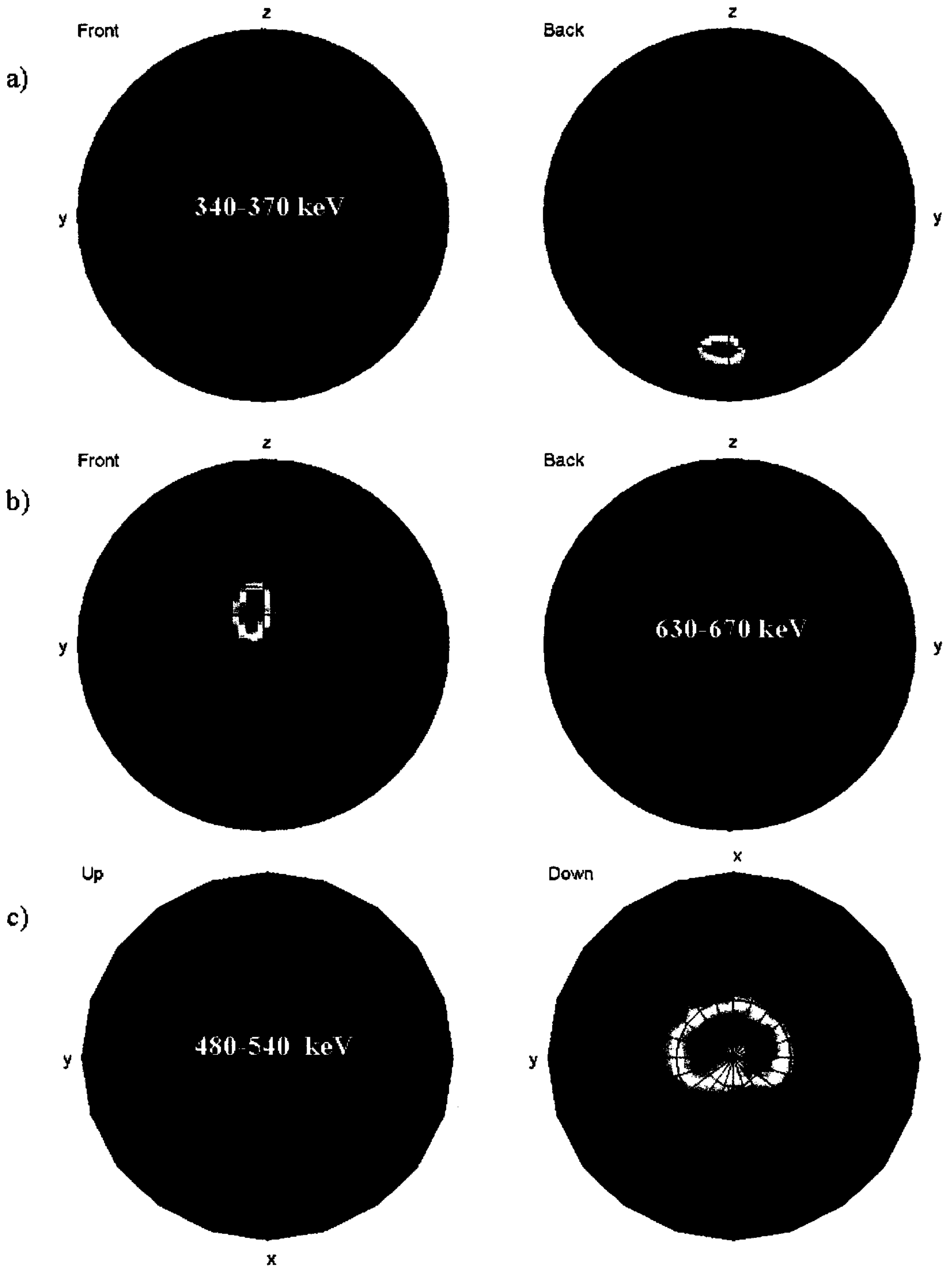

Figure 7.9. WMLEM image of multiple source data reconstructed separately with different energy windows: a) 340-370 keV, b) 630-670 keV, and c) 480-540 keV.

7.5 High-Energy Imaging

7.5.1 ^{232}Th disk source

Detection of enriched uranium is important in many defense applications. All enriched uranium produced in the United States contains some amount of ^{232}U, which is preferentially selected during the low-mass isotopic separation[4]. The decay scheme of ^{232}U is shown in Figure 7.10. Most of the alpha decays do not have an associated gamma emission; however, the beta decay of ^{208}Tl to ^{208}Pb (stable) is followed by a 2.614 MeV gamma ray. Thus, observing a 2.6 MeV photopeak in the energy spectrum can indicate the presence of enriched uranium. ^{232}Th also enters the ^{232}U decay chain, as shown in Figure 7.10. In this way, a ^{232}Th source can mimic the high-energy signature of ^{232}U. In this section the response of the detector to 2.6 MeV gamma rays is examined with the use of a thorium disk source.

Because the dynamic range of the VAS2/TAT2 system is only 1000 keV, the VAS3/TAT3, which has a dynamic range of 1600 keV, was used for measuring the response to 2.6 MeV gamma rays. With this system, two events can sum to the full

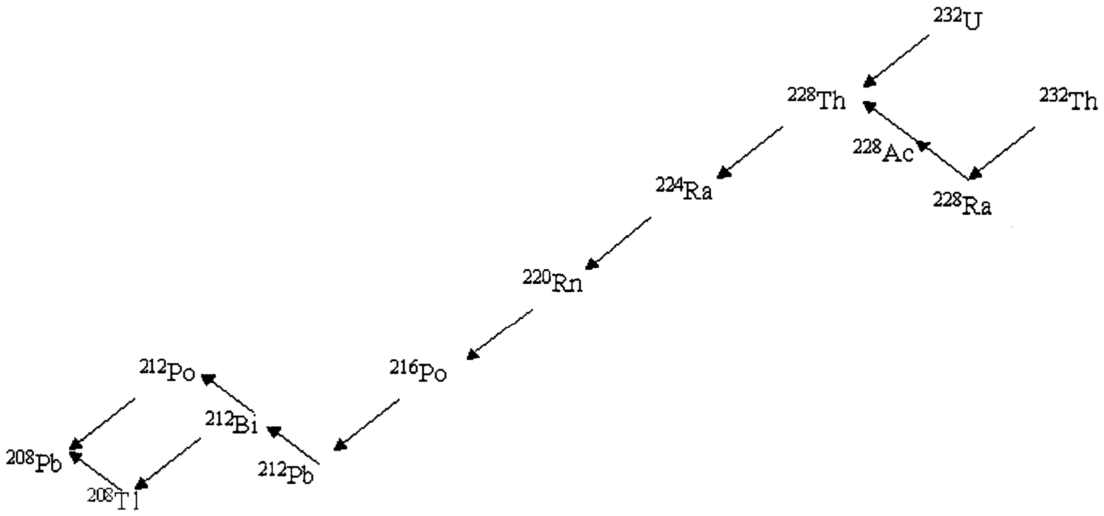

Figure 7.10. Decay scheme for ^{232}U. The 2.6 MeV gamma rays are emitted by ^{208}Tl.

gamma-ray energy. An uncalibrated thorium disk source was placed 3 cm above the detector. The observed energy spectra for two-, three-, and four-pixel sequences are shown in Figure 7.11. The 2.6 MeV peak is evident along with its single and double escape peaks, as are peaks at other various energies. These are gamma rays released in the decays of other daughter products in the decay chain. Note that the double escape peak is still prominent in the four-pixel spectrum. This is due to charge sharing. At 1.6 MeV, the electron range is larger than the pixel pitch, and more than one pixel may collect charge. When charge sharing is significant, it is necessary to exclude sequences in which neighboring pixels both collect charge.

Using two-pixel sequences, the backprojection image was obtained as in Figure 7.12. The source location cannot be determined due to the charge sharing. The axis of the backprojection cone will always be parallel with either the *x*- or *y*-axis because

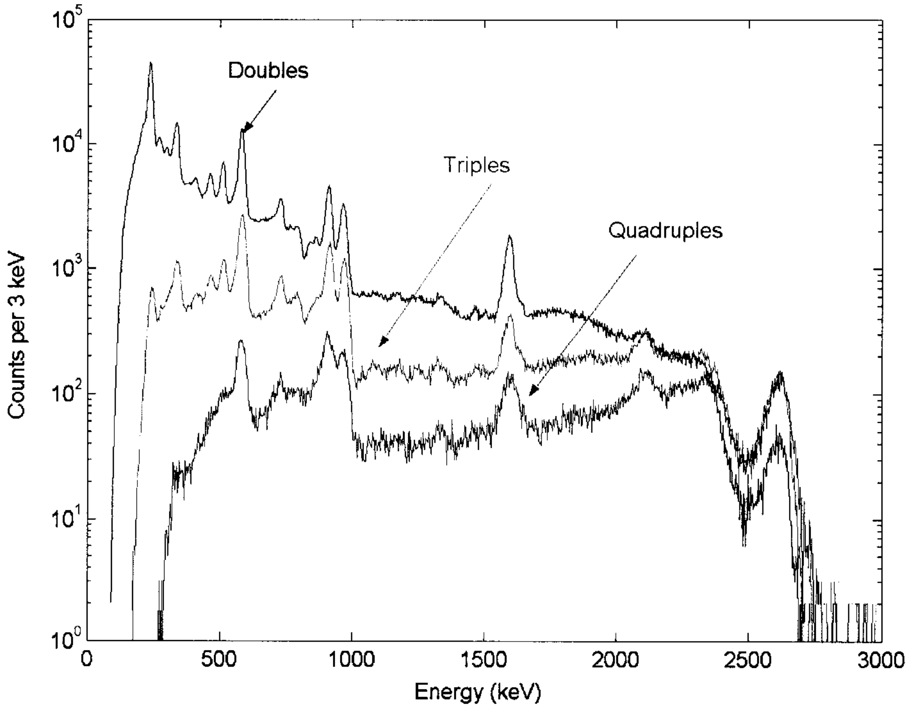

Figure 7.11. Thorium disk two-, three-, and four-pixel energy spectra measured using the VAS3/TAT3 system.

neighboring pixels both collect charge at the same depth. However, when nearest neighbor pixels are excluded from contributing, the backprojection appears as in Figure 7.13. Now, clearly the image points to the correct source location.

The efficiency of the 4π imager at 2.6 MeV could not be accurately measured because the activity of the thorium disk was unknown, but an order-of-magnitude estimation can be made. The emission rate of the 2.6 MeV gamma ray was estimated

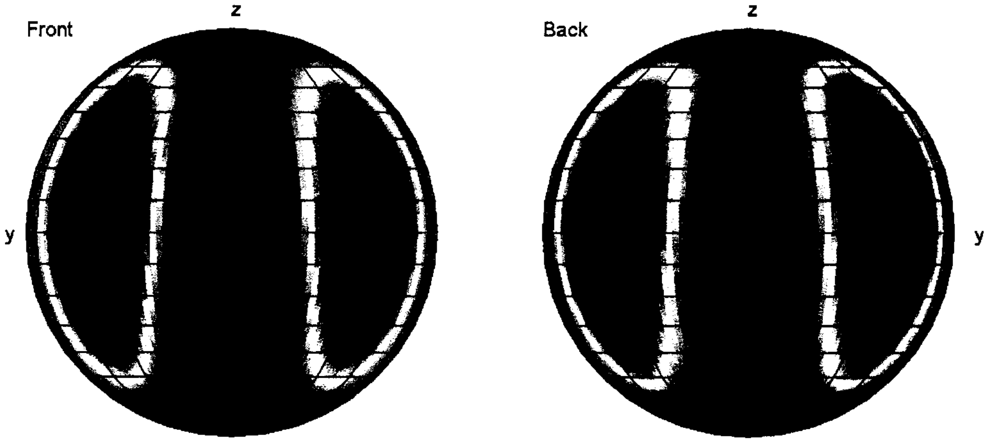

Figure 7.12. Backprojection image of the thorium disk source using two-pixel sequences. This image behavior is typical of charge sharing events, in which the cone axes are always located along the *x*- or *y*-axis.

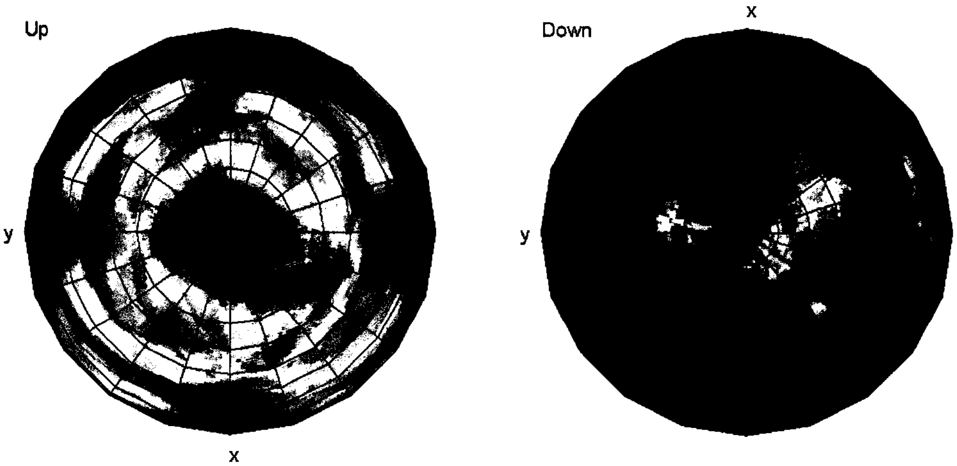

Figure 7.13. Backprojection image of the thorium disk source using two-pixel sequences with non-neighboring events. Much of the charge sharing contribution has been eliminated.

using a standard 2″×2″ NaI(Tl) scintillator detector. Efficiency curves for these detectors are well known[5]. The observed count rate at 2.6 MeV in the NaI(Tl) detector was 933 cpm. With a known NaI(Tl) absolute efficiency of 0.04 and a peak-to-total ratio of 0.125 for a source at 2.5 cm, the estimated emission rate of 2.6 MeV gamma rays from the thorium disk is 2634 γ/s. The dynamic range of the ASIC and effects of charge sharing limited the imageable two-pixel sequences in the CdZnTe detector to 187 over 36 hours of measurement. The geometric efficiency of a point source 3 cm from a square detector with sides 1.5 cm is 0.0187. The calculated intrinsic efficiency is then 2.9×10^{-5}. This is two orders of magnitude lower than the calculated efficiency using simulated 2.5 MeV data. The discrepancy between the simulated and measured data is clear: charge sharing was not modeled in the simulations. Although the simulations did take into account the reduction in efficiency due to eliminating sequences in which neighbor pixels collect charge, the simulations did not model the effects of two-pixel sequences appearing as three- or four-pixel sequences. At 2.5 MeV the number of full-energy two-pixel sequences is predicted to be double that of the three-pixel sequences, but this is not observed in the 2.6 MeV peak areas in Figure 7.11. Charge sharing is the major culprit for the reduction in the two-pixel peak efficiency from the predicted value.

7.5.2 High-energy distributed source

Mapping hydrogen concentrations can be very important for interplanetary rover missions. The presence or absence of water is key to understanding the formation of planets in the solar system. One common way to detect the presence of hydrogen in water is to bombard the surface with neutrons, which are thermalized in the hydrogen. The neutrons can be captured by the hydrogen nuclei forming deuterium, which deexcites via a 2.2 MeV gamma ray. Therefore, observing a 2.223 MeV gamma ray is indicative of the $^{1}H(n,\gamma)^{2}H$ process.

In this experiment a 1-Ci ^{239}PuBe neutron source was placed at the center of a high-density polyethylene sphere, as shown in Figure 7.14. Neutrons are thermalized and captured throughout the sphere, which becomes a large and nearly isotropic emitter of 2.2 MeV gamma rays. Some of these gamma rays reach the detector and interact in observable sequences that can be used for imaging. The center of the sphere was located approximately 45 cm from the detector. The single-, double-, triple-, and quadruple-pixel energy spectra observed from this source are shown in Figure 7.15. There is a full-energy peak at 2.2 MeV, as expected, and its associated single and double escape peaks can also be seen. The limited dynamic range is evident in the single-pixel spectrum, which rapidly decreases above 1600 keV. There is a gamma-ray peak at 511 keV due to pair production events occurring outside the detector; the associate annihilation photons can be absorbed in the detector. There are also two prominent low-energy gamma-ray lines visible in the spectrum at 560 keV and 651 keV. These are the two most likely gamma-ray emissions from the absorption of thermal neutrons by cadmium, which is obviously present in the CdZnTe detector. Also shown in the three- and four-pixel spectra is a peak near 3.4 MeV. This is most likely the double escape peak from the 4.4 MeV gamma ray generated by the PuBe neutron source itself.

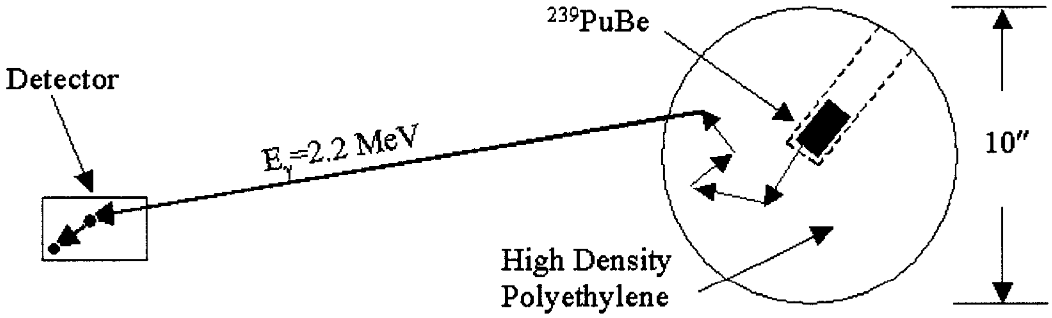

Figure 7.14. Ilustration of the high-energy distributed source experiment. The PuBe neutron source is placed inside a high-density polyethylene sphere, which is located to the side of the detector.

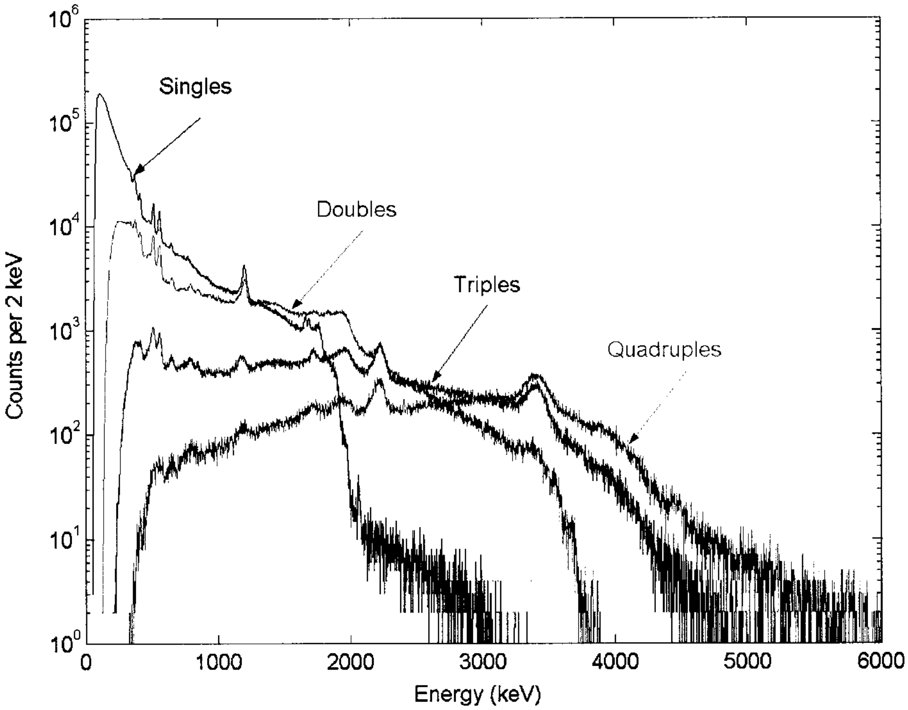

Figure 7.15. One-, two-, three-, and four-pixel energy spectra observed from the $^1H(n,\gamma)^2H$ spherical gamma-ray source. The effects of limited dynamic range are evident in high-energy cutoffs for each spectrum.

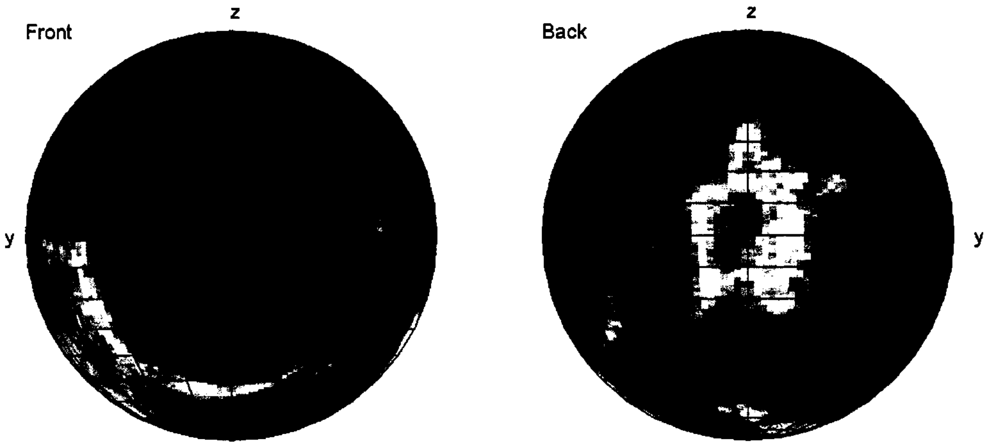

Figure 7.16. Backprojection image of 2.2 MeV spherical source located to the side of the detector.

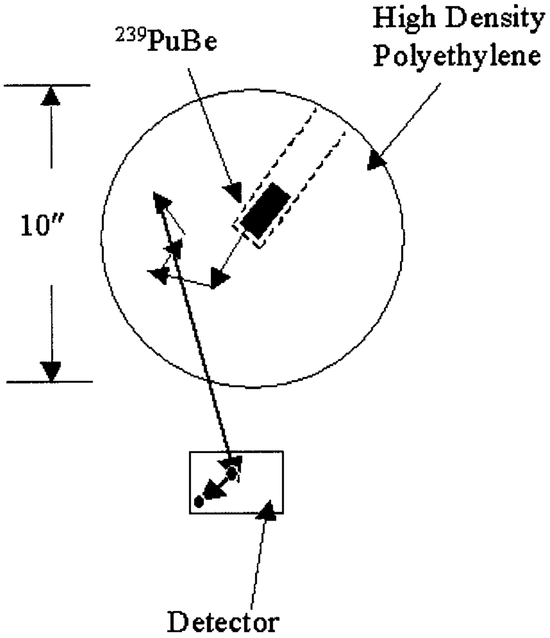

Figure 7.17. Illustration of the revised high-energy distributed source experiment. The moderating sphere is placed above the detector.

Using only the two-pixel sequences at 2.2 MeV and rejecting nearest neighbor pixels yields the backprojection image shown in Figure 7.16. The source appears in the correct location in the image, although the statistics were too poor to observe the spherical shape of polyethylene. The ring-like structure on the front hemisphere is due to incorrectly sequencing the two-pixel sequences, as discussed in Chapter 6. Note that it occurs about 105° away from the true source position as predicted.

To obtain better statistics, the experiment was repeated with the moderating sphere above the detector, as illustrated in Figure 7.17. In this experiment the center of the sphere was only about 34 cm from the detector. The count rate increased dramatically, and the size of the source in the field-of-view also increased. The backprojection image of the source is shown in Figure 7.18 using full-energy two-pixel sequences in which events are separated by at least one pixel. The correct source location can be found. The diamond shape present in the background around the hotspot is a result of charge sharing between corner pixels. These sequences have not been eliminated.

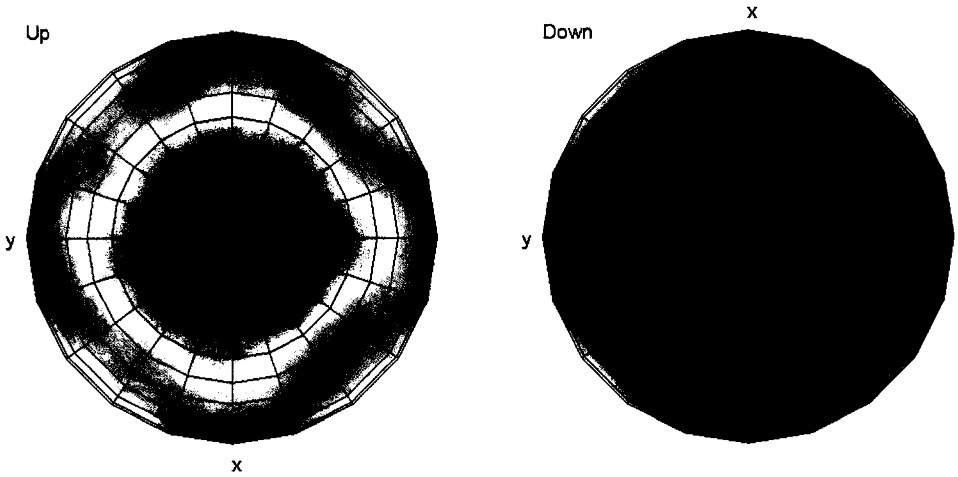

Figure 7.18. Backprojection image of spherical gamma-ray source located above the detector. Sequences with two events in *x* and *y* neighboring pixels have been discarded.

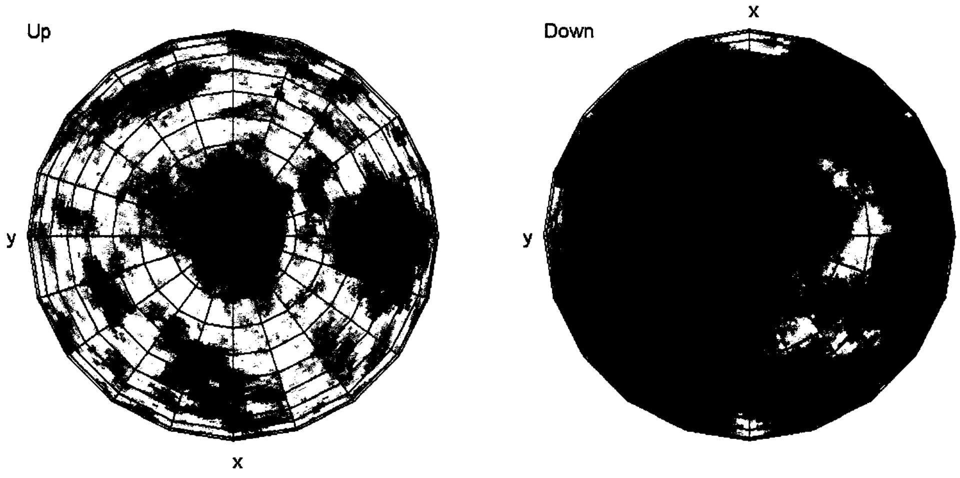

Figure 7.19. Backprojection image of spherical gamma-ray source above the detector discarding sequences in which two events occur in pixels that neighbor in any direction.

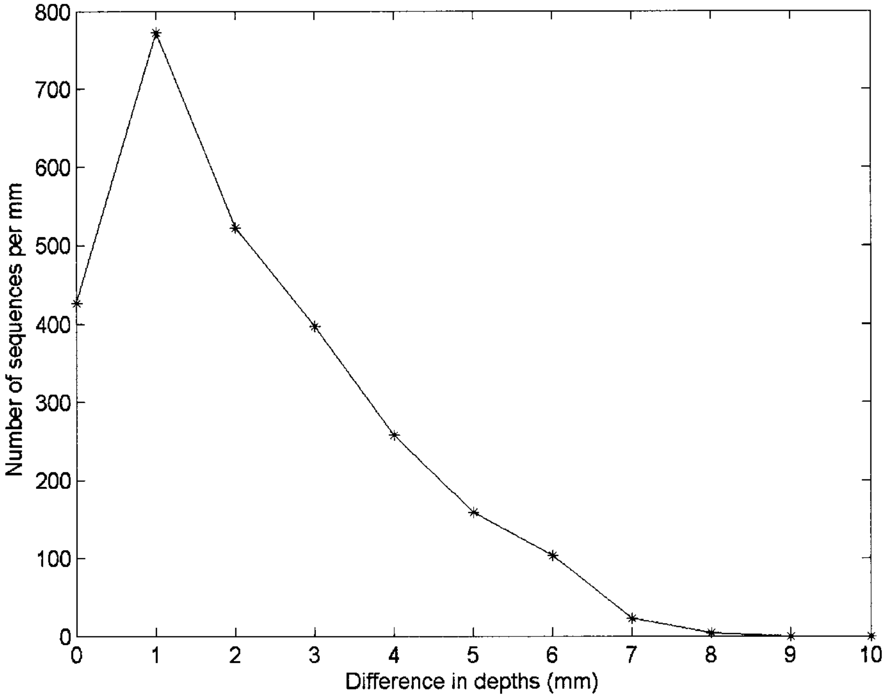

Figure 7.20. Distribution of the difference in event depths in two-pixel sequences. The average difference in depth is just over 2 mm.

If an attempt is made to eliminate even the charge sharing between corner pixels, a much different image is obtained, as seen in Figure 7.19. In this backprojection image if any of the eight neighboring pixels collect charge, the sequence is discarded. There is actually a cold spot at the top of the image sphere where the source should be. Although it may be possible to accept that the source is above as opposed to below the detector, the image in Figure 7.19 would appear to be due to a ring source, as opposed to spherical.

This effect is caused by several phenomena occurring in the detector simultaneously. First, the dynamic range of the ASICs and the sequence reconstruction algorithm limit the calculated Compton scatter angles to the range 40°-70°. Second, the difference in depth between any two interactions is not typically large. Figure 7.20 shows the measured depth difference for two-pixel sequences in which events do not occur in any neighboring pixels. The average difference in depth between events is just over 2 mm. (This is comparable to simulated data which shows an average depth difference of 2.5 mm under similar conditions.) Finally, sequences with neighbor pixels collecting charge are excluded.

To illustrate the effect that these factors have on imaging the sphere above the detector consider Figure 7.21. The red and blue cones represent the minimum and maximum backprojection cone angles, respectively. With small depth differences and at least 2.4 mm lateral spacing between events the inclination angle is typically only between 20° and 30°. In this way few backprojection cones reach the center of the sphere, and only gamma rays that originate from the periphery of the sphere will be imaged. The gamma rays from the central region of the sphere can only be observed if the lateral distance between events is small or the depth difference is large.

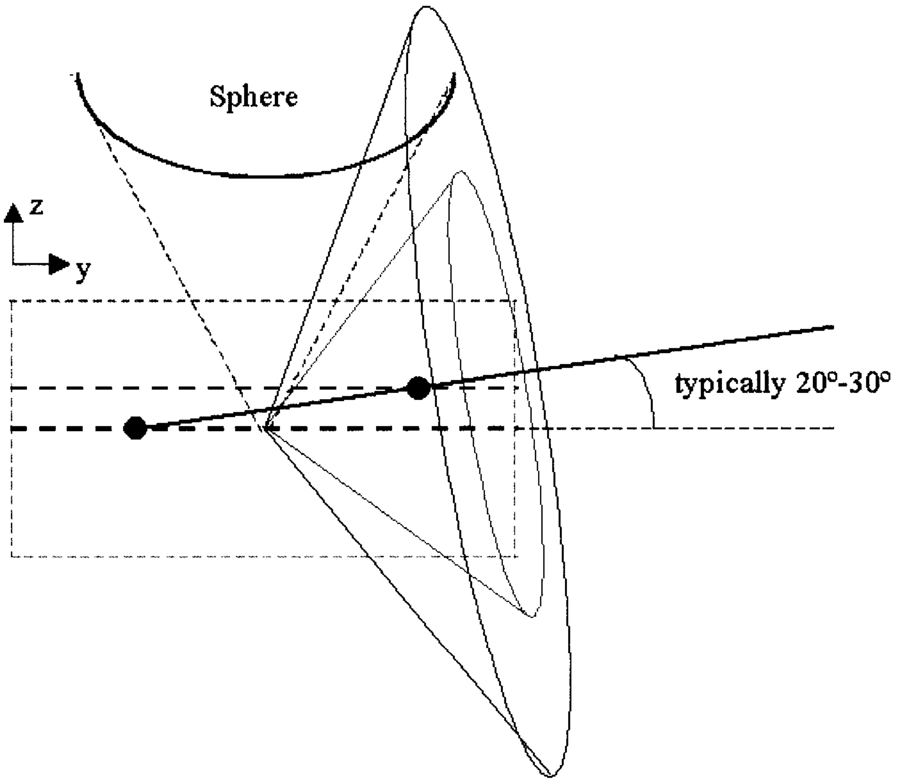

Figure 7.21. Illustration of the effects of limited dynamic range and small depth differences in two-pixel sequences for a source above the detector. The red and blue cones represent the minimum and maximum cone angles, respectively.

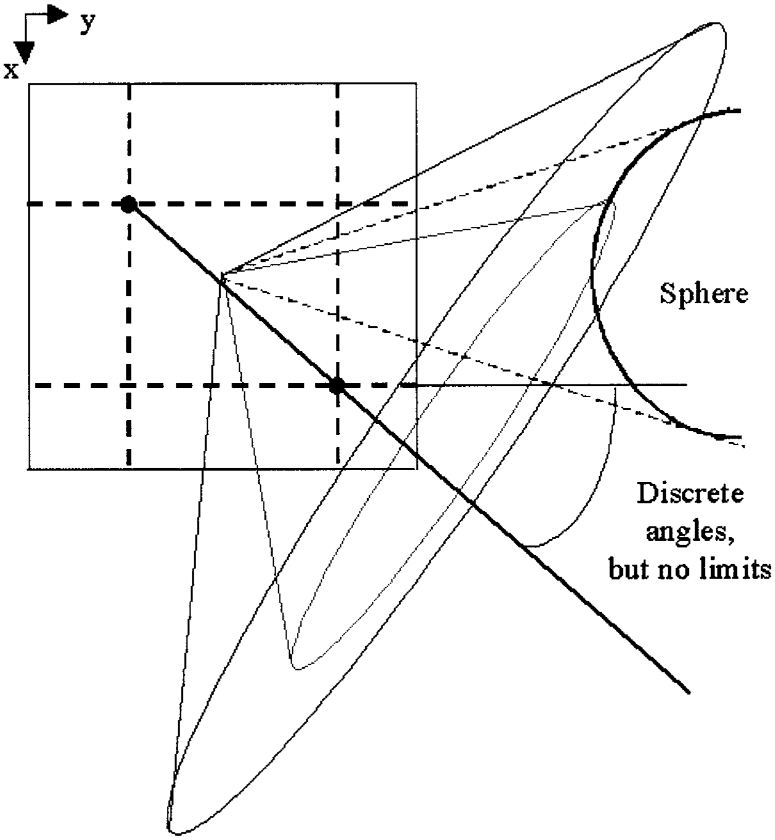

Figure 7.22. Illustration of the effects of limited dynamic range and small depth differences in two-pixel sequences for a source to the side of the detector.

The effects of the dynamic range and charge sharing on a sphere located to the side of the detector are not as severe. As illustrated in Figure 7.22 the backprojection cones can overlap the entirety of the sphere because the cone axis can rotate in the *x*-*y* plane. Two events can occur in the same row of pixels, whereas two events cannot occur under the same pixel. This is defining difference between a source located above the detector and one located to the side. It is important to note that the inclination angle of the backprojection cone with respect to the image sphere equator is still limited for a source located to the side, and some blurring is expected in the image along the azimuthal direction. This is observed somewhat in Figure 7.16, where the source hotspot extends over 40° in the azimuthal direction and only about 20° in the lateral angular dimension.

The experiments discussed in this chapter demonstrate that a single CdZnTe detector can be operated successfully as a Compton imager. The intrinsic efficiency measured at 1.84% is less than predicted by simulations, but is still three orders of magnitude better than the previous two-detector design. The imaging resolution of 17° FWHM was experimentally confirmed using two sources, and sources with different energies were easily distinguished. The high energy experiments were successful as well, despite the significant loss in efficiency due to the limited dynamic range. For the current detector system, high-energy sources to the side of the detector yield better images than sources above the detector due to eliminating neighbor sequences (in an attempt to reduce charge sharing effects) in conjunction with the limited dynamic range.

7.6 References

[1] Y. Du, "Development of a prototype Compton scattering camera using 3-D position sensitive CZT detectors," in *Nuclear Engineering and Radiological Sciences*. Ann Arbor: University of Michigan, 2001, pp. 137.

[2] M. J. Berger, J.H. Hubbell, S.M. Seltzer, J.S. Coursey, D.S. Zucker, "XCOM: Photon cross sections database," [Online], 2004.

[3] M. Woodring, D. Beddingfield, D. Souza, G. Entine, M. Squillante, J. Christian, A. Kogan, "Advanced multi-dimensional imaging of gamma-ray radiation," *Submitted to Nuclear Instruments and Methods in Physics Research*, 2002.

[4] T. B. Gosnell, "Determining the presence of HEU with passive detection methods," *Arms Control and Nonproliferation Technologies*, vol. Spring 2001, pp. 46-47, 2001.

[5] G. F. Knoll, *Radiation Detection and Measurement*, 3rd ed. New York: John Wiley & Sons, Inc, 2000.

CHAPTER 8

SUMMARY AND FUTURE WORK

8.1 Project Summary

The CdZnTe 4π Compton imager was the first successful demonstration of Compton imaging in a single detector with a full 4π field-of-view. The imager consists of a 1.5 cm × 1.5 cm × 1.0 cm CdZnTe detector operated at room temperature. The detector has a planar cathode on one square face, and an array of pixellated anodes on the opposite face. The detector relies on single-polarity charge sensing in which only the motion of electrons generates signals in the detector; holes are severely trapped in CdZnTe. The anodes provide position sensitivity for gamma-ray interactions in two dimensions. The third coordinate is determined by the drift time of electrons. For every gamma-ray interaction in the detector the energy deposited and the three-dimensional interaction position is determined. The position resolution in the lateral dimensions is determined by the pixel pitch of 1.3 mm, while the depth resolution is determined by timing (~1mm). Energy resolution in this detector for two-pixel sequences at 662 keV was measured at 1.91% full-width at half-maximum (FWHM).

Unlike other Compton imaging devices, the sequences of gamma-ray interactions in the detector are not known *a priori*. Two methods were explored to determine the correct sequence order. In two-pixel sequences, the event that deposits the highest (lowest) energy was assumed to occur first if the total energy deposited is higher (lower) than 400 keV. This method worked increasingly well with higher gamma-ray energies. At 662 keV the two-pixel technique succeeded in 73% of simulated full-energy sequences.

For three events in which there are six possible sequence orders a different technique was used. Each sequence was assumed to terminate with a photoelectric event (all of the gamma-ray energy was deposited). Then, the second scatter angle could be calculated for each possible order using the known position information and the known energies independently. The sequence order that minimized the difference between the independently calculated scatter angles was chosen to be the correct sequence. This method, which is highly subject to the position resolution in the detector, was successful at 662 keV in 51% of full-energy sequences. The method improved as the gamma-ray energy increased.

Once the order of interactions in the detector was determined, it was possible to reconstruct the source distribution using the principles of Compton imaging. Two methods were used in this work: backprojection and maximum likelihood estimation. In backprojection each sequence of events results in a cone of probable incident gamma-ray directions. The sum of these cones over many sequences yields the position of the source. The image resolution using backprojection was very poor at 662 keV (~68° FWHM measured for a source to the side of the detector). Backprojection was only useful for imaging point sources that were widely separated. Maximum likelihood estimation was also used in this work in order to improve the imaging resolution. A weighting method was introduced that emphasizes the contribution of sequences in which the angular uncertainty was small and reduces the impact of sequences with less information. The weighted maximum likelihood technique (WMLEM) was shown to converge faster than traditional maximum likelihood reconstruction, and yielded a measured imaging resolution at 662 keV of only 17° FWHM after 10 iterations. The WMLEM reconstruction method required approximately 0.1 seconds per sequence per iteration when performed on a personal computer with a 1.1 GHz Pentium III processor. The backprojection method was nearly eight times faster.

Several factors that can degrade the performance of the 4π imager were analyzed. Physics processes, such as Doppler broadening, coherent scatter, and pair production, can degrade the imaging resolution. Coherent scatter was found to have little effect on the backprojection because the scatter angles were found to be less than 10° for most sequences. Pair production sequences will not interfere with imaging if full-energy windowing is performed. Doppler broadening had the largest effect on imaging, and set the minimum angular resolution to a few degrees FWHM in CdZnTe. The anode threshold and dynamic range of the detector system reduced the efficiency by requiring all events to deposit greater than 100 keV and less than 1600 keV. The effect was largest for 300 keV and 2500 keV photons. The techniques used to determine the order of interactions in the detector also affected the performance by limiting the observable angles and creating ring artifacts in the image when the sequences were incorrectly ordered. Finally, an anisotropy was observed when imaging using backprojection sources above the detector compared with sources to the side of the detector. This was a result of the normalization method used in the backprojection process.

The resolution of the imager was tested with two ^{137}Cs sources separated by 18°. The two sources were resolved in the WMLEM image after 10 iterations. No formal stopping criterion was implemented to determine the number of iterations that should be performed. However, the improvement in resolution after 10 iterations was insufficient to justify the additional reconstruction time.

The measured intrinsic efficiency of the detector—defined as the fraction of incident gamma rays that result in imageable sequences—at 662 keV was 1.86%. This was only 44% of the value predicted from simulations. An 18% difference could be explained by the fact that charge sharing was not considered in the simulations, but examination of other factors did not reveal other major causes for the discrepancy. The reduced number of sequences observed in detector compared with the simulations indicates that the simulation parameters—and not the sequence ordering and image reconstruction technique—were most likely to blame for the difference.

Measurements with multiple sources were performed. By using backprojection three point sources with different energies could be identified in the image, although one source dominated due to its high activity. When the image was reconstructed using specific windows for gamma-ray energy the individual point sources were easily identified.

High-energy measurements using the 4π imager were also performed. In one experiment a ^{232}Th disk source was placed above the detector, and the source was successfully located using the emitted 2.6 MeV gamma rays. In another experiment a 1-Ci PuBe neutron source was placed inside a large high-density polyethylene sphere. The neutrons were moderated in the sphere and some were absorbed by hydrogen nuclei, which then deexcited via a 2.2 MeV gamma ray. The sphere was placed to the side and above the detector, and in both cases the location of the sphere could be determined. The dynamic range of the system (1600 keV) limited the imaging efficiency at high energies because many sequences could not be observed. Also, when combined with techniques to reduce the influence of charge sharing on the image, the dynamic range limited the capability to image sources directly above or below the detector. Sources to the side of the detector appeared elongated in the images, but could still be identified.

8.2 Suggestions for Future Work

There are several topics regarding the 4π Compton imager that should be explored in future work. Improvement in the detector system, including reducing the anode thresholds and increasing the dynamic range, will increase the efficiency of the imager. At 2.5 MeV there is a 96% reduction in efficiency due to the dynamic range, and the fraction of observable sequences that are correctly sequenced decreases from 97% to

65%. Also, for high-energy imaging it may be necessary to increase the pixel pitch in order to reduce the charge sharing among pixels. The presence of a double escape peak in the four-event spectrum from 2.2 MeV gamma rays indicates that a 1.2 MeV recoil electron can traverse many pixels.

The sequencing techniques can be improved by including additional information. For example, a probabilistic approach could account for survival probabilities and distances between interactions for both two- and three-pixel sequences. With the current method only 51% of three-event sequences at 662 keV are correctly determined. There is much room for improvement.

The backprojection algorithm currently employs a step response; image pixels that intersect the backprojection cone are given a value of 1 for that sequence, while all other pixels are given a value of 0. It is possible to use a smooth function—perhaps a sum of Gaussian functions, as proposed by Wilderman *et al.*[1]—to improve the resolution obtained through backprojection. Also, defining a proper de-blurring filter, similar to those used in x-ray tomography, would greatly improve the resolution by removing the blur introduced by the backprojection step. In addition near-field imaging can be performed by backprojecting cones from the first interaction site rather than the center of the detector. The imaging resolution should improve as a result. Finally, real-time backprojection reconstruction is possible if the data acquisition software and image reconstruction software are connected. Then, it would be possible to track a slowly moving source near the detector.

There is also more to explore in maximum likelihood reconstruction. First, in this work there was no defined stopping criterion. Determining an appropriate criterion for this detector is important and should be investigated. Furthermore, it may be possible to do almost real-time imaging using the ordered subset techniques proposed by Hudson and Larkin[2] or the block-iterative methods proposed by Byrne[3]. With these methods the data can be separated in time groups, and the resulting maximum likelihood image after one iteration from the first group is used as the starting image of the next group. This process accelerates the convergence of the image. It may be possible to reduce computation time to minutes rather than hours.

Employing the 3-D $f(\theta,\phi,E)$ imaging techniques discussed in Chapter 7 should be possible with both backprojection and maximum likelihood. With this capability the image for any peak in the energy spectrum can be individually identified without having to perform a separate reconstruction for each energy. Furthermore, it should be possible to generate a spectrum based on a section of the field-of-view. This capability would allow a source in the image to be identified by its energy spectrum. Thus, every pixel in the image would have a corresponding energy spectrum, and every energy bin in the spectrum would have a corresponding image. Summing over all energies or all image pixels would give the total image or total energy spectrum, respectively.

This work is the first successful demonstration of 4π Compton imaging in a single detector. The concept has been proven, but there are some areas of detector design, event sequencing, and image reconstruction that can be improved.

8.3 References

[1] S. J. Wilderman, J.A. Fessler, N.H. Clinthorne, J.W. LeBlanc, W.L. Rogers, "Improved modeling of system response in list mode EM reconstruction of Compton scatter camera images," *IEEE Transactions on Nuclear Science*, vol. 48, pp. 111-115, 2001.

[2] H. M. Hudson, R.S. Larkin, "Accelerated image reconstruction using ordered subsets of projection data," *IEEE Transactions on Medical Imaging*, vol. 13, pp. 601-609, 1994.

[3] C. L. Byrne, "Block-iterative methods for image reconstruction from projections," *IEEE Transactions on Image Processing*, vol. 5, pp. 792-794, 1996.

APPENDIX

APPENDIX: Geant4 Simulation Parameters

Geant4[1] is a Monte Carlo physics simulation package available free from the European Organization for Nuclear Research (CERN). It was originally designed for high-energy physics simulations (up to GeV), but a low-energy patch can be included to extend the physics of gamma-ray and charged particle interactions to as low as several keV. However, the effects of finite electron momentum are not included in the model for Compton scatter. As a result, a different patch that properly treats Compton and Rayleigh scatter including the effects of electron momentum (called G4 Low Energy Compton Scattering G4LECS package[2]) at low energies was used.

The purpose of this appendix is to detail the assumptions made in the simulations used throughout this work. Clearly, results reported from simulations have little meaning without a discussion of the parameters under which they were obtained. The modeling of the detector geometry, physics processes, and gamma-ray sources is discussed.

A.1 Detector Geometry

The detector is modeled as a bare crystal with dimensions 1.5 cm × 1.5 cm × 1.0 cm. The square face of the detector is parallel to the *x-y* plane. The material is $Cd_{0.9}Zn_{0.1}Te_{1.0}$ with a density of 6 g/cm^3. The center of the detector is located at the origin. The contacts, ceramic plate, and PVC mount are not included in the simulations. The contacts are extremely thin, only about 100 μm, and the ceramic plate is made of low-atomic number materials. In addition, the 2-mm thick aluminum housing in which the detector sits is also not modeled. In this way, the results presented in this work are not dependent on the particular choice of detector package.

A.2 Physics Processes

Rayleigh scatter, photoelectric absorption, Compton scatter, and pair production are all modeled in the simulations. As previously stated, the effects of finite electron momentum on Compton scatter are included in the simulations. This is extremely important for modeling Compton imagers, in which the Doppler broadening can contribute a significant fraction of the overall angular uncertainty. The effective range cut off is 100 μm, meaning that gamma-rays are not created if their energies are sufficiently low such that they will not travel on average at least 100 μm.

In any real interaction in which the gamma ray loses energy, the electron is ejected and given a kinetic energy equal to the energy lost by the gamma-ray minus the binding energy of the electron. The electron then undergoes multiple scattering in the detector, creating a shower of electrons—an "electron cloud"—and radiating bremsstrahlung as it decelerates. The bremsstrahlung photons also interact in the detector, ejecting more electrons, and the cycle continues until the electrons have less kinetic energy than the binding energy of the outermost atomic shell. Meanwhile, the binding energy from the initial electron ejection is transferred to the ion. The ion traps another electron and deexcites by emitting an x-ray with an energy equal to the binding energy. The x-ray then interacts some distance away from the original interaction site, ejects an electron from another atom, depositing more energy. The location of the initial gamma-ray interaction is blurred by the size of the electron cloud, and if the x-ray energy is large enough to travel outside the electron cloud, then two electron clouds can be created from the single gamma-ray interaction. In this case a single interaction can appear as two. Thus, the proper way to model the energy deposited in the detector is to measure the total energy deposited by all electrons ejected by the gamma ray, bremsstrahlung photons, and x-rays, in addition to all those involved in multiple scattering.

Fortunately, modeling all these processes is not necessary to accurately predict the the performance of the CdZnTe detector. With a pixel pitch of 1.3 mm the highest energy x-ray (Te k_α at 32 keV) rarely escapes from one pixel into the next. The location of the interaction is only known to be under the pixel at some depth within 1 mm. Thus, it is not necessary to track the x-ray interaction locations. Furthermore, if all the energy is deposited in the same location, it is not necessary to add up all the individual energies deposited by electrons. Rather, the energy deposited in the whole process can be determined by simply tracking the energy lost by the gamma ray. This is the method used in the simulations in this work.

Because the electrons are not tracked in the detector, charge sharing is not modeled. When the electron cloud is large enough and the interaction occurs near a pixel boundary, the cloud can divide and be collected by neighboring pixels. Thus, a single interaction may appear as two events if the energy collected by each pixel exceeds the anode threshold. If the energy collected by one pixel is less than the anode threshold, the energy observed on the other pixel will still be reduced from the total energy deposited in the event. See Chapter 6 for a discussion of the effects of charge sharing.

In the case of pair production, the gamma ray loses all of its energy, but this energy is not all deposited at the interaction site. When pair production occurs, the deposited energy is then calculated as the energy of the gamma ray minus $2m_ec^2$ (1022 keV). The 511-keV annihilation photons can travel large distances relative to the pixel size. If a photon is created by annihilation, it is treated like a gamma ray in that its energy loss and interaction locations are tabulated. A single pair production event may result in several observable interactions in the detector.

The number of interactions, positions, and energies deposited from each gamma ray are written to a file during the Geant4 simulations. With data analysis software the precise position and energy data are blurred to better model the actual detector conditions. The pixel under which the interaction occurred is determined, and the x and y

interaction positions are replaced with the location of the center of the pixel. The depth coordinate is blurred with a Gaussian distribution using an uncertainty of 0.5 mm, taking care not to allow depths that are outside the detector volume. The energy, E, is blurred with a Gaussian whose FWHM is given by the relation: $a + b\sqrt{E}$, where a and b are fit to the measured energy resolution data for two-pixel events. This energy spread accounts for variability in charge generation and collection, as well as system noise. In this manner, the precise Geant4 data is altered to better simulate detector conditions.

A.3 Gamma-Ray Sources

The gamma-ray source is usually modeled as a monoenergetic single gamma-ray emitter. Coincident emissions are not considered. Most of the simulations involve 662 keV gamma rays, which are emitted from ^{137}Cs. Technically, ^{137}Cs is a beta emitter. The daughter nucleus ^{137}Ba then deexcites via gamma-ray emission at 661.7 keV. The true source emits some beta radiation, the 662 keV gamma rays, and also bremsstrahlung from the decelerating betas. In the interest of reducing comptutation time and simplifying the program only the gamma rays are modeled in the source distribution here. Because the beta and bremsstrahlung energies are low, the modeling of full-energy sequences are not affected by neglecting this radiation. For simulating polyenergetic sources like ^{133}Ba and ^{22}Na, the gamma-ray energy chosen for a specific history is chosen based on the relative probabilities of observing each energy. Again, no beta or bremsstrahlung radiation is simulated.

The source is modeled as an isotropic emitter. The emission direction is sampled using two angles. The lateral angle is randomly sampled linearly in the interval $[0,2\pi]$. The cosine of the azimuthal angle is then randomly sampled linearly in the interval [-1, 1]. In this way an emission direction is chosen. The sources modeled here are emitted from a point at a distance of 20 cm such that the cathode face is irradiated, unless otherwise stated. Only gamma rays whose trajectories intersect the detector are generated; when any other emission direction results from the 4π sampling, it is discarded, and a new direction is chosen. This technique saves computation time because the gamma rays directed away from the detector are not generated and tracked. A total of 10^6 gamma-rays that intersect the detector are generated for each simulation.

A.4 References

[1] S. Agostinelli, J. Allison, K. Amako, J. Apostolakis, H. Araujo, P. Arce, M. Asai, D. Axen, S. Banerjee, G. Barrand, F. Behner, L. Bellegamba, J. Boudreau, L. Broglia, A. Brunengo, H. Burkhardt, S. Chauvie, J. Chuma, R. Chytracek, G. Cooperman, et al., "Geant4 - a simulation toolkit," *Nuclear Instruments and Methods in Physics Research*, vol. A506, pp. 250-303, 20003.

[2] R. M. Kippen, "G4LECS: Geant4 low-energy Compton scattering package." [Online], 2003.